Strength of Transversely Isotropic Rocks

by

Jianyong Pei

M.S., Civil and Environmental Engineering
Massachusetts Institute of Technology (2004)

Submitted to the Department of Civil and Environmental Engineering
in Partial Fulfillment of the Requirements for the Degree of

Doctor of Philosophy in the field of Civil and Environmental Engineering

at the

Massachusetts Institute of Technology

June, 2008

Signature of Author: _____
Department of Civil and Environmental Engineering
May 22, 2008

Certified by: _____
Herbert H. Einstein
Professor of Civil and Environmental Engineering
Thesis Supervisor

Certified by: _____
Andrew Whittle
Professor of Civil and Environmental Engineering
Thesis Supervisor

Accepted by: _____
Daniele Veneziano
Chairman, Departmental Committee for Graduate Students

Strength of Transversely Isotropic Rocks

by

Jianyong Pei

Submitted to the Department of Civil and Environmental Engineering
in Partial Fulfillment of the Requirements for the Degree of
Doctor of Philosophy in the field of Civil and Environmental Engineering

ABSTRACT

This thesis proposes a new Anisotropic Matsuoka-Nakai (AMN) criterion to characterize the failure of transversely isotropic rocks under true triaxial stress states. One major obstacle in formulating an anisotropic criterion is that it usually involves six stress components, instead of three principal stresses. As such, anisotropic criteria usually lead to complicated mathematical expressions, and cannot be directly visualized in three-dimensional space. This problem is solved by introducing the Material Normal Stress System (MNSS), which is the space formed by the three normal stress components reflecting the material anisotropy. Within this system, the failure behavior of transversely isotropic rocks in conventional triaxial tests can be represented with geometrical features in the MNSS. These features are then incorporated into the failure surface of the original Matsuoka-Nakai criterion in the Material Normal Stress System, resulting in the Anisotropic Matsuoka-Nakai criterion. This criterion, combined with the Coulomb criterion, is validated against both conventional and true triaxial test data, that are collected from an extensive literature review. The combination of the AMN criterion and the Coulomb criterion satisfactorily characterizes the measured strength from an extensive program of true triaxial tests on a schist, which confirms the ability of the proposed criterion. Finally, this combination of criteria is applied to the borehole stability problem. The necessary mud pressure against borehole collapse and the onset of borehole failure are examined.

Thesis Supervisor: Herbert H. Einstein
Title: Professor of Civil and Environmental Engineering

Thesis Supervisor: Andrew J. Whittle
Title: Professor of Civil and Environmental Engineering

Acknowledgement

I am indebted to many people for the work presented in this thesis.

My sincere thanks go to my thesis supervisors, Prof. Herbert Einstein and Prof. Andrew Whittle. Prof. Einstein led me into the wonderful world of rock mechanics. He helped me to choose this topic. His guidance, encouragement, and patience are indispensable for the completion of this work. Prof. Whittle has provided many good thoughts, and offered great help in setting up the theoretical framework. Both professors have invested a great amount of time reading my thesis draft and offered many good suggestions.

I am grateful to Dr. John Germaine and Dr. Lucy Jen. Both of them have offered much help and advice in and out of my research. Their financial support has helped me during the most difficult times.

I would like to thank Ms. Carolyn Jundzilo-Comer and Ms. Shiela Fay for their help and kindness. The friendship of my former and current colleagues must be acknowledged. They are: Guoping Zhang, Eng Sew Aw, Anamika Prasad, Maria-Aikaterini Nikolinakou, Sherif Akl, James Miller.

I am deeply indebted to my wife, Wei. Her support, love, and patience enabled me to complete this work. I would also like to thank my daughter, Allison, who has been showing me the joys of life.

Table of Contents

List of Figures

List of Tables

1 Introduction

The strength of rock is a very important topic in the research and practice of civil engineering. For example, in underground construction shafts, caverns, and tunnels have to remain stable for the entire life time. Recently, the oil industry is drilling deeper and uses inclined boreholes in search of unexplored oil reserves. The strength of rock must be such that no borehole collapse is induced. Other scenarios in which rock strength can be critical include rock slope stability, etc.

Characterization of rock strength in the laboratory started as early as the 19th century. The earliest conventional triaxial tests on rock specimens seem to be reported by Von Kármán (1911) and Böker (1915). Over the years, conventional triaxial tests (including uniaxial compression tests) became standard tests for rock strength determination. Meanwhile, many researchers proposed mathematical models to fit the observed rock strength in conventional triaxial tests. For example, one of the widely used failure criteria was proposed by Hoek and Brown (Hoek and Brown, 1980), based on data from conventional triaxial tests on many different rocks and rock masses.

Nowadays, conventional triaxial failure criteria are still widely used in real world applications, because they require few parameters. There is a significant database of experience accumulated for a range of parameters for different rock types. Besides, the mathematical formulations of these criteria are usually simple, which also facilitates their use in practice. However, it is gradually realized that there are two limitations of the conventional triaxial failure criteria. On the one hand, two of the principal stresses are always equal in the conventional triaxial tests. The conventional triaxial criteria therefore cannot describe the failure of rock under true triaxial stress. On the other hand, these criteria usually assume that the rock is isotropic. Natural rocks, however, are more or less anisotropic. This assumption is not applicable to some sedimentary and metamorphic rocks (for example, shale, slate, schist, etc.).

It is well recognized that the strength of rock does vary with the level of the intermediate principal stress σ_2. In a real project, obviously the three principal stresses are usually not the same. In order to characterize rock strength under a true triaxial stress state, laboratory tests were performed on specimens subject to true triaxial stresses (with three independent principal stresses). It seems that these types of tests were first performed in the 1960's. To date, quite a few rocks have been tested in true triaxial tests, by different researchers (Chang and Haimson, 2000, 2005, 2007; Haimson and Chang, 2000; Hojem and Cook, 1968; Hoskins, 1969; Hunsche, 1990; Mogi, 2007; Takahashi and Koide, 1989; Wawersik et al., 1997; etc.). Mathematical models that describe the strength of rock under true triaxial stresses were also proposed (Lade, 1993; Lundborg, 1972; Wiebols and Cook, 1968; Zhou, 1994; etc.). For example, the modified Lade criterion (Lade, 1993) seems to give good predictions for many different rocks. However,

strength anisotropy (or the directional dependence of strength) was not measured in most of the experimental efforts. As a result, most of the true triaxial failure criteria still treat the rock as an isotropic material.

In general, natural rocks are more or less anisotropic. Typical anisotropic rocks include the sedimentary rocks (e.g. shale, mudrock, sandstone, etc.) and the metamorphic rocks (e.g. slate, schist, phyllite, gneiss, etc.). Research has also been performed to characterize the strength of anisotropic rocks. The behavior of anisotropic rock is different in different directions, which causes difficulties in characterizing their strength. Many experiments have been performed on these materials, most of which are conventional triaxial tests. It is found that the conventional triaxial strength of an anisotropic rock is a function of both the confining pressure and the material orientation. There is a much smaller database of true triaxial tests on anisotropic rocks. Several authors have proposed failure criteria for anisotropic rocks (Tsai and Wu, 1971; Pariseau, 1972; Cazacu, 1998, 1999; etc.), but they have only been validated under conventional triaxial stress states.

To the author's knowledge, there have been no failure criteria that are able to predict the strength of anisotropic rock subject to true triaxial stress states. The research presented in this thesis aims at filling this gap. The strength and failure of rock is a very rich topic. For example, many different failure modes have been observed for anisotropic rock in conventional triaxial tests. It is obvious that one cannot expect to describe all phenomena with one unified model. It is therefore very important to restrict the type of phenomena that will be described by this research. The scope of this research is as follows:

- One specific type of anisotropy, the transverse isotropy, is dealt with in detail in this thesis. Transversely isotropic materials have only one privileged direction, and they have rotational symmetry with regard to this direction. Within planes perpendicular to this direction, the mechanical behavior is isotropic. Rocks with bedded structures, for example, shales, slates, etc., can be considered to be transversely isotropic.
- The research aims at proposing a failure model to describe the *continuous type of strength anisotropy*, i.e. the continuous variation of strength with orientation. This continuous type of strength anisotropy can be caused by microscopic features. For example, in some crystals the density of atoms in different directions are different; clays that have experienced one-dimensional loading have oriented platy clay minerals, etc. Contrary to the continuous type of strength anisotropy, anisotropy can also be caused by macroscopic discontinuities. For example, jointed rocks have anisotropic strength due to the existence of joints, even if the strength of the host rock is isotropic. This type of anisotropy is called a *discontinuous type of strength anisotropy*. It is frequently observed that the failure of transversely isotropic materials possesses both continuous and discontinuous features. Therefore, they are somewhere along the smooth transition from a continuous to a discontinuous type of anisotropy. This research will provide a model to first describe the continuous component of the strength of transversely isotropic rocks. Finally, the proposed continuous criterion will be

used together with a discontinuous criterion to characterize the strength of transversely isotropic rocks.

- Only shear failure under all compressive stress is intended to be captured. There does not seem to be abundant data sets for tensile failure of anisotropic rocks.

The entire thesis is organized in the following manner:

Chapter 2 concentrates on the true triaxial testing on rocks that are close to isotropic (i.e. rocks that do not have anisotropic features like bedding planes, oriented minerals, etc., and the measured strength of them seem to fit in isotropic failure criteria). Experimental results are first collected on these true triaxial experiments. The properties of the rock specimens in each data set, and the instruments are briefly introduced. The measured strength in each data set is tabulated in Appendix A. True triaxial failure criteria for isotropic rocks are then reviewed and discussed. Based on the analysis of collected data, it is found that a convenient way to represent the failure surface of an isotropic rock is to describe its meridian cross-section and its normalized π-plane cross-section. For many of the collected data sets, the π-plane cross-sections are curved triangles. Finally, a failure model is proposed based on the idea of describing the meridian and the π-plane cross-section separately.

Failure of anisotropic rocks is studied in Chapter 3. This chapter is composed of two parts. The first part compiles the experimental data on anisotropic rocks published in the literature. Altogether, the experimental measurements for fifteen different rocks are reported, and they belong to five different rock types (shale, phyllite, slate, schist, and diatomite). The magnitude of strength and the failure modes as functions of the confining pressures and isotropic plane orientations are summarized and discussed in detail. It will be shown that the conventional triaxial strength of anisotropic rocks can be represented by "U" shaped curves with uneven ends. The second part of this chapter concentrates on the existing anisotropic failure criteria, which are categorized into four different types: the empirical criteria, the continuous criteria, the critical plane approach, and the discontinuous models. Some of the existing criteria have been applied to predict the conventional triaxial strength of anisotropic rocks, and they seem to be able to generate the observed "U" shaped curves. However, there does not seem to be a model that gives satisfying results for anisotropic rock in true triaxial tests.

Chapter 4 presents the major result of this research. It proposes a new failure criterion for transversely isotropic rocks under true triaxial stress states. A new approach, the Material Normal Stress System, is introduced. This new system has the ability to describe the coupling between material orientation and principal stress orientation. The stress path of a conventional triaxial test is first examined in the Material Normal Stress System. An isotropic failure criterion, the Matsuoka-Nakai criterion, is then studied. It will be shown that a failure criterion can be visualized in the Material Normal Stress System by a bounding failure surface when the shear stresses are all zero, and by the variation of the geometry of this bounding failure surface with

non-zero shear stresses. Anisotropy is then introduced into both the bounding failure surface, and its geometry variation. The proposed Anisotropic Matsuoka-Nakai criterion is then applied to interpret the experimental results from both conventional and true triaxial tests of transversely isotropic rocks. The agreement between the predicted and the measured strengths is satisfactory.

In Chapter 5, the proposed criterion is applied to the borehole stability problem. Assumptions are made for a borehole at 4000m below ground. Based on the Anisotropic Matsuoka-Nakai criterion, the critical mud pressures that keep the borehole from collapsing and the development of failure around a certain borehole are calculated. The results are consistent with the failures observed in real boreholes.

2 Failure of Isotropic Rocks

2.1 Introduction

Isotropy means that the behavior of the material is the same in all directions. Natural rocks, due to their complicated formation process, mineral composition, and stress history, are rarely isotropic. Whether a rock specimen behaves more or less isotropically can only be known after being tested in the lab. In addition, even if a rock specimen is isotropic with regard to strength, it may not have isotropic stiffness. The word "isotropy" is therefore used here only as an approximation in the sense of strength. In some cases, the strength of rock in different directions is quantitatively measured. For example, before running his true triaxial tests, Mogi (1967) observed that the uniaxial compression strength of a rock specimen in different directions differ less than 5%. In other cases, rock specimens are identified as isotropic because they do not have significant physical features that generate anisotropy, for example, bedding planes, aligned joints, oriented minerals, etc.

In order to describe the behavior of anisotropic rocks, it is necessary to start by studying isotropic rocks. To date, most of the lab experiments are performed on (more or less) isotropic rocks. The results from these tests are analyzed with isotropic constitutive laws, where principal stresses and stress invariants play a major role. The observations and the isotropic formulations, serve as a starting point for further generalization to anisotropy.

Depending on the type of experiment, the stress states a rock specimen is subject to can be divided into two categories: the conventional triaxial stress and the true triaxial stress (or polyaxial stress). In a conventional triaxial test, σ_2 is identical to either the minor or the major principal stresses. The test is called a conventional triaxial compression (CTC) test in the first case, and a conventional triaxial extension test (CTE) in the second. Uniaxial compression (UC) test is a special case of the conventional triaxial compression test, with the minor principal stress $\sigma_3 = 0$. A number of different experiments can create the true triaxial stress state, in which all three principal stresses can be varied independently. Among these experiments, the thick-walled hollow cylinder test (without imposing the torsional shear) and the true triaxial test seem to give reliable measurements of the principal stresses. The biaxial test is another important type of test to create a true triaxial stress state. It can be considered a special case of a true triaxial test, where one of the three principal stresses is always zero. Obviously, the conventional triaxial stress is a special case of the true triaxial stress.

Conventional triaxial compression tests (including uniaxial compression tests) are widely used in practice to obtain the strength of rock. Throughout the years, theoretical endeavors and experimental facts all indicate that the intermediate stress has a considerable effect on rock strength. The effect of the intermediate stress on rock strength was noticed at the beginning of the 20th century, by performing CTC and CTE tests on the same type of rock. Von Kármán (1911) performed conventional triaxial compression tests on cylindrical specimens of Carrara marble, in which the confining fluid pressure was kept constant, and the specimens was brought to failure with increasing axial load. Böker (1915), with the same rock, kept the axial stress constant while increasing the confining pressure to bring the specimens to failure. The strength at the same confining pressure was consistently higher for Böker's tests than for Von Kármán's tests (Figure 2.1). However, the strength difference between Böker and Von Kármán's measurements might be caused by other factors, for example, the accuracy of measurements, the specimen size, the natural heterogeneity of the specimens, the anisotropy of the material, etc. Therefore, it is not a conclusive evidence of the effect of the intermediate stress.

Mogi (1967) compared the CTC and CTE strength of three different rocks: Westerly granite, Dunham dolomite, and Solnhofen limestone. The results from Mogi's tests are plotted in Figure 2.2. Mogi's tests were very carefully controlled. The isotropy of the rocks was verified by UC tests in different directions, and the strength variation with orientation was within 5%. Various corrections were applied to improve the accuracy of strength measurements in CTE tests. According to Mogi's test results, both Westerly granite and Dunham dolomite showed larger CTE strength, which confirmed the finding of Böker. In the case of Solnhofen limestone, the difference between two strengths was not significant.

In order to obtain how rock strength varies continuously with the intermediate stress, it is necessary to apply a true triaxial stress state on rock specimens. Many researchers made their contributions along this line. For example, Handin et al. (1967) reported on thin-walled hollow cylinder tests. Hoskins (1969) performed thick-walled hollow cylinder tests on a few different types of rock. True triaxial tests were reported by Mogi (1969, 1970), Michelis (1985), Hunsche (1990), Smart (1995), Wawersik et al. (1997), etc. Today, the true triaxial test results are available for various types of rock, even though it is still not standard practice.

Meanwhile, theories that can explain the effect of the intermediate stress were also proposed. The earliest theory was proposed by Wiebols and Cook (1968), from an energy point of view. Lundborg (1972) proposed a statistical theory, which seems to be more general than Wiebols and Cook's approach. Mogi (1971) proposed that the failure criterion should be formulated by writing the octahedral shear stress as a function of the average of the major and minor principal stresses. Many existing models were also modified for this purpose, among which the most widely used is the Drucker-Prager model. These theories are more general than the many criteria that describe the strength of rock in conventional triaxial tests. Since the intention of this research is to describe a more general phenomenon, the anisotropic strength, it is necessary to

start from such a general isotropic strength theory.

This chapter first reviews the significant work that advanced the true triaxial test technology, and the various experiments that are reported in the literature. The general isotropic strength theories are then described. In order to achieve more flexibility in modeling, it is proposed that the failure surface should be described by a meridian cross-section (describes the pressure dependence of the rock) and a normalized π-plane cross-section (describes the Lode angle dependence of the rock).

2.2 Tests with True Triaxial Stress States

In order to explore the effect of the intermediate stress, it is necessary to perform experiments that can create true triaxial stress states in the specimen. Mogi (2007) classifies these tests into four categories (Figure 2.3), based on the shape of the specimen and the application of the boundary conditions. According to Mogi's classification, Type (A) test is the hollow cylinder test, while Type (B), (C) and (D) are all true triaxial tests with rectangular prismatic specimens. The difference between Type (B), (C) and (D) tests are the application of stresses, where a thick arrow stands for a solid piston, while a thin arrow stands for fluid pressure. The difference between these two types of boundary conditions will be explained later. This section summarizes the different type of tests that are reported in the literature, and their experimental results.

2.2.1 Hollow Cylinder Test

True triaxial stress state can be created in hollow cylinder tests (Figure 2.4). By independently controlling the internal and external pressures (p_i and p_e, respectively), the radial and tangential stress σ_r and σ_θ at any radius r can be obtained based on the elastic theory:

$$\sigma_r = \frac{R_e^2 p_e - R_i^2 p_i}{R_e^2 - R_i^2} - \frac{R_e^2 R_i^2 (p_e - p_i)}{r^2 (R_e^2 - R_i^2)} \tag{2.1}$$

$$\sigma_r = \frac{R_e^2 p_e - R_i^2 p_i}{R_e^2 - R_i^2} + \frac{R_e^2 R_i^2 (p_e - p_i)}{r^2 (R_e^2 - R_i^2)} \tag{2.2}$$

where R_i and R_e are the inner and outer radius, respectively. Varying the internal and external pressure, different values of σ_r and σ_θ can be obtained. The axial stress σ_z is increased to bring the specimen to failure. Figure 2.5 shows the stress distribution along the wall of the hollow cylinder with $R_e/R_i = 2$, but different p_e/p_i. $p_e/p = 2.0$ in Figure 2.5 (a), while it is 0.5 in Figure 2.5 (b). Obviously, the shear stress $(\sigma_r - \sigma_\theta)/2.0$ is always larger at the inner wall of the hollow cylinder. Therefore, it is usually assumed in the literature that failure initiates from the inner wall.

Handin et al. (1967) used thin walled hollow cylinders to create polyaxial stress state in rock. The materials they tested include limestone, dolomite and glass. This approach was later

criticized by Mogi (2007) to be of low accuracy and repeatability, because in "fabrication of such thin hollow cylinder of brittle rock, generation of micro-cracks is inevitable (Mogi, 2007)".

Hoskins (1969) made use of thick-walled hollow cylinders to create a true triaxial stress state. Hoskins' tests were performed in an altered triaxial pressure cell (Figure 2.6). The rock specimens Hoskins used had 5 cm outer diameter, and 2.5 cm inner diameter. The internal and external pressures were controlled separately to create different principal stress ratios. The principal stresses at the inner wall were calculated with the elastic equations. The specimens were brought to failure by the piston in the axial direction. The materials that Hoskins tested include Bowral Trachyte, Gosford Sandstone, Carrara Marble.

Apart from these rocks, the same researcher also performed hollow cylinder tests on smaller specimens (2.2 cm outer diameter and 1.2 cm inner diameter) on a limestone and a quartz-dolomite rock, together with conventional triaxial compression tests (2.2 cm diameter by 5.7 cm long solid cylinder). The results of all these tests are reported in Table A.1 through Table A.7. A brief description of the physical properties of these rocks can be found at the end of each table.

More recently, Wang and Kemeny (1995) reported on conventional triaxial tests and thick-walled hollow cylinder tests on Apache Leap Tuff. The data are compiled in Table A.8 and Table A.9. The hollow cylinder specimens had an external diameter of 50mm, and internal diameter of 25mm, 16mm and 13mm. They observed that failure of the hollow cylinder initiated from the inner wall.

Thick-walled hollow cylinders, although easier to fabricate and introducing fewer microcracks, are still not ideal for applying a true triaxial stress state. The stress distribution along the radial direction in the wall is not uniform. Both σ_r and σ_θ vary from inner surface to outer surface. The variation depends on both the boundary conditions and the material behavior. On the one hand, the stress gradient may have an effect on the rock strength, which is unknown before the test. Also, at the onset of failure, part of the rock may become plastic and the elastic solutions in Equations (2.1) and (2.2) are not applicable. Therefore, the principal stresses at which the specimens fail can be different from those calculated from the elasticity theory.

2.2.2 True Triaxial Test

In view of the shortcomings of the hollow cylinder apparatus in creating the true triaxial stress conditions, true triaxial testing apparati were designed. The specimens in these tests are usually of rectangular prismatic shape. Three different principal stresses can be simultaneously applied to the three directions on the specimen to create polyaxial stress state. These tests correspond to Type (B), (C), and (D) of Mogi's classification (Figure 2.3).

2.2.2.1 Type (B) True Triaxial Cell

Many of these apparati involve independent loading in three axes, using rigid pistons (Type (B) in Figure 2.3). Due to the friction between the pistons and the surfaces of the specimen, the uniformity of stress in the specimen is in question. In order to overcome this problem, lubrication is usually used to reduce friction. However, the strength measured maybe different for different types of lubrication (Mogi, 2007). Although there is a certain problem with the stress uniformity, this type of true triaxial test apparatus is still popular because it is relatively easy to construct, the load capacity can be very large, and its cost is relatively low.

Hunsche and Albrecht (1990) used this type of true triaxial apparatus to test the strength of rock salt under a true triaxial stress state and at elevated temperature (Figure 2.7). The pistons on the opposite side of the specimen were hydraulically connected so that the center of the specimen did not move even for large deformation. The vertical pistons were equalized by a counter-weight. The maximum force can be applied was 2000 kN per axis. The shape of the specimen was cubical, with a maximum of 20 cm side length. The size of the specimen that was actually used was 5 cm. The use of solid pistons also facilitated the installation of heaters to control the specimen temperature (up to 400 °C).

In Hunsche's tests, the specimens were first loaded isotropically up to the desired isotropic stress level. Then deviatoric load was applied to bring the specimen to failure, where the three principal stresses were changed simultaneously so that the isotropic stress remained constant. A total of 183 tests were performed, under different stress states and temperatures.

2.2.2.2 Type (C) True Triaxial Cell

It is possible to increase the uniformity of stress in the specimen by using fluid pressure in different axes (Type (C) in Figure 2.3). For example, Hojem and Cook (1968) reported on a true triaxial apparatus where both the least and the intermediate principal stresses were applied with copper flat jacks with fluid pressure (Figure 2.8). Rectangular prismatic specimens (6 in Figure 2.8) were used, with the dimension of 1 inch square and 3 inch long. Lateral pressure was applied by two opposing pairs of copper flat jacks (9 in Figure 2.8). These flat jacks press against segmental brass spacers (4 in Figure 2.8), which in turn transfer the pressure to the steel cylinder (3 in Figure 2.8). Hojem and Cook (1968) used their true triaxial cell to study the intermediate stress effect on Karroo dolerite (Figure 2.8).

In the Type (C) true triaxial cell, different fluid pressures must be applied in two perpendicular directions. The two fluid systems thus must be separated. In the design of Hojem and Cook (1968), this is achieved by using two pairs of copper flat jacks. Due to the limited strength of the

thin copper flat jack, the magnitude of the applied stress is limited. From Figure 2.9, it is evident that the maximum intermediate stress is around 6kpsi, which is slightly lower than 45MPa.

2.2.2.3 Type (D) True Triaxial Cell

Mogi (1969, 1970) reported on another type of true triaxial apparatus, where the minor principal stress was applied by fluid pressure, while the intermediate and the major principal stresses were both applied by solid pistons (Type (D) shown in Figure 2.3). This type of apparatus was designed because the minor principal stress has a greater influence on rock strength than the intermediate principal stress. Therefore, the uniformity of the minor principal stress in the specimen is most important. Since only one fluid pressure is used, the entire assembly can be enclosed in a pressure vessel, thus very high fluid pressures can be obtained. In Mogi's design, the minor principal stress was applied by using a thick walled high pressure vessel, so that the minor principal stress σ_3 > 800MPa (Figure 2.10). The intermediate stress was applied by a piston with 300 kN capacity, while the greatest principal stress piston had a capacity of 700 kN. In this way, Mogi's true triaxial apparatus balances the stress uniformity with the load capacity. In order to keep the rock specimen at the same location during loading, the vertical and horizontal loading pistons were suspended by soft springs. During the deformation of the specimen, the center of the specimen can move with the deformation of it, which also contributed to the stress uniformity. It seems that with this design, Mogi solved this problem of reproducibility and accuracy of true triaxial tests (Takahashi and Koide, 1989).

The specimen that Mogi used was a rectangular prism 1.5 cm square by 3.0 cm long. For most of the tests Mogi performed, Teflon sheets were used to reduce the friction between the piston and the rock specimen. In order to prevent the intrusion of Teflon into the specimen, the surfaces of the specimen were jacketed with thin copper sheets.

Mogi tested seven different isotropic homogeneous rocks in the 1970's. These rocks are Dunham dolomite, Solnhofen limestone, Yamaguchi marble, Mizuho Trachyte, Manazuru andesite, Inada granite, and Orikabe monzonite. The strengths measured from different rocks were compiled in Mogi (2007), and are reported in Table A.10 through Table A.16.

Takahashi and Koide (1989) built a larger Mogi type true triaxial cell, and the specimen size they used was 3.5×3.5×7.0cm (maximum size 5.0×5.0×10.0cm). The minor principal stress in their true triaxial cell was $\sigma_3 \leq$ 50MPa, which is much lower then Mogi's apparatus. The different rocks that were testes include: Shirahama Sandstone, Izumi Sandstone, Horonai Sandstone, Yuubari Shale, and Yamaguchi marble. The data are compiled in Table A.17 through Table A.20. The residual strength of Shirahama sandstone and Yuubari shale were also reported, at certain minor principal stresses (Figure 2.11). It was noted that, although the peak strength depends on the intermediate stress, the residual strength stays more or less constant.

Wawersik et al. (1997) reported on the fabrication of new true triaxial cells at Sandia National Lab, which are similar to Mogi's design (Figure 2.12). A smaller and a larger true triaxial cell were designed, and the larger one was more sophisticated. Therefore, only the larger true triaxial cell will be described here. This true triaxial cell was designed to test larger specimens with controllable pore pressure and fluid transport.

The entire assembly is hosted in a cylindrical pressure vessel, with inside diameter 17.8cm. The specimen size is as large as 7.6×7.6×17.8cm. The minor principal stress is again applied with fluid pressure. The intermediate principal stress is applied with a pair of hydraulically loaded nested pistons, which react against the internal wall of the pressure vessel. To insure the uniform stress distribution, a rubber sheet is put between the two pistons. The largest difference between the intermediate and the least principal stresses is 150 MPa, when the least principal stress is 100 MPa.

This triaxial cell has the ability to control pore pressure and fluid transport, by means of the fluid ports on top and bottom of the specimen. The pressure vessel is set on a circular, inflatable seal, so that the center location of the specimen can be readily adjusted to be half of the axial sample shortening. Therefore, it can accommodate large strains up to at least 15%.

Two sandstones, the Gosford sandstone and the Castlegate sandstone, were tested with this true triaxial cell. The experiments on Gosford sandstone were intended to determine the shape of the failure surface on the π-plane. The stress invariants at failure were reported in Wawersik et al. (1997), and are shown in Table A.21. Principal stresses at failure are calculated based on these stress invariants.

Haimson et al. (2000) described a new true triaxial cell at the University of Wisconsin (Figure 2.13). The structure of the apparatus is similar to Mogi's, with the minor principal stress applied by fluid pressure while the intermediate and the major principal stresses are applied with solid pistons. However, this triaxial cell is more compact and portable since it uses a biaxial loading apparatus for the intermediate and the major principal stresses (Figure 2.13 (a)). Both stresses are in the horizontal direction, and thus no compression testing machine is necessary. The maximum capacity of this triaxial cell is $\sigma_3 \leq 400$ MPa, while σ_2 and $\sigma_1 \leq 1600$ MPa.

The specimen's shape and size used in this triaxial cell are rectangular prismatic specimens with 19 mm sides and 38 mm long. Stearic acid-based lubricant is used to reduce friction. A few measures were taken to make the stress distribution more uniform in the specimen. Metal spacers are placed between the piston and the specimen (Figure 2.13 (b)). A thin copper sheet is in turn placed between the spacer and the specimen to reduce the localization of the applied load. A thin layer of polyurethane is used to cover the surface of the specimen subject to fluid pressure.

Quite a few different rocks were tested with this true triaxial cell by different researchers. The results of experiments on the following rocks were found from the literature: Westerly granite (Haimson and Chang, 2000), KTB amphibolite (Chang and Haimson, 2000), Long Valley hornfels (Chang and Haimson, 2005), Long Valley metapelite (Chang and Haimson, 2005), Pohang Rhyolite (Chang and Haimson, 2007), and Chelungpu siltstone (Oku et al., 2007). Apart from the Pohang Rhyolite, the measurements for all other rocks are tabulated in Table A.22 through Table A.26.

2.2.3 Other Types of Tests

Apart from the true triaxial cells with rectangular prismatic specimens, Smart (1995) presented a design that uses a cylindrical specimen to create true triaxial stress conditions with the trapped tube concept (Figure 2.14). In Smart's design, the pressure on the specimen is supplied by 24 PVC tubes that surround the specimen. The PVC tubes were heat treated so that on one side they are in close contact with the specimen, while on the other side they press against the inner wall of the cell. Since these tubes have limited burst pressure, the largest magnitude of stress is around 50 MPa, with the pressure difference between adjacent tubes less than 7 MPa. The tubes are arranged to apply an elliptical stress distribution on the specimen surface.

2.3 Strength Theories of Isotropic Rock

Many failure criteria have been proposed to characterize the strength of rock. Many of these criteria are formulated with only two principal stresses, σ_1 and σ_3. These criteria, although ignoring the effect of the intermediate principal stress, are widely used because of their simplicity and small number of parameters. Since the effect of the intermediate principal stress was noticed, there have been many researchers who proposed various criteria to characterize this effect. Most of these criteria are phenomenological models. These models will be introduced in the principal stress space.

2.3.1 Principal Stresses and Principal Stress Space

The principal stress space is the space formed by the three principal stresses σ_1, σ_2 and σ_3. Note that in this section, the subscripts "1", "2" and "3" do not imply their relative magnitude. Instead, they are used to define the physical axes of the tests. In triaxial tests, the axial stress is denoted by σ_1, and the confining pressures are $\sigma_2 = \sigma_3$. Therefore, σ_1 can be smaller than σ_2 and σ_3 in CTE tests. In true triaxial tests, σ_1 stands for the stress that is changed to bring the specimen to failure. It is also the greatest principal stresses if it is increased to fail the specimen.

A stress state can be represented by one point (σ_1, σ_2, σ_3) in the principal stress space. In the

principal stress space, the hydrostatic line is defined as the line where $\sigma_1 = \sigma_2 = \sigma_3$. Any plane in this space that is perpendicular to the hydrostatic line is defined as a π-plane (shown in Figure 2.15). A vector in this space can be decomposed into a volumetric component and a deviatoric component:

$$\begin{pmatrix}\sigma_1\\ \sigma_2\\ \sigma_3\end{pmatrix} = \begin{pmatrix}(\sigma_1+\sigma_2+\sigma_3)/3\\ (\sigma_1+\sigma_2+\sigma_3)/3\\ (\sigma_1+\sigma_2+\sigma_3)/3\end{pmatrix} + \begin{pmatrix}(2\sigma_1-\sigma_2-\sigma_3)/3\\ (-\sigma_1+2\sigma_2-\sigma_3)/3\\ (-\sigma_1-\sigma_2+2\sigma_3)/3\end{pmatrix} \tag{2.3}$$

Obviously, the volumetric component is a vector along the hydrostatic line, while the deviatoric component is a vector within the π-plane.

The same point (σ_1, σ_2, σ_3) can also be represented by a polar coordinate system (r, θ, z), based on the decomposition shown in Equation (2.3). The deviatoric component is within the π-plane, the length and direction of which are represented by (r, θ). As shown in Figure 2.15, $\theta = 0°$ coincides with the projection of the σ_1 axis on the π-plane. The hydrostatic line is the Z axis, where $Z = (\sigma_1+\sigma_2+\sigma_3)/\sqrt{3}$ gives the length of the volumetric component in Equation (2.3). In the polar system, a π-plane has the equation of Z = constant.

The general stress tensor usually has six independent components: three normal stresses σ_x, σ_y, σ_z, and three shear stresses σ_{yz}, σ_{zx}, σ_{xy}. When the coordinate system is rotated, these components change accordingly. However, stress invariants are indifferent to coordinate system transformations. The three invariants for the stress tensor are:

$$\begin{aligned} I_1 &= \sigma_x+\sigma_y+\sigma_z = \sigma_1+\sigma_2+\sigma_3\\ I_2 &= -\sigma_x\sigma_y-\sigma_y\sigma_z-\sigma_z\sigma_x+\sigma_{xy}^2+\sigma_{yz}^2+\sigma_{zx}^2 = -(\sigma_1\sigma_2+\sigma_2\sigma_3+\sigma_3\sigma_1)\\ I_3 &= \sigma_x\sigma_y\sigma_z+2\sigma_{xy}\sigma_{yz}\sigma_{zx}-\sigma_x\sigma_{yz}^2-\sigma_y\sigma_{zx}^2-\sigma_z\sigma_{xy}^2 = \sigma_1\sigma_2\sigma_3 \end{aligned} \tag{2.4}$$

Sometimes, the following invariants are used:

$$\begin{aligned} &\mathrm{tr}(\boldsymbol{\sigma}) = \sigma_x+\sigma_y+\sigma_z = I_1\\ &\mathrm{tr}(\boldsymbol{\sigma}^2) = \sigma_x^2+\sigma_y^2+\sigma_z^2+2(\sigma_{yz}^2+\sigma_{zx}^2+\sigma_{xy}^2) = I_1^2+2I_2\\ &\mathrm{tr}(\boldsymbol{\sigma}^3) = \sigma_x^3+\sigma_y^3+\sigma_z^3+3\sigma_x(\sigma_{zx}^2+\sigma_{xy}^2)+3\sigma_y(\sigma_{yz}^2+\sigma_{xy}^2)+3\sigma_z(\sigma_{yz}^2+\sigma_{zx}^2)+6\sigma_{yz}\sigma_{zx}\sigma_{xy} = I_1^3+2I_1I_2+3I_3 \end{aligned} \tag{2.5}$$

The stress deviator tensor $\mathbf{s}$ is defined as:

$$\mathbf{s} = \boldsymbol{\sigma} - \frac{I_1}{3}\mathbf{I} \tag{2.6}$$

where $\mathbf{I}$ is the identity tensor. The three invariants for the stress deviator tensor are:

$$\begin{aligned} J_1 &= \mathrm{tr}(\mathbf{s}) = 0\\ J_2 &= \frac{1}{2}\mathrm{tr}(\mathbf{s}^2) = \frac{1}{3}(I_1^2+2I_2) = \frac{1}{6}[(\sigma_x-\sigma_y)^2+(\sigma_y-\sigma_z)^2+(\sigma_z-\sigma_x)^2]+\sigma_{xy}^2+\sigma_{yz}^2+\sigma_{zx}^2\\ J_3 &= \frac{1}{3}\mathrm{tr}(\mathbf{s}^3) = \frac{1}{27}(2I_1^3+9I_1I_2+27I_3) \end{aligned} \tag{2.7}$$

The invariants that are most frequently used are I_1, J_2 and the Lode angle λ, which is defined as:

$$\lambda = -\frac{1}{3}\sin^{-1}\left[\frac{3\sqrt{3}}{2}\frac{J_3}{J_2^{3/2}}\right] \tag{2.8}$$

The physical meaning of the Lode angle is better revealed by another equivalent expression:

$$\lambda = \arctan\left(\frac{1}{\sqrt{3}}\frac{2\sigma_2-\sigma_1-\sigma_3}{\sigma_1-\sigma_3}\right) = \arctan\left[\frac{1}{\sqrt{3}}\left(\frac{\sigma_2-\sigma_3}{\sigma_1-\sigma_3}-\frac{\sigma_1-\sigma_2}{\sigma_1-\sigma_3}\right)\right] \tag{2.9}$$

If $\sigma_1 > \sigma_2 > \sigma_3$ is assumed, then the Lode angle shows the relative location of σ_2 between σ_1 and σ_3. In conventional triaxial compression tests, $\sigma_2 = \sigma_3$ and $\lambda = -30°$ (or $-\pi/6$). In conventional triaxial extension tests, $\sigma_2 = \sigma_1$ and $\lambda = 30°$ (or $+\pi/6$). This is illustrated in Figure 2.15.

In the polar representation (r, θ, Z), the three coordinates can be easily linked with these invariants. Z is linked with I_1 by:

$$Z = \frac{I_1}{\sqrt{3}} \tag{2.10}$$

Z indicates the volumetric stress level, or the pressure in the specimen. Any criterion that has Z as its parameter describes the pressure dependence. The volumetric stress level is also represented by the octahedral normal stress:

$$\sigma_{oct} = \frac{\sigma_1+\sigma_2+\sigma_3}{3} \tag{2.11}$$

Clearly, I_1, Z, and σ_{oct} have the same physical meaning, but differ only in scalar magnitude.

The coordinate r is associated with J_2 by:

$$r = \sqrt{2J_2} \tag{2.12}$$

J_2 is a measure of the deviatoric stress level. The octahedral shear stress is defined as:

$$\tau_{oct} = \sqrt{\frac{2}{3}J_2} \tag{2.13}$$

Therefore, J_2, r, and τ_{oct} are also linked by scalar relationships.

Finally, θ is geometrically equivalent to the Lode angle but with a few differences (Figure 2.15). The original definition of the Lode angle is from –30° to 30°, due to the assumption that $\sigma_1 \geq \sigma_2 \geq \sigma_3$. Since this is not imposed in the discussion here, θ ranges from 0° to 360°. $\theta = 0°$ corresponds to $\lambda = -30°$. Also, θ is taken to be positive in the clockwise direction. θ can be calculated with the principal stresses by:

$$\tan\theta = \frac{\sqrt{3}(\sigma_3-\sigma_2)}{2\sigma_1-\sigma_2-\sigma_3} \tag{2.14}$$

The r axis in θ direction is denoted r_θ. Based on this definition, r_{60} through r_{300} are shown in

Figure 2.15. Along these axes, two of the principal stresses are equal and the stress state is the conventional triaxial stress state. Starting from an isotropic stress state, the stress path is conventional triaxial compression along r_0, r_{120}, r_{240}, while it is conventional triaxial extension along r_{60}, r_{180}, r_{300}.

Since the polar coordinate (r, θ, Z) is just another way to represent a stress point (σ_1, σ_2, σ_3), the principal stresses can be expressed as functions of (r, θ, Z):

$$\begin{aligned}\sigma_1 &= \frac{Z}{\sqrt{3}} + \frac{\sqrt{6}}{3} r\cos\theta \\ \sigma_2 &= \frac{Z}{\sqrt{3}} - \frac{\sqrt{6}}{3} r\sin(\frac{\pi}{6} + \theta) \\ \sigma_3 &= \frac{Z}{\sqrt{3}} - \frac{\sqrt{6}}{3} r\sin(\frac{\pi}{6} - \theta)\end{aligned} \tag{2.15}$$

Failure is usually described by a continuous failure surface in principal stress space (Figure 2.16). In order to better understand its geometry and physical significance, several cross-sections of the surface are often studied. They are the π-plane cross-section, the triaxial plane cross-section, and the biaxial plane cross-section.

The π-plane cross-section is the intersection of the failure surface with a π-plane at a certain pressure level Z (Figure 2.17 (a)). The distance from a point on this cross-section to the origin is defined as the radius of this π-plane cross-section. The radius of the π-plane cross-section will be denoted by R (instead of r), which signifies that this is the location at failure. Clearly, R is a function of both θ and Z: $R = R(\theta,Z)$. The shape of the π-plane cross-section determines how R varies with θ at a certain Z level. This variation will be termed the *Lode angle dependence* of the strength. For an isotropic material, the failure surface on the π-plane thus possesses the six fold symmetry. There must be $R_0 = R_{120} = R_{240}$, and $R_{60} = R_{180} = R_{300}$ (R_0 through R_{300} shown in Figure 2.17 (a)).

The triaxial plane is the plane (r_0, Z) in Figure 2.16. This plane is described by the equation $\sigma_2 = \sigma_3$. Any point on this plane describes a conventional triaxial stress state, hence its name. The intersection of the triaxial plane with the failure surface contains two branches: one describes the variation of R_0 with Z, the other the variation of R_{180} with Z (Figure 2.17 (b)). Physically, they correspond to the conventional triaxial compression test and extension test, respectively. Together, they show how the size of the π-plane cross-section varies with the octahedral stress level. Therefore, they describe the *pressure dependence* of the material.

The biaxial plane is a plane where one of the principal stresses is always zero. Figure 2.17 (c) shows the intersection of the plane $\sigma_2 = 0$ with the failure surface. This intersection is a closed curve, and it describes the failure of the material in a biaxial test.

2.3.2 Conventional Triaxial Models

Although the intention of this section is to review the more general true triaxial failure criteria, it is necessary to first examine some of the very widely accepted conventional triaxial failure criteria. Many of the true triaxial failure criteria are extensions or modifications of these basic criteria.

The most widely used criterion is probably the Coulomb criterion. According to this criterion, the shear strength on a plane is determined linearly with the normal stress on the same plane:

$$|\tau| = S + \mu\sigma_n \tag{2.16}$$

where S is the cohesion, and μ is the coefficient of internal friction. The Coulomb criterion can also be expressed with the major and minor principal stresses:

$$\sigma_1 = \frac{1+\sin\phi}{1-\sin\phi}\sigma_3 + 2S\frac{\cos\phi}{1-\sin\phi} \tag{2.17}$$

where ϕ is the friction angle, and $\mu = \tan(\phi)$. The Coulomb criterion is plotted in σ_1 vs. σ_3 space in Figure 2.19 (a).

Another widely used criterion is the Hoek-Brown criterion, which was proposed by Hoek and Brown (1980). This is an empirical criterion that can be applied to both intact rock and rock masses. It seems that this criterion is developed purely by curve fitting of conventional triaxial compression data. According to this criterion, the conventional triaxial compression strength of rock is expressed as:

$$\sigma_1 = \sigma_3 + C_0\left(m\frac{\sigma_3}{C_0} + s\right)^{1/2} \tag{2.18}$$

where C_0 is the uniaxial compression strength of the rock, while both m and s are material parameters depending on how broken the rock mass is. For intact rocks, s = 1. The value of m and s for different types of intact rock and rock masses can be found in Hoek and Brown (1980). The Hoek-Brown criterion, when plotted in σ_1 vs. σ_3 space, is a parabola (Figure 2.19 (b)).

The Griffith (1924) Criterion is based on fracture mechanics. It assumes that a rock specimen contains many randomly oriented cracks. When subject to a certain stress field, tensile stresses develop along crack boundary. Crack propagation initiates when the tensile stress along the crack boundary reaches a critical value. The following is a reinterpretation of Griffith's (1924) stress based failure criterion by Hoek (1980). Assuming that $\sigma_1 > \sigma_3$, for a particular crack oriented β degree from σ_1 direction (Figure 2.18), crack propagation starts when:

$$(\sigma_1 \sin^2\beta + \sigma_3\cos^2\beta) - \sqrt{(\sigma_1^2\sin^2\beta + \sigma_3^2\cos^2\beta)} = -2T_0 \tag{2.19}$$

where T_0 is the magnitude of the tensile strength of the specimen, which is positive. Since cracks

are randomly oriented, the specimen fails in the orientation that satisfies Equation (2.19) first. This critical orientation is:

$$\cos\beta = \frac{\sigma_1 - \sigma_3}{2(\sigma_1 + \sigma_3)} \tag{2.20}$$

This critical orientation only exists when $\sigma_1+3\sigma_3>0$. If $\sigma_1+3\sigma_3<0$, then $\sigma_3<0$ is required, and the specimen fails in tension. Substituting Equation (2.20) to (2.19), the failure of the specimen occurs at:

$$\begin{aligned} &(\sigma_1 - \sigma_3)^2 = 8T_0(\sigma_1 + \sigma_3) && \text{if } \sigma_1 + 3\sigma_3 > 0 \\ &\sigma_3 = -T_0 && \text{if } \sigma_1 + 3\sigma_3 < 0 \end{aligned} \tag{2.21}$$

The Griffith criterion, using Hoek's reinterpretation, is plotted in the σ_1 vs. σ_3 space in Figure 2.19 (c).

2.3.3 Soil Mechanics Models

The modified Lade criterion is based on the original Lade criterion, which was proposed by Lade (1977) to describe the plasticity of soils. It was later expanded to describe the behavior of concrete (Lade, 1982) and rock (Kim and Lade, 1984). This criterion takes the form:

$$(I_1'^3 / I_3' - 27)(I_1' / p_a)^m = \eta_1 \tag{2.22}$$

in which p_a is the atmospheric pressure in the same unit of the stresses, so that I'_1/p_a is a dimensionless number. I'_1 and I'_3 are the first and third invariants of the transformed stress tensor, where the normal stresses are transformed by:

$$\sigma_x' = \sigma_x + ap_a; \sigma_y' = \sigma_y + ap_a; \sigma_z' = \sigma_z + ap_a \tag{2.23}$$

With this transformation, the modified Lade criterion produces non-zero cohesion when the material is sheared with $I_1 = 0$. Both m and η_1 are material parameters. Lade (1993) suggested that they can be determined by plotting $(I_1'^3 / I_3' - 27)$ vs. (p_a / I_1') on a log-log diagram and fitting a straight line through the data points. Lade (1993) evaluated this criterion based on experimental data from many different rocks. In most of the case, the agreement is good to excellent. Based on this evaluation, Lade (1993) suggested that typical values of the three parameters are: $a = 100$, $\eta_1 = 10^6$, and $m = 1.0$.

The modified Lade criterion describes non-linear pressure dependence at $m > 0$, and the non-linearity is controlled by both η_1 and m. In order to illustrate this point, the triaxial plane cross-section for the combination of $\eta_1 = 10^6$, 10^8 and $m = 1$, 2 are shown in Figure 2.20 (with $a = 100$ in all combinations). Non-linearity seems to increase with increasing m and decreasing η_1. When η_1 is as large as 10^8, both $r_0(Z)$ and $r_{180}(Z)$ are very close to linear. Increasing m from 1 to 2 only brings in slightly more non-linearity. When η_1 is reduced to 10^6, significant non-linearity is obtained with the same increase of m. It is also shown that the tip of the failure surface is

located at $Z = -a/\sqrt{3}$. The parameter a does not change the shape of the failure surface.

In the π-plane, the modified Lade criterion has a curved triangular shape. This shape is determined by a shape factor β_s, which is defined as:

$$\beta_s(Z) = \frac{R_{180}(Z)}{R_0(Z)} \tag{2.24}$$

The variation of β_s with Z as specified by the modified Lade criterion can be calculated based on the triaxial plane cross-section. The results are shown in Figure 2.21 for the same combination of η_1 and m. The shape varies continuously with the value of β_s. As shown in Figure 2.23. β_s is between 0.5 and 1. When β_s = 0.5, the shape is a right triangle. When β_s = 1.0, the shape is a circle. According to Figure 2.21, β_s approaches 0.5 at the tip of the failure surface, and it gradually increases with increasing Z. Therefore, the π-plane cross-section of the modified Lade criterion is close to a triangle at the tip, and gets more rounded with increasing Z. The rate of variation, however, is dependent on the values of η_1 and m.

The Matsuoka-Nakai criterion was first proposed by Matsuoka and Nakai (1974) based on the concept of "spatial mobilized plane" (SMP). The mobilized plane is the plane where the shear to normal stress ratio is maximized. Physically, it is the plane where soil particles are most mobilized to move by friction. The orientation of this plane can be obtained by drawing a line tangent to the Mohr circle (Figure 2.24 (a)). In a two dimensional case where only σ_1 and σ_3 are considered, the normal direction of the mobilized plane is $(45°+\phi^m_{13}/2)$ from the σ_1 direction ($\sigma_1 > \sigma_3$ assumed). ϕ^m_{13} is the mobilized friction angle in this stress system. Because $\tan(45° + \phi^m_{13}/2) = \sqrt{\sigma_1/\sigma_3}$, the orientation of this mobilized plane can be obtained by drawing a line connecting $\sqrt{\sigma_1}$ on the σ_1 axis and $\sqrt{\sigma_3}$ on the σ_3 axis (Figure 2.24 (b)). It can be verified that the normal to this mobilized plane, which is a line perpendicular to this line, makes an angle of $(45°+\phi^m_{13}/2)$ from the σ_1 direction. Mobilized planes can be obtained in the (σ_2, σ_3) and (σ_1, σ_2) system following the same procedure.

Matsuoka and Nakai (1974) extended this idea of three two-dimensional mobilized planes to one spatial mobilized plane, which is the triangle enclosed by all three two dimensional mobilized planes. A new yield criterion is proposed stating that soil fails when the shear to normal stress ratio on the spatial mobilized plane reaches a critical value:

$$\frac{\tau_{SMP}}{\sigma_{SMP}} = \sqrt{\frac{I_1 I_2 - 9I_3}{I_3}} = K \tag{2.25}$$

This expression can be rearranged to give the following simplified form:

$$I_2 I_1 - kI_3 = 0 \tag{2.26}$$

in which $k = 9(1+K^2)$. This is the first criterion to use all three stress invariants.

The failure surface of the Matsuoka-Nakai criterion is shown in Figure 2.22. This criterion describes a linear pressure dependence with no cohesion. Therefore, on the triaxial plane, $R_0(Z)$ and $R_{180}(Z)$ are both straight lines through the origin. Its π-plane cross-section is also a curved triangle described by the group of curves in Figure 2.23. The Matsuoka-Nakai criterion matches the Mohr-Coulomb criterion at all its six vertices (shown as point A through F in Figure 2.22).

The group of shapes shown in Figure 2.23 can be described by a uniform formulation. Bardet (1990) proposed the LMN (Lade, Matsuoka-Nakai) dependence as a uniform way to describe the shape of this group of curves. The LMN dependence defines the normalized shape of the π-plane cross-sections with $R'_0 = 1.0$ and $R'_{180} = \beta_s$ (with R' representing the normalized radius). Between $\theta = 0°$ and 60°, $R'(\theta)$ is expressed by:

$$R'(\theta) = \frac{\sqrt{3}}{2}\frac{\beta_s}{\sqrt{\beta_s^2 - \beta_s + 1}}\frac{1}{\cos(\theta'')} \tag{2.27}$$

where θ'' is an intermediate variable defined as:

$$\theta'' = \begin{cases} \frac{\pi}{3} - \frac{1}{6}\cos^{-1}\left[\frac{27}{2}\frac{\beta_s^2(1-\beta_s)^2}{(\beta_s^2-\beta_s+1)^3}\cos^2(3\theta) - 1\right] & \text{if } 0 \le \theta < \frac{\pi}{6} \\ \frac{1}{6}\cos^{-1}\left[\frac{27}{2}\frac{\beta_s^2(1-\beta_s)^2}{(\beta_s^2-\beta_s+1)^3}\cos^2(3\theta) - 1\right] & \text{if } \frac{\pi}{6} \le \theta < \frac{\pi}{3} \end{cases} \tag{2.28}$$

This formulation describes the π-plane cross-section of both the Lade criterion and the Matsuoka-Nakai criterion, hence the name LMN dependence. When β_s varies from 0.5 to 1.0, the Equations (2.27) and (2.28) give the shape of the group of curves shown in Figure 2.23.

2.3.4 Mogi Type Models

Mogi, based on his true triaxial test results, found that when the data are plotted in the τ_{oct} vs. $\sigma_{m,2}$ system, the strength of the specimen tested at different σ_3 and σ_2 nicely follow one line. He thus proposed that a general failure criterion can be formulated as:

$$\tau_{oct} = f(\sigma_{m,2}) \tag{2.29}$$

where $\sigma_{m,2} = \frac{\sigma_1 + \sigma_3}{2}$. This criterion later was widely accepted. For example, Al-Ajmi and Zimmerman (2005) proposed taking f to be a linear function $\tau_{oct} = a + b\sigma_{m,2}$, and termed this linear Mogi criterion the Mogi-Coulomb failure criterion since it reduces to the Coulomb criterion given $\sigma_2 = \sigma_3$. Haimson and Chang (2000) used the power law function $\tau_{oct} = A\sigma_{m,2}^b$ to fit their

true triaxial tests data on Westerly granite, and found good agreement between the fitted curve and the data.

The triaxial plane cross-sections of the Mogi type criteria are shown by two examples (Figure 2.25 (a)). The solid lines are based on the equation of Al-Ajmi and Zimmerman (2006), describing the strength of Dunham Dolomite:

$$\tau_{oct} = 58.32 + 0.5454\sigma_{m,2} \tag{2.30}$$

This equation describes a linear pressure dependence. The dashed lines are based on the equation of from Haimson and Chang (2000), describing the strength of Westerly Granite:

$$\tau_{oct} = 1.51\sigma_{m,2}^{0.89} \tag{2.31}$$

A non-linear pressure dependence is clearly seen.

The π-plane cross-section of these two criteria are shown in Figure 2.25 (b), at Z = 577.3MPa. The shapes of these two criteria are very similar, even though they have very different mathematical forms. Both of them are neither smooth, nor convex. In fact, this non-smoothness and non-convexity seem to be common to the Mogi type criterion. Zhang and Zhu (2007), in an attempt to extend the Hoek-Brown criterion to true triaxial stress, also obtained similar π-plane cross-section for their model. Colmenares and Zoback (2002) showed that the non-convexity can cause numerical problems for the uniqueness of the solution. In some cases, two values of σ_1 can be solved from these criteria at the same σ_2 and σ_3.

2.3.5 Drucker-Prager Type Models

The von Mises criterion was proposed by von Mises (1913) to describe the yielding of metals. According to this criterion, failure occurs when the second invariant of the deviatoric stress tensor reaches a critical value:

$$\sqrt{J_2} = k \tag{2.32}$$

The π-plane cross-section for von Mises criterion is a circle, because it does not depend on the Lode angle. In addition, it is pressure independent since it does not depend on the volumetric stress I_1.

Drucker and Prager (1952) introduced pressure dependence to the von Mises model. The Drucker-Prager model writes:

$$\sqrt{J_2} = \alpha I_1 + k \tag{2.33}$$

This criterion describes linear pressure dependence. Its π-plane cross-section is still a circle, but the radius of the circle increases with Z. The Drucker-Prager model is actually an extension of

the Coulomb criterion. If $\sigma_2 = \sigma_3$ is specified in Equation (2.33), it can be represented in the (r, θ, Z) system by a line (Figure 2.26 (a)):

$$r_0 = \frac{\sqrt{3}}{\sqrt{2}}\alpha Z + k \tag{2.34}$$

Using the principal stresses, this can also be written as:

$$\sigma_1 = \frac{2\sqrt{3}\alpha + 1}{1 - \sqrt{3}\alpha}\sigma_3 + \frac{\sqrt{3}k}{1 - \sqrt{3}\alpha} \tag{2.35}$$

which can be identified with Equation (2.17). Therefore, the Coulomb criterion can be represented by a straight line in the principal stress space, which is in the triaxial plane. The Drucker-Prager criterion simply is a revolution of the line with regard to the hydrostatic line (Figure 2.26 (b)).

Along this line, many other criteria were proposed following the function form of:

$$\tau_{oct} = f(\sigma_{oct}) \tag{2.36}$$

Geometrically, this function describes a failure surface that is a revolution of a curve in the triaxial plane, which represents the behavior under conventional triaxial tests. The π-plane cross-sections of these models are circles. For example, Murrell (1963) extended the Griffith theory to three dimensions and proposed that:

$$\tau_{oct}^2 = 8T_0\sigma_{oct} \tag{2.37}$$

This criterion describes quadratic pressure dependence. Zhou (1994) presented a failure criterion which reads:

$$\sqrt{J_2} = A + B\sigma_{oct} + C\sigma_{oct}^2 \tag{2.38}$$

2.3.6 Other Models

Wiebols and Cook (1968) proposed an energy criterion to explain the effect of the intermediate principal stress on the strength of rock. The basic assumptions of their theory are:

- The rock specimen is considered a homogeneous isotropic elastic material, with a large number of uniformly distributed, randomly oriented, closed plane cracks.
- All principal stresses are compressive, so all of the cracks are closed. The coefficient of sliding friction between the crack walls are a constant for all the cracks.
- The total strain energy stored in the rock specimen can be divided into two parts: the strain energy of the same specimen subject to the same boundary conditions but with no cracks, and the additional strain energy due to the existence of the cracks.
- The rock specimen fails when the additional strain energy reaches a threshold value.

An effective shear stress is then defined as:

$$\tau_{eff} = |\tau| - \mu\sigma_n \tag{2.39}$$

with $\sigma_n = l^2\sigma_1 + m^2\sigma_2 + n^2\sigma_3$ and $\tau^2 = l^2\sigma_1^2 + m^2\sigma_2^2 + n^2\sigma_3^2 - \sigma_n^2$ being the normal and shear stress along a crack, where l, m, n are the direction cosines of the normal to the crack surface with respect to the principal stress axes. μ is the coefficient of sliding friction between crack walls. If τ_{eff} is positive, then sliding occurs between the crack walls and additional strain energy is stored compared with the non-cracked media. Wiebols and Cook (1968) then assume that the additional strain energy due to the existence of one average crack is:

$$W_c = \bar{k}\tau_{eff}^2 \text{ if } \tau_{eff} > 0 \tag{2.40}$$

where $\bar{k}$ is a factor obtained by averaging the contribution for all of the cracks. W_c is summed for all of the cracks in all orientations to obtain the effective shear strain energy W_{eff}, which is the strain energy contribution by the sliding of cracks. For a general stress state, this summation process is performed by numerical integration with a computer. Failure is supposed to occur when W_{eff} reaches a critical value.

Figure 2.27 shows one example of Wiebols and Cook's results, with the coefficient of sliding friction, μ = 0.5. C_0 in Figure 2.27 is the uniaxial compression strength, which is used to normalize the stress values. Some of the key observations are summarized below:

- For conventional triaxial tests, no matter $\sigma_2 = \sigma_3$ (CTC) or $\sigma_2 = \sigma_1$ (CTE), the strength σ_1 varies linearly with σ_3. As shown in Figure 2.27, along the lines of $\sigma_2 = \sigma_3$ and $\sigma_2 = \sigma_1$, σ_1 varies linearly with σ_3. This is not true for most of the rocks, since the σ_1 usually varies non-linearly with σ_3.
- At any σ_3, the CTC strength is always smaller than the CTE strength, which agrees with the observations of Böker and Mogi.
- At $\sigma_3 = 0$, the ratio between the CTE strength and the CTC strength increase linearly with μ.
- When σ_2 is increased from σ_3 to σ_1, the strength of the rock first increases and then decreases, which again agrees with the many observations described earlier..

Wiebols and Cook (1968) qualitatively explained the effect of σ_2. However, the coefficient of sliding friction μ is hard to obtain.

Lundborg (1972) proposed a statistical theory to explain the effect of σ_2 on the strength of rock. Similar to Wiebols and Cook (1968), the effective shear stress is defined by Equation (2.39). However, in Lundborg's theory, μ stands for the coefficient of internal friction, instead of sliding friction. Lundborg's procedure also involves identifying the orientations with $\tau_{eff} > 0$. An example was shown in Lundborg (1972) where σ_1 = 8kb, σ_3 = 1kb and μ = 1 (Figure 2.28). The orientation in which $\tau_{eff} > 0$ at different σ_2 levels are marked on a unit sphere by the area Ω in

Figure 2.28.

Weibull (1939) defined the probability of rupture in tension with:

$$S(x) = 1 - \exp(-kX) \tag{2.41}$$

where $X = \int \sigma^M d\Omega$, and k and M are material constants. Lundborg (1972) similarly defined the probability of failure in shear in the same form but with the definition of X being:

$$X = \int \tau_{eff}^M d\Omega \tag{2.42}$$

where Ω is the solid angle with $\tau_{eff} > 0$. The rock specimen is assumed to fail when the probability $S(x)$ reaches a critical value. If k is assumed to be a constant, then the rock specimen will fail when X reaches a critical value. X can be calculated through Equation (2.42) with the knowledge of μ and M. An additional freedom of the model is provided by assuming μ to be function of the normal stress σ_n. Lundborg (1972) used the function:

$$\mu = \frac{\mu_0}{1 + \mu_0 \sigma_n / \tau_x} \tag{2.43}$$

where μ_0 is a constant and τ_x is the friction stress when σ_n tends to infinity.

The strength variation with σ_2 at different M when $\mu = 1$ and $\sigma_3 = 0$ is shown in Figure 2.29. Clearly, when M varies from 2 to infinity, different strength dependence on σ_2 can be described. When $M = 2$, the Wiebols and Cook (1968) theory is obtained. When $M = \infty$, the strength is independent of σ_2.

2.4 A New True Triaxial Model for Intact Isotropic Rock

The models that were described in the previous section have been applied in different areas. Colmenares and Zoback (2002) reported on a comprehensive evaluation of the predictive power of some of the models. It seems that the modified Lade model (Equation (2.22)) can predict the strength of different types of rocks reasonably well. The pressure dependence and Lode angle dependence of this model have been analyzed in previous sections, and are shown in Figure 2.20 through Figure 2.23. It was also shown in the literature that the original Lade criterion captures the isotropic failure behavior of soil very well. The original and the modified Lade criterion differ only in their pressure dependence. While the original formulation has a linear pressure dependence, in the modified criterion this dependence is non-linear. Therefore, it is reasonable to believe that the predictive power of these models comes from their π-plane cross-section, which is described by the LMN dependence.

In order to obtain a generalized model, it is desirable to separate the pressure dependence and the Lode angle dependence, so that the π-plane cross-section of the Lade models can be used

together with any triaxial plane cross-section. The modified Lade model, however, has a coupled pressure dependency and Lode angle dependency. The same parameters m and η_1 define both the triaxial cross-section and the π-plane cross-section, as is evident from Figure 2.20 and Figure 2.21. With this coupling, any changes on the π-plane cross-section will inevitably affect the triaxial plane cross-section. This seriously restricts the flexibility of the model, when more complicated features are added to the π-plane cross-sections to describe the failure of anisotropic rocks.

Apart from the desired flexibility of the model, there are other reasons why the pressure dependence and the Lode angle dependence should be separately described. On the one hand, these two dependencies have different physical backgrounds. Pressure dependency describes the strength variation with octahedral stress. This is geometrically shown as the triaxial plane cross-section. Lode angle dependency describes the strength dependence on stress path orientation at the same octahedral stress. This is geometrically shown as the π-plane cross-section. On the other hand, the data compiled seem to support that the shape of the π-plane cross-section is not significantly affected by octahedral stress level.

The idea of separating these two dependencies will be explored in this section, and a new failure criterion is proposed based on it.

2.4.1 Formulation of the Proposed Model

The idea of decoupling pressure and Lode angle dependence is not new. Desai and Salami (1987) proposed the following functions for the yielding behavior of soft rock:

$$J_2 = F_b F_s = \left(-\frac{\alpha}{\alpha_0} I_1^n + \gamma I_1^2 \right) (1 - \beta S_r)^m \tag{2.44}$$

in which α, n, γ, β and m are material parameters, and $\alpha_0 = 1$ (but with the same unit as stress). $S_r = \sqrt[3]{J_3} / \sqrt{J_2}$ is the stress ratio, which has the same role as the Lode angle. Clearly, $F_b = -\frac{\alpha}{\alpha_0} I_1^n + \gamma I_1^2$ describes the pressure dependence of the criterion. $F_s = (1 - \beta S_r)^m$ describes the Lode angle dependence.

Hunsche and Albrecht (1990) used the following function to describe the failure of rock salt:

$$\tau_0 = f(\sigma_{oct}) g(m) h(T) \tag{2.45}$$

where m is the Lode parameter, and T is temperature. Obviously $f(\sigma_{oct})$ describes the pressure dependence, while $g(m)$ describes the Lode dependence. $h(T)$, on the other hand, describes the variation of strength with temperature.

Aubertin and Simon (1996) proposed the MSDP criterion which writes:

$$\sqrt{J_2} = F_0 F_\pi \tag{2.46}$$

In this formulation, F_0 describes the pressure dependence, with:

$$F_0 = \begin{cases} \sqrt{\frac{1}{3}[(\sigma_c - \sigma_t)I_1 + \sigma_c\sigma_t]} & \text{for } I_1 < I_T \\ \alpha I_1 + k & \text{for } I_1 \geq I_T \end{cases} \tag{2.47}$$

where I_T marks the point of brittle-ductile transition. When $I_1 < I_T$, a non-linear pressure dependence is specified, with σ_c and σ_t being material parameters. When $I_1 > I_T$, there is a linear pressure dependence. F_π describes the Lode angle dependence:

$$F_\pi = \frac{b}{\sqrt{b^2 + (1-b^2)\sin^2(45° - 1.5\lambda)}} \tag{2.48}$$

Where b specifies the ratio R_{180}/R_0, and λ is the Lode angle.

Along the line of these models, it is proposed here that the separation should be obtained by two different functions. The most direct way to obtain pressure dependence is through conventional triaxial tests at different confining pressures. The measured strengths from these tests give one branch of the triaxial plane cross-section $R_0(Z)$ (Figure 2.17 (b)). It is found that power law functions can usually be used to fit the data to obtain $R_0(Z)$:

$$R_0(Z) = a \cdot Z^b \tag{2.49}$$

However, one can use any functional form that fits the experimental data, and physically makes sense.

The shape of the π-plane cross-section is assumed to be described by the LMN dependence, which is a group of curved right triangles with $R'_0 = 1.0$ (refer to Figure 2.23). As indicated before, the shapes are normalized against R_0. Under this assumption, the radius (the distance between a certain point on the π-plane cross-section and the hydrostatic line) of the π-plane cross-section at a certain Z level and a certain orientation θ is:

$$R(\theta, Z) = R_0(Z)R'(\theta) = R_0(Z)\frac{\sqrt{3}}{2}\frac{\beta_s(Z)}{\sqrt{\beta_s(Z)^2 - \beta_s(Z) + 1}}\frac{1}{\cos(\theta'')} \tag{2.50}$$

where $R'(\theta)$ is the LMN dependence expressed by Equation (2.27), and θ″ is the intermediate variable defined by Equation (2.28). The shapes shown in Figure 2.23 will be frequently used in this research, because they are applicable to both soils and rocks and because there is only one parameter β_s involved. Lade (1993) indicates that the shape of the π-plane cross-section may change with the pressure level. The shape is closer to a triangle at lower Z values, and increasingly resembles a circle with the increase of Z. This indicates that β_s should be a function

of Z, as explicitly shown in Equation (2.50). While applying the proposed model to the existing data sets, however, it will be shown that in most case β_s can be treated as a constant.

2.4.2 Application of the Proposed Model

The application of the model will be shown by a numerical example, based on Mogi's data on Dunham dolomite (Table A.10). Since this model is constructed based on the idea of separation of pressure and Lode angle dependency, there are obviously two steps when applying it. The first step is to find the pressure dependence function $R_0(Z)$. The second step is to determine the shape factor β_s in the LMN dependence.

Step 1: Determination of $R_0(Z)$

From Table A.10, the data in which the rock specimens fail in conventional triaxial stress states ($\theta = 0°$) are first retrieved and listed in Table 2.1. With the principal stresses at failure known, the values of R_0 and Z at failure can be calculated based on Equations (2.12) and (2.10). The results are also shown in Table 2.1.

These data can be plotted in the R_0-Z system, as shown in Figure 2.30. It was found that a power function can be used to fit the conventional triaxial compression data. In the case of the Dunham dolomite, the pressure dependence can be expressed by:

$$R_0(Z) = 8.8637 Z^{0.6366} \tag{2.51}$$

This gives one branch of the triaxial plane cross-section of the failure surface for Dunham dolomite.

Step 2: Determination of $\beta_s(Z)$

In order to obtain $\beta_s(Z)$, those data points in Table A.10 where the rock fails in true triaxial stress state must be used. These data are collected in Table 2.2. For each data point, the failure stress in the polar coordinate system (R,θ,Z) is calculated. R and Z can be calculated with Equations (2.12) and (2.10), as shown in Step 1. θ can be calculated with Equation (2.14). Since this point represents failure, it must be located on the π-plane cross-section of the failure surface. Then the conventional triaxial strength R_0 at this Z level is obtained from the power law function, Equation (2.51). Normalizing R to R_0, a point $(R/R_0,\theta,Z)$ on the normalized π-plane cross-section at this Z level is obtained. To fully define the shape of the π-plane cross-section at this Z level, a few data points are necessary which have various θ values from 0° to 60° (due to the six-fold symmetry). β_s value at this Z level can then be calculated by its definition (Equation (2.24)):

$$\beta_s(Z) = \frac{R_{180}(Z)}{R_0(Z)} = \frac{R_{60}(Z)}{R_0(Z)} \tag{2.52}$$

β_s may also be obtained visually by comparing the shape determined by the data points against Figure 2.23, the group of shapes determined from LMN dependence. If, however, all the normalized failure points fall on a unique π-plane cross-section regardless of their failure Z level, then the shape of the π-plane cross-section is indifferent to the Z value and β_s can be taken as a constant.

For Dunham dolomite, all the normalized data points are plotted on the π-plane in Figure 2.31. Each data point fails a different Z value, ranging from 475 MPa to 900 MPa. However, after normalization, all points indeed fall on a unique failure surface. A constant β_s can thus be used in Equation (2.50) to describe the strength of Dunham dolomite. Comparing the shape determined by the data points in Figure 2.31 against Figure 2.23, β_s is obtained to be around 0.74. The π-plane cross-section with β_s = 0.74 is also shown in Figure 2.31. The final expression to describe the strength of Dunham dolomite subject to a true triaxial stress state is:

$$R(\theta, Z) = 8.8637 Z^{0.6366} \cdot \frac{\sqrt{3}}{2} \frac{0.74}{\sqrt{0.74^2 - 0.74 + 1}} \frac{1}{\cos(\theta'')} \tag{2.53}$$

where θ' is a function of θ specified by Equation (2.28). The strength of Dunham Dolomite, as described by Equation (2.53), is compared with the experimental data in Figure 2.32.

It is important to note that the conventional triaxial compression data only covers Z values around 150-560 MPa, while true triaxial tests cover a Z range from 475 to 900 MPa. Between 560MPa and 900MPa, the form of $R_0(Z)$ shown in Equation (2.51) is not supported by any data points. One should be cautious of its applicability in this range of Z values. Whenever possible, it is recommended that more conventional triaxial tests should be performed to cover the entire range of Z values at which the rock may fail.

It is also important to note that the data points in Figure 2.31 only cover θ value from 0° to –30°. In order to define the π-plane cross-section with the least uncertainty, ideally the data should be distributed between 0° to –60°. Again, caution should be exercised when the model predicts a failure where θ is between –30° and –60°.

Most of the other data sets from true triaxial tests were processed in the same manner. The pressure dependence functions $R_0(Z)$ are fitted with power functions. Data with all three different principal stresses are then normalized to the R_0 value calculated from $R_0(Z)$. The normalized data are then plotted on the π-plane. For most of the data sets, a unique π-plane cross-section can be obtained. This indicates that the shape factor β_s is either constant or it does not vary significantly with pressure level. The data points and the predicted π-plane cross-section are plotted in Figure 2.33 through Figure 2.46. For most of them, it can be seen that the LMN dependence describes the π-plane cross-section very well.

The pressure dependence function $R_0(Z)$, and the parameter β_s are tabulated in Table 2.3. In order

to show the quality of the data, three additional columns are included in the table:

- Z from CTC tests: This column gives the Z value range covered by the available conventional triaxial compression data. The pressure dependence function $R_0(Z)$ fitted with these data is most reliable within this range of Z value. Outside of this range, one should be careful about the applicability of the fitted $R_0(Z)$ function.
- Z from TTT tests: This column gives the Z values that are covered by the true triaxial data.
- Minimum θ: In order to define the shape of the π-plane cross-section, it is best to have data points ranges from $\theta = 0°$ to $-60°$. However, none of the data set covers such a wide range. The closer this minimum θ is to $-60°$, the better defined the shape of the π-plane cross-section is.

In short, the closer the "Z from CTC tests" to the "Z from TTT tests", the better the quality of the data, since $R_0(Z)$ that is used to normalize the data is more reliable. The closer "Minimum θ" is to $-60°$, the better quality of the data, since it covers wider Lode angle.

To summarize, a true triaxial failure model for intact isotropic rock is proposed in this section, based on the separation of pressure and Lode angle dependence. The application of this model is shown through a numerical example. In order to obtain the necessary parameters, the results from a few conventional triaxial compression tests and a few true triaxial tests should be available. The prediction power of the model depends on the available data based on which the model parameters are obtained. The conventional triaxial data should cover as wide a range of Z values as possible, while the true triaxial data should cover θ values from 0° to 60°.

2.5 Summary

The problem of isotropic intact rock strength was examined in this section, from the experimental methods to the theoretical prediction. The experimental data where rock specimens are subject to a polyaxial stress state were compiled. It seems that many different types of rocks have been tested under a true triaxial stress state.

The modified Lade criterion seems to perform very well in predicting the strength of rock. In order to preserve its predictive power while at the same time obtaining more flexibility, a new criterion is proposed based on the separation of pressure dependence and Lode angle dependence. The π-plane cross-section of the proposed model is the same as that of the modified Lade criterion, while its pressure dependence is described by $R_0(Z)$, which is obtained from conventional triaxial compression tests. The proposed model is applied to most of the data that were collected here.

For most of the rocks, it seems that the shape of the π-plane cross-section is not significantly affected by pressure level. Therefore, β_s can be taken as a constant. It was pointed out that the

accurate determination of β_s requires true triaxial tests.

Based on the data shown in Table 2.3, it seems that most of the rocks have a π-plane cross-section with β_s ranging from 0.55 to 0.75. This explains why the Drucker-Prager criterion, which has a π-plane cross-section with $\beta_s = 1.0$, does not predict the strength of rocks very well.

Table 2.1 Tests on Dunham Dolomite with Conventional Triaxial Stress State

σ_3 (MPa)	σ_2 (MPa)	σ_1 (MPa)	Z (MPa)	θ (°)	R_0 (MPa)
0	0	265	152.998	0	216.372
0	0	258	148.956	0	210.656
25	25	400	259.808	0	306.186
45	45	486	332.554	0	360.075
60	60	540	381.051	0	391.918
65	65	568	402.99	0	410.698
85	85	620	456.107	0	436.826
105	105	682	514.996	0	471.119
125	125	725	562.917	0	489.898

Table 2.2 Tests on Dunham Dolomite with True Triaxial Stress State

σ_3 (MPa)	σ_2 (MPa)	σ_1 (MPa)	Z (MPa)	θ (°)	Normalized R
25	66	475	326.78	–4.72593	0.99588
25	96	495	355.648	–8.05467	0.96085
25	129	560	412.228	–10.5628	0.97929
25	174	571	444.56	–15.3057	0.92861
25	229	586	484.974	–21.0517	0.88394
25	272	545	486.129	–28.3465	0.80848
45	97	570	411.073	–5.15681	1.00042
45	126	576	431.281	–8.13887	0.95959
45	160	606	468.231	–11.1887	0.94332
45	183	639	500.563	–12.8243	0.94841
45	240	670	551.37	–17.7521	0.91737
45	266	670	566.381	–20.405	0.8938
45	294	622	554.834	–25.4803	0.82692
65	117	638	473.427	–4.70642	1.00168
65	153	644	497.676	–8.10719	0.95539
65	208	687	554.256	–12.6783	0.93147
65	262	685	584.278	–18.1153	0.87587
65	318	746	651.828	–21.5609	0.8877
65	393	701	669.149	–31.0401	0.80662
85	128	684	517.883	–3.68951	0.9975
85	153	719	552.524	–5.6056	0.99722
85	233	744	613.146	–12.3581	0.92707
85	306	773	672.036	–18.3359	0.88839
85	376	818	738.431	–23.2173	0.87914
85	445	793	763.834	–30.5607	0.82529
105	167	778	606.218	–4.7808	1.00454
105	205	786	632.776	–7.81482	0.96637
105	270	863	714.76	–11.9442	0.96942
105	268	805	680.119	–12.8566	0.91935
105	334	824	729.193	–18.1632	0.88196
105	356	840	751.133	–19.6283	0.8803
105	415	822	774.804	–25.5338	0.83071
125	187	824	655.87	–4.59553	0.99387
125	239	860	706.677	–8.28489	0.96897
125	293	863	739.586	–12.5421	0.92047

125	362	897	799.053	−17.4362	0.89585
125	414	941	854.478	−20.4414	0.89807
125	463	918	869.49	−25.1311	0.85424
125	516	886	881.614	−30.9128	0.80974
145	253	883	739.586	−7.78638	0.94846
145	296	927	789.815	−10.4865	0.94668
145	324	923	803.672	−12.6888	0.91962
145	349	922	817.528	−14.6671	0.89936
145	392	1015	896.048	−15.9896	0.94417
145	410	1002	898.934	−17.5764	0.92214
145	455	952	896.048	−22.3799	0.85732

Table 2.3 Parameters of the Proposed Criterion for Different Rock Types

Rock Name	Data Source	$R_0(Z)$[1]	β_s	Z from CTC[2] tests (MPa)	Z from TTT[3] tests (MPa)	Minimum θ
Dunham Dolomite	Mogi (2007)	$r_0 = 10.28Z^{0.612}$	0.74	560 MPa	900 MPa	–31°
Solnhofen Limestone	Mogi (2007)	$r_0 = 23.09Z^{0.464}$	0.75	400 MPa	820 MPa	–46°
Yamaguchi Marble	Mogi (2007)	$r_0 = 5.331Z^{0.656}$	0.79	186 MPa	517 MPa	–39°
Mizuho Trachyte	Mogi (2007)	$r_0 = 5.977Z^{0.653}$	0.75	367 MPa	573 MPa	–55°
Manazuru Andesite	Mogi (2007)	$r_0 = 3.427Z^{0.807}$	0.62	660 MPa	680 MPa	–24°
Inada Granite	Mogi (2007)	$r_0 = 4.057Z^{0.791}$	0.6	1129 MPa	1200 MPa	–12°
Orikabe Monzonite	Mogi (2007)	$r_0 = 5.334Z^{0.738}$	0.65	870 MPa	1210 MPa	–16°
Westerly Granite	Haimson and Chang (2000)	$r_0 = 2.946Z^{0.846}$	0.57	700 MPa	890 MPa	–19°
KTB Amphibolite	Chang and Haimson (2000)	$r_0 = 3.144Z^{0.824}$	0.63	835 MPa	1185 MPa	–53°
Long Valley Hornfels	Chang and Haimson (2007)	$r_0 = 7.084Z^{0.640}$	0.63	385 MPa	543 MPa	–53°
Chelungpu Siltstone	Oku et al. (2007)	$r_0 = 3.243Z^{0.756}$	0.7	370 MPa	560 MPa	–58°
Shirahama Sandstone	Takahashi and Koide (1989)	$r_0 = 7.131Z^{0.584}$	0.71	187 MPa	300 MPa	–46°
Izumi Sandstone	Takahashi and Koide (1989)	$r_0 = 3.017Z^{0.829}$	0.57	381 MPa	480 MPa	–18°
Yuubari Shale	Takahashi and Koide (1989)	$r_0 = 4.732Z^{0.659}$	0.73	200 MPa	270 MPa	–43°

Note:

1: All $R_0(Z)$ are fitted with power law functions.

2: CTC stands for conventional triaxial compression tests.

3: TTT stands for true triaxial tests.

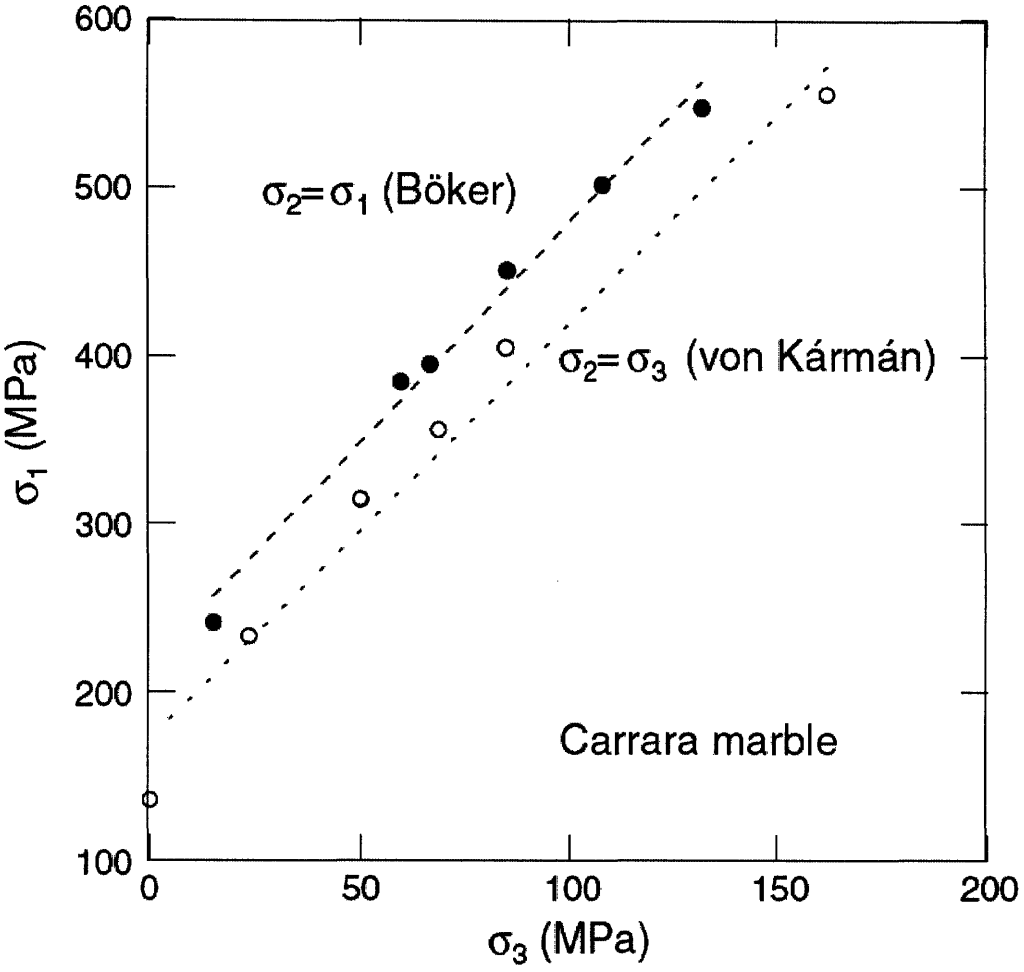

Figure 2.1 Comparison between Böker and Von Kármán's Strength (from Haimson, 2006)

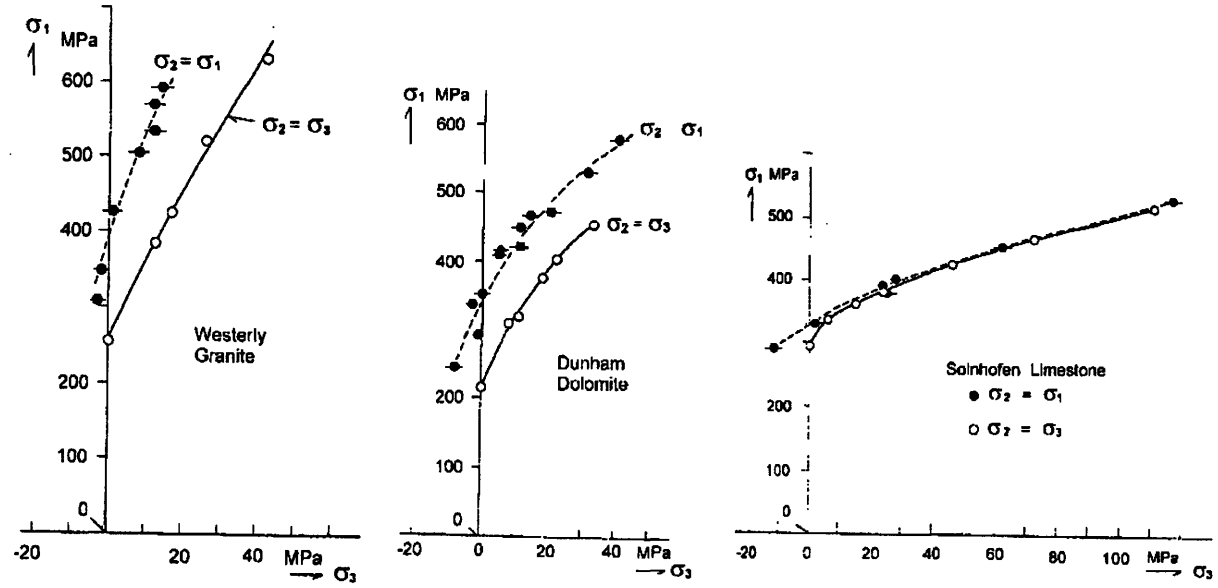

Figure 2.2 Comparison of Conventional Triaxial Compression and Extension Strength (from Mogi, 2007)

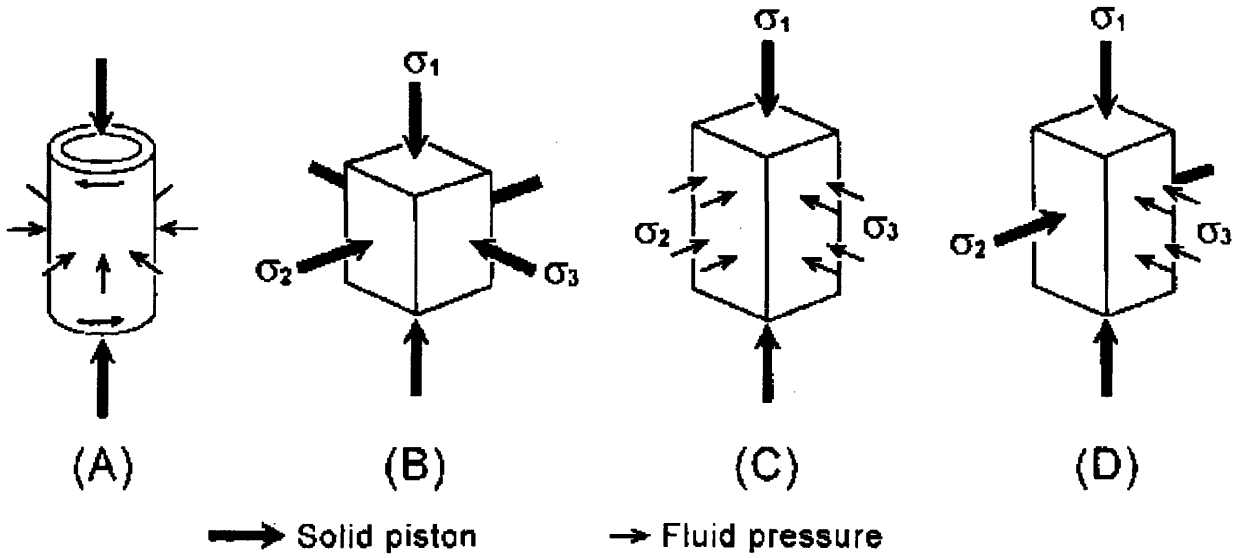

Figure 2.3 Mogi's Classification of Experiments with Polyaxial Stress State (from Mogi, 2007)

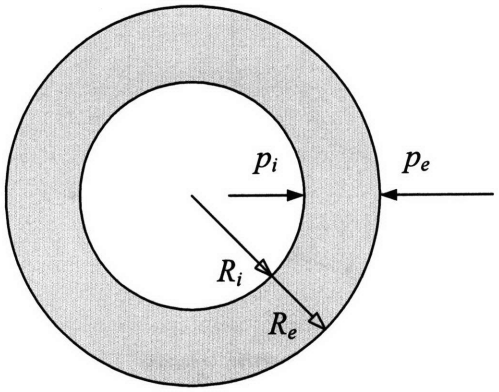

Figure 2.4 Thick-walled Hollow Cylinder

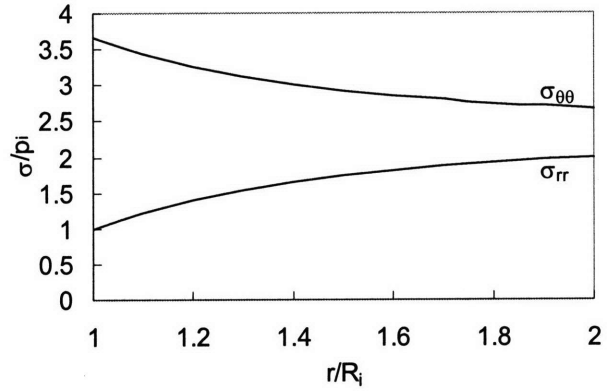

(a) $R_e/R_i = 2.0, p_e/p_i = 2.0$

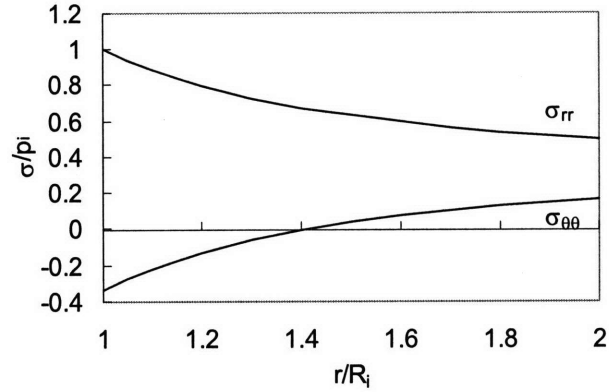

(b) $R_e/R_i = 2.0, p_e/p_i = 0.5$

Figure 2.5 Stress Distribution along the Wall of a Thick Walled Hollow Cylinder

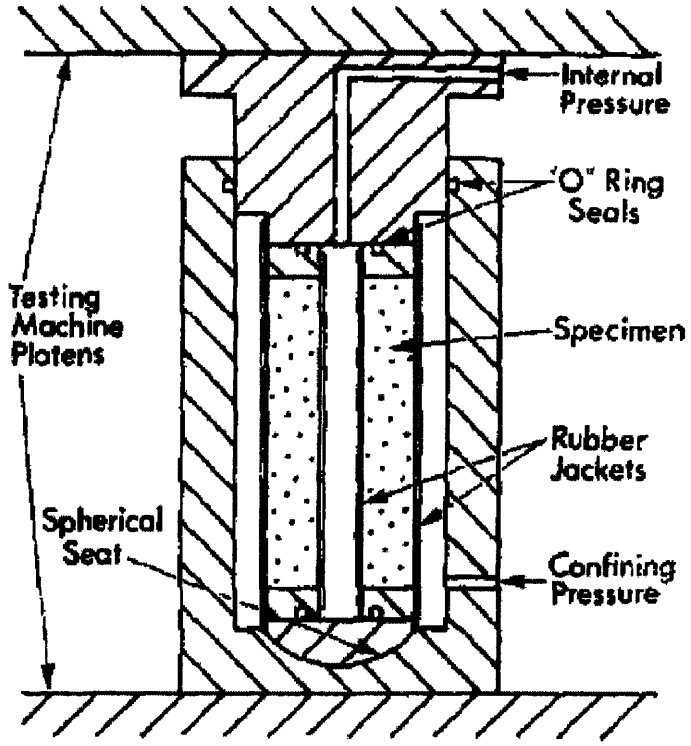

Figure 2.6 Hoskins' Thick-walled Hollow Cylinder Tests

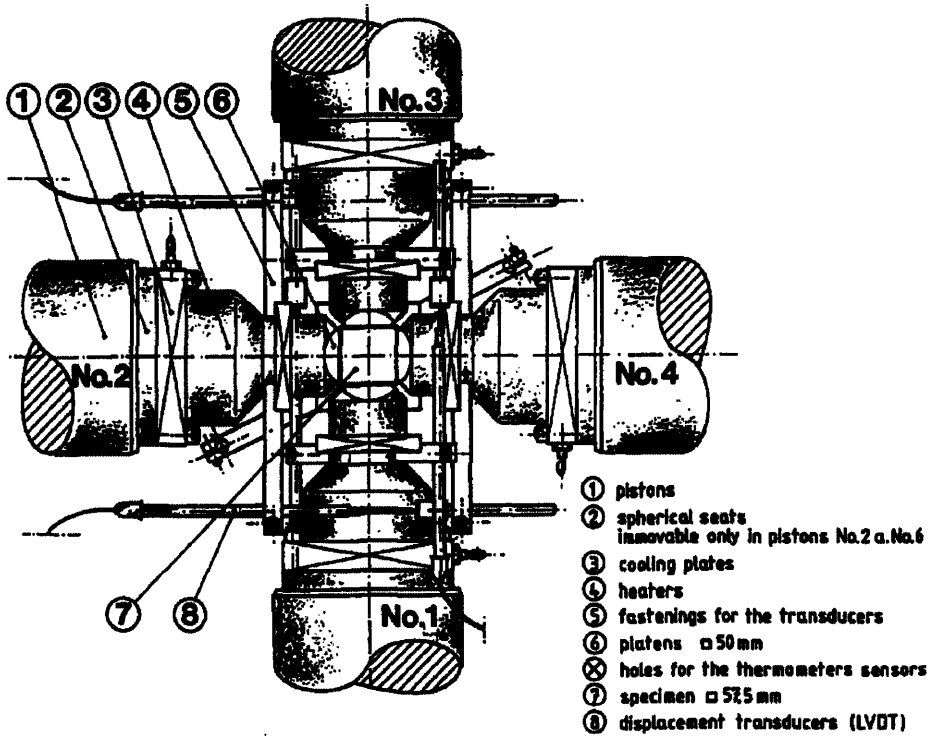

Figure 2.7 True Triaxial Tests Performed by Hunsche (Hunsche, 1990)

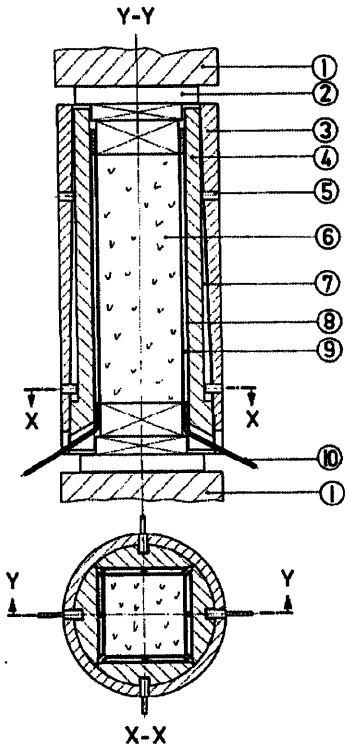

1: Machine platens
2: Cell end-piece
3: Constraining cylinder
4: Tapered segments
5: Locating dowels
6: Rock specimen
7: Locating slots
8: Copper flat-jacks
9: Pressure fluid space
10: Capillary tube pressure connection

Figure 2.8 True Triaxial Cell Reported by Hojem and Cook (1968)

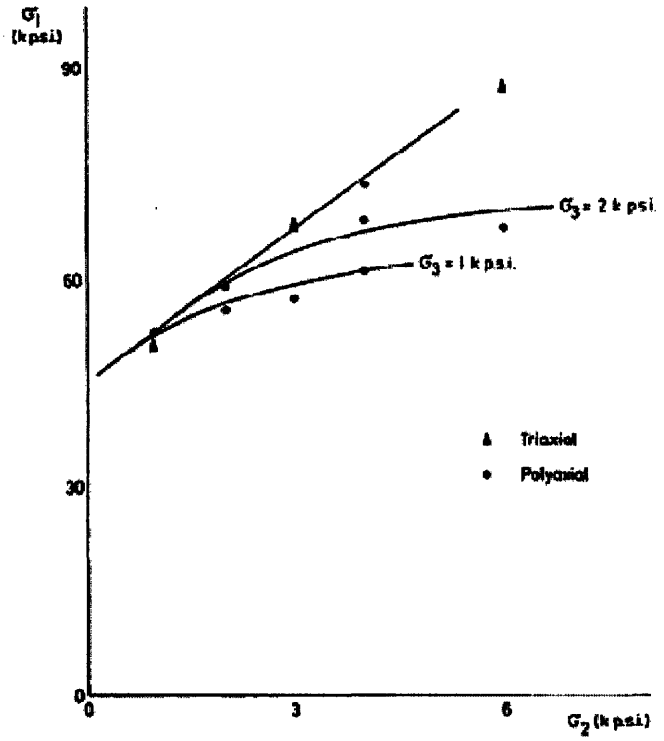

Figure 2.9 Intermediate Stress Effect on Karroo Dolerite (Hojem and Cook, 1968)

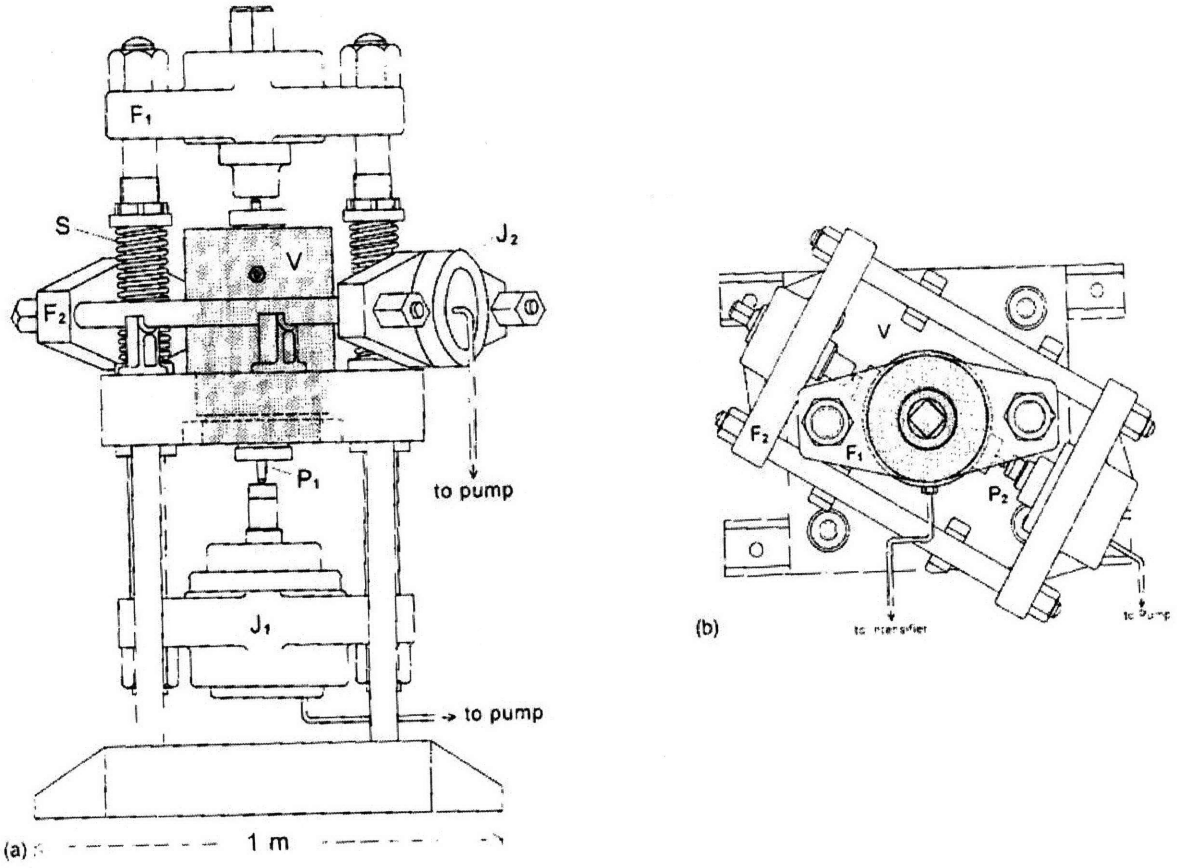

Figure 2.10 Sketch of Mogi's True Triaxial Apparatus (after Mogi, 2007)

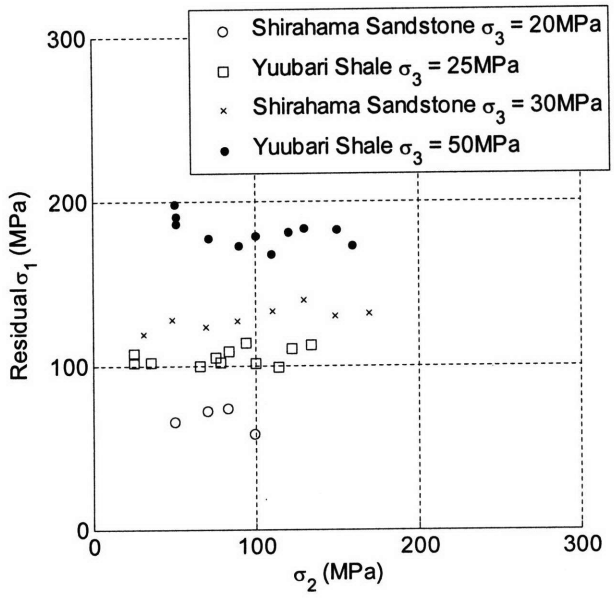

Figure 2.11 Residual Strength of Shirahama Sandstone and Yuubari Shale (Takahashi and Koide, 1989)

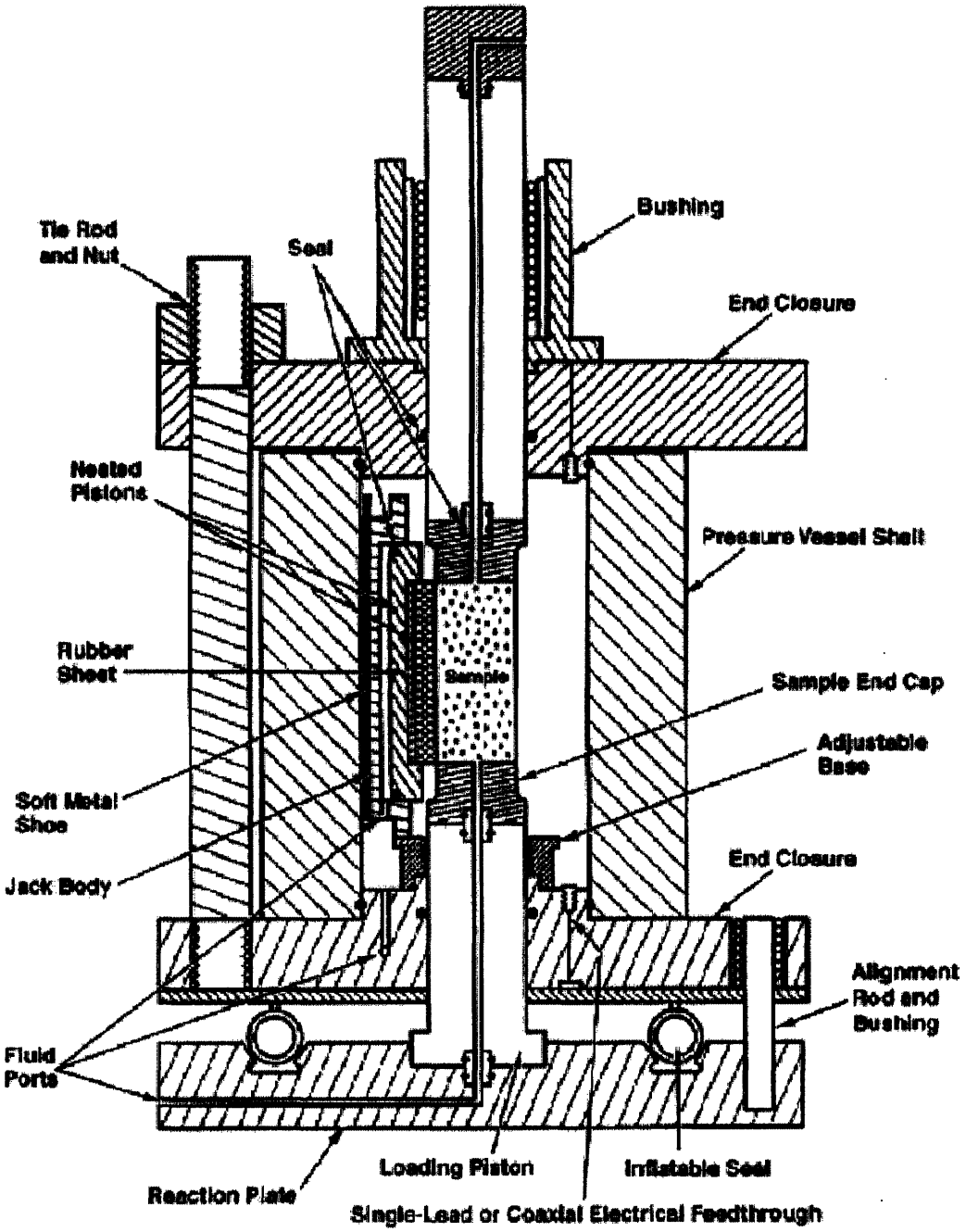

Figure 2.12 True triaxial cell at Sandia National Lab (Wawersik, 1997)

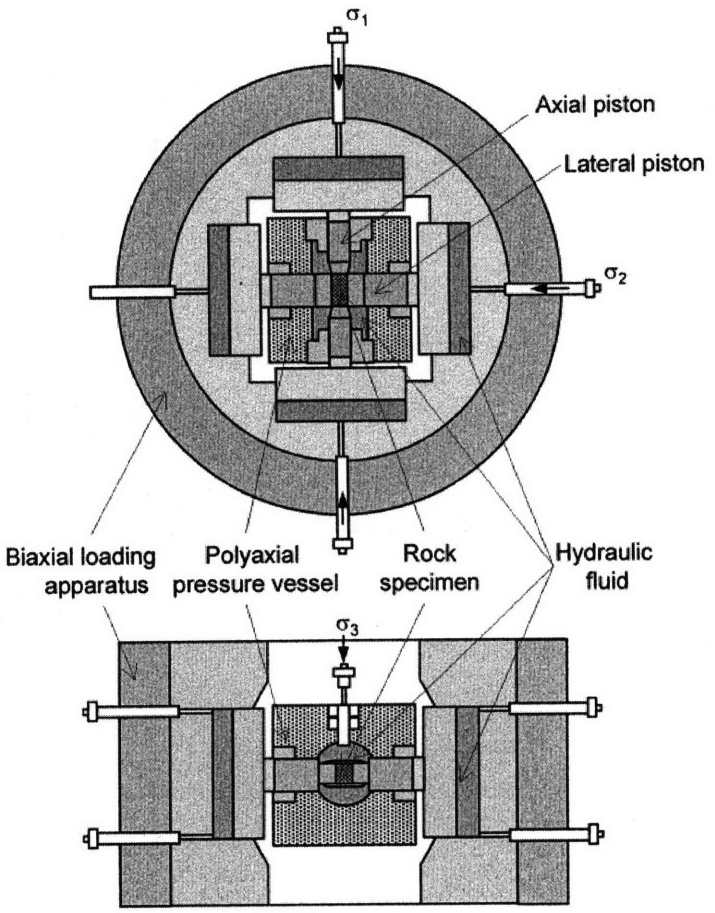

(a)

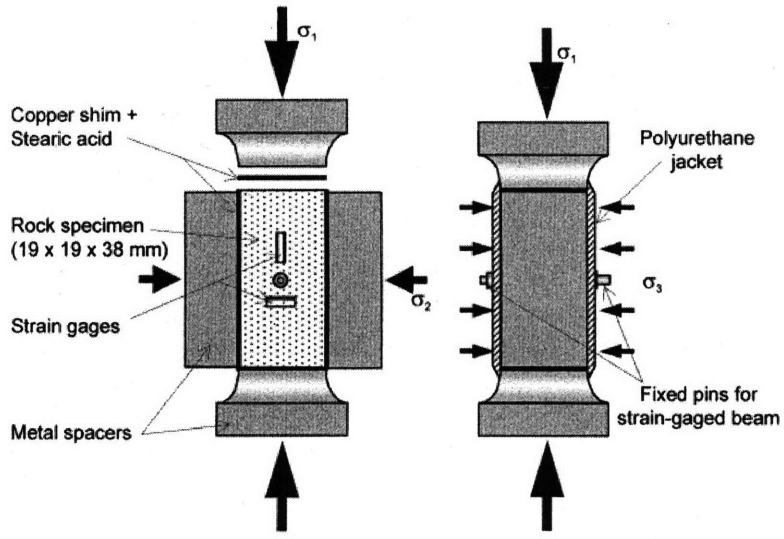

(b)

Figure 2.13 True triaxial cell of the University of Wisconsin (Haimson, 2000)

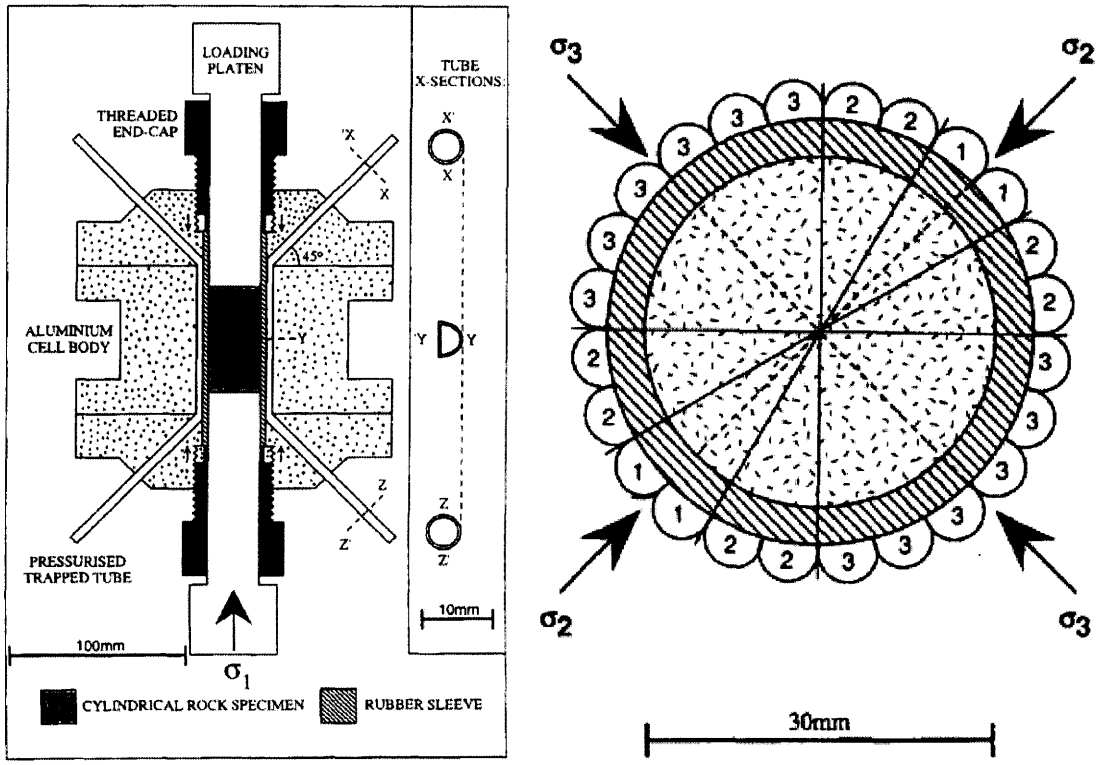

Figure 2.14 True triaxial cell reported by Smart (1990)

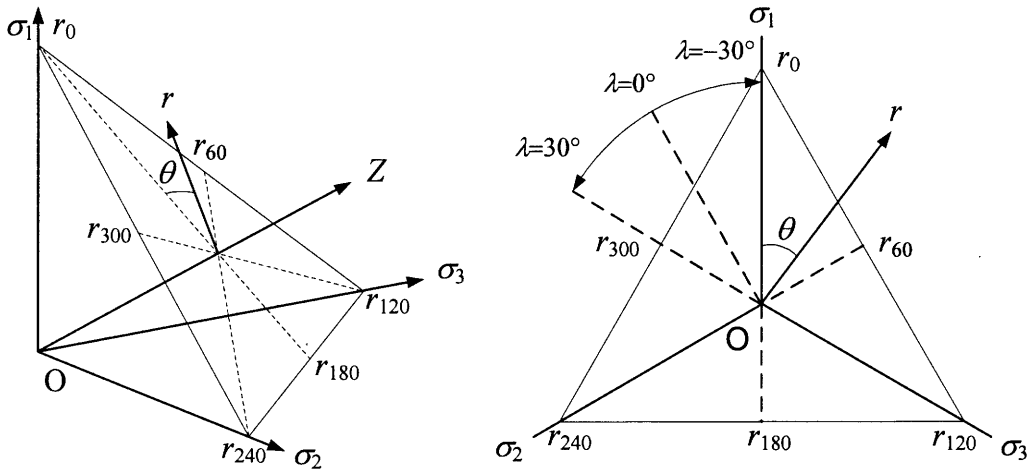

Figure 2.15 Principal Stress Space and the π-Plane

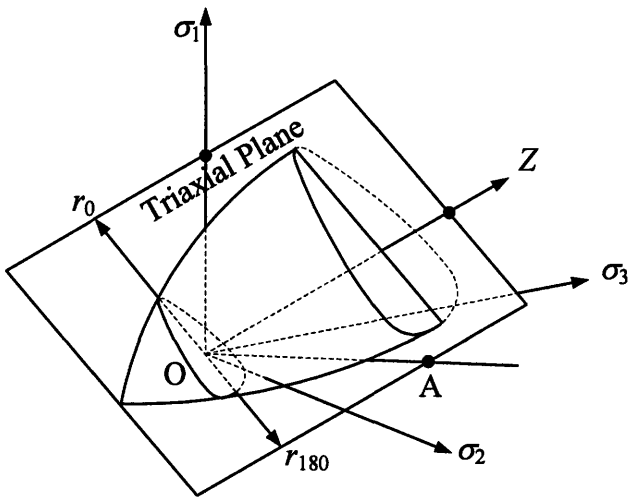

Figure 2.16 Three Dimensional View of Failure Surface in Principal Stress Space

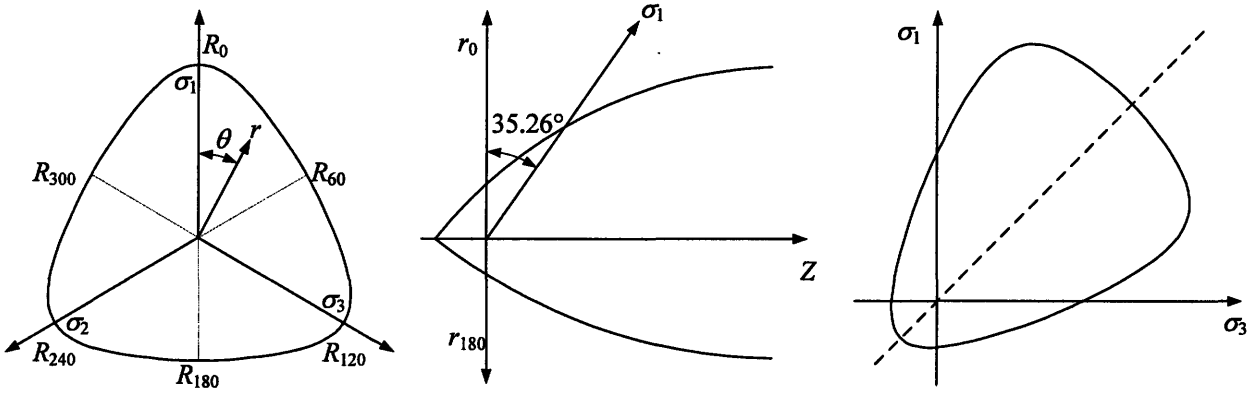

(a) π-Plane Cross-Section (b) Triaxial Plane Cross-Section (c) Biaxial Plane Cross-Section

Figure 2.17 Cross-Sections of the Failure Surface

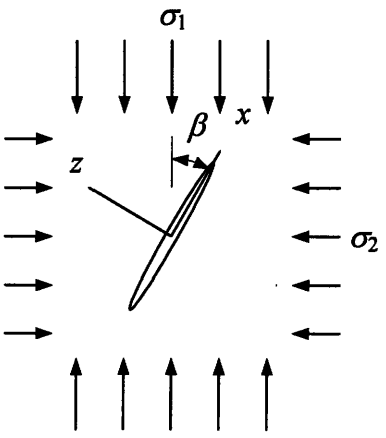

Figure 2.18 Assumption of Crack Orientation in Griffith Criterion

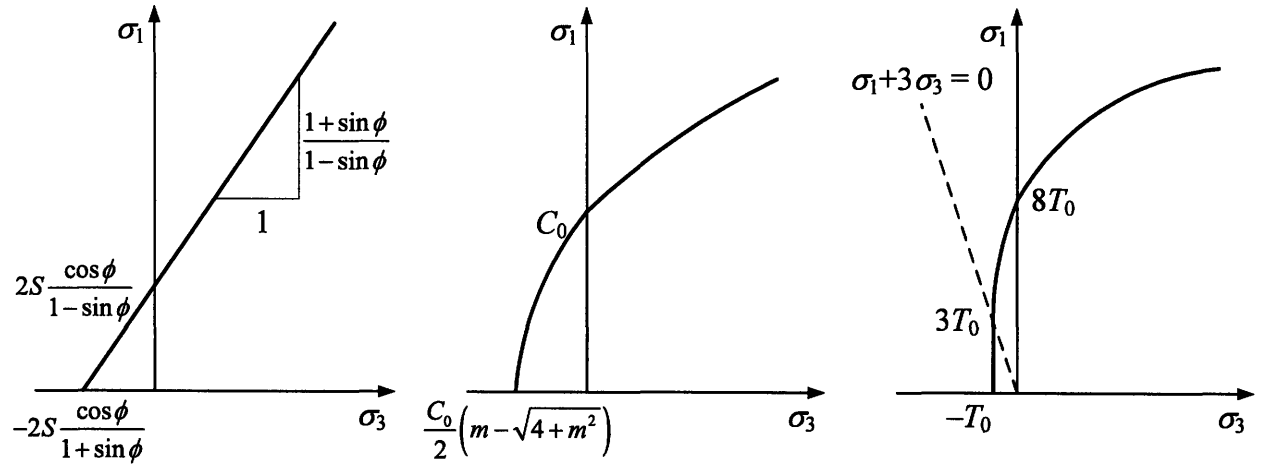

(a) Mohr-Coulomb Criterion (b) Hoek-Brown Criterion (c) Griffith Stress Based Criterion

Figure 2.19 Failure Criteria for Conventional Triaxial Tests (a) Mohr-Coulomb (b) Hoek-Brown (c) Griffith

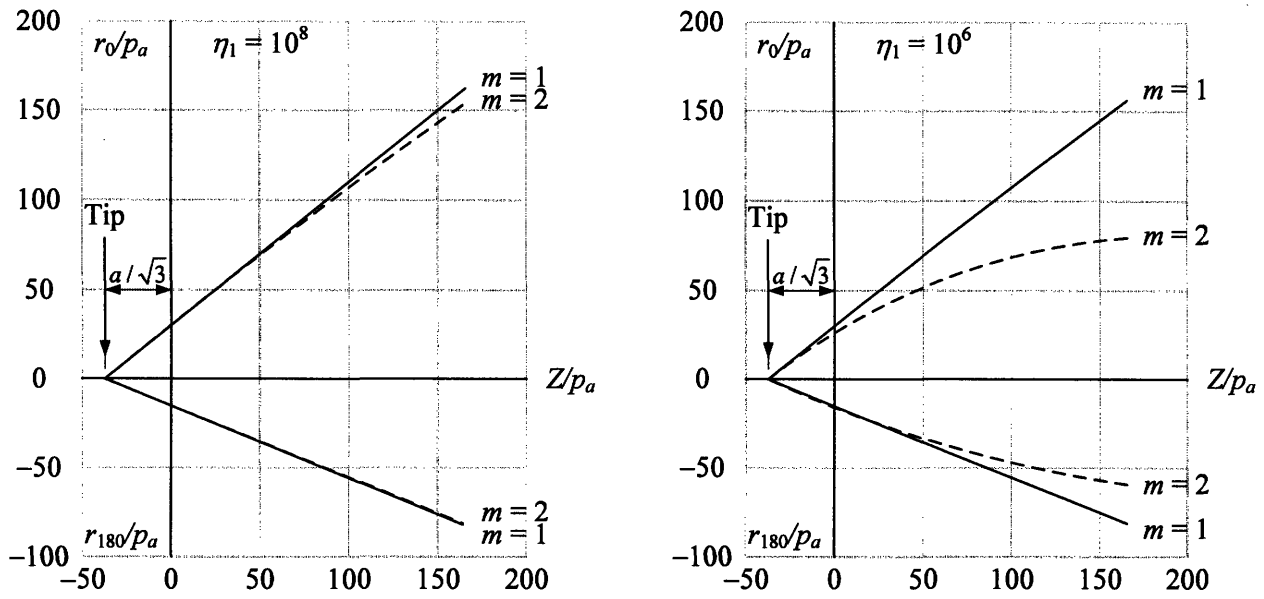

(a) $\eta_1 = 10^8$ (b) $\eta_1 = 10^6$

Figure 2.20 Triaxial Plane Cross-Section of Modified Lade Criterion

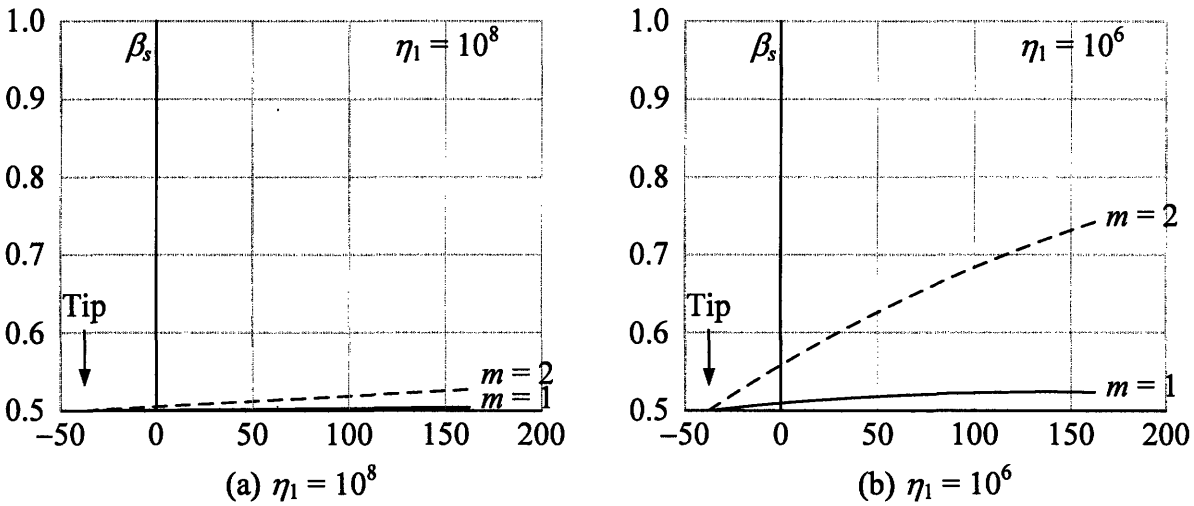

Figure 2.21 Shape factor β_s of Modified Lade Criterion

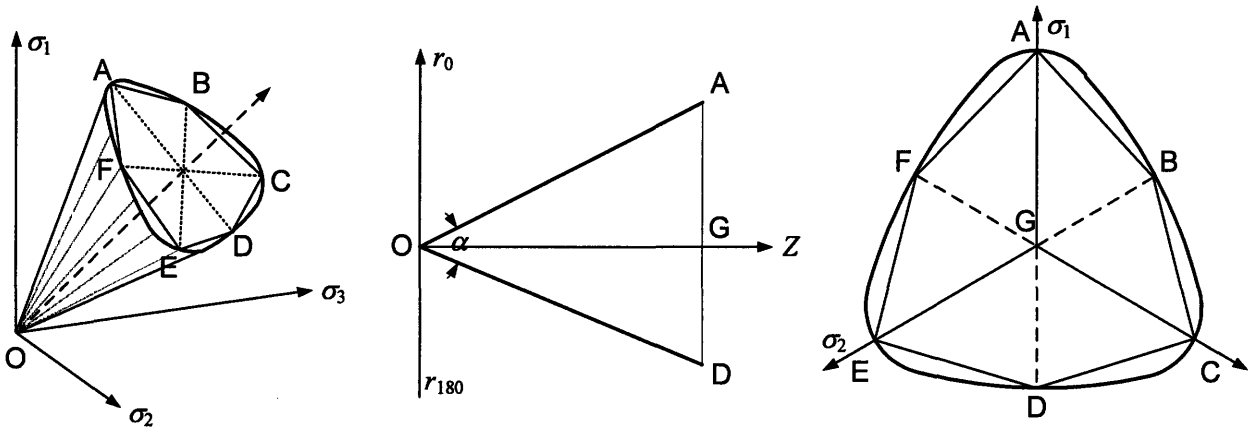

(a) 3D View (b) Triaxial Plane Cross-Section (c) π-Plane Cross-Section

Figure 2.22 Failure Surface of the Matsuoka-Nakai Criterion

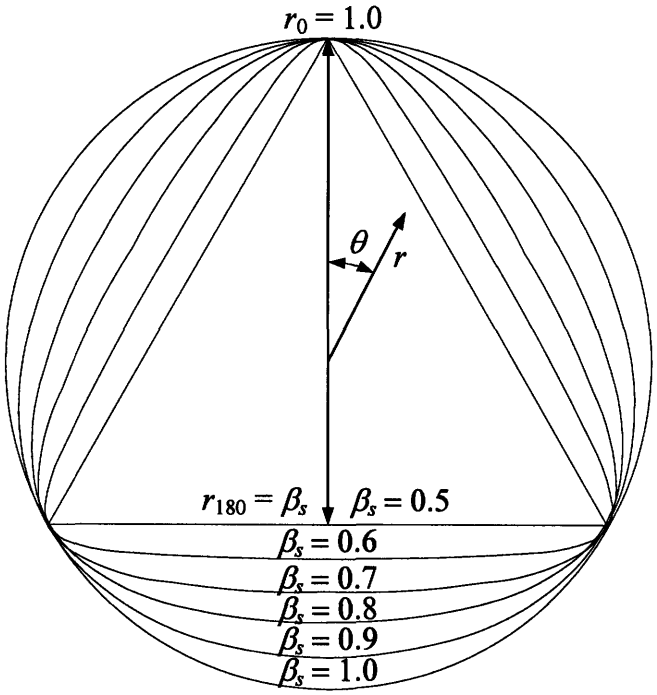

Figure 2.23 π-Plane Cross-Section Specified by the LMN Dependence

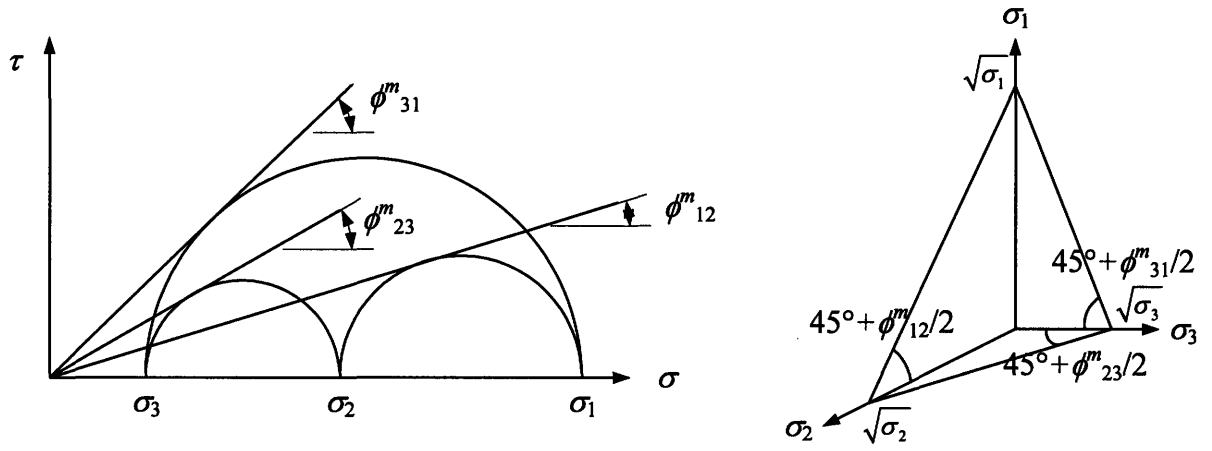

(a) Mohr Circles and the Mobilized Friction Angles (b) Construction of the Spatial Mobilized Plane

Figure 2.24 The SMP Concept by Matsuoka and Nakai (1974)

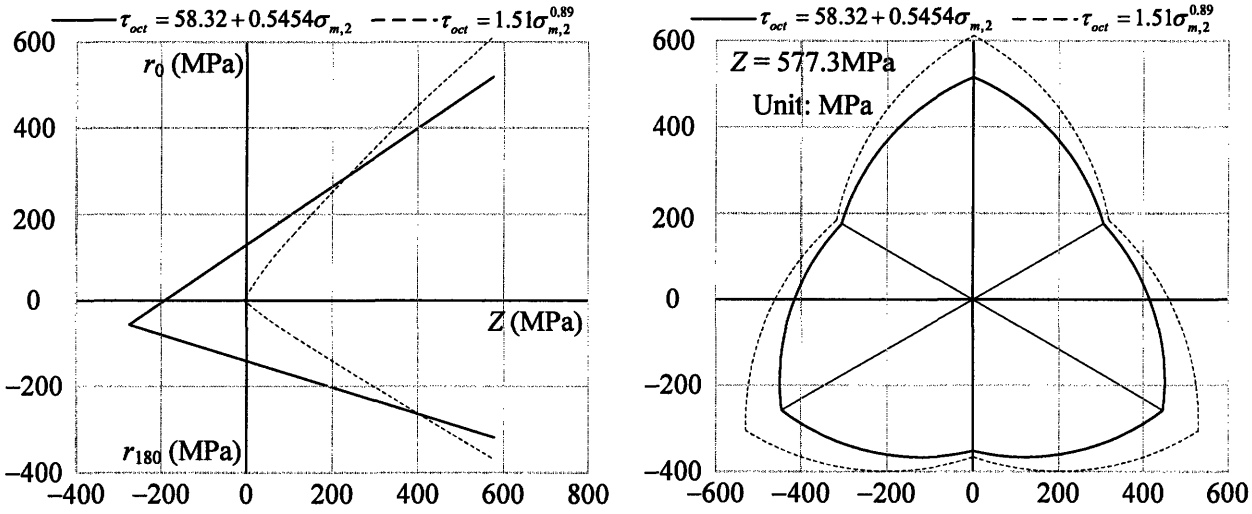

(a) Mohr Circles and the Mobilized Friction Angles (b) Construction of the Spatial Mobilized Plane

Figure 2.25 The Triaxial Plane Cross-Section and π-Plane Cross-Section of the Mogi Type Criteria

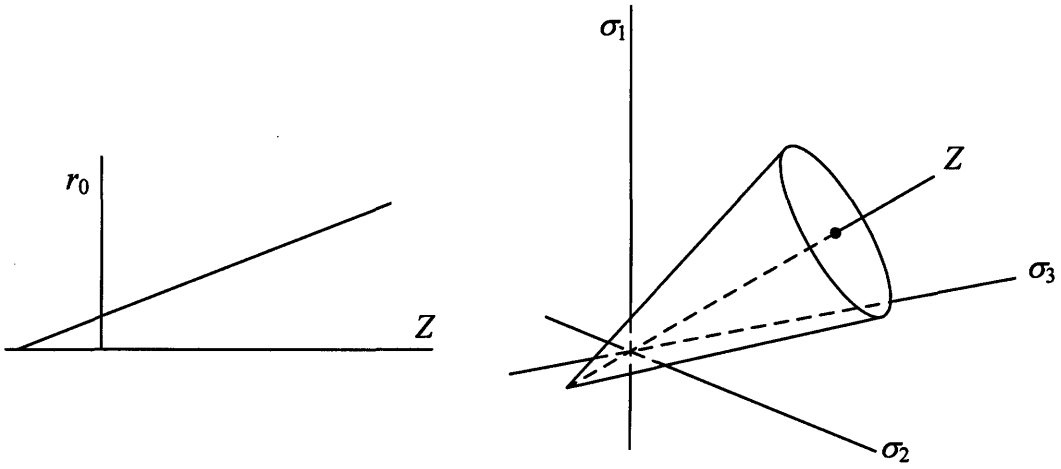

(a) Triaxial Plane Cross-Section (b) Three Dimensional View

Figure 2.26 Drucker-Prager Model

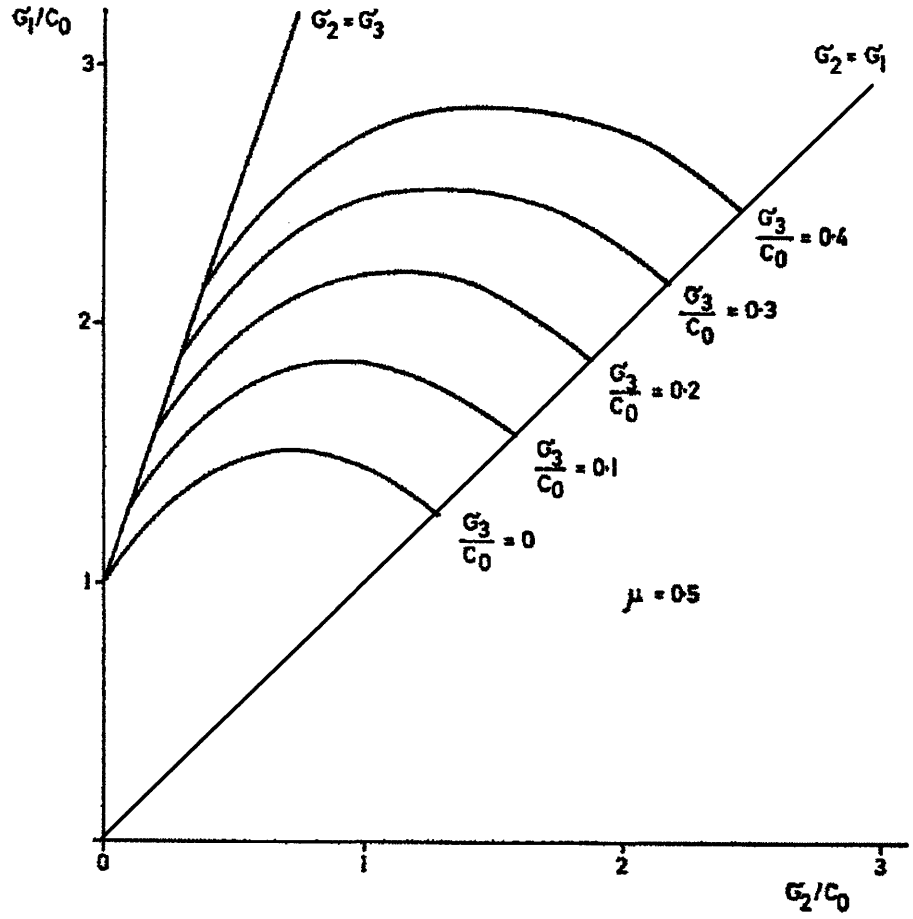

Figure 2.27 Prediction of Rock Strength by Wiebols and Cook (1968)

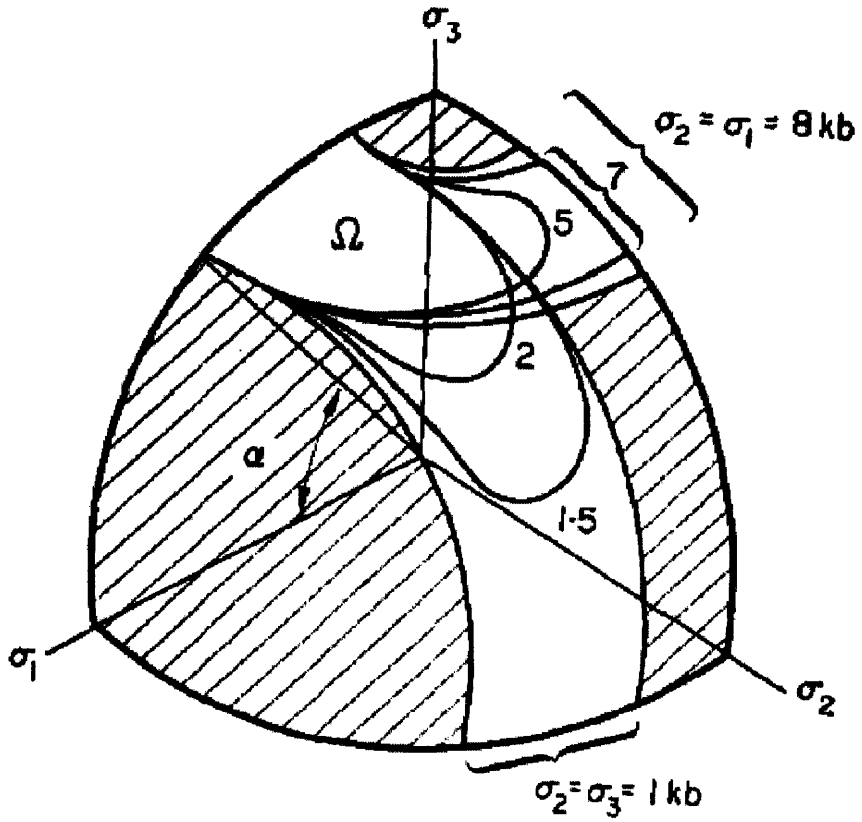

Figure 2.28 Area Ω on a Unit Sphere with $\tau_{eff} > 0$ (Lundborg, 1972)

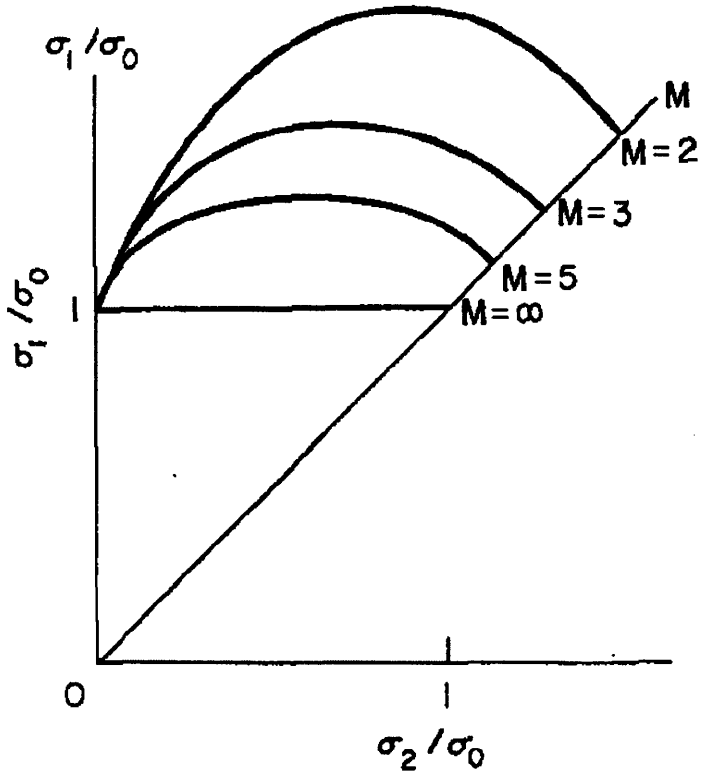

Figure 2.29 Prediction of Rock Strength with $\mu = 1$ and $\sigma_3 = 0$ (modified from Lundborg, 1972)

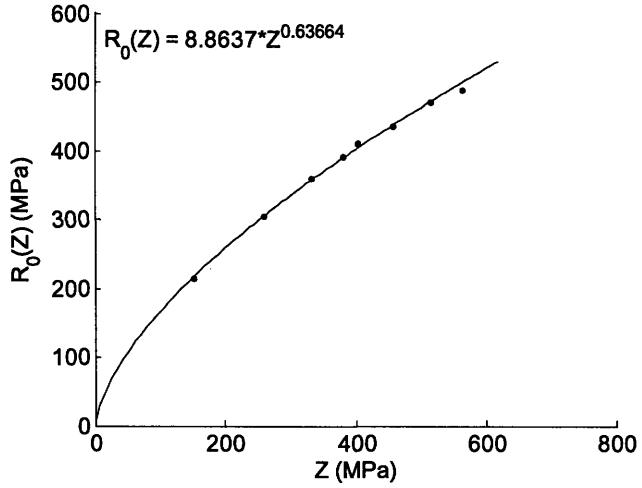

Figure 2.30 Conventional Triaxial Compression Data for Dunham Dolomite (data from Mogi, 2007)

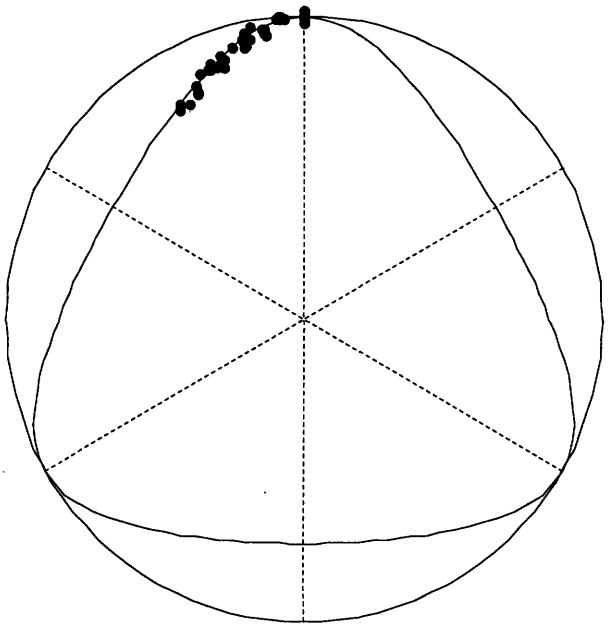

Figure 2.31 Normalized Failure Points of Dunham Dolomite on the π-Plane with $\beta_s = 0.74$ (data from Mogi, 2007)

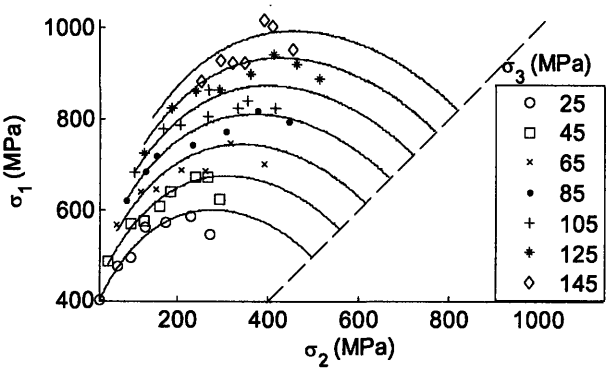

Figure 2.32 Predicted Strength with Proposed Criterion for Dunham Dolomite (data from Mogi, 2007)

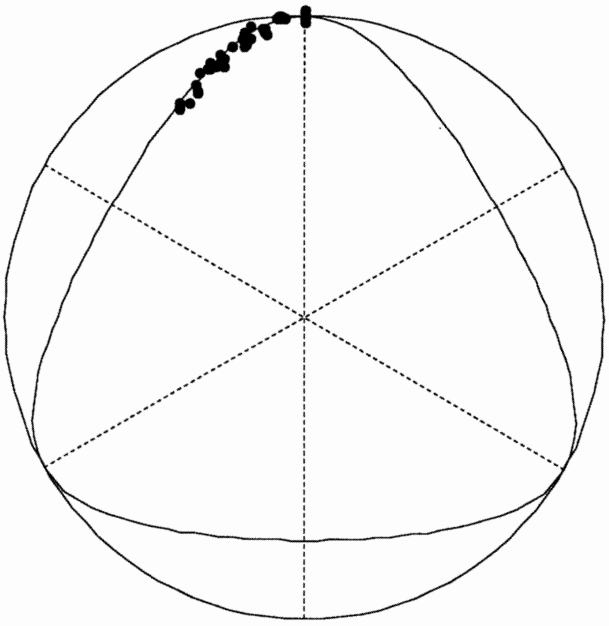

Figure 2.33 Dunham Dolomite: Measured and Predicted Normalized π-Plane Cross-Section (β_s=0.74, data from Mogi, 2007)

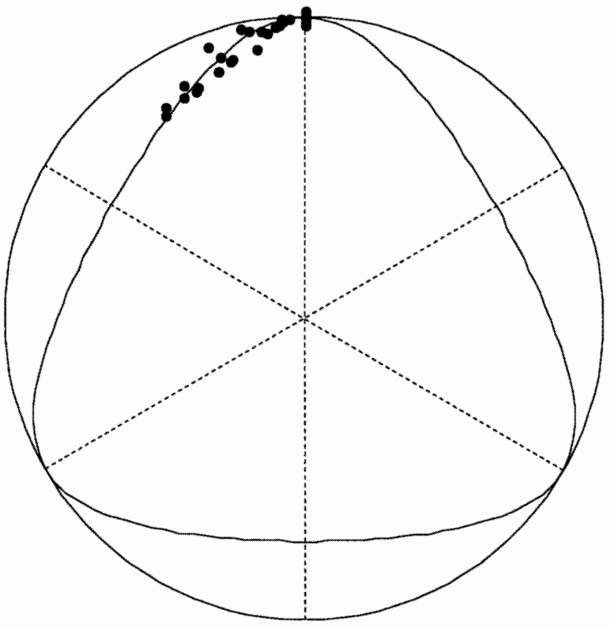

Figure 2.34 Solnhofen Limestone: Measured and Predicted Normalized π-Plane Cross-Section (β_s=0.75, data from Mogi, 2007)

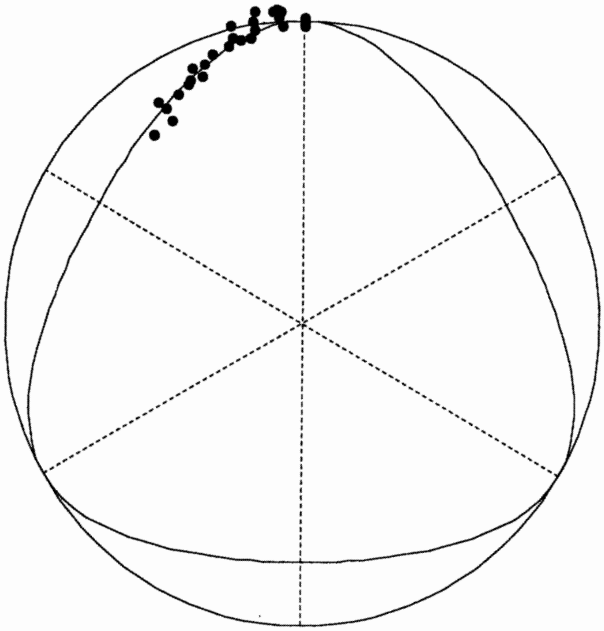

Figure 2.35 Yamaguchi Marble: Measured and Predicted Normalized π-Plane Cross-Section (β_s=0.79, data from Mogi, 2007)

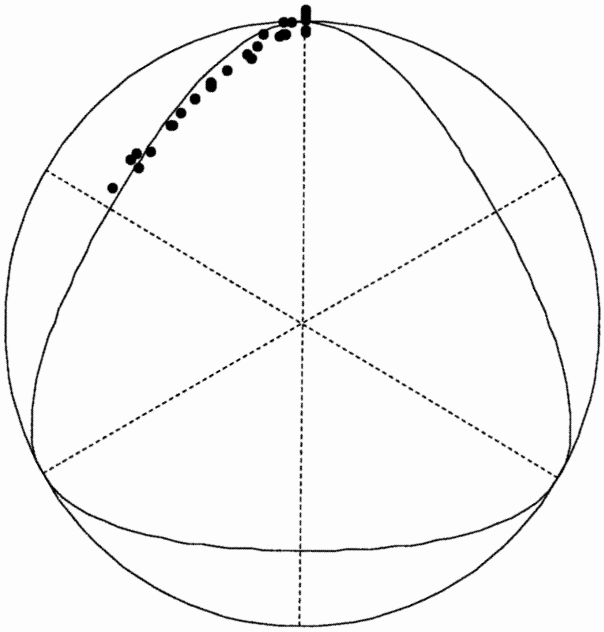

Figure 2.36 Mizuho Trachyte: Measured and Predicted Normalized π-Plane Cross-Section (β_s=0.75, data from Mogi, 2007)

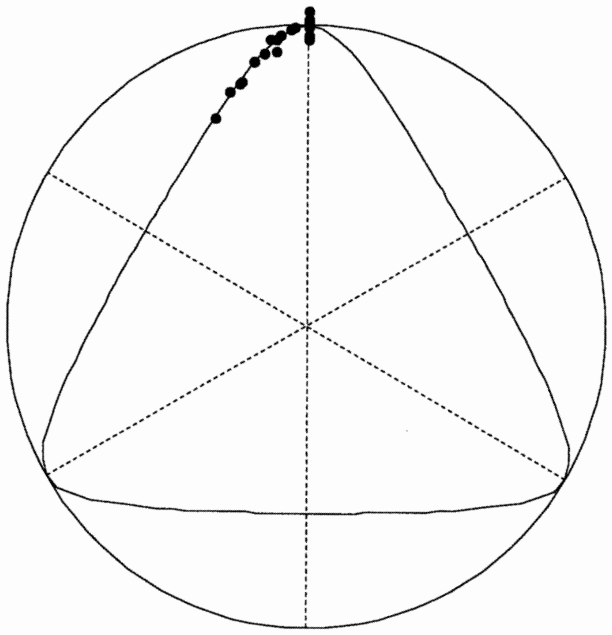

Figure 2.37 Manazuru Andesite: Measured and Predicted Normalized π-Plane Cross-Section (β_s=0.62, data from Mogi, 2007)

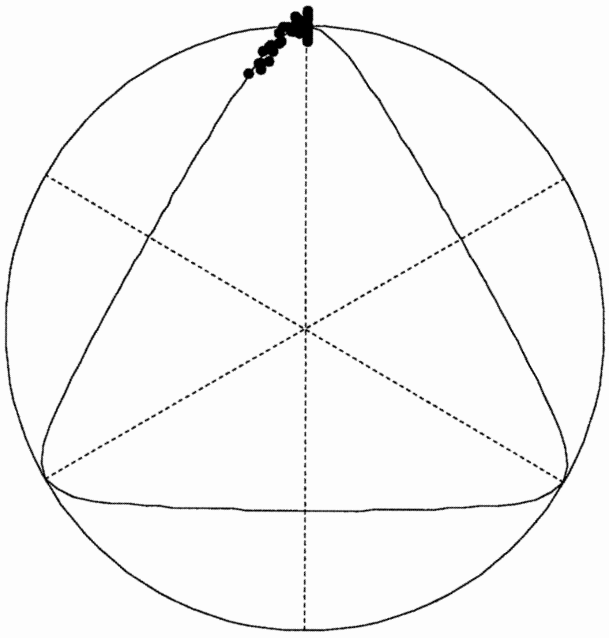

Figure 2.38 Inada Granite: Measured and Predicted Normalized π-Plane Cross-Section (β_s=0.6, data from Mogi, 2007)

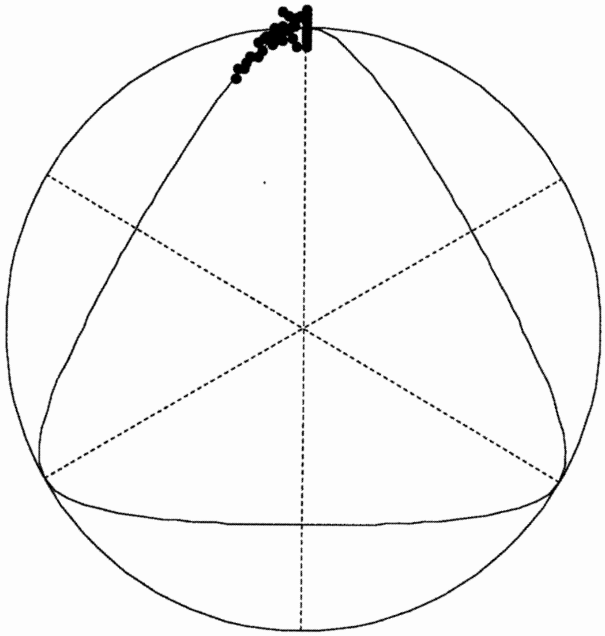

Figure 2.39 Orikabe Monzonite: Measured and Predicted Normalized π-Plane Cross-Section (β_s=0.65, data from Mogi, 2007)

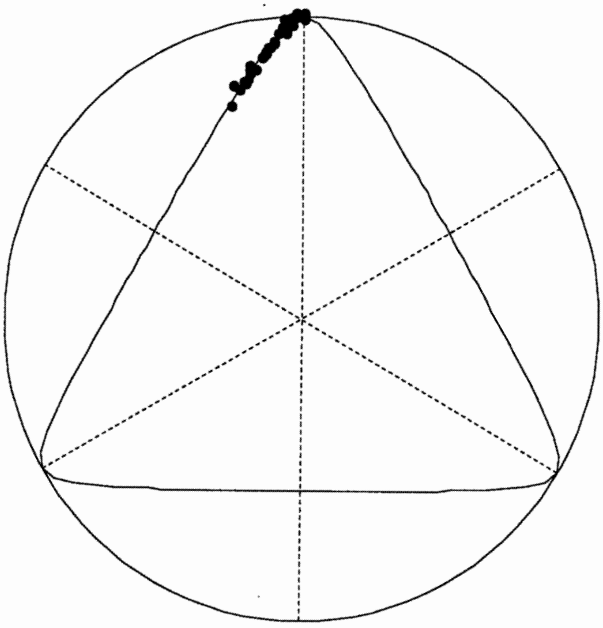

Figure 2.40 Westerly Granite: Measured and Predicted Normalized π-Plane Cross-Section (β_s=0.57, data from Haimson and Chang, 2000)

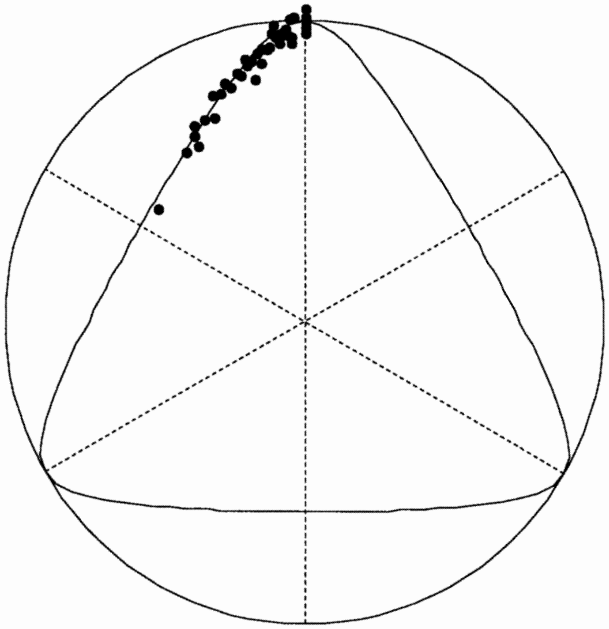

Figure 2.41 KTB Amphibolite: Measured and Predicted Normalized π-Plane Cross-Section (β_s=0.63, data from Chang and Haimson, 2000)

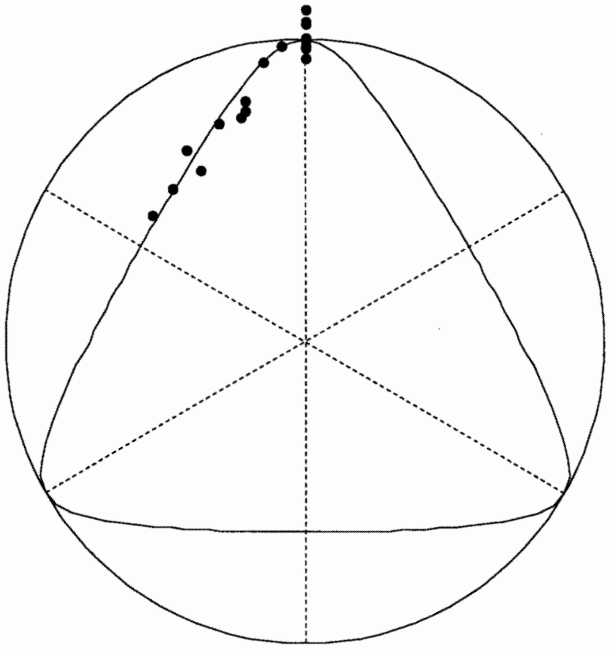

Figure 2.42 Long Valley Hornfels: Measured and Predicted Normalized π-Plane Cross-Section (β_s=0.63, data from Chang and Haimson, 2007)

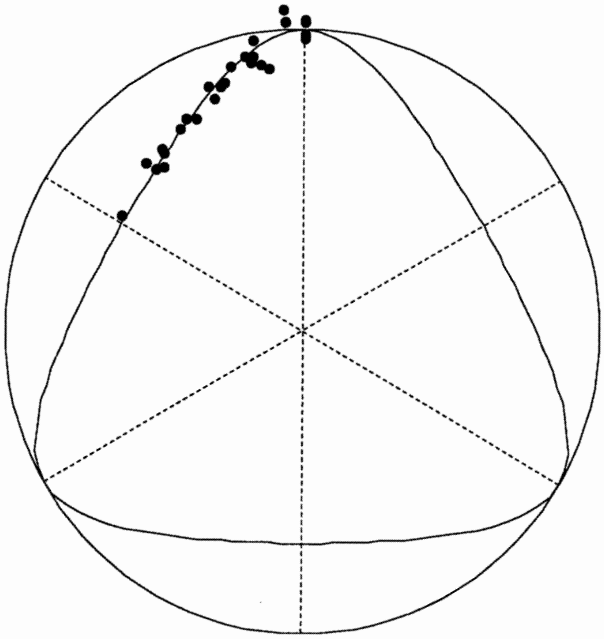

Figure 2.43 Chelungpu Siltstone: Measured and Predicted Normalized π-Plane Cross-Section (β_s=0.7, Oku et al., 2007)

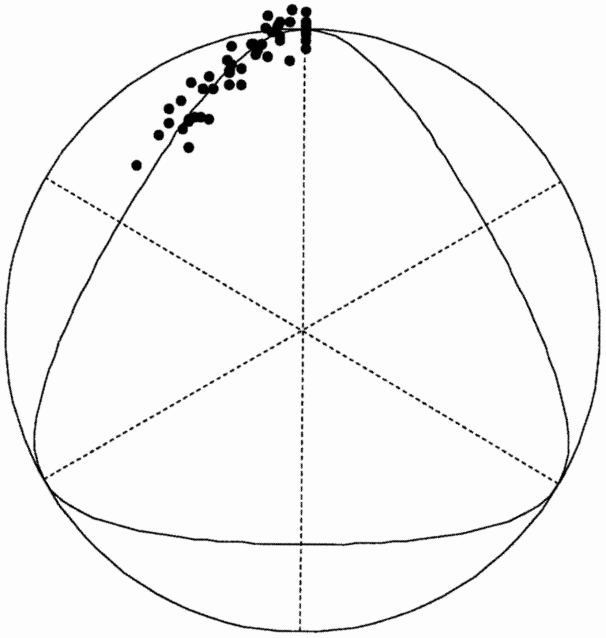

Figure 2.44 Shirahama Sandstone: Measured and Predicted Normalized π-Plane Cross-Section (β_s=0.71, Takahashi and Koide, 1989)

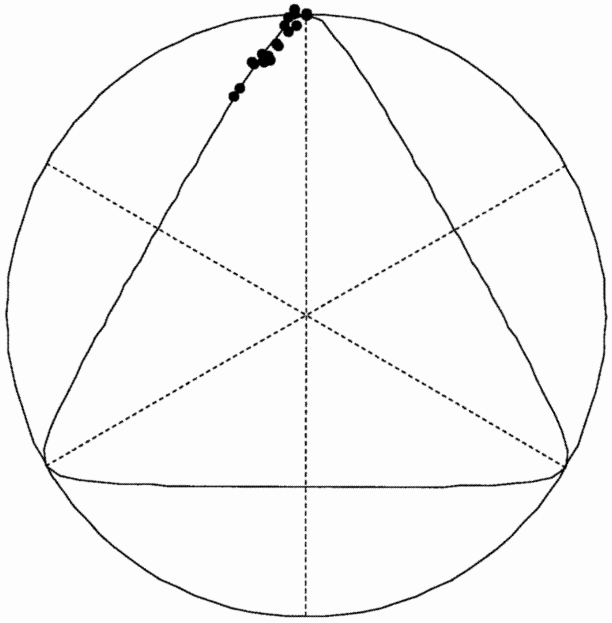

Figure 2.45 Izumi Sandstone: Measured and Predicted Normalized π-Plane Cross-Section (β_s=0.57, Takahashi and Koide, 1989)

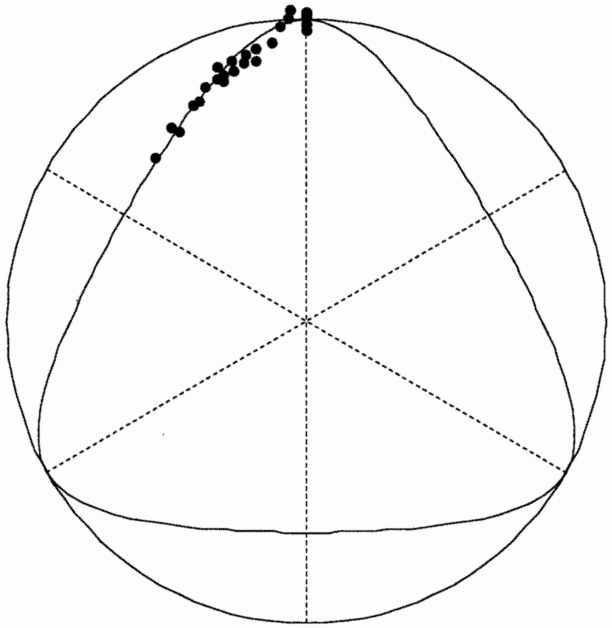

Figure 2.46 Yuubari Shale: Measured and Predicted Normalized π-Plane Cross-Section (β_s=0.73, Takahashi and Koide, 1989)

3 Failure of Anisotropic Rocks

In the previous chapter, rocks are treated as isotropic materials. However, natural rocks are more or less anisotropic, and isotropy is therefore only an approximation. Whether the strength of a particular rock can be reasonably well described by isotropic models or not is only known after extensive testing of the rock at different orientations. If it turns out that the strength strongly depends on orientation, then an anisotropic strength model must be used to characterize its strength. It is usually hard to identify rocks whose strengths are close to isotropic by visual inspection. Rocks that are strongly anisotropic, however, may reveal its strength anisotropy through various structural features that are easily identified. For example, shales are known to have the bedded structure that is formed by sedimentation; slates can sometimes split along the cleavage planes; schists may clearly show the elongated minerals, etc. For these rocks, an isotropic failure criterion is usually inadequate.

Anisotropy comes from very different origins. For intact rocks, anisotropy can be generated from the orientation of minerals or other textural features, and from stress history. For rock masses, the anisotropy is more complicated due to the existence of large scale discontinuities. It is not the intention of this thesis to study all these various types of anisotropy. In fact, the focus of this research is on a particular type of anisotropic rocks, those that can be reasonably described as transversely isotropic materials.

Many different geo-materials can be reasonably well described to be transversely isotropic, for example, soft clay that has experienced one dimensional consolidation. The clay particles are compressed in the direction of the consolidation, which makes this direction the privileged direction of anisotropy. In the plane orthogonal to the direction of deposition, mechanical properties are assumed to be isotropic. Many sedimentary rocks and some metamorphic rocks can also be classified as transversely isotropic, for example, shales, slates, etc. In the case of shale, due to the sedimentary process, shale usually possesses layered features, which is called the bedding planes. The mechanical behavior is isotropic within the bedding planes, but is different from that perpendicular to them.

For a transversely isotropic material, there is always a plane in which the mechanical behavior is isotropic. This plane will be termed the *isotropic plane* in a general mathematical model. While describing a specific data set, the isotropic plane will be referred as the cleavage plane, bedding plane etc., depending on the materials that are under discussion. There is one privileged direction of a transversely isotropic material, which is the normal to the isotropic planes. Therefore, the behavior of a transversely isotropic material is orientation dependent.

The failure of anisotropic rock is a very complicated topic. The strength is not only a function of

the stress tensor, like the failure of isotropic rock, but also a function of the material structure. In addition, there are different modes of failure that have been observed. This chapter summarizes past efforts on characterization of anisotropic rock strength. The material of this chapter is divided into two parts: experimental results and existing models.

The first part of this chapter presents experimental results on fifteen transversely isotropic rocks, which belong to five different rock types: Slate, Phyllite, Schist, Shale, and Diatomite. The experiments performed are mainly conventional triaxial tests, except for one rock (the Chichibu Green Schist), where true triaxial test results are available. The variation of strength and failure modes with isotropic plane orientation and principal stresses will be presented for each anisotropic rock.

In order to present the test results in a clear and consistent manner, it is necessary to set up coordinate systems. Two different coordinate systems are shown in Figure 3.1. The $\mathbf{x_1x_2x_3}$ system is the principal stress system, where $\mathbf{x_1}$ is the direction of the principal stress σ_1, etc. The **STN** system is the material coordinate system, where **N** is the direction normal to the isotropic planes, while the **ST** plane is the isotropic plane. In order to describe the relative orientation of the **STN** system with regard to the $\mathbf{x_1x_2x_3}$ system, three angles must be specified. The angle between $\mathbf{x_1}$ and **N** is θ, while ω stands for the angle between $\mathbf{x_3}$ and the projection of **N** onto $\mathbf{x_2x_3}$ plane. The orientation of **N** is completely defined by θ and ω. In order to fix the directions of **S** and **T**, λ is defined as the angle between **T** and the intersection of the **ST** plane and the x_2x_3 plane. Under the assumption of transverse isotropy, the material behaves isotropically within the **ST** plane. Therefore, the constitutive law should be independent of λ.

In the case of the conventional triaxial tests, where $\sigma_2 = \sigma_3$, the angle ω is irrelevant too, and the orientation of the isotropic planes with regard to the principal stresses can be represented by θ only. This is evident by setting the direction **S** and $\mathbf{x_2}$ to coincide (Figure 3.1 (b)). In Figure 3.2, a triaxial specimen is shown to illustrate the orientation of the isotropic plane with regard to the axial direction. Most of the experiments presented in this chapter are conventional triaxial tests, where the configuration is the same as Figure 3.2. Instead of using θ to describe the isotropic plane orientation with regard to $\mathbf{x_1}$, many researchers use the angle between the isotropic plane and $\mathbf{x_1}$, which is $(\pi/2 - \theta)$. From now on, θ is called the isotropic plane normal orientation, while $(\pi/2 - \theta)$ will be called the isotropic plane (or cleavage plane, bedding plane, etc.) orientation. The isotropic plane orientation is denoted β following McLamore and Gray (1967). Figure 3.2 also shows the special cases where the isotropic planes are parallel and perpendicular to the axial direction.

Existing anisotropic strength criteria are summarized in the second part of this chapter. Based on how these criteria are derived, they are divided into four categories: empirical criteria, continuous criteria, critical plane approach, and discontinuous models. Efforts were made to show the interrelations between the different criteria.

3.1 Experimental Results on Anisotropic Rocks

3.1.1 Donath's Data

Donath (1964) reported a series of conventional triaxial tests on Martinsburg slate. The specimens were prepared so that the cleavage plane orientation $\beta = 0°$ to 90° with 15° intervals. The specimens were ground at both ends to form perfect right cylinders. The specimens had two different sizes. Larger specimens had 1 inch diameter and 2.5 inch length. They were subject to three different confining pressures: 35, 105 and 350 bars. Smaller specimens had 0.5 inch diameter and 1 inch length. They were subject to higher confining pressures: 500, 1000 and 2000 bars. For each combination of orientation and confining pressure, two tests were performed to ensure the repeatability. The axial stresses at failure are compiled in Table B.1. The variation of σ_1 at failure with cleavage plane orientation and confining pressure is shown in Figure 3.3. At any β value, the strength clearly increases with the confining pressure. At any confining pressure, the strength variation with isotropic plane orientation β can be represented by a "U" shaped curve with uneven shoulders, as is evident in Figure 3.3. Two local maxima are reached at $\beta = 0°$ and 90°. In the case of the Martinsburg slate, the strength at $\beta = 90°$ is larger than that at $\beta = 0°$. The minimum strength is reached around $\beta = 30°$. This is most probably because of the slip along the cleavage planes.

Donath (1964) also carefully described the failure mode of the specimens. It seemed that all of the specimens were failed by shear faulting, so that one part of the specimen moved relative to the other part along the fault. The shear faults were formed by either slipping along the cleavage planes, or shearing across them (i.e. faulting through matrix material). The faulting process can be brittle or ductile, depending on the level of confining pressure. The strike of the fault plane was always parallel to that of the cleavage. It seemed that the *fault orientation* (the angle between the fault plane and the axial direction) was very heavily dependent on the cleavage orientation. The fault orientations at various confining pressures were measured and plotted against the cleavage orientation in Figure 3.4. Any points that fall along the 45° line indicate the fault orientation is the same as the cleavage plane orientation, and thus failure along the cleavage plane is observed. The following phenomena are noted:

- $\beta = 0°$: There is a wide scatter of fault orientations. At smaller confining pressure (triangular symbols in Figure 3.4), the fault orientations are close to 0°, so that the faults more or less follow the cleavage. This is believed to be caused by tensile failure along the cleavage at small confining pressure. The fault orientation is larger for larger confining pressure (circular symbols), and it can get close to 30°. In this case, the faulting is through the matrix material.
- $\beta = 15°$ to 30°: For these β values, the cleavage planes are steeply inclined. At smaller

confining pressures, it seems that the specimens fails by slipping along a single cleavage plane in a brittle manner. With increasing confining pressure, it seems that the failure mode changes to slipping along multiple cleavage planes, and then to development of kink bands (see Figure 3.5 for failed specimens with β = 15°). The kink band is a zone where the cleavage is rotated from its original orientation. Further deformation causes faulting within and parallel to the kink band boundaries. It is obvious that large deformation occurs with the development of kink bands. Therefore, it is a ductile type of failure. Figure 3.6 shows the kink band on the cross-sections of failed specimens with increasing confining pressure. At 1000bar confining pressure, a very wide kink band can be identified in which the cleavage planes rotate. At the two ends of the specimen, the cleavage orientation is not changed, possibly because of the constraint of rigid platens. The width of the kink band gets smaller with increasing confining pressure, as can be shown for specimens failed at 1600 to 2000bar.

- β = 45° to 75°: In this range of cleavage plane orientation, the specimen can fail along or across the cleavage planes. For β = 45°, most of the specimens fail by slipping along the cleavage planes (Figure 3.4). Again, slipping along single cleavage plane is observed for smaller confining pressure, and multiple slipping for larger confining pressure (Figure 3.7). With increasing β, the fault orientation deviates from the cleavage plane orientation (Figure 3.4) and is smaller than β. Based on Figure 3.4, this deviation is larger for smaller confining pressures. The fault orientation peaks around β = 75°.
- β = 90°: The fault orientation is close to 30° regardless of the confining pressure. Therefore, faulting only occurs through matrix material.

It is worth noting that the observed trend of fault orientation on Martinsburg slate may not be applicable to other anisotropic rocks. For example, Donath (1961) reported the fault orientation measured from Longwood shale specimens subject to 420bar confining pressure (Figure 3.8). It seems the fault orientation remains close to 30° for any isotropic plane orientation larger than 30°.

3.1.2 Hoek's Data

Hoek (1964) reported proportional triaxial compression tests on a South African slate. Proportional triaxial compression tests were performed with the ratio σ_3/σ_1 being constant through the entire test. Three different ratios were applied: σ_3/σ_1 = 0 (uniaxial tests), 0.113 and 0.171. β, the orientation of bedding planes, was from 0° to 90° at 15° intervals. The size of the specimens was 0.85 inch diameter and 1.7 inch length. At any combination of β and σ_3/σ_1, two specimens were tested to check the repeatability of the results. The failure axial stresses are listed in Table B.2, and plotted in Figure 3.9.

Since the tests reported are proportional triaxial tests, each curve in Figure 3.9 represent the tests with a certain σ_3/σ_1 ratio. Therefore, they are different from the curves shown in Figure 3.3 for Martinsburg slate. Nevertheless, the general trends are the same. For each β value, the strength increases with the stress ratio. At a certain stress ratio, the strength variation with β forms a "U" shaped curve. The minimum strength is reached at $\beta = 30°$. However, a description of failure modes is not given by Hoek (1964).

3.1.3 McLamore and Gray's Data

McLamore and Gray (1967) investigated the behavior of three different anisotropic rock materials: a fine-grained black slate (termed the Austin slate) and two types of Green River Shale. The slate has "no discernible bedding planes within the material but cleavage was well developed". Green River Shale is "composed of fine-grained calcite and dolomite particles interbedded with a solid native high molecular weight organic material called kerogen". The first type of Green River Shale has higher strength among the two and usually fails in a brittle manner. The second type, on the other hand, is more ductile and fails after considerable plastic strain.

Conventional triaxial tests were performed on these materials. The final dimension of the triaxial specimens was approximately 0.5inch diameter by 1.0 inch long. The confining pressure and the bedding plane orientation were varied to observe strength anisotropy. The anisotropic strengths for these three materials are plotted in Figure 3.10 through Figure 3.12. The numerical values of axial stresses at failure are tabulated in Table B.3 through Table B.5. The basic trends are similar to those of Martinsburg slate and South African Slate. However, there is something special for the Austin slate. The cleavage plane orientation β where the minimum strength is reached increases with the confining pressure, from 30° at 5000psi to around 40° at 40000psi. This is not observed in the Green River Shale specimens.

McLamore and Gray (1967) also discussed carefully the observed failure modes and summarized their observations (Figure 3.13). The failure modes that were observed are generally consistent with those reported by Donath (1964). The "Shear" failure mode describes brittle failures either along or across the bedding planes, at lower confining pressures. The failure mode "Plastic Flow or Slip" along bedding planes in Figure 3.13 roughly corresponds to multiple slip along cleavage planes in Donath's observations (for example, see failed Martinsburg specimen in Figure 3.7 with $\beta = 45°$ and $\sigma_3 = 1000$bar). The "Kink Flow" failure mode describes the development of ductile kink band.

All three different failure modes in Figure 3.13 were observed in the Austin slate specimens. At confining pressures below 15000psi, brittle failure was observed. The fault developed along the bedding planes for $\beta = 10°$, 20° and 30°. At larger confining pressures, the failure mode becomes

plastic flow along the bedding planes or kinking. McLamore and Gray (1967) also observed that the kink zone usually have two parallel boundaries, and kinking occurred only at $\beta = 10°$, 20° and 30°, while plastic flow occurred for other orientations. Figure 3.14 shows the failed specimens of slate, with $\beta = 30°$ and various confining pressures.

All Green River Shale I specimens failed in the "Shear" failure mode. Figure 3.15 shows the failed specimens of Green River Shale-1 at 15000psi confining pressure and various bedding plane orientations. Specimens with $\beta = 20°$ and 30° failed along the bedding planes at this confining pressure. This rock seemed to be very brittle, and a small amount of plastic deformation was only observed on specimens with 25000psi confining pressure.

All three failure modes were observed in Green River Shale II specimens. Figure 3.16 shows the failed specimens with $\beta = 10°$ at various confining pressures. As summarized before, the failure mode changes from brittle failure to wide kink zone with an indistinct boundary, then to narrow kink zone with a distinctive boundary. For specimens of $\beta = 20°$ to 40°, shear faulting occurs along bedding planes, with multiple slip at higher confining pressures. For specimens with $\beta = 60°$, shear faulting occurs across the bedding planes for lower confining pressures (1000 to 10000psi), while it follows the bedding planes for higher confining pressures. This is consistent with the observations made by Donath (1964) (Figure 3.4 $\beta = 60°$). For specimens with $\beta = 90°$, ductile shear fault develops across the bedding planes at a fault orientation of 34°, for all confining pressures larger than 5000psi.

3.1.4 Attewell & Sandford's Data

Attewell & Sandford (1974) reported on conventional triaxial tests on Penrhyn slate specimens, with 1 inch diameter and 2.5 inch length. The cleavage plane orientation β ranges from 0° to 90° with 15° intervals. Six different confining pressures are applied: 0, 2000, 4000, 6000, 8000, and 10000 lb/in^2. The measured peak strengths are listed in Table B.6 and plotted in Figure 3.17 (a).

After a shear fault is clearly defined, the axial stress is then reduced to obtain the post-peak behavior, which is plotted in Figure 3.18. The post-peak strengths, when plotted against the cleavage plane orientation β, also produce "U" shaped curves. However, when comparing Figure 3.17 with Figure 3.18, it is clear that the post-peak "U" shaped curves are flatter. Therefore, the post-peak strength anisotropy is much smaller than the peak strength anisotropy.

The shear fault orientations are plotted in Figure 3.19 against the cleavage plane orientation. It seems that the shear faults roughly follow the cleavage planes for $\beta = 15°$ and 30°. At larger β values, the shear fault orientation increases to between 30° and 40°, then decrease slightly at $\beta = 90°$. The trend is consistent with the observation of Donath (1964) on Martinsburg slate (Figure 3.5). However, the maximum shear fault orientation is smaller than that of Martinsburg slate.

3.1.5 Mogi's Data

Mogi (2007) reported on true triaxial tests performed on Chichibu green schist, with the true triaxial apparatus described in Section 2.2.2.3. The experimental measurements were summarized. Chichibu green schist is a macroscopically homogeneous green crystalline schist with a distinct, dense foliation, from the Chichibu Mountain, west of Tokyo.

In true triaxial tests, the specimens were prepared so that four different loading modes were performed (Figure 3.20). β is 30° for loading modes I, II and III. The difference between these three modes lies in ω, which defines the dip direction of the foliation planes. In mode I, the foliation planes dip into σ_3 direction. In mode II, the dip of the foliation planes is 45° between σ_2 and σ_3. In this case, the angle between the side of the specimen and the trace of the bedding planes on the specimen surface is $\beta' \approx 39°$ (see Figure 3.20, Mode II). In mode III, the dip direction is in the σ_2 direction. Mode IV, on the other hand, has $\beta = 90°$ so that the foliation planes coincide with the $\mathbf{x_2x_3}$ plane. For all the true triaxial tests, the minor principal stress is σ_3 = 50MPa. The principal stresses at failure are summarized in Table B.8. The failure σ_1 vs. σ_2 is plotted in Figure 3.21 for all four different modes.

Conventional triaxial compression tests were also performed with mode I, II and IV specimens, with the following confining pressures: 0, 25, 50, 75MPa. Since $\sigma_2 = \sigma_3$ in a conventional triaxial test, Mode I and Mode II are essentially the same, and both correspond to $\beta = 30°$. Mode IV specimens, on the other hand, correspond to $\beta = 90°$. The principal stresses at failure in conventional triaxial tests are summarized in Table B.7 and plotted in Figure 3.22.

It seems that most of the specimens failed in a brittle manner. Mogi (2007) showed the pictures of failed specimens for Mode I, II, and IV specimens. In order to present their results in a clear manner, Plane A and B in Figure 3.23 are defined as the two surfaces of the specimen that are perpendicular to the σ_2 direction. Figure 3.24 shows a failed specimen of Mode I, where the failure principal stresses (σ_1, σ_2, σ_3) = (206MPa, 100MPa, 50MPa). A single, very even failure plane is clearly observed, which is around 30° from the σ_1 direction and dips into σ_3 direction. Therefore, this failure plane most probably occurs along one of the foliation planes.

Failure is more complicated in Mode II, where the dip of the foliation planes is 45° between σ_2 and σ_3 directions. Figure 3.25 (a) shows the failed specimen with (σ_1, σ_2, σ_3) = (244MPa, 50MPa, 50MPa). Although tested in the true triaxial apparatus, this is actually a conventional triaxial stress state, which may explain why the images on Plane A and Plane B are more or less symmetric. Multiple sub-parallel fault planes can be identified on both planes. The orientation of these faults is close to β', which is the orientation of the trace of foliation planes ($\beta' \approx 39°$, refer to Figure 3.20). Therefore, they most likely occur along the foliation. In Figure 3.25 (b) where (σ_1, σ_2, σ_3) = (346MPa, 168MPa, 50MPa), the stress state is true triaxial. The faults are less

planar, and the fracture patterns on Plane A and Plane B are no longer symmetric.

In Mode III, where the foliation dips in σ_2 direction, the fault planes also dip in σ_2 direction. This clearly shows the influence of anisotropy features to the failure mode. If the rock were isotropic, the fault planes should always dip in σ_3 direction. Unfortunately, no picture of failed specimens is reported for this mode.

One failed specimen is shown for Mode IV (Figure 3.26). The fault plane seems to be well developed and its orientation is about 30° to the σ_1 direction. However, the failure surface does not seem to be very planar. The reason may be that the fault is across the foliation planes.

Based on these experimental results, it is clearly shown that the orientation of the foliation plane has a significant impact on the orientation of the shear fault in a true triaxial test.

3.1.6 Allirot and Boehler's Data

Allirot and Boehler reported conventional triaxial tests on diatomite specimens (Allirot and Boehler, 1979). Their specimens had 39mm diameter and 78mm length. The bedding plane orientation β ranges from 0° to 90° with 15° intervals. Six different confining pressures were applied: 0, 0.5, 1.0, 2.0, 4.0 and 6.0MPa. However, only the strengths at 0.5, 1.0 and 2.0MPa confining pressure were reported in Allirot and Boehler (1979). The strength variation with β at these three confining pressures are listed in Table B.9 and plotted in Figure 3.27. A brief description of the mineralogy of diatomite from Dolley (2000) is attached at the end of Table B.9.

Allirot and Boehler (1979) also supplied the pictures of failed specimens with β = 90°, 30° and 0° (shown as θ = 0°, 60° and 90° in Figure 3.28). At zero confining pressure, tensile splitting is observed at β = 0° and 90°, while faulting along the bedding plane is observed for β = 30°. For non-zero but small confining pressures (less than 2MPa), the specimens fail in a brittle manner, either across or along the bedding planes, depending on the value of β. For larger confining pressures, ductile failures are observed. Kink bands can be observed for the specimen with β = 30° and σ_3 = 6MPa. The specimen with β = 0° and σ_3 = 4MPa obviously has experienced large plastic deformation. It is very interesting to see that for σ_3 > 1MPa, conjugate shear faults are always observed on specimens with β = 0°.

3.1.7 Aristorenas' Data

Aristorenas (1992) performed a series of tests on Opalinus and Lias α shale samples. Two batches of samples were used in the tests. One batch of samples was taken from the Diepflingen and Wittinsburg boring sites of the Wisenberg tunnel project in Switzerland. The other batch was

from Erzingen in Southern Germany. The samples and their initial properties are listed in Table B.10. The mineralogy of these samples is shown in Table B.11. The shale samples had an average diameter of 7.9cm. They were received wrapped in thick aluminum foil and sealed with wax. They were stored in a humid room until specimens were prepared for testing.

Several different types of experiments were performed, including isotropic consolidation tests, K_0 consolidation tests, and conventional triaxial tests. Shear strength data from the conventional triaxial tests will be described below.

The conventional triaxial tests in this data set were performed with three conventional triaxial apparati, one large high pressure triaxial cell and two small high pressure triaxial cells were used. The large triaxial cell was developed by Bellwald (1990). The specimens for the large triaxial cell have an average diameter of 8cm. The large specimens were directly cut from the samples, to a length that was at least twice the diameter, by a disc saw. Lateral displacement was measured by proximity sensors for large specimens. Since it takes a very long time for the large specimens to reach full drainage, the large triaxial cell was used solely for undrained tests, and the small triaxial cells were used for drained tests. The specimens for the small triaxial cell have an average diameter of 3.6cm. They were cored from the bored samples with a diamond-tipped coring device.

Based on the stress analysis for a circular tunnel in an isotropic elastic medium with an isotropic in-situ stress (vertical and horizontal stresses are equal), one can assume that an element at the crown or springline of the tunnel is subject to pure shear plane strain stress change (total stress) due to excavation. Therefore, the total stress paths were selected to be pure shear, where both the axial pressure and the cell pressure were changed so that the mean total stress remains constant. The typical total stress path in compression is shown in Figure 3.29, where:

$$\sigma_{oct} = \frac{\sigma_1 + 2\sigma_3}{2}, \sigma'_{oct} = \frac{\sigma'_1 + 2\sigma'_3}{2}, q = \frac{\sigma_1 - \sigma_3}{2} \tag{3.1}$$

with σ_1 being the axial stress, and σ_3 the lateral stress (in a conventional triaxial test, $\sigma_2 = \sigma_3$). The specimen was first brought to a low effective octahedral stress (point A, 0.5MPa to 1.0MPa) for saturation with a back pressure of 1.0MPa to 1.3MPa. The B-value was checked to confirm saturation. The specimen was then consolidated (from point A to B) to its pre-shear stress state. It was then sheared up to failure in pure shear (from point B to C). Three different combinations of drainage and loading conditions were applied: undrained compression (UC), undrained extension (UE) and drained compression (DC).

A total of 15 conventional triaxial shear tests were performed on Opalinus shale, of which 5 were undrained compression tests, 4 were undrained extension tests, and 6 were drained compression tests. The tests performed are listed in Table B.12. Each "Specimen ID" in this table is composed of two parts. The first part stands for the sample from which the specimen was cut. The second part shows the type of test performed on it. Only one test was performed on the Erzingen

specimens because they were not properly wrapped. Note that all the specimens have bedding plane orientation (i.e. β) to be 90°.

While performing the tests, however, some of the specimens did not strictly follow the stress path shown in Figure 3.29, due to different practical reasons. In undrained extension tests, specimens 26B-4(UE), 26B-6(UE), and ERZ4(UE) were not isotropically consolidated. In the drained compression tests, specimen 26B-8(DC) was not isotropically consolidated. The ratio between the confining pressure and axial stress during consolidation is defined by K_A:

$$K_A = \frac{\sigma_3'}{\sigma_1'} \tag{3.2}$$

If the consolidation is performed so that the horizontal strain is zero, then K_A is specifically denoted as K_0. The values of K_A and K_0 are shown in Table B.12. In the five drained compression tests, only two follow the pure shear stress path (Table B.12): 26B-6(DC) and 26B-8(DC). The other three are explained below:

- Specimen 23-1(DC) was sheared with $\Delta p' = 0$, where $p' = (\sigma'_2+\sigma'_3)/2$ is the MIT definition of mean effective stress. The third load increment involved a lowering of the back pressure by 0.5MPa to keep the back pressure smaller than the cell pressure. Otherwise, tensile effective stress may be generated in radial direction.
- Specimen 23-5(DC) was sheared to simulate an undrained effective stress path.
- Specimen 23-9(DC) was aimed at determining the material's time dependent behavior at 60% and 98% of the estimated shear strength.

For all tests, the following results were reported in Aristorenas (1992):

- The total and effective stress paths (example shown in Figure 3.30 (a)). For undrained tests, the effective stress path was obtained by the total stress minus the pore pressure, which was directly measured in the tests.
- The shear stress vs. shear strain relationship (example shown in Figure 3.30 (b)). Here, the shear stress is defined as:

$$q = \frac{\sigma_1 - \sigma_3}{2} \tag{3.3}$$

  while the shear strain is defined as:

$$\gamma = |\varepsilon_1 - \varepsilon_3| \tag{3.4}$$

  Therefore, they are different from the axial stress-strain curves usually reported. For the large specimens, the lateral strain ε_3 was directly measured. For the small specimens, the lateral strain was back calculated from the volumetric and axial strains.
- For undrained tests, the development of excess pore pressure was reported (example shown in Figure 3.30 (c)). For drained tests, the volumetric strain caused by shearing was reported.
- For drained tests, the volumetric and shear strains were reported against time, so that the

time dependent behavior can be studied. For specimen 26B-8(DC), variation of volumetric and shear strains with time were also reported for its isotropic and anisotropic consolidation.

- The modes of failure were described for different types of tests. Two different modes of failure were observed in the tests, which are illustrated in Figure 3.31.

Table B.13 partly reproduces these results, for the purpose of strength analysis. The principal effective stresses after consolidation and at failure, the excess pore pressure due to shearing, and the failure mode recorded by Aristorenas are summarized. Since the isotropic plane orientation is not varied, strength anisotropy due to material structure is not obtained from this data set. However, this dataset is the only one that has pore pressure measurements. From Table B.13, it can be seen that for most of the undrained shear tests, the excess pore pressure Δu is negative. This is very similar to the observations on highly over-consolidated clays. Considering that Opalinus shale samples have a considerable clay content (refer to Table B.11), the models that are developed for over-consolidated clay may be able to describe the behavior of this shale too.

In addition, this data set is the only one where conventional triaxial extension tests are performed. Very interesting observations on different failure modes for triaxial compression and extension were made by Aristorenas (1992). It is noted that specimens subject to undrained and drained compression mostly fail in Mode A, which is characterized by the presence of one or more shear faults (see illustration in Figure 3.31). Specimens subject to undrained extension tests, on the other hand, fail predominantly in Mode B, where "fracture planes" develop more or less along the bedding planes. On these fracture planes, local areas of smooth and rough surfaces are observed. Aristorenas (1992) therefore proposed that the failure mechanism of Mode B maybe a combination of shearing and tension, with some of the fracture planes failing by tension only. This statement is supported by the principal stresses at failure. Based on Table B.13, it is evident that the σ'_{1f} at failure for all of the undrained extension tests are very small. In specimen 26B-6(UE), it is even negative, which clearly shows that tensile effective stress developed at failure. Besides, it is also observed that Mode B failure occurs suddenly, which also hints that tensile stress may be the major factor of failure.

3.1.8 Ramamurthy's Data

Ramamurthy (1993) reported experimental results on three different phyllites: a quartzitic phyllite, a carbonaceous phyllite, and a micaceous phyllite. Uniaxial compression tests and conventional triaxial compression tests were performed to obtain the compressive strength of the phyllites.

The specimens used in triaxial tests were cubic specimens with 3.8cm side length. The orientation of the foliation planes β took the following values: 0°, 15°, 30°, 45°, 60°, 75°, 90°. However, the real β can be a few degrees off these values because the foliation planes are not

perfectly planar. The strength data were reported with real β values. The following confining pressures were applied: 0, 5, 15, 30, 50 and 70MPa. The four edges parallel to the axial loading direction were rounded to prevent membrane rupture. Ramamurthy (1993) shows some of the triaxial specimens (Figure 3.32).

The measured triaxial strengths are shown in Figure 3.33 through Figure 3.35 for all three phyllites. The numerical values of these strengths are listed in Table B.14 through Table B.16. Typical failure modes observed on the failed specimens were sketched (Figure 3.36). For specimens with $\beta = 0°$, tensile splitting develops at low confining pressure. Increasing confining pressure partly inhibits the development of tensile fracture, so that shear faults across the foliation planes and tensile crack along the foliation planes are both observed. For specimens with $\beta = 30°$ and 60°, slipping along the foliation planes is observed for smaller confining pressures. At higher confining pressure, the shear fault is step-shaped, composed of shear faults both along and across the foliation planes. Specimens with $\beta = 90°$ fails mostly by shearing across the foliation planes. There is no information on whether failures are brittle or ductile.

3.1.9 Niandou's Data

Niandou (1994) reported on a series of tests performed on Tournemire shale specimens. These tests were conducted at the University of Lille of France. The samples were taken from the Tournemire site near Aveyron, France. Tournemire shale is from the Toarcian stage, Lower Jurassic period. The mineralogy of Tournemire shale determined from X-Ray diffraction test is: Argillite (clay) minerals: 55%, Quartz: 19%, Calcite: 15%, others: 11% (including dolomite, siderite, feldspar, and pyrite). Among the clay minerals are Kaolinite 50%, Illite 30%, and Mixed Layer Clays (Interstratified I/S) 15%, and Chlorite 5%. The water content of the material varies from 4.5% to 8%. The porosity and density of the rock dried at different temperatures are shown in the Table B.17.

Various experiments were performed on these samples, including isotropic compression tests, conventional triaxial compression tests, and the proportional triaxial tests. The triaxial tests are described here since they give shear strengths.

3.1.9.1 Conventional Triaxial Compression Tests

Conventional triaxial compression tests were performed on specimens of 37mm diameter and 75mm length. Each test is uniquely defined by the following three factors:

- Confining pressure: Varies between 0MPa (uniaxial compression test) to 50MPa.
- Bedding plane orientation β: Varies between 0° to 90°.
- Loading sequence: Three different loading sequences are possible, monotonic loading, cyclic

loading with partial unloading cycles, and cyclic loading with complete unloading cycles. The entire matrix of different combinations of these three factors is shown in Table B.18. Each of these tests will be identified by the following notations:

Bedding plane orientation/Confining pressure/Loading sequence-Test Number

For example, 0/50/M-1 stands for a test with β = 0°, confining pressure 50MPa, monotonic loading test 1.

The axial strain rate for monotonic loading was $\dot{\varepsilon}_a = 2.0\times10^{-6}$ sec^{-1}, and that for load-unload cycles was $\dot{\varepsilon}_a = 4.5\times10^{-6}$ sec^{-1}. The loading rate for force controlled tests was 1.86×10^{-3}MPa per second. The conventional triaxial tests were performed with the drainage line open to the atmosphere. However, there was no fluid coming out of the drainage line, probably due to the partial saturation of the specimens, or the small permeability of the shale. The saturation of each specimen was not checked.

Three strain gauges were applied on each specimen. Figure 3.37 shows their configuration for a general bedding plane orientation. Gauge 1 measured axial strain ε_1. An LVDT was also used to measure the axial deformation of the sample. Both the gauge strain and the LVDT strain were reported by Niandou (1994). When the axial loading direction is not perpendicular to the bedding planes, the lateral strains are anisotropic. Gauge 2 measured strain in x_2 direction, which was also the strain in S direction. Gauge 3 measured the strain in x_3 direction, which was the strain in NT plane. In a triaxial compression test, the two lateral strains are generally different, with $\varepsilon_3 < \varepsilon_2$ (positive in compression).

For all conventional triaxial tests, the stress-strain curves were reported in Niandou (1994), including the axial strain (measured by gauge and LVDT), two lateral strains, and the volumetric strain. Pictures were also included for some of the failed specimens. LVDT strain measurements were only reported for tests with monotonic loading and for complete unload cycles.

Sample stress-strain curves are shown in Figure 3.38 (a) and (b), for a specimen with β = 90° and σ_3 = 30 MPa. Strains measured from strain gauges are shown in Figure 3.38 (a). They seem to give better measurements during specimen deformation, and are less affected by the seating problems than the LVDT measurements. LVDT measured strains are shown in Figure 3.38 (b). LVDT tends to give downward convex stress strain curves during initial loading due to seating problems. However, strain gauges ceased to work after the peak, where major fractures are likely to be created in the specimen, and the strain is localized. The LVDT can still give post-peak stress strain curves, which is the only source for post-peak behavior.

Peak strength and post-peak strength are read from the stress-strain curves, and are compiled in Table B.19 and Table B.20. When there are multiple tests for the same experimental settings, the

strength values are averaged. As explained before, post-peak strengths are only available for tests where LVDT strains are reported. The peak strengths are plotted in Figure 3.39. The post-peak strengths are plotted in Figure 3.40, for confining pressures of 1 and 20MPa only. Comparing Figure 3.39 and Figure 3.40, it is evident that the variation of the post-peak strength with β is much smaller than that of the peak strength. In fact, the post-peak strength "U" shaped curves are so flat that they are almost independent of β. The post-peak strength, therefore, is less anisotropic than the peak strength.

3.1.9.2 Proportional Loading Triaxial Compression Tests

In this group of experiments, the ratio between the axial and lateral stress is kept constant for the entire loading process. The way this loading path is achieved is by a stepwise approximation. First, both σ_3 and σ_1 were set to zero. Then σ_3 is increased by a small increment $\Delta\sigma_3$ (5bars or 10bars). Then σ_1 is increased by $K\Delta\sigma_3$, where K is the desired ratio. This stepwise approximation is shown in Figure 3.41.

This type of test was only performed for specimens with $\beta = 0°$ and 90°, with the following K values: 1.5, 2.5, 3.5, 5, and 8. For the tests with K no greater than 2.5, the specimen was not failed even if σ_3 reached the limit of the equipment (σ_3 = 60MPa), *because the amount of shear stress is not adequate*. These specimens were then brought to failure by reducing σ_3 while keeping σ_1 constant, i.e. following the horizontal dotted line shown in Figure 3.41.

The stress-strain curves are reported for these tests. However, the failure stresses cannot be obtained from these curves.

3.1.9.3 Unloading Triaxial Compression Tests

In this group of test, the stress on the specimen is first raised isotropically to a high level. Then σ_1 is kept constant while σ_3 is decreased to bring the specimen to failure. These tests, therefore, are triaxial compression unloading tests. This type of tests was also only performed on specimens with $\theta = 0°$ and 90°. The initial isotropic stresses were 30MPa, 50MPa and 60MPa. In the case of 30MPa initial isotropic stress, the specimens were not failed even if σ_3 is reduced to 0MPa.

The pictures of some of the failed specimens are reported in Niandou (1994). Niandou (1997) summarized the observed failure modes in a sketch (Figure 3.42). It seems that for smaller β ($0° < \beta < 15°$), failure occurs by tensile splitting at smaller confining pressures, and by shear across the bedding planes at higher confining pressures. For $15° < \beta < 60°$, failure generally occurs by slipping along the bedding planes. However, at larger confining pressures, shearing through the matrix material is also possible. For $65° < \beta < 90°$, the specimens usually fail by shearing across

the bedding planes, and the shear fault orientation increases with confining pressure.

3.1.10 Behrestaghi and Nasseri's Data

Behrestaghi (1996), Nasseri (1997) and Nasseri (2003) reported various tests on Himalayan schists. Four different varieties of schists were obtained from the Himalaya region: Quartzitic schist, Chlorite Schist, Quartz mica schist and Biotite schist. The specimens had a size of 3.8cm diameter and 7.6cm length. The foliation plane orientation β ranges from 0° to 90°, with 15° intervals (Figure 3.43). The specimens were oven dried at 105°C for 24 hours. The specimens were tested with the following confining pressures: 5, 15, 35, 50 and 100MPa. The triaxial strengths for all of the schists are summarized in Table B.21 through Table B.24, and plotted in Figure 3.44 through Figure 3.47.

3.1.11 Duveau et al.'s Data

Duveau et al. (1998) assessed the predictive power of a few anisotropic failure criteria, based on the conventional triaxial tests on a middle Ordovician schist from Angers, France. A total number of 78 triaxial compression tests were performed. Most of the specimens have isotropic plane orientation of 0° to 90° with 15° intervals. The rest of the specimens may be a few degrees off these orientations. The confining pressures were 0, 5, 10, 20, 30 and 40MPa. The raw data are plotted in Figure 3.48 (a). It can be seen that for each combination of confining pressure and foliation plane orientation, more than one test may have been performed. In this case, an averaged strength was reported for this combination. The averaged strengths are reported in Table B.25 and plotted in Figure 3.48 (b).

Duveau et al. (1998) described the failure modes that were observed from the tests. At smaller confining pressure, specimens with $\beta = 0°$ are dominated by tensile splitting. Increasing the confining pressure causes a mixed mode of failure, where both shearing through the matrix and tensile splitting along foliation planes can be observed. Specimens with $\beta = 90°$ usually fail by shear faulting through the matrix, and the fault orientation is usually 25°, regardless of the confining pressures. Slipping along the foliation planes usually occurs for β between 30° and 60°. For other foliation plane orientations, both slipping along the foliation planes and shearing across them can be observed.

3.1.12 Summary

Experimental results, mainly from conventional triaxial compression experiments, are obtained from the literature and compiled in this section. In addition to conventional triaxial compression experiments, proportional triaxial compression and true triaxial compression results are also

presented, if available. Five different types of anisotropic rock are involved:

1. Slate: Martinsburg slate, Austin slate, Penrhyn slate, South African slate each reported in a different reference.
2. Phyllite: Quartzitic phyllites, Carbonaceous phyllites, Micaceous phyllites, all from one reference.
3. Schist: Quartzitic schist, Chlorite schist, Quartz Mica schist, Biotite schist, Angers schist. The first four are from one reference, and the Angers schist from another reference.
4. Shale: Green River shale I, Green River shale II, Tournemire shale, Opalinus shale. The first two from one reference and the other two from two references.
5. Diatomite.

The axial stresses at failure are tabulated in Appendix B for all different anisotropic rocks, and are plotted against the isotropic plane orientation β. It can be seen that the variation of the failure axial stress with β forms a "U" shaped curve, regardless of the type of rock. However, the shapes of the "U" shaped curves vary with the confining pressure for certain types of rock. Since there is only one Diatomite tested, it is unlikely to give any general conclusions regarding its strength. Therefore, only the other four rock types will be analyzed here.

3.1.12.1 Geometry of the "U" Shaped Curves

In order to capture the geometry of the "U" shaped curves, two ratios are defined. One ratio is $\frac{(\sigma_1-\sigma_3)_{0°}}{(\sigma_1-\sigma_3)_{90°}}$, which is the *unevenness ratio*. This ratio describes the strength difference between β = 0° (i.e. axial direction of specimen parallel to isotropic planes) and β = 90° (i.e. axial direction of specimen perpendicular to isotropic planes). Geometrically, it shows how uneven the two ends of a "U" shaped curve are.

The other ratio is $\frac{\min(\sigma_1-\sigma_3)}{\max(\sigma_1-\sigma_3)}$, which is the *depth ratio* of the "U" shaped curves. The maximum strength $\max(\sigma_1 - \sigma_3)$ can be obtained either at β = 0° or at β = 90°, whichever is larger. In a geometrical sense, this ratio shows the relative depth of the "U" shaped curve. This ratio does not have a very clear physical meaning, because the minimum strength $\min(\sigma_1 - \sigma_3)$ can be obtained either by failure along the isotropic planes or across them.

The two ratios are calculated for each "U" shaped curve, and then plotted against the confining pressure for each group of rocks.

Figure 3.49 shows the variation of unevenness ratio with confining pressure for different types of rocks. Some interesting observations can be obtained by examining these plots:

- The unevenness ratio can be larger or smaller than 1 for all four rock types, which means that maximum strength can be obtained either at β = 0° or at β = 90°.

- This unevenness ratio is insensitive to confining pressure for shales, and relatively insensitive to confining pressure for slates. Although it varies a little (for both shales and slates) when confining pressure is increased from 0 to around 50MPa, continued increase of the confining pressure has very small effects on the ratio. At high confining pressures (150 to 200 MPa), the unevenness ratio is between 0.8 to 1.2.
- For most rocks in the phyllite and schist category, the unevenness ratio seems to increase with confining pressure. It varies with confining pressure up to 100MPa (but no data are available beyond that). The unevenness ratio moves toward 1 with increasing confining pressure, and the rate of change decreases. As a result, the unevenness ratios are quite close to 1 for these two types of rocks at high confining pressure (around 100MPa). For example, the last data points for all the schists and two of the phyllites are between 0.9 and 1.

These observations may indicate that the anisotropy has two components. One component is effectively reduced with increasing confining pressure. The other, however, is not sensitive to the confining pressure change. For shales and slates, the second component is predominant, while the first component predominates for phyllites and schists. At this stage, it is very difficult to associate these two components with the mineralogy and structure of the rocks.

Figure 3.50 shows the variation of the depth ratio with confining pressure for different types of rocks. Again, some interesting observations are summarized:

- For all the rocks, the depth ratio increases with confining pressure.
- Apart from the Angers schist, the depth ratio is the smallest for all slates, and the Micaceous phyllites. This indicates that there is some mechanism that seriously decreases the overall strength from the matrix strength (obtained for $\beta = 0°$ and 90°). For slates, this mechanism is most probably related to the well developed cleavage planes, so that at a certain β (usually between 30° and 45°), it is the shear resistance along the cleavage planes that controls the strength. For Micaceous phyllites, it can be the mica plates, which is a platy mineral with very smooth surfaces. It is not clear why Angers schist has such a low depth ratio (around 0.1).
- For all other rocks, the magnitude of this ratio is comparable. It increases from 0.4-0.6 at 0 confining pressure, to 0.6-0.8 at larger confining pressures (between 100MPa to 200MPa). The rate of increase decreases with increasing confining pressure.

As a result, it seems that the "U" shaped curves for a certain rock gets shallower with increasing confining pressure.

Obviously, the closer these two ratios are to 1, the smaller the anisotropy is. Based on these observations just summarized, it seems that increasing confining pressure does decrease the degree of anisotropy for most of the rocks.

3.1.12.2 Failure Modes

Many different failure modes have been observed from the failed specimens. These failure modes have been presented in the previous part of this section. These failure modes are summarized in Table 3.1. It must be noted that the division of confining pressure and β is somewhat arbitrary and it is only in a relative sense. For example, medium confining pressure for one rock can be high confining pressure for another rock.

For two different rocks (Penrhyn slate and Tournemire shale), the post-peak strength is also available. It has been shown that the anisotropy for the post-peak strength is weaker than that of the peak strength.

It has been stated at the beginning of this thesis that failure of rocks is a very rich topic. The failure modes shown in Table 3.1 are summarized from previous research, and therefore can only be regarded as a rough guideline. In reality, the true failure mode of a specimen is only known by carefully examining the specimen after failure. For example, Figure 3.51 (a) shows a shear fault that is non-planar. In this case, even if the fault orientation and the isotropic plane orientation are very close to each other, it does not indicate a slip along the isotropic plane. On the other hand, Figure 3.51 (b) with a close to planar shear fault, most probably failed by slipping along the isotropic planes.

3.2 Anisotropic Failure Criteria

The experimental work reported in the literature was compiled in the previous section. The results cover many different transversely anisotropic rocks. The strength of the anisotropic rock varies with the isotropic plane orientation, with minimum strength attained around $\beta = 30°\text{-}40°$. It was also shown that different failure modes are possible for anisotropic rocks. It can be brittle or ductile. Shear faults can occur along the isotropic planes or across them. Tensile splitting can occur at small confining pressure. The failure of anisotropic rock, therefore, is a very complicated problem. Nevertheless, there have been long standing efforts of characterizing the failure strength and failure modes with theoretical models. These models and their development will be reviewed in this section.

Duveau et al (1998) classified the widely used anisotropic failure criteria into three categories: the mathematical continuous criteria, the empirical continuous criteria, and the weakness plane criteria. Duveau et al (1998) also compared the predictions of some of the failure criteria with the conventional triaxial experiments on a schist from Angers, France. The organization of this section roughly follows Duveau et al (1998)'s classification. However, the existing criteria are classified into four categories: Empirical Approaches, Continuous Criteria, Critical Plane Approaches, and Discontinuous Criteria.

The empirical approaches are introduced first. These approaches are based purely on the observation of anisotropic strength of rocks in conventional triaxial tests. They aim at fitting the variation of strength with isotropic plane orientation, rather than explaining the physics behind it. As a result, they are simple but cannot be extended to more complicated scenario.

Continuous criteria are introduced next, where failure is described with a continuous failure surface in the stress space. There are many different ways to construct a continuous criterion. The most rational and rigorous approach seems to be based on the tensor representation theory. It is a general theory that is applicable to the description of both strength and stress-strain behavior. It gives the necessary conditions a constitutive law must satisfy, and the general forms that the constitutive law must take. Therefore, the tensor representation theory approach is first introduced. Other ways of constructing a continuous criterion include extending the existing isotropic criterion, or reducing from a general form of criterion. Many of these criteria seem to be originally proposed to characterize the failure of composite materials. Some of the composite materials, like glass-fiber reinforced plastic, are also transversely isotropic. The failure modes observed in the experiments on these materials are quite similar to those observed in rocks. This gives a physical basis to apply these models on rock strength anisotropy.

The critical plane approach is introduced next. This approach assumes that failure occurs through planes, and a failure function is assumed for planes at different orientations. The form of this failure function is usually the same for all planes. However, the parameters can vary continuously with plane orientation. The direction of the plane which first satisfies this failure function is called the critical direction, which must be found by maximizing the failure function. The failure of the material is then identified with the failure along the critical plane. This method, therefore, gives both the failure strength and the failure direction.

Discontinuous criteria are finally described. These criteria assume that different types of discontinuities exist in a matrix material, for example, joints and cracks in rock. Failure occurs when joints start to slip, or cracks start to propagate. Under certain assumptions, for example randomly oriented cracks, this method is similar to the critical plane approach, because the crack orientation that propagates first needs to be identified, which is the critical orientation. However, there are still important differences between the critical plane approach and the discontinuous approach. In the critical plane criteria, the plane defines the orientation of failure. Before failure occurs, the material can be a continuous medium. In the discontinuous criteria, however, the discontinuities exist even before failure occurs.

The coordinate system that is set up in the previous section will again be used in this chapter, for consistent presentation. The **STN** system is a material coordinate system. In case of transverse isotropy, **S** and **T** are in the isotropic plane while **N** is the normal. In case of orthotropy, **S**, **T** and **N** are the three principal directions of anisotropy. $\mathbf{x_1x_2x_3}$ is the principal stress system, which is

aligned with the principal stresses σ_1, σ_2 and σ_3.

3.2.1 Empirical Criteria

The criteria in this category are proposed based on the observation of the conventional triaxial compression strength variation with isotropic plane orientation. Different functional forms are proposed to produce the "U" shaped curve, and any shoulders that it may have. The material parameters in these models are obtained from curve fitting. Consequently, these criteria have little or no physical significance, and are only applicable to conventional triaxial compression strength.

3.2.1.1 McLamore and Gray's Approach

In an attempt to extend Jaeger's Variable Cohesive Strength Theory (introduced later in this chapter), McLamore and Gray (1967) proposed that the cohesive strength of a specimen can be expressed by:

$$\begin{aligned} S &= A_1 - B_1[\cos 2(\beta - \beta_m)]^n \quad \text{for } 0° < \beta < \beta_m \\ S &= A_2 - B_2[\cos 2(\beta - \beta_m)]^n \quad \text{for } \beta_m < \beta < 90° \end{aligned} \tag{3.5}$$

where β_m is the orientation of isotropic planes where S takes its minimum. It usually has the value of 30°. A and B's are constants describing the variation of S over the two ranges. The factor n determines the shape of the curve. Smaller n values produce "U" shaped curves, while larger n values give "U" shaped curves with shoulders. The coefficient of internal friction μ is also supposed to vary with the same type of law:

$$\begin{aligned} \mu &= C_1 - D_1[\cos 2(\beta - \beta'_m)]^m \quad \text{for } 0° < \beta < \beta'_m \\ \mu &= C_2 - D_2[\cos 2(\beta - \beta'_m)]^m \quad \text{for } \beta'_m < \beta < 90° \end{aligned} \tag{3.6}$$

The strength of the specimen at a certain orientation of isotropic planes can then be obtained by invoking the Coulomb law, with the orientation dependent cohesion and friction.

McLamore and Gray (1967) applied their criterion to the experimental data on the Austin slate (shown in Figure 3.10). At any orientation β, the values of μ and S can be obtained by plotting the Mohr failure circles at different σ_3 and constructing a linear envelope over all the Mohr circles. McLamore and Gray (1967) reported the variation of μ and S with β for Austin slate (circular and triangular symbols in Figure 3.52 (a), where the cohesion is denoted by τ_0). The parameters in Equations (3.5) and (3.6) are obtained by curve fitting, so that:

$$\mu = 0.600 - 0.280[\cos 2(\beta - 50°)]; S = 9440 - 5600[\cos 2(\beta - 30°)]^3 \tag{3.7}$$

The fitted functions are shown in Figure 3.52 (a) as a dashed line for the coefficient of friction, and as a solid line for the cohesion. The predicted strengths based on Equation (3.7) are

compared with the measured strengths in Figure 3.52 (b), for confining pressures of 5000psi and 20000psi.

3.2.1.2 Ramamurthy et al.'s Approach

Ramamurthy and coworkers (Ramamurthy, 1993) proposed a nonlinear strength criterion for intact isotropic rocks in conventional triaxial compression:

$$\frac{\sigma_1 - \sigma_3}{\sigma_3} = B_i \left(\frac{\sigma_c}{\sigma_3} \right)^{\alpha_i} \tag{3.8}$$

where σ_c is the uniaxial compressive strength. B_i and α_i are material parameters that are obtained by fitting the experimental data. Ramamurthy indicated that this expression should only be applied at confining pressure $\sigma_3 > 0.05\sigma_c$. This nonlinear criterion was later extended to describe the dependence of conventional triaxial compression strength on isotropic plane orientation. At a certain orientation β, the strength of the anisotropic is expressed by:

$$\frac{\sigma_1 - \sigma_3}{\sigma_3} = B_j \left(\frac{\sigma_{cj}}{\sigma_3} \right)^{\alpha_j} \tag{3.9}$$

where σ_{cj} is the uniaxial compression strength at this orientation. B_j and α_j are also parameters specific to this orientation, and they can be obtained from σ_{cj}:

$$\frac{\alpha_j}{\alpha_{90}} = \left(\frac{\sigma_{cj}}{\sigma_{c90}} \right)^{1-\alpha_{90}} ; \quad \frac{B_j}{B_{90}} = \left(\frac{\alpha_{90}}{\alpha_j} \right)^{0.5} \tag{3.10}$$

where the subscript 90 means the corresponding parameters at β = 90°. The variation of the uniaxial compression strength σ_{cj} with β is proposed to be:

$$\begin{aligned} \sigma_{cj} &= A_1 - D_1[\cos 2(30° - \beta)] \quad \text{for } \beta \text{ between } 0° \text{ and } 30° \\ \sigma_{cj} &= A_2 - D_2[\cos 2(30° - \beta)] \quad \text{for } \beta \text{ between } 30° \text{ and } 90° \end{aligned} \tag{3.11}$$

where A's and D's are parameters that must be obtained from curve fitting.

While applying this criterion, a few uniaxial compression tests at different β values are necessary to obtain the parameters involved in Equation (3.11). Ramamurthy (1993) recommended that three uniaxial tests at β = 0°, 30°, 90° can be used to determine the parameters in Equation (3.11). The determination of α_{90} and B_{90} in Equation (3.10) requires a minimum of two conventional triaxial tests on specimens with β = 90°. Once these parameters are obtained, Equation (3.9) can be applied to predict the strength of transversely isotropic rocks. Ramamurthy applied this approach to a few different data sets. Figure 3.53 shows its predicted strength for Penrhyn slate, tested by Attewell and Sanford (1974).

3.2.1.3 Hoek and Brown's Approach

Hoek and Brown (1980) modified the original Hoek Brown criterion to describe anisotropic rock strength. It is proposed that the two parameters m and s shown in Equation (2.18) must vary with the isotropic plane orientation β. By a process of trial and error, Hoek and Brown (1980) proposed that:

$$m = m_{90}[1 - N_1 \exp(-\theta)^4]; \quad s = 1 - P_1 \exp(-\zeta)^4 \tag{3.12}$$

where m_{90} is the value of m for intact rock with $\beta = 90°$. θ and ζ are defined as:

$$\theta = \frac{\beta - \beta_m}{N_2 + N_3\beta}; \quad \zeta = \frac{\beta - \beta_s}{P_2 + P_3\beta} \tag{3.13}$$

in which β_m and β_s are the orientation where m and s are minimum, respectively. All the N's and P's are constants, which must come from fitting the experimental data.

Hoek and Brown (1980) applied this approach on the slate tested by McLamore and Gray (1967), and reasonable agreement was achieved. Nevertheless, Hoek and Brown (1980) pointed out that the agreement is not surprising because the number of parameters is large, and questioned the use of this model in practice.

3.2.2 Continuous Criteria

3.2.2.1 Tensor Representation Theory

The application of tensor representation theory in describing the yielding and failure of anisotropic material is mainly reported by Boehler and coworkers. They performed a series of theoretical and experimental works on anisotropic material behavior. To name a few of them, Boehler and Sawczuk (1976, 1977) thoroughly examined the formulation of yield criteria for transversely isotropic bodies based on tensor representation theory. Boehler and Raclin (1985) reported the experiments on glass-fiber reinforced composites, and proposed a failure criterion for this type of material. Allirot and Boehler (1977, 1979, 1981) reported experiments on a diatomite, and on a corresponding failure criterion. These experimental and theoretical efforts were later summarized in Boehler (1987).

Tensor representation theory treats the basic problem of representing a tensor as a function of other tensors. Since a constitutive law links the stress tensor with the strain tensor, both of which are symmetric second order tensors, it is of interest to study the following function form:

$$\mathbf{T} = \mathbf{F}(\mathbf{D}, \mathbf{M}) \tag{3.14}$$

where both $\mathbf{T}$ and $\mathbf{D}$ are symmetric second order tensors. One of them is identified with stress,

and the other is identified with strain (or stress and strain increment). **M** is the structural tensor, which describes the symmetry of the material. It is also a symmetric second order tensor. In the case of transverse isotropy, for example, the privileged direction is the isotropic plane normal **n**, which can be represented by [0,0,1] in the **STN** coordinate system. The material structure **M** can be expressed by the following tensor in the **STN** system:

$$\mathbf{M} = \mathbf{n} \otimes \mathbf{n} = \begin{bmatrix} 0 & 0 & 0 \\ 0 & 0 & 0 \\ 0 & 0 & 1 \end{bmatrix} \tag{3.15}$$

In order for Equation (3.14) to be a constitutive equation, it must first satisfy the *Principle of Isotropy of Space*, which means that the equation is objective and it does not change when the coordinate system changes. If **Q** stands for any rigid body rotation, then under this rotation the tensors in Equation (3.14) can be transformed:

$$\mathbf{T}' = \mathbf{Q}\mathbf{T}\mathbf{Q}^{\mathrm{T}}; \quad \mathbf{D}' = \mathbf{Q}\mathbf{D}\mathbf{Q}^{\mathrm{T}}; \quad \mathbf{M}' = \mathbf{Q}\mathbf{M}\mathbf{Q}^{\mathrm{T}}; \tag{3.16}$$

The Principle of Isotropy of Space is the mathematically expressed as:

$$\mathbf{F}'(\mathbf{D}, \xi) = \mathbf{F}(\mathbf{D}', \xi') \tag{3.17}$$

Equation (3.14) must also satisfy the requirement of *material symmetry*. For example, a transversely isotropic material has rotational symmetry with regard to its privileged direction (normal to the isotropic planes). Therefore, the constitutive equation must be invariant to any rotation with regard to the privileged direction. Suppose **P** stands for a rotation that retains material symmetry, then the structural tensor **M** is invariant under this rotation. It follows that:

$$\mathbf{F}(\mathbf{D}, \xi) = \mathbf{F}(\mathbf{D}, \xi') \tag{3.18}$$

Tensor representation theory specifies the general form of Equation (3.14), so that it automatically satisfies the Principle of Isotropy of Space and the material symmetry.

A failure criterion is usually formulated as a scalar function $f(\boldsymbol{\sigma}, \mathbf{M})$, with $f \geq 0$ corresponding to failure. In order for this scalar function to satisfy both the Principle of Isotropy of Space and material symmetry, tensor representation theory states that it must be represented by a basic set of polynomial scalar invariants (I_1, I_2, ..., I_n) of $\boldsymbol{\sigma}$ and **M**. This group of invariants is called a "functional basis", following Boehler (1987). For different types of anisotropy, there are different sets of functional basis.

The functional basis for transversely isotropic materials includes the following invariants of the stress and the mixed invariants of the stress $\boldsymbol{\sigma}$ and the structure tensor **M**:

$$\mathrm{tr}\boldsymbol{\sigma}, \mathrm{tr}\boldsymbol{\sigma}^2, \mathrm{tr}\boldsymbol{\sigma}^3, \mathrm{tr}\mathbf{M}\boldsymbol{\sigma}, \mathrm{tr}\mathbf{M}\boldsymbol{\sigma}^2 \tag{3.19}$$

The first three quantities have been shown in Section 2.3.1, and they are represented by:

$$\begin{aligned}
&\mathrm{tr}(\boldsymbol{\sigma}) = \sigma_s + \sigma_t + \sigma_n = I_1 \\
&\mathrm{tr}(\boldsymbol{\sigma}^2) = \sigma_s^2 + \sigma_t^2 + \sigma_n^2 + 2(\sigma_{tn}^2 + \sigma_{ns}^2 + \sigma_{st}^2) = I_1^2 + 2I_2 \\
&\mathrm{tr}(\boldsymbol{\sigma}^3) = \sigma_s^3 + \sigma_t^3 + \sigma_n^3 + 3\sigma_s(\sigma_{ns}^2 + \sigma_{st}^2) + 3\sigma_t(\sigma_{tn}^2 + \sigma_{st}^2) + 3\sigma_n(\sigma_{tn}^2 + \sigma_{ns}^2) + 6\sigma_{tn}\sigma_{ns}\sigma_{st} = I_1^3 + 2I_1I_2 + 3I_3
\end{aligned} \tag{3.20}$$

They are equivalent to the three stress invariants. With Equation (3.15), one can obtain:

$$\mathrm{tr}\mathbf{M}\boldsymbol{\sigma} = \sigma_{nn}; \mathrm{tr}\mathbf{M}\boldsymbol{\sigma}^2 = \sigma_{nn}^2 + \sigma_{ns}^2 + \sigma_{tn}^2 \tag{3.21}$$

Therefore, the representation of a scalar function in transversely isotropic media must take the form:

$$f(\boldsymbol{\sigma}, \mathbf{M}) = f(\mathrm{tr}\boldsymbol{\sigma}, \mathrm{tr}\boldsymbol{\sigma}^2, \mathrm{tr}\boldsymbol{\sigma}^3, \mathrm{tr}\mathbf{M}\boldsymbol{\sigma}, \mathrm{tr}\mathbf{M}\boldsymbol{\sigma}^2) \tag{3.22}$$

which has five independent parameters. For an isotropic material, only three parameters are necessary, which are the three stress invariants. The two new invariants involve **M** and hence introduce material anisotropy into the criterion. Tensor representation theory thus provides a rigorous and strict foundation for the development of strength criteria. Any strength theory that can be written as the function of the invariants in (3.22) is free of contradictions.

The functional basis shown in Equation (3.19) is further reduced for triaxial tests, where the only independent variables are the isotropic plane orientation (θ or β), the confining pressure σ_3, and the axial stress σ_1. This reduction was given by Boehler and Raclin (1985). Defining the stress deviator tensor **s**:

$$\mathbf{s} = \boldsymbol{\sigma} - \left(\frac{1}{3}\mathrm{tr}\boldsymbol{\sigma}\right)\mathbf{I} \tag{3.23}$$

The functional basis is reduced to three invariants:

$$\begin{aligned}
&\mathrm{tr}\boldsymbol{\sigma} = 2\sigma_3 + \sigma_1 \\
&\mathrm{tr}\mathbf{s}^2 = \frac{2}{3}(\sigma_1 - \sigma_3)^2 \\
&\mathrm{tr}\mathbf{M}\mathbf{s} = \frac{1}{3}(\sigma_1 - \sigma_3)(3\cos^2\theta - 1)
\end{aligned} \tag{3.24}$$

Boehler and Raclin (1985) performed a series of triaxial compression and uniaxial tension tests on a chopped strand mat laminate. The specimens for the triaxial compression tests were prisms with square cross-section, whose dimensions are shown in Figure 3.54. The orientation of the mat planes, which are the isotropic planes in this material, were varied from 0° to 90°, with 15° intervals. Four different confining pressures were applied: 0, 25, 50 and 75MPa. Figure 3.55 shows the failed specimens. The orientations of mat strata (which cannot be identified in the picture) are specified with $\theta = \pi/2 - \beta$. Two distinctive failure modes were identified by observing the failed specimens: the "parallel mode" and the "across mode". The parallel mode is the slip along the mat planes, which is observed in specimens with the isotropic plane normal orientation θ = 45°, 60° and 75°. The across mode is faulting across the mats' strata, which is generally observed for other orientations. At θ = 90° and zero confining pressure, the specimen fails by

splitting of the mats' strata. These failure modes are very similar to those observed in rock specimens.

For the "parallel mode" of failure, Boehler and Raclin (1985) proposed a generalized Coulomb's law to describe the friction between mats:

$$|\tau| = (1 + a_0\sigma_3 + a_1\sigma_3^2)\sigma_n \tan\phi_0 + (1 + a_2\sigma_3 + a_3\sigma_3^2)c_0 \tag{3.25}$$

where σ_n and τ are the normal and shear stresses on the isotropic planes. ϕ_0 and c_0 are the friction angle and cohesion at zero confining pressure characterizing the frictional behavior of the isotropic planes. a_0 through a_3 are material parameters specifying the confining pressure dependence. This criterion indeed can be expressed as a function of the three invariants in (3.24), because:

$$\begin{aligned} |\tau| &= \sqrt{\frac{1}{3}\mathrm{tr}\mathbf{s}^2 + \frac{1}{\sqrt{6}}\mathrm{tr}\mathbf{M}\mathbf{s}\sqrt{\mathrm{tr}\mathbf{s}^2} - \mathrm{tr}^2\mathbf{M}\mathbf{s}} \\ \sigma_n &= \mathrm{tr}\mathbf{M}\mathbf{s} + \frac{1}{3}\mathrm{tr}\boldsymbol{\sigma} \\ \sigma_3 &= \frac{1}{3}\left(\mathrm{tr}\boldsymbol{\sigma} - \sqrt{\frac{3}{2}\mathrm{tr}\mathbf{s}^2}\right) \end{aligned} \tag{3.26}$$

where $\sigma_1 > \sigma_3$ is assumed.

For the "across mode" of failure, the following criterion was proposed:

$$(1 + a_1\sigma_3 + a_2\sigma_3^2)(\sigma_1 - \sigma_3)^2 + (b_0 + b_1\sigma_3 + b_2\sigma_3^2)(\sigma_1 - \sigma_3)^2\cos^2\theta + (c_0 + c_1\sigma_3 + c_2\sigma_3^2)(\sigma_1 - \sigma_3)^2\cos^4\theta = k^2 \tag{3.27}$$

where a_i, b_i, and c_i are material parameters (different from those in Equation (3.25)) and k is a constant. This criterion can also be expressed with the invariants in Equation (3.24), because:

$$\begin{aligned} \sigma_1 - \sigma_3 &= \sqrt{\frac{3}{2}\mathrm{tr}\mathbf{s}^2} \\ \cos^2\theta &= \frac{1}{3} + \sqrt{\frac{2}{3\,\mathrm{tr}\mathbf{s}^2}}\,\mathrm{tr}\mathbf{M}\mathbf{s} \end{aligned} \tag{3.28}$$

The predicted strength is compared with the measured strength in Figure 3.56, with the following parameters (Boehler and Raclin, 1985):

- For "Parallel Mode": $\tan\phi_0$ = 0.42, c_0 = 47.5, a_0 = 2.127GPa^{-1}, a_1 = 31.10GPa^{-2}, a_2 = 6.741GPa^{-1}, a_3 = –6.66GPa^{-2}
- For "Across Mode": k = 0.335GPa, a_1 = 7.842GPa^{-1}, a_2 = 25.31GPa^{-2}, b_0 = 1.539, b_1 = 28.36GPa^{-1}, b_2 = 309.8GPa^{-2}, c_0 = 2.052, c_1 = 34.14GPa^{-1}, c_2 = 328.5GPa^{-2}

The predictions from both the "parallel mode" criterion and the "across mode" criterion are shown in the figure. For θ around 60°, the "parallel mode" criterion predicts lower strength, and the specimen therefore fails along the isotropic planes. For θ values on the two sides, the "across mode" criterion predicts lower strength. Correspondingly, failure occurs across the isotropic

planes. The overall agreement is excellent.

3.2.2.2 General Polynomial Approach

Some researchers start from a general function form, which is supposed to apply to the most general case of anisotropy, and then simplify the function form to fit for specific types of anisotropy. This function form is usually of polynomial type. This seems to have been inspired by the von Mises criterion, which involves the invariant J_2. When expressed with principal stresses, J_2 is a homogeneous quadratic polynomial of the principal stresses.

Homogeneous Quadratic Polynomial

One group of researchers starts from a polynomial that is a homogeneous quadratic of the stress components (similar to the Mises criterion), and states that the material reaches failure when:

$$H_{ijkl}\sigma_{ij}\sigma_{kl} = 1 \tag{3.29}$$

In order for the fourth order tensor **H** to satisfy the Principal of Isotropy of Space, both **H** and $\boldsymbol{\sigma}$ must be transformed according to tensor transformation rules. When the coordinate system is rotated with the rotation tensor **Q**, the new components of **H** must be calculated by:

$$H'_{mnpq} = Q_{im}Q_{jn}Q_{pk}Q_{ql}H_{ijkl} \tag{3.30}$$

Due to the symmetry of the stress tensor, certain symmetry must also be possessed by **H**:

$$H_{ijkl} = H_{jikl} = H_{ijlk} = H_{klij} \tag{3.31}$$

Therefore, **H** has at most 21 independent elements for the most general anisotropy. It usually takes the simplest form when the coordinate system is aligned with the principal direction of anisotropy **STN**. For example, in the case of orthotropic anisotropy, the components of **H** in the **STN** system are:

$$\mathbf{H} = \begin{bmatrix} H_{1111} & H_{1122} & H_{1133} & 0 & 0 & 0 \\ H_{1122} & H_{2222} & H_{2233} & 0 & 0 & 0 \\ H_{1133} & H_{2233} & H_{3333} & 0 & 0 & 0 \\ 0 & 0 & 0 & 4H_{2323} & 0 & 0 \\ 0 & 0 & 0 & 0 & 4H_{3131} & 0 \\ 0 & 0 & 0 & 0 & 0 & 4H_{1212} \end{bmatrix} \tag{3.32}$$

The number of independent parameters is reduced to 9. In the case of transversely isotropic material with index 1 and 2 in the isotropic plane, the following conditions must apply:

$$H_{1111} = H_{2222}; H_{1133} = H_{2233}; H_{2323} = H_{3131}; H_{1212} = \frac{1}{2}(H_{1111} - H_{1122}) \tag{3.33}$$

The number of independent parameters is further reduced to 5. The matrix **H** is similar to the

elastic matrix of anisotropic material as shown in Equation (3.32) and (3.33), because Equation (3.29) has a similar form as the elastic strain energy.

Olszak and Urbanowski (1956) proposed one such form of yield criterion, in an effort of extending the von Mises criterion. The von Mises criterion for isotropic material is also called the maximum distortion strain energy criterion. It states that metal yields when the elastic energy of distortion W_D reaches a critical value. For a material with general anisotropy, the elastic strain energy cannot be decomposed into a volumetric part and a distortion part. Olszak and Urbanowski (1956), however, defined the generalized distortion energy Φ_f for an anisotropic medium:

$$\Phi_f = \frac{1}{4G^*} S_{ijkl}\sigma_{ij}\sigma_{kl} \tag{3.34}$$

where the tensor $\mathbf{S}$ is obtained from the elasticity matrix of the anisotropic material $\mathbf{E}$:

$$S_{ijkl} = 2G^*\left[E_{ijkl} - V^* E_{ijmn}E_{pqkl}\delta_{pq}\delta_{mn}\right] \tag{3.35}$$

V^* and G^* are the generalized bulk modulus and shear modulus:

$$\frac{1}{V^*} = E_{ijkl}\delta_{ij}\delta_{kl}; \frac{1}{G^*} = \left(E_{ijij} - \frac{1}{3}E_{ijkl}\delta_{kl}\right)\delta_{ij} \tag{3.36}$$

Φ_f does not change with an isotropic stress increment. Following the von Mises criterion, a yield criterion can be formulated by stating that yielding occurs when Φ_f reaches a critical value K:

$$\Phi_f = \frac{1}{4G^*} S_{ijkl}\sigma_{ij}\sigma_{kl} = K \tag{3.37}$$

Obviously, this yield criterion can be simplified as:

$$H_{ijkl}\sigma_{ij}\sigma_{kl} = 1 \tag{3.38}$$

Since it was intended to extend the von Mises criterion, which satisfies the condition of incompressibility (plastic volumetric strain is always 0), this condition is also imposed by Olszak and Urbanowski (1956). The condition of incompressibility can be expressed by:

$$H_{ijkl}\delta_{ij} = 0 \tag{3.39}$$

Equation (3.39) consists of 6 independent equations. Therefore, in the most general case, $\mathbf{H}$ in Equation (3.38) has 15 independent components. In the case of orthotropic anisotropy and transverse isotropy and expressed in the **STN** system, Equation (3.32) can be substituted into (3.39), and the condition of incompressibility is simplified to:

$$\begin{aligned} H_{1111} + H_{1122} + H_{1133} &= 0 \\ H_{2211} + H_{2222} + H_{2233} &= 0 \\ H_{3311} + H_{3322} + H_{3333} &= 0 \end{aligned} \tag{3.40}$$

The number of independent components of $\mathbf{H}$ is reduced to 6 for orthotropic anisotropy and 3 for transverse isotropy.

Dafalias (1979), also in an effort to extend Mises yield criterion, proposed the following yield

criterion:

$$f = H_{ijkl}(s_{ij} - \gamma_{ij})(s_{kl} - \gamma_{kl}) = 1 \tag{3.41}$$

where **s** is the stress deviator, while **γ** is the translation of yield surface in deviatoric stress space. Since there are only 5 independent components in a stress deviator, the number of independent elements in **H** reduces to 15, which is consistent with Olszak and Urbanowski (1956)'s results. However, Dafalias (1979) also examined the hardening of material, i.e. the variation of **H** with the development of plastic strain ϵ^p. He stated that the form of **H** as shown in Equation (3.32) is only applicable to an orthotropically anisotropic material before any plastic deformation is developed. Once there is any plastic strain, the material loses its initial structure and it now possesses general anisotropy. Tensor **H** becomes fully populated even in the original **STN** system.

Both Dafalias' criterion and Olszak and Urbanowski's criterion, however, are indifferent to isotropic stresses. Therefore, they are not applicable to materials like rocks. Kaar et al. (1989), realizing this deficiency, proposed to remove the incompressibility condition from the formulation of Olszak and Urbanowski (1956). In the case of a transversely isotropic material without the incompressibility condition, Equation (3.38) can be expanded to be:

$$A_{ss}(\sigma_s^2 + \sigma_t^2) + A_{nn}\sigma_n^2 + A_{ns}\sigma_n(\sigma_s + \sigma_t) + A_{st}\sigma_s\sigma_t + (2A_{ss} - A_{st})\sigma_{st}^2 + B_{ns}(\sigma_{ns}^2 + \sigma_{tn}^2) = 1 \tag{3.42}$$

in the **STN** system. It can be identified that:

$$A_{ss} = H_{1111}, A_{nn} = H_{3333}, A_{ns} = 2H_{1133}, A_{st} = 2H_{1122}, B_{ns} = 4H_{2323} \tag{3.43}$$

Kaar (1989) also introduced an exponential term to describe pressure dependence, and used this criterion to model the failure of columnar grained sea ice.

Quadratic Polynomial with Linear Terms

Any criterion based on the homogeneous quadratic polynomial, containing only quadratic terms, predicts the same strength in uniaxial tension and uniaxial compression. This is not real for some materials, including rocks and soils. Gol'denblat and Kopnov (1966), in their effort to describe glass reinforced plastics, realized that a model should predict different uniaxial tensile strength and uniaxial compressive strength in the same direction, due to the different failure mechanism. In addition, shear strength in a certain direction depends not only on the magnitude of shear stress, but also on its sign. Figure 3.57 (a) and (b) shows the pure shear stress states where the magnitude of the shear stresses are the same, which the directions of the shear stresses are reversed. Each of the pure shear stress states is equivalent to a deviatoric normal stresses state. If the gray lines represent isotropic planes in rock, then the strength in Figure 3.57 (a) and (b) must be different.

Gol'denblat and Kopnov (1966) proposed a general expression that has these features:

$$(\Pi_{ij}\sigma_{ij})^{\alpha} + (\Pi_{klmn}\sigma_{kl}\sigma_{nm})^{\beta} + (\Pi_{abcdef}\sigma_{ab}\sigma_{cd}\sigma_{ef})^{\gamma} + \cdots = 1 \tag{3.44}$$

where Π_{ij}, Π_{klmn}, Π_{abcdef}, ... are strength tensors of different orders. When the coordinate system is transformed, these tensors must change according to tensor transformation rules. Gol'denblat and Kopnov (1966) then proceeded to examine a specific case where $\alpha = 1$ and $\beta = 0.5$, and their strength criterion is written as:

$$\Pi_{ij}\sigma_{ij} + \sqrt{\Pi_{klmn}\sigma_{kl}\sigma_{mn}} = 1 \tag{3.45}$$

Due to the symmetry of the stress tensor, and the invariance of the equation, the strength tensors are also symmetric in the following sense:

$$\begin{aligned} \Pi_{ij} &= \Pi_{ji} \\ \Pi_{klmn} &= \Pi_{lkmn} = \Pi_{klnm} = \Pi_{mnkl} \end{aligned} \tag{3.46}$$

Therefore, in the most general case, there are 6 elements in the second degree tensor, and 21 elements in the fourth degree tensor.

Tsai and Wu (1971) developed a general criterion for filamentary composites. In order to simplify the notation, the stress components are numbered from 1 through 6:

$$\{\sigma_1, \sigma_2, \sigma_3, \sigma_4, \sigma_5, \sigma_6\} = \{\sigma_{xx}, \sigma_{yy}, \sigma_{zz}, \sigma_{yz}, \sigma_{zx}, \sigma_{xy}\} \tag{3.47}$$

Tsai and Wu (1971) started from a general quadratic form:

$$F_i\sigma_i + F_{ij}\sigma_i\sigma_j = 1 \tag{3.48}$$

F_i and F_{ij} are tensors that obey the transformation rules. F_i is a second degree tensor, while F_{ij} is a fourth degree tensor (similar to **H** in Equation (3.29)). In their most general form, F_i has 6 independent elements, and F_{ij} has 21. Moreover, certain stability conditions were imposed on the elements of the tensor F_{ij}: all diagonal terms must be positive, and the off diagonal terms must satisfy the following inequality:

$$F_{ii}F_{jj} - F_{ij}^2 \geq 0 \tag{3.49}$$

where F_{ii} and F_{jj} are diagonal terms (repeated subscripts do not stand for summations) and F_{ij} is an off-diagonal term. This specifies that the failure surface must be an ellipsoid, and it intercepts all stress axes. This general form proposed by Tsai and Wu (1971) is actually equivalent to Gol'denblat and Kopnov's criterion (3.45). This can be readily shown by moving the first term in Equation (3.45) to the right hand side, squaring both sides, and regrouping all the terms into linear and quadratic groups.

The number of independent elements decreases with increasing material symmetry. For orthotropically anisotropic material, where the coordinate system coincides with the principal axes of symmetry **STN**, the independent elements reduce to 3 and 9 for these two tensors. If the stress vector is defined as:

$$\{\sigma_1, \sigma_2, \sigma_3, \sigma_4, \sigma_5, \sigma_6\} = \{\sigma_s, \sigma_t, \sigma_n, \sigma_{tn}, \sigma_{ns}, \sigma_{st}\} \tag{3.50}$$

in the **STN** system, the two tensors F_i and F_{ij} can be expressed as:

$$F_i = [F_1 \quad F_2 \quad F_3 \quad 0 \quad 0 \quad 0]$$

$$F_{ij} = \begin{bmatrix} F_{11} & F_{12} & F_{13} & 0 & 0 & 0 \\ F_{12} & F_{22} & F_{23} & 0 & 0 & 0 \\ F_{13} & F_{23} & F_{33} & 0 & 0 & 0 \\ 0 & 0 & 0 & F_{44} & 0 & 0 \\ 0 & 0 & 0 & 0 & F_{55} & 0 \\ 0 & 0 & 0 & 0 & 0 & F_{66} \end{bmatrix} \tag{3.51}$$

For transversely isotropic materials with **ST** being the isotropic plane, due to material symmetry there must be:

$$F_1 = F_2; F_{11} = F_{22}, F_{13} = F_{23}, F_{44} = F_{55}, F_{66} = 2(F_{11} - F_{12}) \tag{3.52}$$

The last expression in Equation (3.52) is obtained because a pure shear stress state in the isotropic plane is equivalent to a deviatoric normal stress state (Figure 3.58). If the specimen fails at $\sigma_{st} = Q$ in pure shear, Tsai and Wu criterion gives:

$$F_{66}Q^2 = 1 \tag{3.53}$$

The material also fails $\sigma_s = -Q$ and $\sigma_t = Q$, which is the deviatoric stress state. Therefore, it must also be satisfied that:

$$F_{11}(-Q)^2 + 2F_{12}Q \cdot (-Q) + F_{22}Q^2 = 2(F_{11} - F_{12})Q^2 = 1 \tag{3.54}$$

where the condition $F_{11} = F_{22}$ is used. Comparing Equation (3.53) and (3.54), F_{66} must always be identical to $2(F_{11} - F_{22})$. The criterion (3.48) can be written out as:

$$A_{ss}(\sigma_s^2 + \sigma_t^2) + A_{nn}\sigma_n^2 + A_{ns}\sigma_n(\sigma_s + \sigma_t) + (2A_{ss} - B_{st})\sigma_s\sigma_t + B_{st}\sigma_{st}^2 + B_{ns}(\sigma_{ns}^2 + \sigma_{tn}^2) + a_n\sigma_n + a_s(\sigma_s + \sigma_t) = 1 \tag{3.55}$$

There are 7 independent parameters involved in Equation (3.55), and they can be identified as:

$$A_{ss} = F_{11}, A_{nn} = F_{33}, A_{ns} = 2F_{13}, B_{st} = F_{66}, B_{ns} = F_{44}, a_n = F_3, a_s = F_1 \tag{3.56}$$

Equation (3.55) has both quadratic and linear terms. The quadratic terms are the same as those in Equation (3.42).

The parameters involved in Equation (3.55) can be determined from the engineering strengths of the material. In the following discussion, C_n, T_n, both larger than 0, will be used to denote the magnitudes of the uniaxial compressive and tensile strength, respectively. Under simple compression and tension, the failure of the material can be predicted by Tsai and Wu criterion as (with compression positive):

$$A_{nn}C_n^2 + a_nC_n = 1, A_{nn}T_n^2 - a_nT_n = 1 \tag{3.57}$$

Solving these two equations simultaneously, two parameters can be obtained:

$$A_{nn} = \frac{1}{C_n T_n}, a_n = \frac{1}{C_n} - \frac{1}{T_n} \tag{3.58}$$

Similar equations can be written for **S** direction:

$$A_{ss} C_s^2 + a_s C_s = 1, A_{ss} T_s^2 - a_s T_s = 1 \tag{3.59}$$

to obtain the following parameters:

$$A_{ss} = \frac{1}{C_s T_s}, a_s = \frac{1}{C_s} - \frac{1}{T_s} \tag{3.60}$$

Denoting the pure shear strength in the **TN** plane to be R, Tsai and Wu criterion predicts that the material fails at:

$$B_{ns} R^2 = 1 \tag{3.61}$$

There must be:

$$B_{ns} = \frac{1}{R^2} \tag{3.62}$$

If the pure shear strength in the **ST** plane is Q, there should be:

$$B_{st} Q^2 = 1 \tag{3.63}$$

and B_{st} can be obtained to be:

$$B_{st} = \frac{1}{Q^2} \tag{3.64}$$

The only parameter that is left to be determined is A_{ns}, or F_{13}. The determination of F_{13} requires the measured strength under combined stress state. For example, an isotropic stress state in the **ST** plane: $\sigma_s = \sigma_n = P$ can be used. Applying Tsai and Wu criterion to this stress state, one can obtain:

$$P^2 (A_{ss} + A_{nn} + A_{ns}) + P(a_s + a_n) = 1 \tag{3.65}$$

Since A_{nn}, A_{ss}, a_n and a_s are already obtained, A_{ns} can be solved. Tsai and Wu (1971) discussed extensively the determination of F_{13} and concluded that it "is a very sensitive and critical quantity in this proposed theory". It seems that the reliability of F_{13} depends heavily on the stress combination that is used to determine it.

3.2.2.3 Extension of Isotropic Criteria

The continuous failure criteria in this category are obtained from extension of existing isotropic criteria. One of the earliest of these models seems to be proposed by Hill (1948) to describe metal anisotropy. Anisotropy can be introduced in isotropic metal through various forming processes. For example, in cold rolling process, the metal is extended in one direction and squeezed in the other. The yielding stress after rolling is orientation dependent. In order to

describe metal anisotropy, Hill (1948) assumed that the anisotropy is orthotropic. In the material coordinate system **STN**, the following yielding criterion is proposed:

$$F(\sigma_{tt}-\sigma_{nn})^2+G(\sigma_{nn}-\sigma_{ss})^2+H(\sigma_{ss}-\sigma_{tt})^2+2L\sigma_{tn}^2+2M\sigma_{ns}^2+2N\sigma_{st}^2=1 \tag{3.66}$$

where F, G, H, L, M, N are material parameters. Six material parameters are involved, which can be determined by three simple tension tests and three simple shear tests with respect to the principal axes of anisotropy. If the tensile strengths are denoted X, Y, Z while the shear strengths are denoted R, S, T, the six parameters can be expressed by:

$$\begin{aligned} 2F&=\frac{1}{Y^2}+\frac{1}{Z^2}-\frac{1}{X^2}; \quad 2L=\frac{1}{R^2} \\ 2G&=\frac{1}{Z^2}+\frac{1}{X^2}-\frac{1}{Y^2}; \quad 2M=\frac{1}{S^2} \\ 2H&=\frac{1}{X^2}+\frac{1}{Y^2}-\frac{1}{Z^2}; \quad 2N=\frac{1}{T^2} \end{aligned} \tag{3.67}$$

It should be pointed out that the Hill criterion, which has a homogeneous quadratic form, is a special case of the general homogeneous quadratic polynomial criterion (Equation (3.29)) subject to the incompressibility condition (Equation (3.40)). Indeed, substituting Equation (3.40) into the reduced **H** matrix in Equation (3.32) for orthotropic anisotropy material, the **H** matrix becomes:

$$\mathbf{H}=\begin{bmatrix} -H_{1122}-H_{1122} & H_{1122} & H_{1133} & 0 & 0 & 0 \\ H_{1122} & -H_{1122}-H_{2233} & H_{2233} & 0 & 0 & 0 \\ H_{1133} & H_{2233} & -H_{1133}-H_{2233} & 0 & 0 & 0 \\ 0 & 0 & 0 & 4H_{2323} & 0 & 0 \\ 0 & 0 & 0 & 0 & 4H_{3131} & 0 \\ 0 & 0 & 0 & 0 & 0 & 4H_{1212} \end{bmatrix} \tag{3.68}$$

Substituting this **H** matrix to Equation (3.29) and regrouping the terms, it can be obtained that:

$$-H_{1122}(\sigma_{11}-\sigma_{22})^2-H_{2233}(\sigma_{22}-\sigma_{33})^2-H_{3311}(\sigma_{33}-\sigma_{11})^2+4H_{2323}\sigma_{23}^2+4H_{3131}\sigma_{31}^2+4H_{1212}\sigma_{12}^2=1 \tag{3.69}$$

The similarity between Equation (3.69) and Equation (3.66) is obvious. In addition, this clearly shows that the Hill's criterion satisfies the incompressibility condition, and cannot be applied to rocks.

Pariseau (1972) proposed a yield criterion for materials with orthotropic anisotropy. Pariseau observed that criteria describing failure in a conventional triaxial test can be expressed as:

$$\left|\frac{1}{2}(\sigma_1-\sigma_3)\right|^n=\frac{1}{2}(\sigma_1+\sigma_3)A+B \qquad (n\geq 1) \tag{3.70}$$

where A, B, and n are material parameters. For example, the Tresca criterion can be obtained by setting $A = 0$, $B = C_0/2$, $n = 1$. Pariseau continued to extend Equation (3.70) to the general stress state, by introducing stress invariants:

$$\left(\sqrt{J_2}\right)^n=AI_1+B \tag{3.71}$$

This equation is then extended to orthotropic anisotropy, in a way that is similar to Hill's

approach. The final expression reads:

$$\left(\sqrt{F(\sigma_t-\sigma_n)^2+G(\sigma_n-\sigma_s)^2+H(\sigma_s-\sigma_t)^2+L\sigma_{tn}^2+M\sigma_{ns}^2+N\sigma_{st}^2}\right)^n-(U\sigma_s+V\sigma_t+W\sigma_n)=1 \qquad (3.72)$$

Clearly, the extension of the J_2 part is exactly the same as Hill's criterion.

It seems that Pariseau (1972) only examined the case where $n = 1$. In this case, this criterion can be expressed as a homogeneous quadratic of the stress components. When $n = 2$, this criterion has both quadratic and linear terms of the stress components. In both cases, it is a special case of Tsai and Wu's criterion. For $n > 2$, higher order terms are involved.

3.2.2.4 Transformed Stress Tensor Approach

Based on the general theory outlined previously, Boehler and Sawczuk (1977) also provided a simplified approach, which involves the linear transformation of the stress tensor by a fourth order tensor **A**:

$$\boldsymbol{\sigma}' = \mathbf{A}\boldsymbol{\sigma} \qquad (3.73)$$

Existing isotropic failure criteria can then be extended to anisotropy by substituting $\boldsymbol{\sigma}$ with $\boldsymbol{\sigma}'$. For the case of transversely isotropy, Boehler and Sawczuk (1977) suggested using the following tensor:

$$\mathbf{A}=\begin{bmatrix}\gamma & 0 & 0 & 0 & 0 & 0\\ 0 & \gamma & 0 & 0 & 0 & 0\\ 0 & 0 & \alpha & 0 & 0 & 0\\ 0 & 0 & 0 & \beta/2 & 0 & 0\\ 0 & 0 & 0 & 0 & \beta/2 & 0\\ 0 & 0 & 0 & 0 & 0 & \gamma/2\end{bmatrix} \qquad (3.74)$$

By substituting the stress tensor with the transformed stress tensor in an existing isotropic criterion, an anisotropic criterion is readily obtained. This simplified method is very straightforward to use, and it can make use of the existing isotropic criteria.

Cazacu (1998) used a different transformation tensor, and developed a criterion that seems to work well for a number of anisotropic rocks under conventional triaxial compression. For transversely isotropic rock, the transformation tensor was proposed to be:

$$\mathbf{B}=\begin{bmatrix}a & b & b & 0 & 0 & 0\\ b & d & e & 0 & 0 & 0\\ b & e & d & 0 & 0 & 0\\ 0 & 0 & 0 & (d-e)/2 & 0 & 0\\ 0 & 0 & 0 & 0 & c/2 & 0\\ 0 & 0 & 0 & 0 & 0 & c/2\end{bmatrix} \qquad (3.75)$$

A new criterion is then proposed using the transformed stress tensor $\boldsymbol{\sigma}'$:

$$\frac{3}{2}\mathrm{tr}\mathbf{s}'-\frac{m}{3}\mathrm{tr}\boldsymbol{\sigma}'=1 \tag{3.76}$$

where **s** is the deviator of the transformed stress. In the case of isotropy, this criterion reduces to the Mises-Schleicher criterion. Hence this criterion is name the Anisotropic Mises-Schleicher criterion (AMS) by Cazacu (1998). Equation (3.76) can be expanded into the following form:

$$A_{nn}\sigma_n^2+A_{ss}(\sigma_s^2+\sigma_t^2)+2A_{ns}\sigma_n(\sigma_s+\sigma_t)+(2A_{ss}-B_{st})\sigma_s\sigma_t+B_{st}\sigma_{st}^2+B_{ns}(\sigma_{ns}^2+\sigma_{tn}^2)+a_n\sigma_n+a_s(\sigma_s+\sigma_t)=1 \tag{3.77}$$

There are seven parameters involved in Equation (3.77). Since there are originally six independent quantities in this formulation (*a*, *b*, *c*, *d*, *e* in the matrix **B** and *m* from Equation (3.76)), only six of the parameters are independent. Cazacu (1998) gives the expression of the following six parameters:

$$\begin{aligned}&A_{ss}=\frac{(b-e)^2+(d-e)^2+(b-d)^2}{2};A_{nn}=(a-b)^2;B_{st}=3(d-e)^2;\\&B_{ns}=3c^2;a_n=-\frac{m(a+2b)}{3};a_s=-\frac{m(b+e+d)}{3}\end{aligned} \tag{3.78}$$

The parameter A_{ns} is not independent and takes the following form (Cazacu, 1998):

$$A_{ns}^2=\frac{A_{nn}(A_{ss}+A_{st})}{2} \tag{3.79}$$

According to the geometrical theory of conical surfaces, the value of A_{ns} ensures that when all shear stresses are zero, the failure surface of AMS criterion is an elliptic paraboloid in the space (σ_s, σ_t, σ_n). This is not surprising since the original Mises-Schleicher criterion has a parabolic ellipsoid failure surface in the principal stress space.

In addition, Cazacu (1998) applied the AMS criterion to a transversely isotropic specimen subject to principal stresses σ_1, σ_2 and σ_3. The isotropic plane orientation is β from the σ_1 direction, and the dip of the isotropic planes is into the σ_3 direction. In the principal stress space (σ_1, σ_2, σ_3), the geometry of the failure surface is dependent on β. Cazacu (1998) stated that in order for the failure surface to be an elliptic paraboloid for any β values, the following conditions must be satisfied:

$$A_{ns}<0;A_{nn}=4A_{ss}-B_{st} \tag{3.80}$$

The number of independent parameters is then further reduced to 5.

Comparing Equation (3.77) with (3.55), it is obvious that the AMS criterion and the Tsai and Wu criterion have the same quadratic and linear terms. In terms of mathematical form, they are essentially the same. However, the following differences should be noted:

1. The Tsai and Wu criterion keeps all the seven parameters independent, while there are only five independent parameters in the AMS criterion.
2. With the stability requirement in Equation (3.49), the failure surface of the Tsai and Wu criterion is an ellipsoid. With the expression of A_{ns} in Equation (3.79) and A_{nn} in Equation

(3.80), the failure surface of the AMS criterion is an elliptic paraboloid.

3. In the AMS criterion the parameter A_{ns} is not independent. It is automatically obtained through Equation (3.79) once all other parameters are obtained. The sensitivity problem of F_{13} to the different stress state combinations that exists for the Tsai and Wu criterion is thus avoided.

Due to the same mathematical structure, other parameters involved in the AMS criterion can be determined from the engineering strength following the same procedure outlined for the Tsai and Wu criterion. Following the same notation, the independent parameters that are involved in the AMS criterion can be expressed by:

$$a_n = \frac{1}{C_n} - \frac{1}{T_n}, a_s = \frac{1}{C_s} - \frac{1}{T_s}, A_{nn} = \frac{1}{C_n T_n}, A_{ss} = \frac{1}{C_s T_s}, B_{ns} = \frac{1}{R^2} \tag{3.81}$$

Clearly, they are the same as the corresponding parameters in the Tsai and Wu criterion. With these parameters, A_{ns} is then obtained from Equation (3.79), and B_{st} is obtained from Equation (3.80).

Cazacu (1998, 1999) applied this criterion on several anisotropic rocks under conventional triaxial tests. The applications of the AMS criterion to Tournemire shale, Diatomite and Martinsburg slate are shown in Figure 3.59, Figure 3.60, Figure 3.61, respectively. It seems that "U" shaped curves with uneven ends can be generated by this criterion.

3.2.3 Critical Plane Approach

This approach assumes that a material fails along a plane. The failure condition along any plane is described by a failure function, which usually takes the same form for planes in all possible orientations. The parameters in this failure function, however, can vary with plane orientation to create anisotropic behavior. Through one material point, failure is possible along planes in all directions. Failure actually occurs along the plane where this failure function is first satisfied. The direction of this plane is called the critical direction, which must be determined through maximizing the failure function.

According to this definition, Coulomb criterion is probably the earliest critical plane criterion. In a two dimensional stress state, the direction of a plane can be represented by β, the angle between this plane and the major principal stress σ_1 ($\sigma_1 > \sigma_3$ is assumed, see Figure 3.62). For the time being, β is assumed to be between 0° than 90°. The normal and shear stress along this plane can be written as:

$$\sigma = \sigma_m - \tau_m \cos 2\beta; \quad \tau = \tau_m \sin 2\beta \tag{3.82}$$

with $\sigma_m = (\sigma_1 + \sigma_3)/2$ and $\tau_m = (\sigma_1 - \sigma_3)/2$. Failure along this plane, according to the Coulomb criterion, occurs when:

$$\tau_m \sin 2\beta = \mu(\sigma_m - \tau_m \cos 2\beta) + S \tag{3.83}$$

where μ is the coefficient of friction, and S is the cohesion. The failure function is then defined as:

$$F = \tau_m(\sin 2\beta + \mu \cos 2\beta) - (\mu\sigma_m + S) \le 0 \tag{3.84}$$

The critical direction can be obtained by finding the β that maximizes F. Let:

$$\frac{\partial F}{\partial \beta} = 0 \tag{3.85}$$

and solve for β, the critical direction is obtained:

$$\beta_c = 45° - \phi/2 \tag{3.86}$$

In fact, there are two critical directions symmetric to the σ_1 direction. Substitute Equation (3.86) into (3.83), the failure condition for the material is obtained:

$$\sigma_1 = \sigma_3 \frac{1+\sin\phi}{1-\sin\phi} + 2S\frac{\cos\phi}{1-\sin\phi} \tag{3.87}$$

Therefore, the critical plane method gives both the strength of the material and the direction of the failure.

Since the same parameters are applied to all the planes, the Coulomb criterion is an isotropic criterion. In order to describe the failure of anisotropic rock, Jaeger (1960) proposed that the cohesive strength S in the Coulomb criterion should be made direction dependent. The cohesive strength along a direction β from the major principal stress σ_1 ($\sigma_1 > \sigma_3$ is assumed) is supposed to vary according to:

$$S = S_1 - S_2 \cos 2(\beta - \beta_m) \tag{3.88}$$

where β_m is the orientation where S takes a minimum. The coefficient of internal friction μ, on the other hand, is independent to orientation. The failure function now becomes:

$$F = (\tau_m + S_2 \sin 2\beta_m)\sin 2\beta + (\mu\tau_m + S_2 \cos 2\beta_m)\cos 2\beta - (S_1 + \mu\sigma_m) \le 0 \tag{3.89}$$

The critical orientation can again be obtained by maximizing the failure function. It can be solved that this maximum is reached when β satisfies:

$$\tan 2\beta_c = \frac{(\sigma_1 - \sigma_3) + 2S_2 \sin 2\beta_m}{\mu(\sigma_1 - \sigma_3) + 2S_2 \cos 2\beta_m} \tag{3.90}$$

Substituting Equation (3.90) into (3.89), the failure criterion for the specimen is obtained:

$$\mu^2\left(\frac{\sigma_1+\sigma_3}{2} + \frac{S_1}{\mu}\right)^2 - (1+\mu^2)\left(\frac{\sigma_1-\sigma_3}{2} + S_2\frac{\sin 2\beta_m + \mu\cos 2\beta_m}{1+\mu^2}\right)^2 = S_2^2\left(1 - \frac{(\sin 2\beta_m + \mu\cos 2\beta_m)^2}{1+\mu^2}\right) \tag{3.91}$$

The ideas have been revived by Pietruszczak and Mróz (2000, 2001), where a general failure parameter η is supposed to vary according to a second degree tensor:

$$\eta = \eta_{ij} n_i n_j = \eta_0 (1 + \Omega_{ij} n_i n_j) \tag{3.92}$$

where **n** is the normal of the plane whose failure parameter is to be determined. η_0 is the volumetric component while **Ω** is the deviatoric component normalized by η_0. As such, the trace of **Ω** is zero. In the case of transverse anisotropy **Ω** and **n** can be represented by:

$$\mathbf{\Omega} = \begin{bmatrix} \Omega_s & 0 & 0 \\ 0 & \Omega_t & 0 \\ 0 & 0 & \Omega_n \end{bmatrix}; \quad \mathbf{n} = \begin{Bmatrix} n_s \\ n_t \\ n_n \end{Bmatrix} \tag{3.93}$$

in the principal axis of anisotropy. Considering that $\Omega_s = \Omega_t = -0.5\Omega_n$ and $n_s^2 + n_t^2 + n_n^2 = 1$, Equation (3.92) can also be written as:

$$\eta = \eta_0 [1 + \Omega_s (1 - 3n_n^2)] \tag{3.94}$$

Pietruszczak and Mróz (2001) extended the Coulomb criterion in which both the coefficient of friction and the cohesion vary according to Equation (3.94). The critical plane orientation and the strength of the material can again be found by maximizing procedure, even though the mathematics is more complex.

This general form of failure parameter is later extended to include higher order terms in Pietruszczak et al. (2002):

$$\eta = \eta_0 [1 + \Omega_{ij} n_i n_j + b_1 (\Omega_{ij} n_i n_j)^2 + b_2 (\Omega_{ij} n_i n_j)^3 + \cdots] \tag{3.95}$$

Equation (3.95) was applied in Pietruszczak et al. (2002) to describe the variation of uniaxial compression strength of Tournemire shale specimens with bedding plane orientation. A satisfactory fit of the experimental data was achieved with the inclusion of up to the fourth order term (Figure 3.63), with parameters η_0 = 22MPa, Ω_s = 0.0170251, b_1 = 515.49, b_2 = 61735.3, b_3 = 2139820.0 (Pietruszczak et al., 2002). The fitted uniaxial compression strength is then introduced into the formulation of a yield function, so that anisotropy in the stress-strain relationship is described.

3.2.4 Discontinuous Models

In the previous section, various ways of introducing anisotropy into the constitutive laws are described. All those models treat the material as an anisotropic continuum, where stress and strain have a continuous distribution over the entire material body. This can be a very good approximation of the physical image, for example, when anisotropy is caused by a stress history, or when minerals in a rock are aligned. However, anisotropy in rocks can also be caused by various discontinuous features, including joints and cracks. In this section, a few discontinuous models will be introduced.

3.2.4.1 Single Plane of Weakness Model

Jaeger (1960) examined the failure of isotropic rock with one set of joints. Both the rock and the joints are supposed to obey the Coulomb criterion. The coefficient of internal friction for the intact rock is $\mu = \tan\phi$, and the cohesion is S. For joints, these two parameters are $\mu' = \tan\phi'$ and S'. Jaeger (1960) considered a two dimensional stress state where the joint orientation is β from the major principal stress σ_1 ($\sigma_1 > \sigma_3$ is assumed, see Figure 3.62). For a certain σ_3, the σ_1 necessary to induce failure along the joint is expressed as:

$$\sigma_1 = \frac{S' + \sigma_3(\mu' + \mu'\cos 2\beta + \sin 2\beta)}{(-\mu' + \mu'\cos 2\beta + \sin 2\beta)} \tag{3.96}$$

This σ_1 has a minimum at $\beta = 45° - \frac{\phi'}{2}$, and approaches infinity when β approaches 0° or 90°. In order to induce matrix failure, the necessary σ_1 is:

$$\sigma_1 = \sigma_3 \frac{1+\sin\phi}{1-\sin\phi} + 2S\frac{\cos\phi}{1-\sin\phi} \tag{3.97}$$

This σ_1 does not depend on β since the matrix material is supposed to be isotropic. The actual σ_1 at failure will be the smaller of the two. The effect of the joint is that there is a "U" shaped portion of the failure σ_1 versus β at a certain σ_3 (Figure 3.64). In addition, for a certain joint orientation β, σ_1 is a linear function of σ_3.

A necessary prediction of Jaeger's criterion is that the strength of the specimen is the same for β = 0° and 90°, so that the "shoulders" of the curve in Figure 3.64 are at the same level. However, this is not true for many anisotropic rocks, as clearly shown from the data sets presented in the previous section. In order to describe this difference, Duveau and Shao (1998) propose that different parameters should be used for β close to 0° and 90°. Four different parameters are used: S_0, μ_0 for β close to 0°, and S_{90}, μ_{90} for β close to 90°. This way, the two shoulders are at different levels (Figure 3.65). It is also assumed that a non-linear friction law is applicable to describe slipping along the weak plane. The friction law proposed by Barton (1976) is used here, which reads:

$$\tau = \sigma \tan\left(a \log\frac{\sigma_{c0}}{\sigma + b}\right) \tag{3.98}$$

where σ and τ are the normal and shear stress along the weak plane. σ_{c0} is the uniaxial compression strength in the direction normal to the weak plane. a and b are both material parameters. Duveau and Shao (1998) applied this criterion to Angers schist, and found better agreement with the experimental data than with Jaeger's original criterion. Figure 3.66 shows the comparison of experimental data and the prediction at 40 MPa confining pressure. The parameters for the predicted curve are: $\mu_0 = 0.94$, $S_0 = 26.10$MPa, $\mu_{90} = 0.86$, $S_{90} = 40.04$MPa, $a = 28.12$, $b = 9.29$MPa, $\sigma_{c0} = 150$MPa.

3.2.4.2 Fracture Mechanics Models

The Griffith criterion introduced in Section 2.3.2 was improved by McClintock and Walsh (1962), by considering the crack closure effect and friction between crack walls when they are closed. The assumptions of Griffith (1924) were retained. In addition, it was assumed that a crack closes when the normal stress normal to the crack walls reaches a critical value σ_c (note that the sign convention here is compression positive, which is different from McClintock and Walsh's original work.). The normal stress along the crack wall is thus expressed:

$$\sigma_n = \begin{cases} 0 & \text{for open crack} \\ \sigma_{zz} - \sigma_c & \text{for closed crack} \end{cases} \tag{3.99}$$

where σ_{zz} is the applied stress normal to crack walls. The coefficient of friction between crack walls is μ, so the shear stress that the crack can sustain is:

$$\sigma_f = \mu \sigma_n \tag{3.100}$$

In order to initiate crack propagation for the cracks oriented β degrees from the σ_1 direction, the following condition must be satisfied when the cracks are fully closed:

$$2T_0 = \frac{\sigma^{*2}}{\sigma_c + \sqrt{\sigma_c^2 + \sigma^{*2}}} \tag{3.101}$$

where σ^* is defined as:

$$\sigma^* = (\sigma_1 - \sigma_3)\sin 2\beta - \mu[(\sigma_1 + \sigma_3) - (\sigma_1 - \sigma_3)\cos 2\beta] \tag{3.102}$$

The critical orientation is found to be:

$$\beta = 45° - \frac{\phi}{2} \tag{3.103}$$

where ϕ is the friction angle between crack walls. The failure of the specimen is again identified with crack propagation in the critical orientation. McClintock and Walsh (1962) showed that failure occurs when:

$$\sigma_1 = \frac{1}{\sqrt{1+\mu^2} - \mu}\left[\sigma_3(\sqrt{1+\mu^2} + \mu) + 4T_0\sqrt{1 + \frac{\sigma_c}{T_0}} - 2\sigma_c\mu\right] \tag{3.104}$$

This is clearly a linear dependence of σ_1 on σ_3. When the confining pressure σ_3 is small enough that all the cracks are open, then the original Griffith's criterion still applies. According to the original Griffith criterion, the cracks oriented β degree from the σ_1 direction start to propagate when:

$$(\sigma_1 \sin^2\beta + \sigma_3 \cos^2\beta) - \sqrt{(\sigma_1^2 \sin^2\beta + \sigma_3^2 \cos^2\beta)} = -2T_0 \tag{3.105}$$

The critical orientation is specified by:

$$\cos\beta = \frac{\sigma_1 - \sigma_3}{2(\sigma_1 + \sigma_3)} \tag{3.106}$$

The failure of the specimen occurs at:

$$\begin{aligned} (\sigma_1-\sigma_3)^2 &= 8T_0(\sigma_1+\sigma_3) \qquad \text{if } \sigma_1+3\sigma_3>0 \\ \sigma_3 &= -T_0 \qquad\qquad\qquad\quad \text{if } \sigma_1+3\sigma_3<0 \end{aligned} \tag{3.107}$$

McClintock and Walsh (1962) also give the transition criterion when only part of the cracks are closed.

If $\sigma_c = 0$ is assumed then Equation (3.104) takes a simpler form:

$$\sigma_1 = \frac{4T_0+\sigma_3(\mu+\mu\cos 2\beta+\sin 2\beta)}{(-\mu+\mu\cos 2\beta+\sin 2\beta)} \tag{3.108}$$

It is remarkable to see that Equation (3.108) and (3.96) are almost identical, except that $S' = 4T_0$. In this case, the McClintock and Walsh theory reduces to Jaeger's Single Plane of Weakness theory.

3.2.5 Summary

Existing anisotropic failure criteria have been summarized in this section. It seems that most of the criteria that have been applied to rocks in conventional triaxial experiments. For example, the AMS criterion by Cazacu (1998, 1999) was applied to predict the conventional triaxial experiments of several anisotropic rocks. Therefore, it is important to develop and evaluate criteria that can capture the strength of anisotropic rock under true triaxial stress states. However, it is difficult to extend the existing models. For example, the criterion of Tsai and Wu (1971) is a general quadratic polynomial, and therefore gives the general form of failure criterion for transversely isotropic rock with only linear and quadratic terms. If more complicated criteria are to be constructed along this line, cubic terms must be added. Possible cubic terms can be expressed by $F_{ijk}\sigma_i\sigma_j\sigma_k$. Clearly, there are 6×6×6 = 216 possible cubic terms possible, which makes it impractical to either keep all of them or select a few terms that are applicable to a certain rock. In order to bypass this problem, a new approach will be proposed in the next chapter, which leads naturally to a true triaxial failure criterion of anisotropic rock.

Table 3.1 Possible Failure Modes of Anisotropic Rocks in Conventional Triaxial Compression Tests

	Brittle Failure		Ductile Failure
β values (0° to 90°)	Low Confining Pressure	Medium Confining Pressure	High Confining Pressure
0°	Tensile splitting	Mixed mode of tensile splitting and shearing through the matrix	Shearing across the isotropic planes, with plastic deformation
Low (typical range $0°<\beta<30°$)	Tensile splitting, or shearing along the isotropic planes	Shearing along the isotropic planes, or Mixed mode of shearing along and across the isotropic planes	Development of kink band, with plastic deformation
Medium (typical range $30°<\beta<60°$)	Shearing along the isotropic planes	Shearing along the isotropic planes, or Mixed mode of shearing along and across the isotropic planes	Shearing along multiple isotropic planes, or shearing across the isotropic planes, with plastic deformation
High (typical range $60°<\beta<90°$)	Shearing across the isotropic planes	Shearing across the isotropic planes	Shearing across the isotropic planes, with plastic deformation

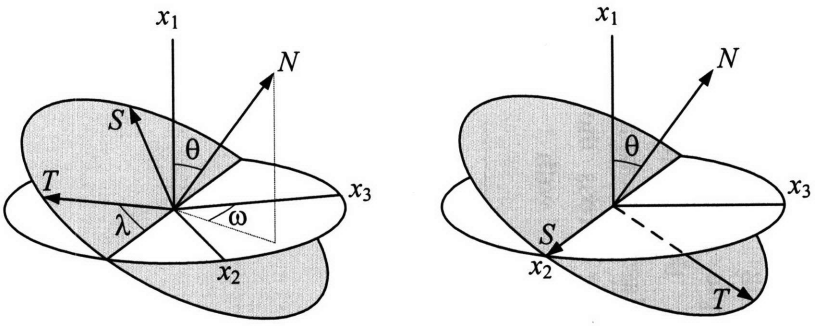

(a) General Case (b) S coincides with x_2

Figure 3.1 Orientation of Bedding Planes with regard to the Principal Stresses

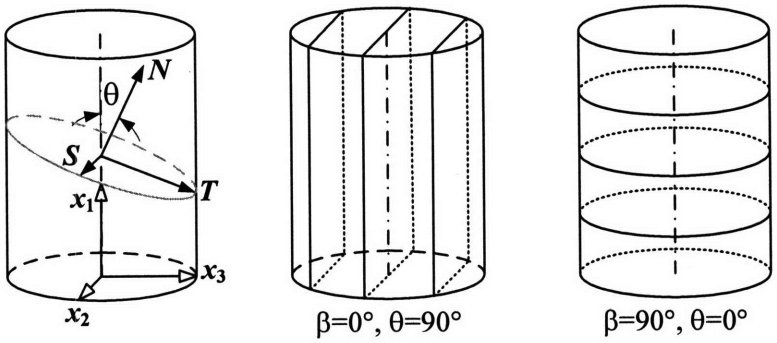

Figure 3.2 Orientation of Bedding Planes with regard to the Principal Stresses

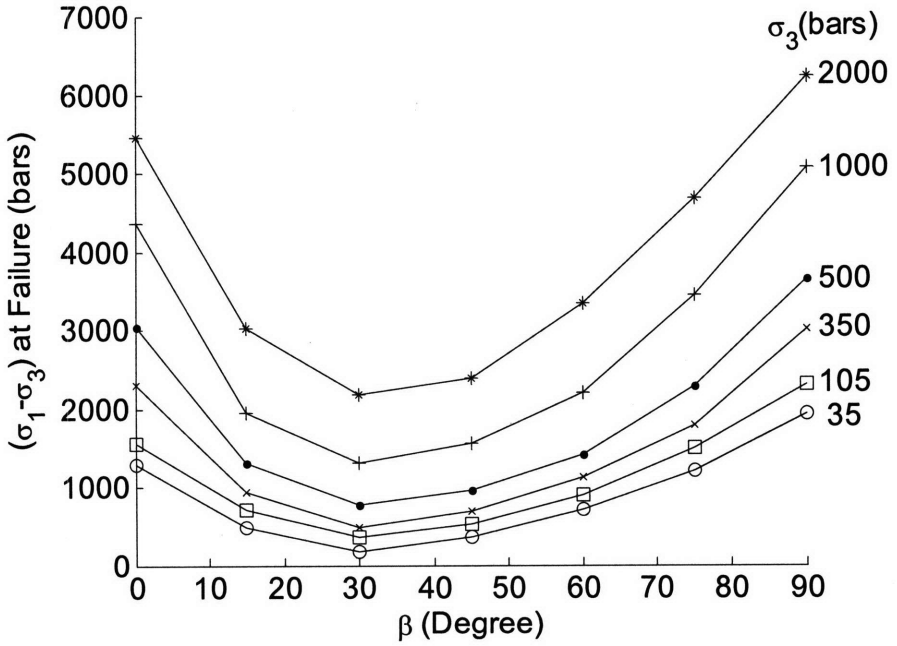

Figure 3.3 Triaxial Strength of Martinsburg Slate (data from Donath, 1964)

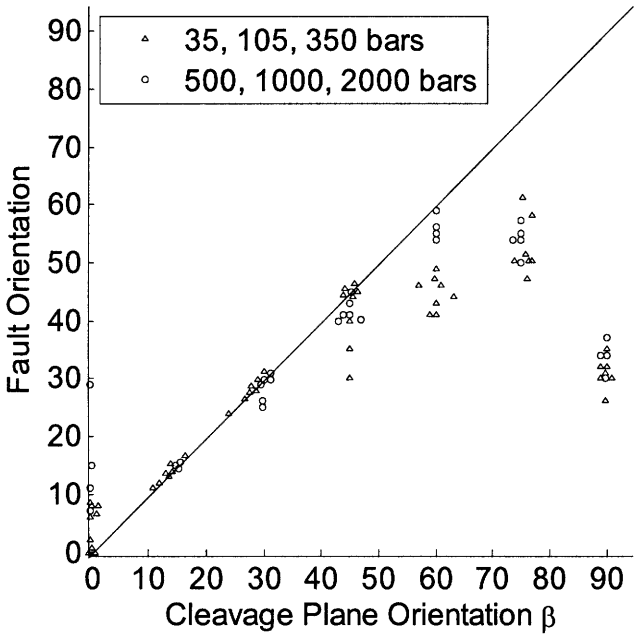

Figure 3.4 Fault vs. the Cleavage Orientation for Martinsburg Slate (data from Donath, 1964)

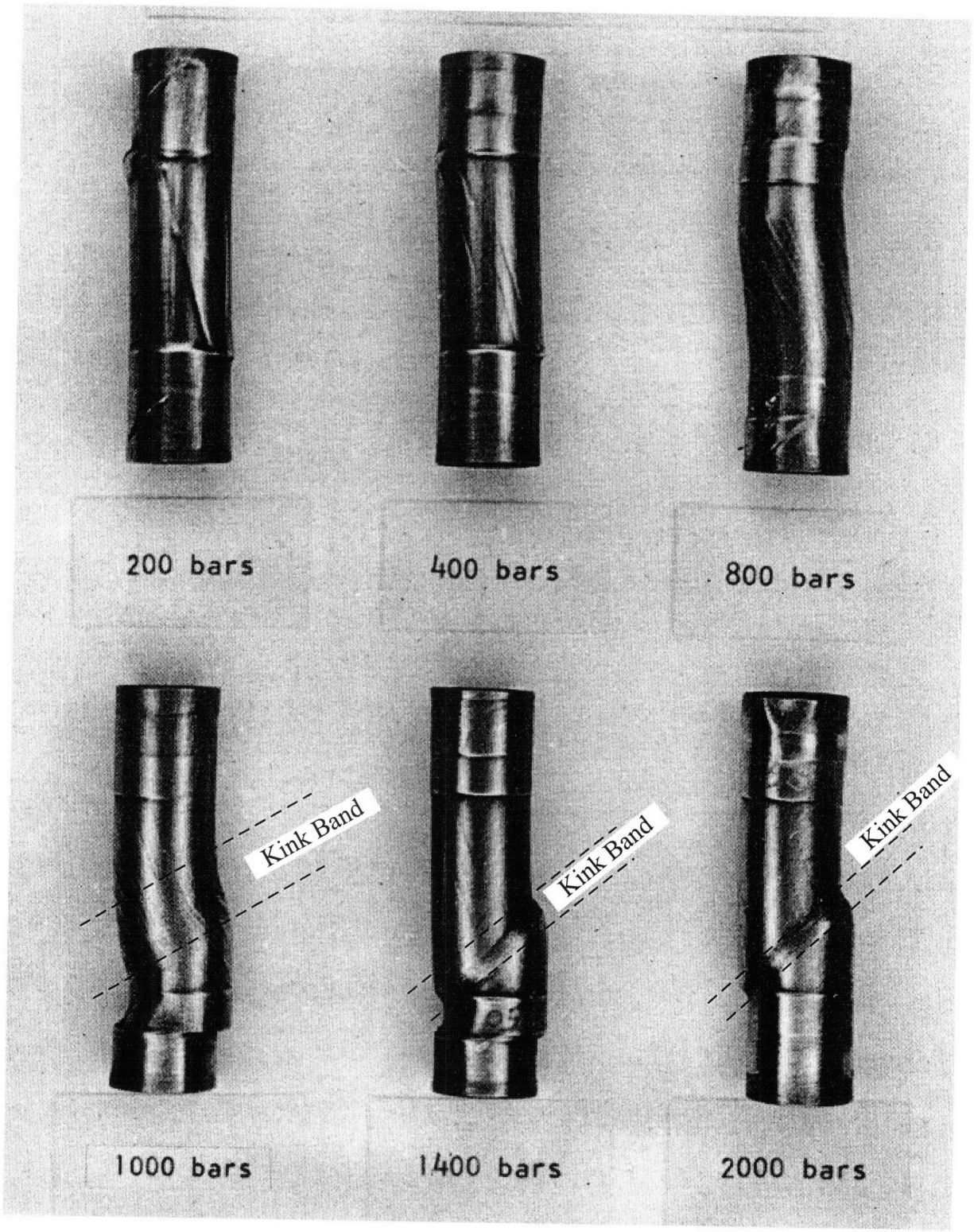

Figure 3.5 Variation of Failure Mode with Confining Pressure for $\beta = 15°$ (from Donath, 1964)

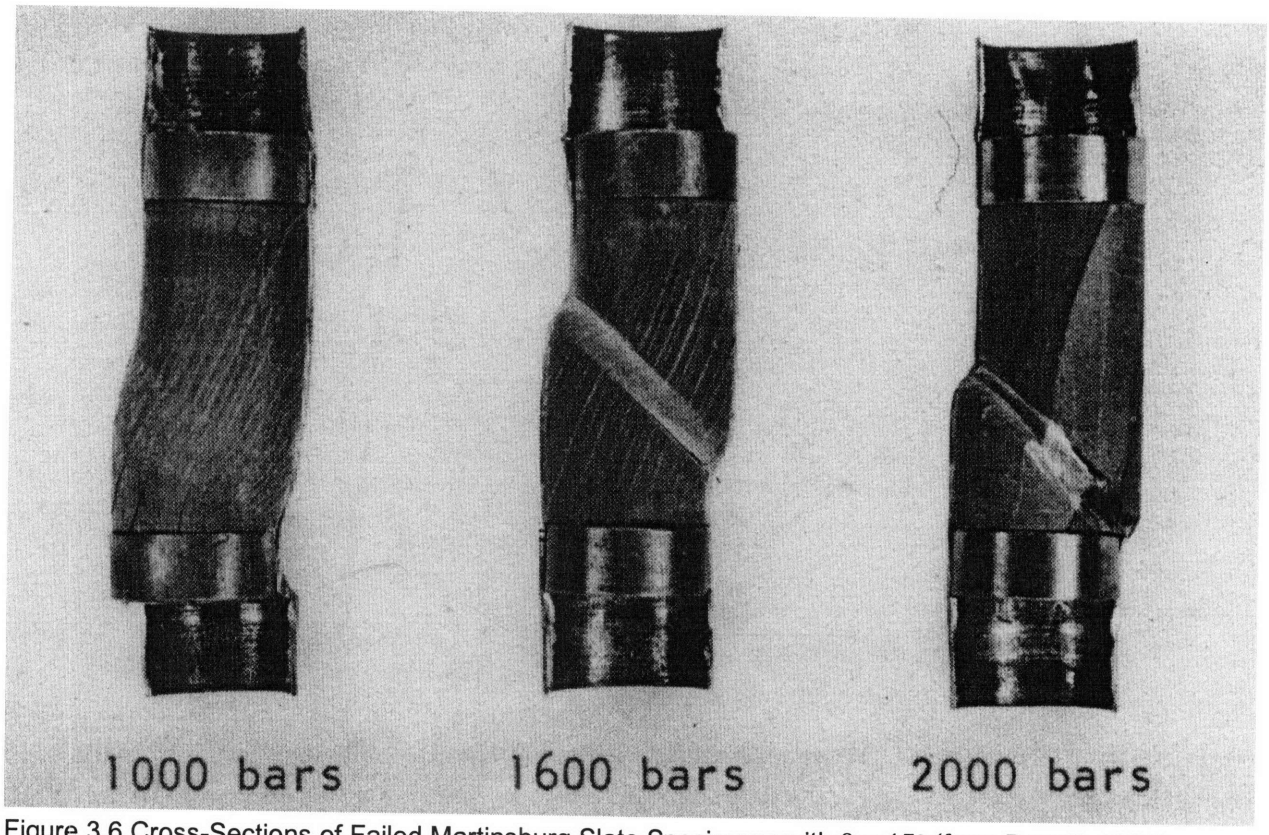

Figure 3.6 Cross-Sections of Failed Martinsburg Slate Specimens with $\beta = 15°$ (from Donath 1964)

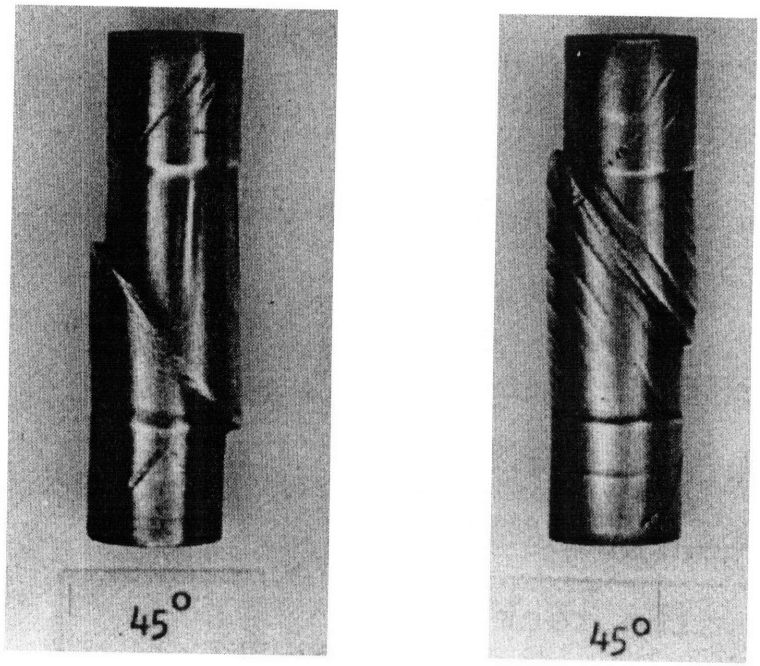

(a) 500bar (b) 1000bar

Figure 3.7 Failed Specimens with $\beta = 45°$ at Different Confining Pressure (from Donath 1964)

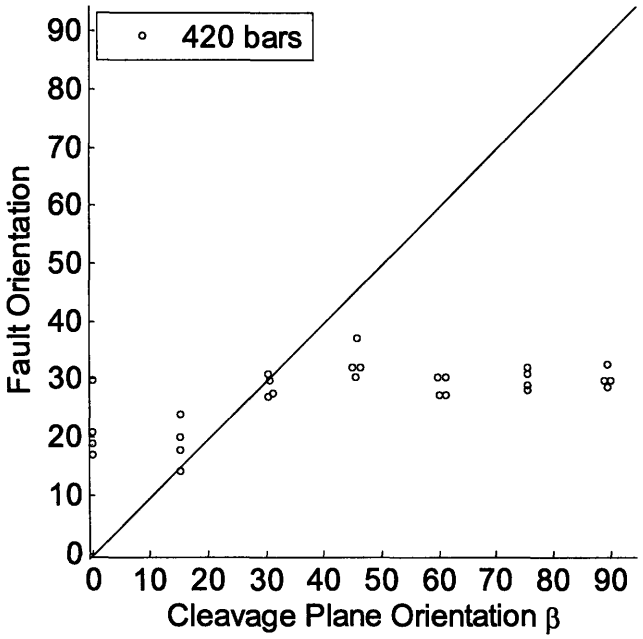

Figure 3.8 Fault Orientation vs. Cleavage Orientation for Longwood Shale with σ_3 = 420bar (data from Donath, 1964)

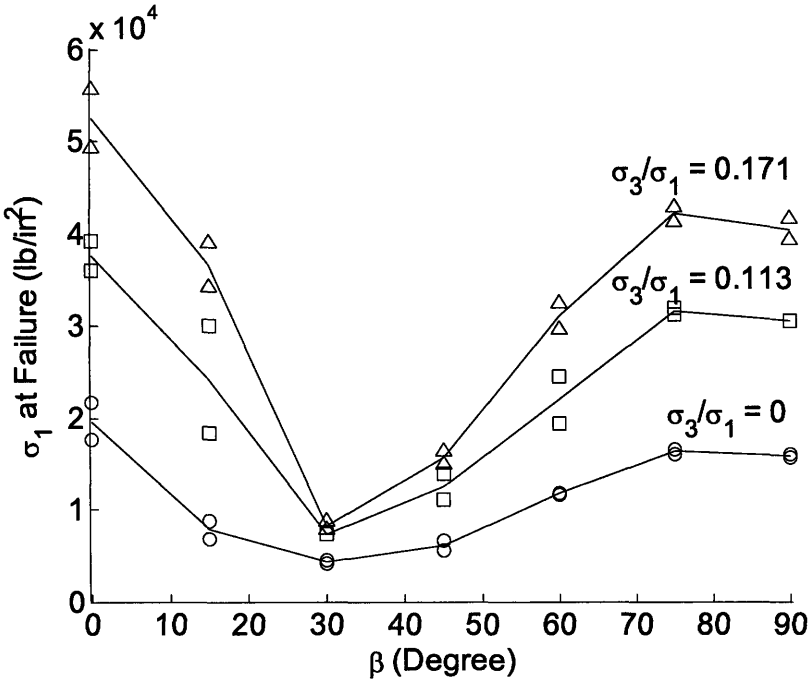

Figure 3.9 Proportional Triaxial Strength of South African Slate (data from Hoek, 1964)

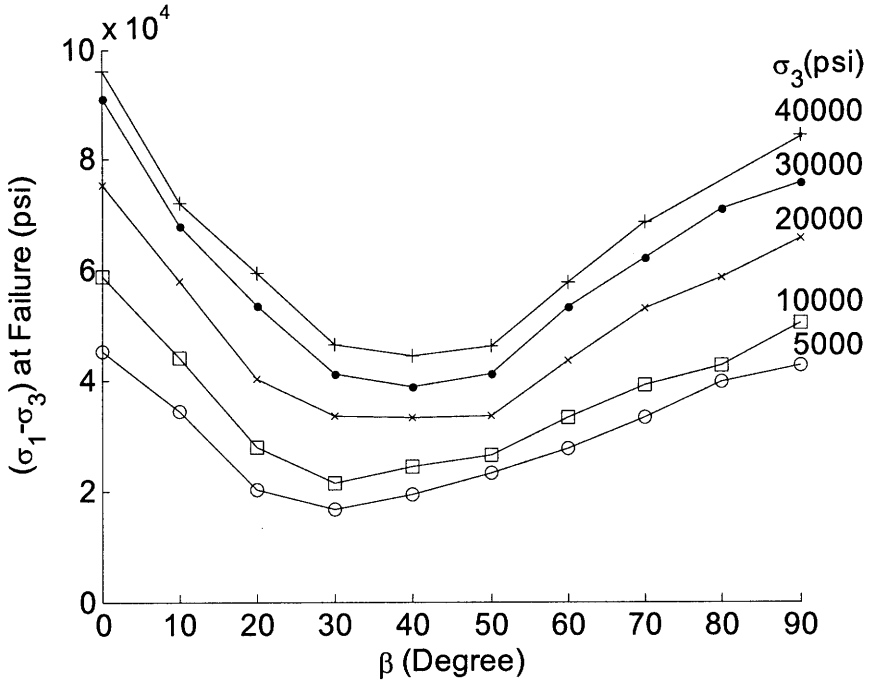

Figure 3.10 Triaxial Strength of Austin Slate (McLamore and Gray, 1967)

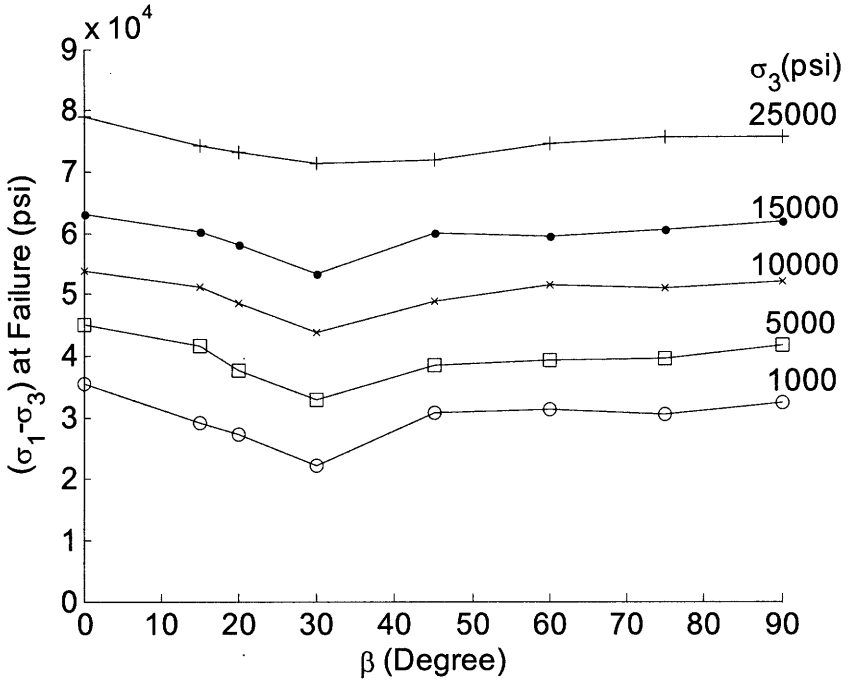

Figure 3.11 Triaxial Strength of Green River Shale-1 (McLamore and Gray, 1967)

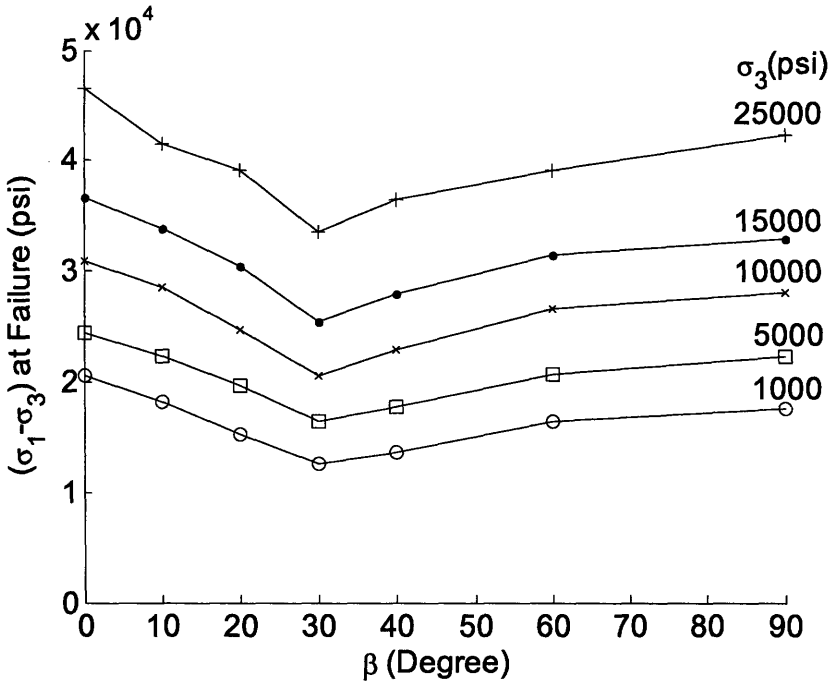

Figure 3.12 Triaxial Strength of Green River Shale-2 (McLamore and Gray, 1967)

1. SHEAR

   a. Along bedding plane

   b. Across bedding plane

2. "PLASTIC" FLOW or SLIP

   a. Along bedding plane

3. "KINK" FLOW

   Consists of a rotation of bedding plane

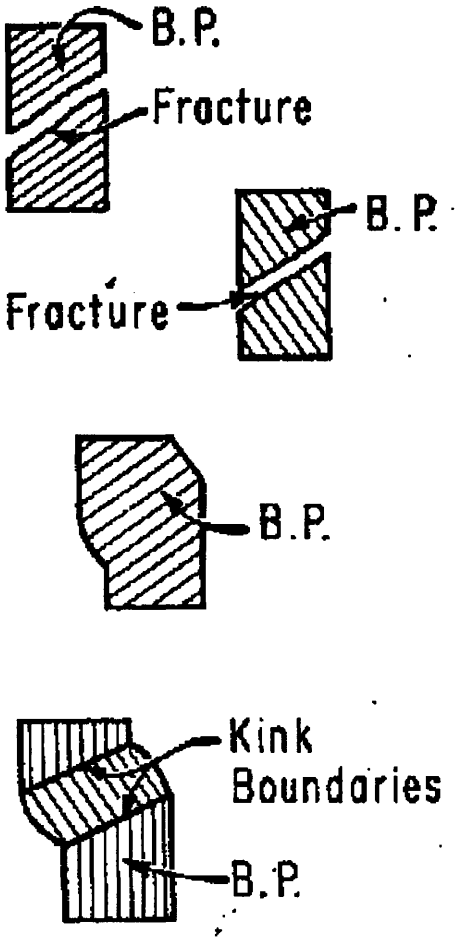

Figure 3.13 Failure Modes Observed by McLamore and Gray (McLamore and Gray, 1967)

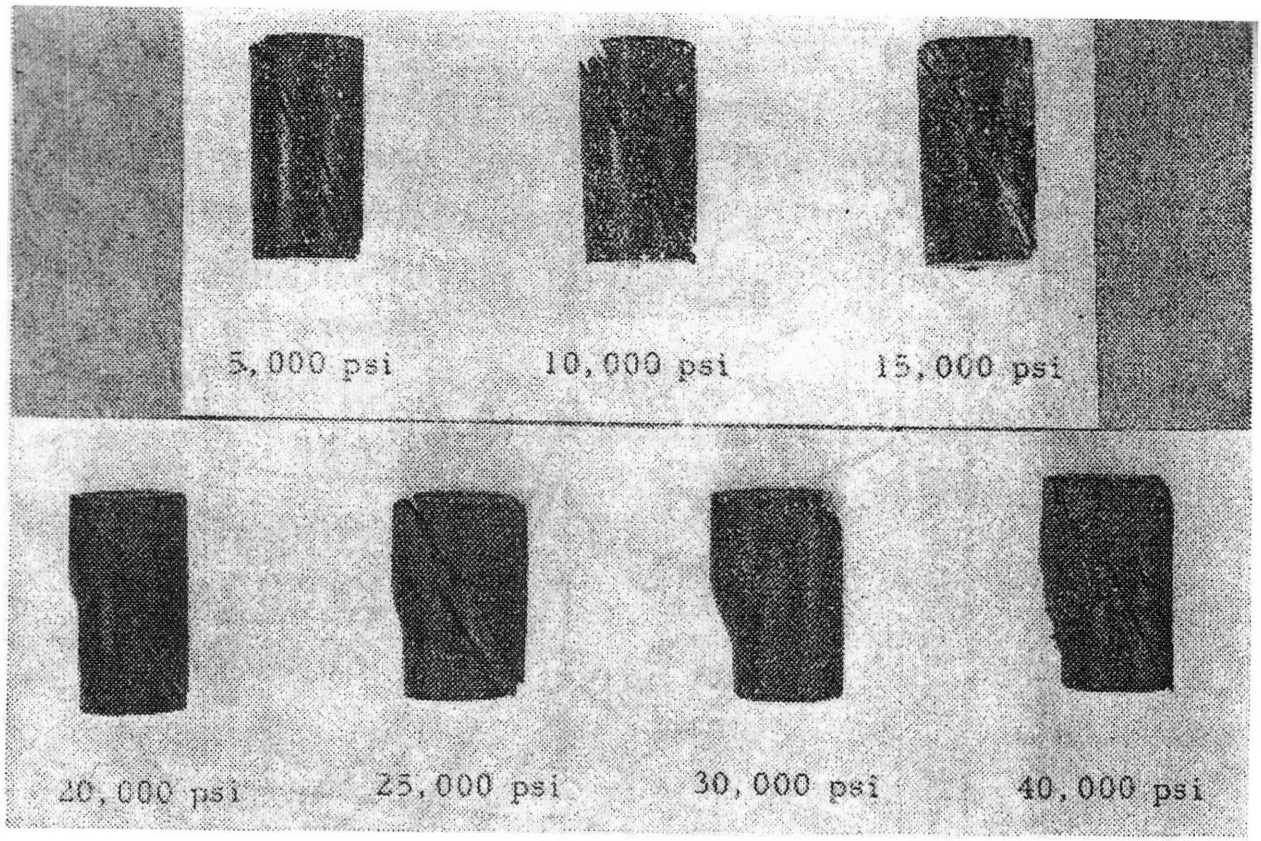

Figure 3.14 Failed Specimens of Austin Slate at $\beta = 30°$ and Various Confining Pressures (McLamore and Gray, 1967)

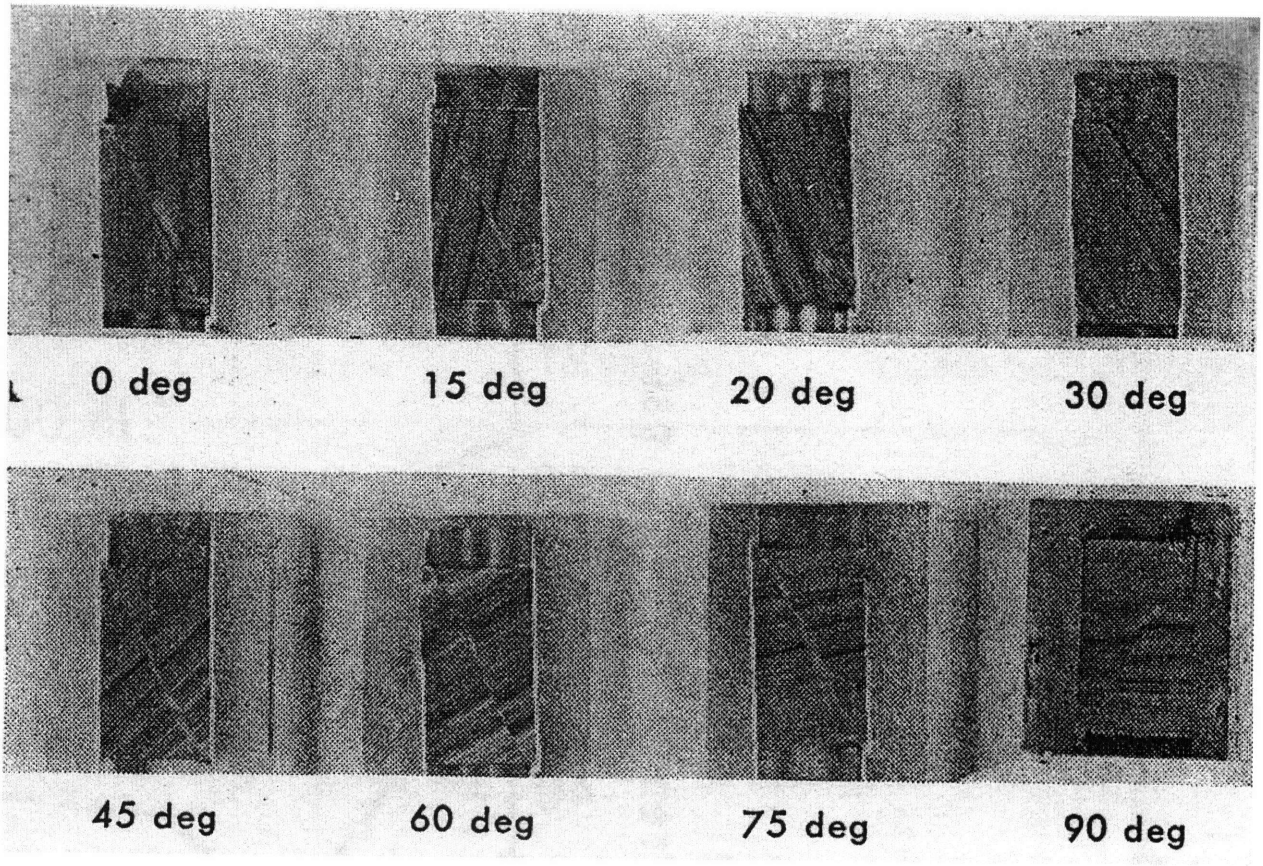

Figure 3.15 Failed Specimens of Green River Shale-1 at Confining Pressure 15000psi and Various Bedding Plane Orientations (McLamore and Gray, 1967)

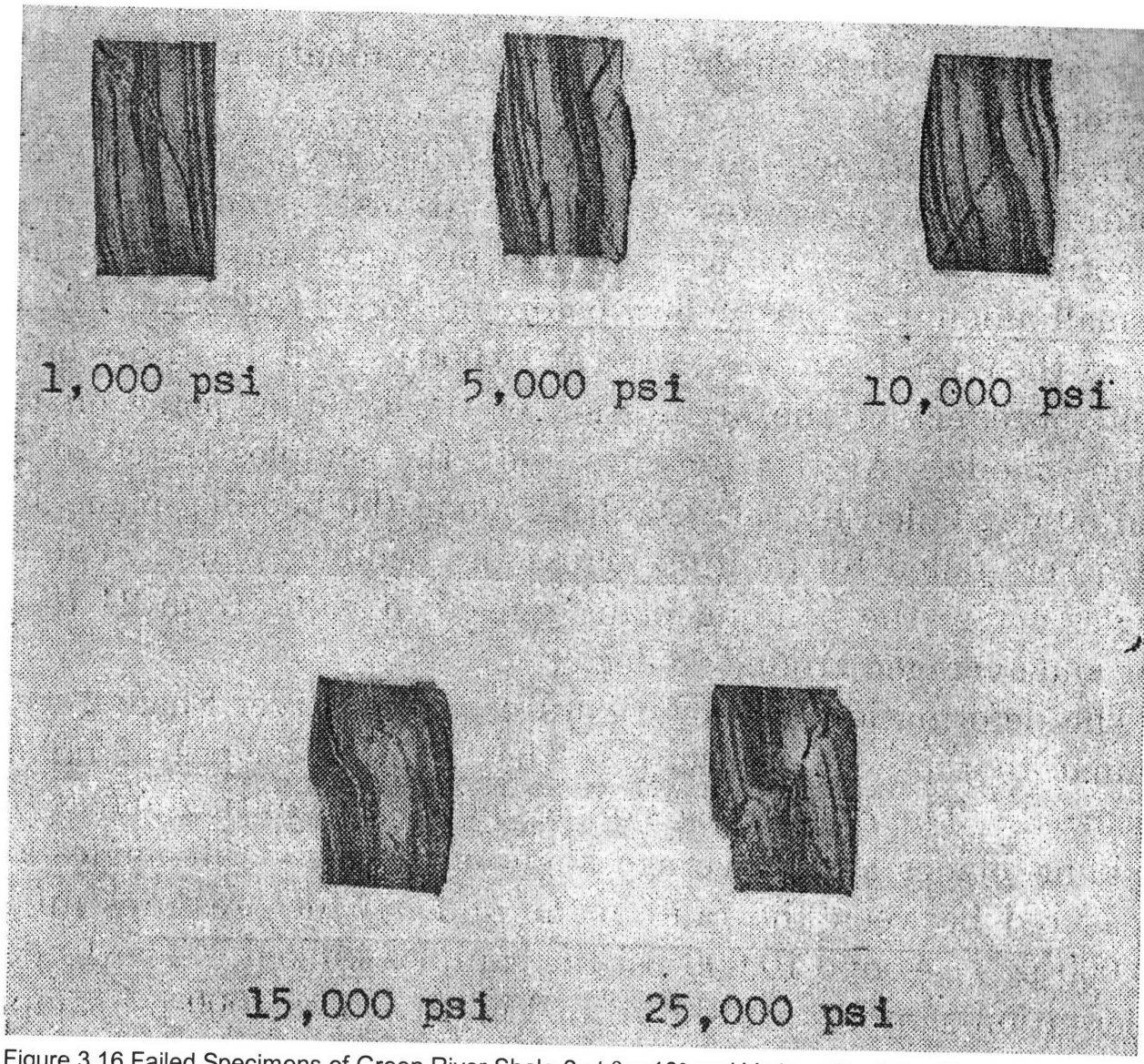

Figure 3.16 Failed Specimens of Green River Shale-2 at $\beta = 10°$ and Various Confining Pressures (McLamore and Gray, 1967)

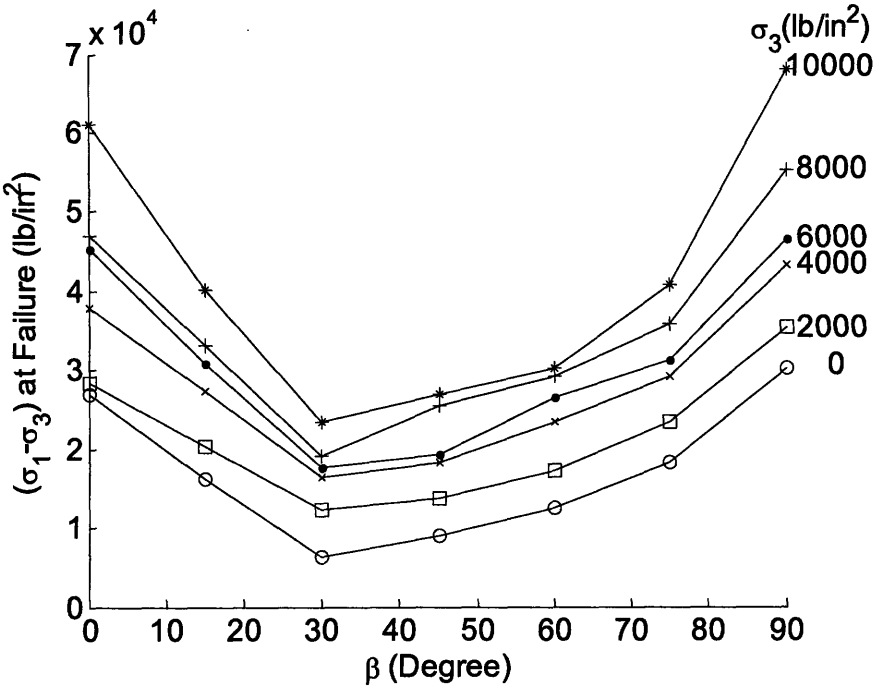

Figure 3.17 Triaxial Strength of Penrhyn Slate (data from Attewell and Sandford, 1974)

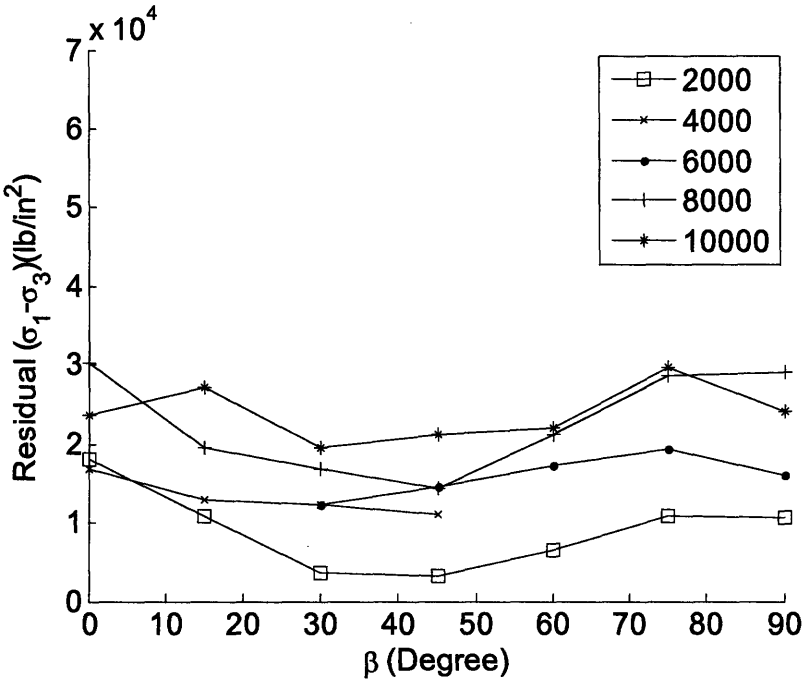

Figure 3.18 Post-Peak Strength of Penrhyn Slate (data from Attewell and Sandford, 1974)

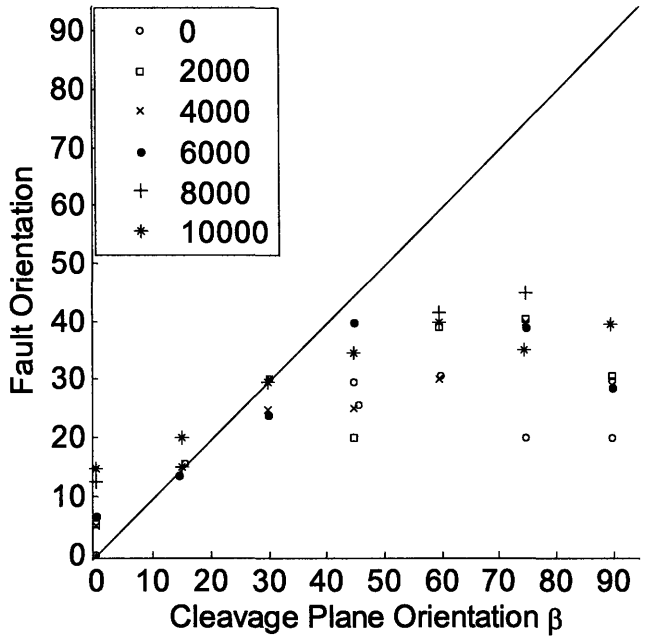

Figure 3.19 Shear Fault Orientation vs. Cleavage Plane Orientation Penrhyn Slate (Symbol definition same as Figure 3.17) (data from Attewell and Sandford, 1974)

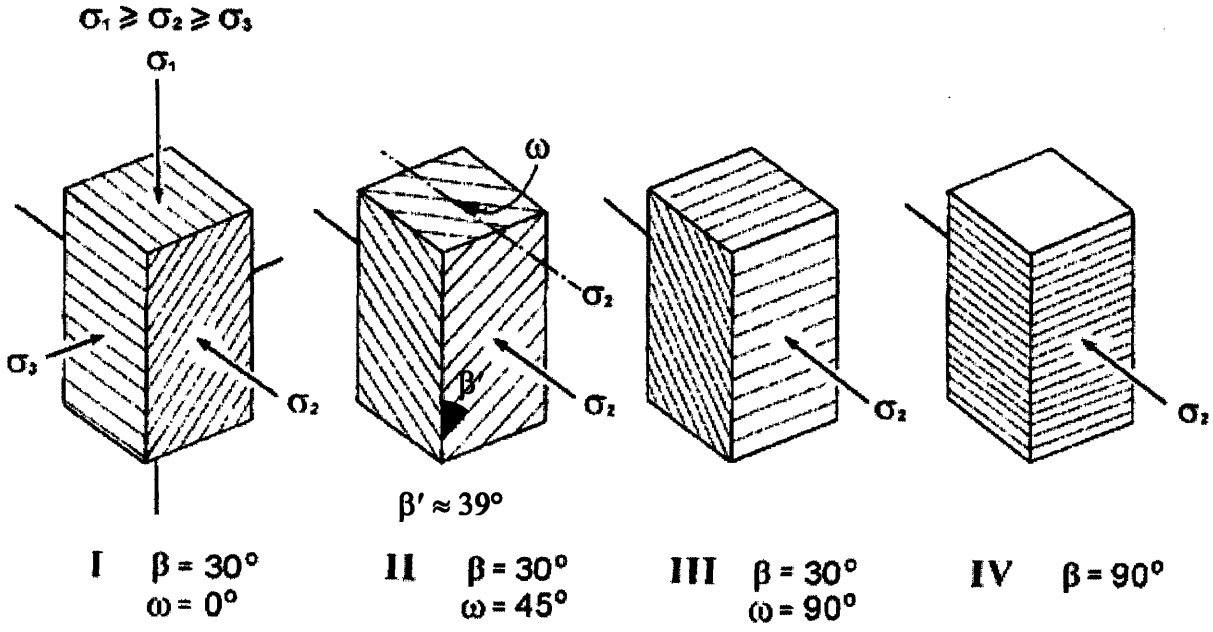

Figure 3.20 Loading Modes for True Triaxial Tests of Chichibu Green Schist (from Mogi, 2007)

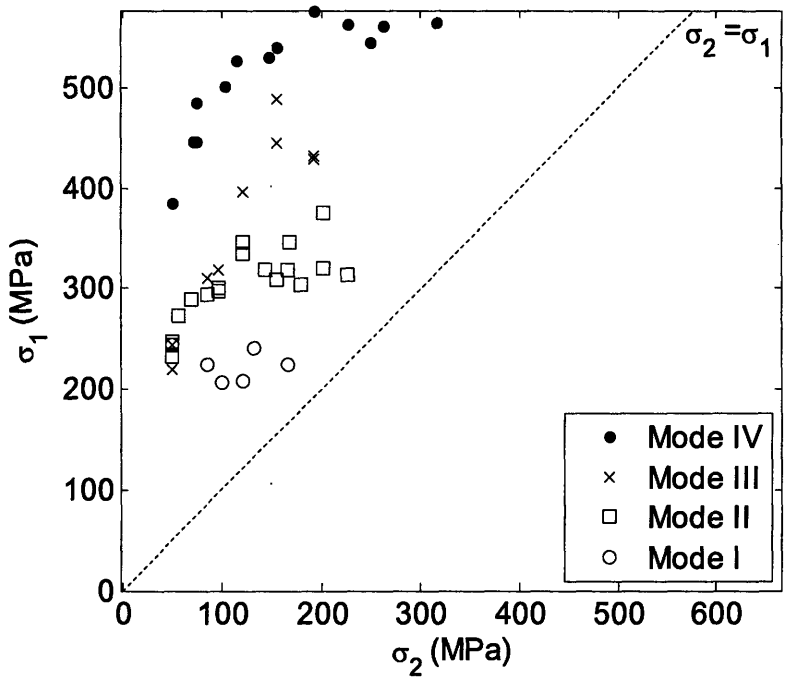

Figure 3.21 True Triaxial Strength of Chichibu Green Schist at σ_3 = 50MPa (data from Mogi, 2007)

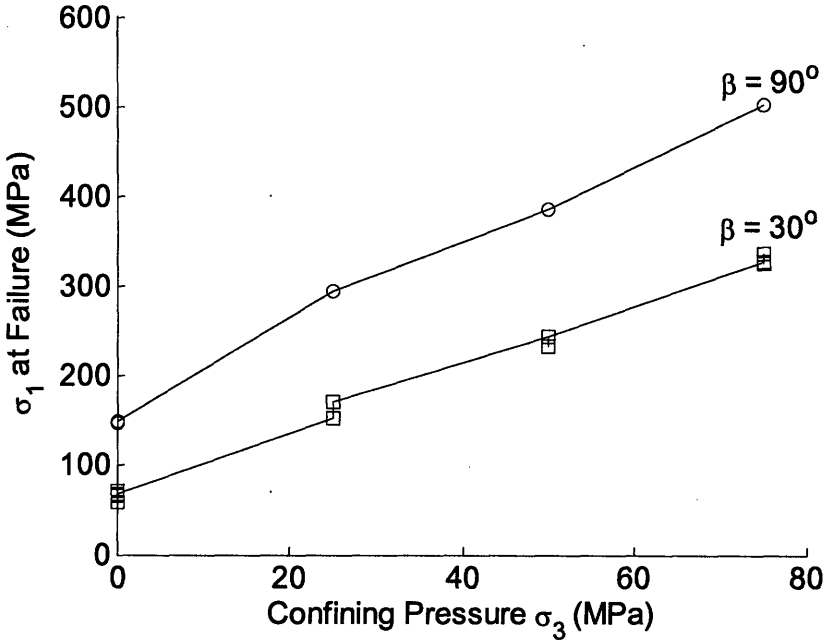

Figure 3.22 Conventional Triaxial Strength of Chichibu Green Schist (data from Mogi, 2007)

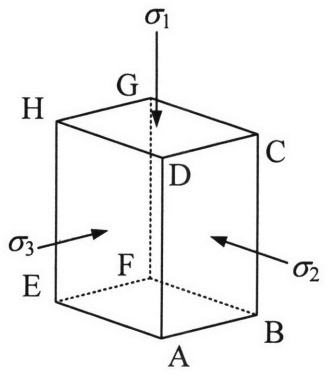

Plane A = Plane ABCD

Plane B = Plane EFGH

Figure 3.23 Definition of Planes A and B (from Mogi, 2007)

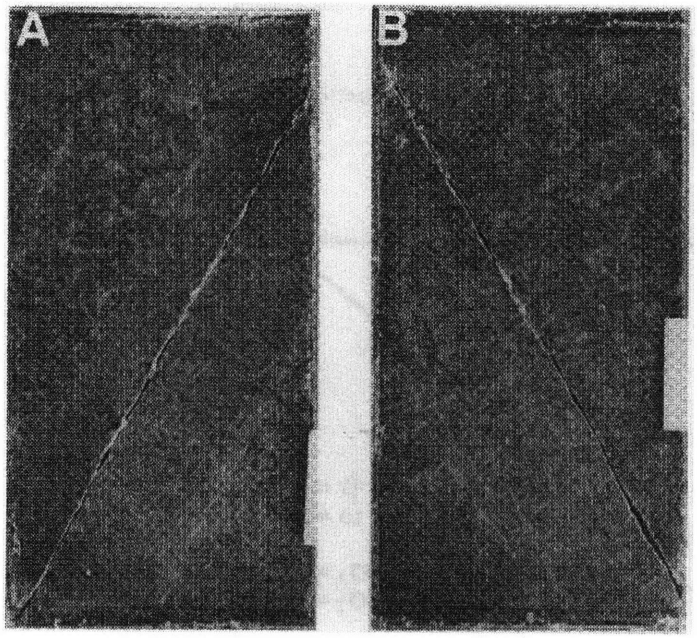

Figure 3.24 Failed Specimens of Chichibu Green Schist Mode I (σ_1=206MPa, σ_2=100MPa, σ_3=50MPa) (from Mogi, 2007)

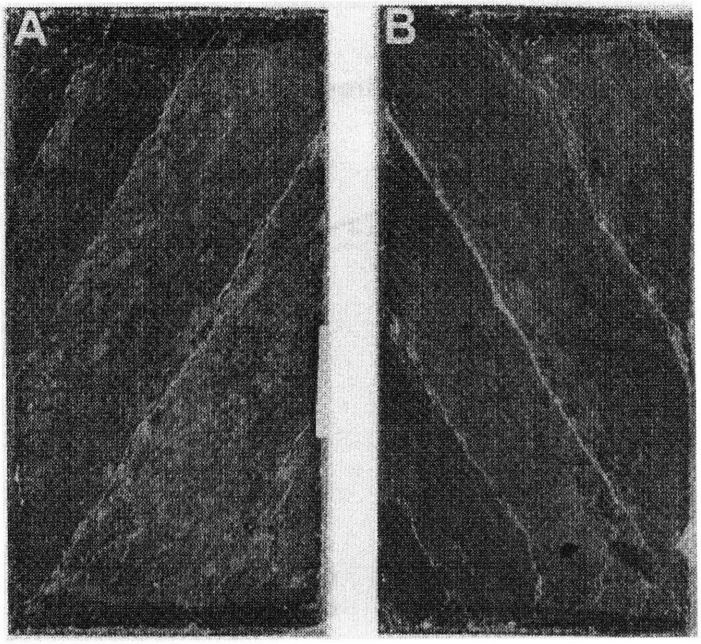

(a) Mode II, (σ_1, σ_2, σ_3) = (244MPa, 50MPa, 50MPa)

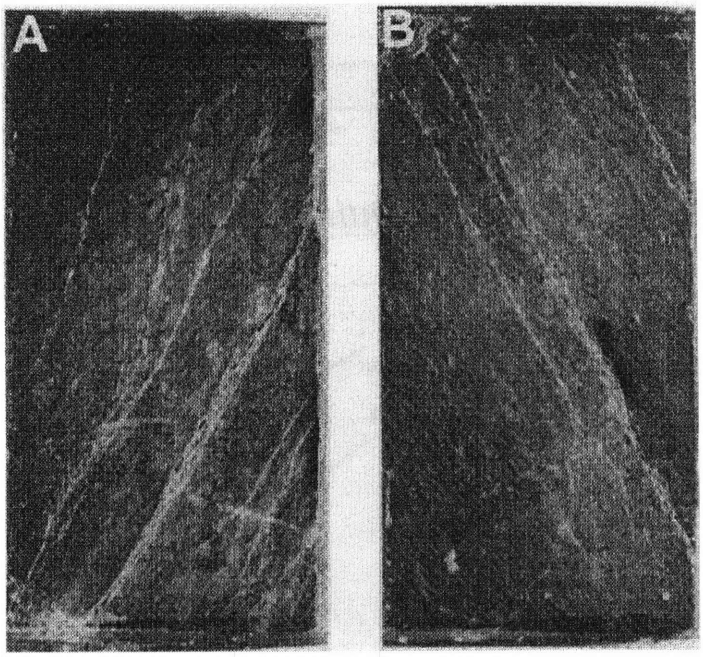

(b) Mode II, (σ_1, σ_2, σ_3) = (346MPa, 168MPa, 50MPa)

Figure 3.25 Failed Specimens of Chichibu Green Schist Mode II (from Mogi, 2007)

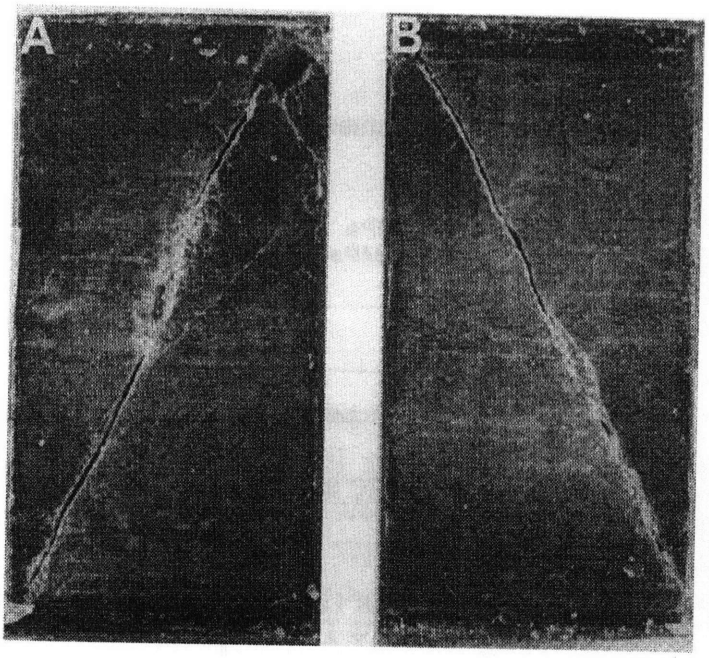

Figure 3.26 Failed Specimens of Chichibu Green Schist Mode IV (σ_1=540MPa, σ_2=156MPa, σ_3=50MPa) (from Mogi, 2007)

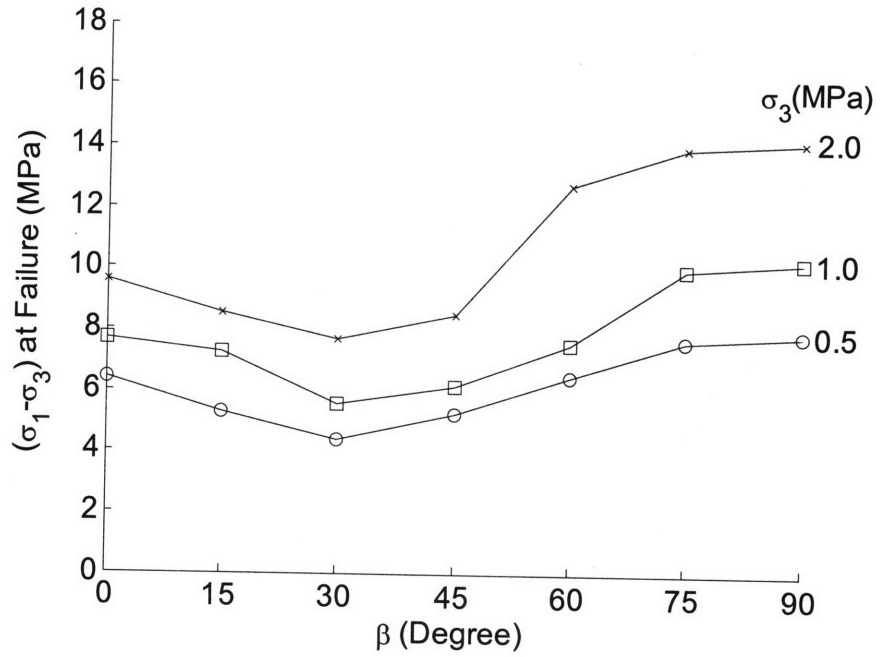

Figure 3.27 Triaxial Strength of Diatomite (data from Allirot and Boehler, 1979)

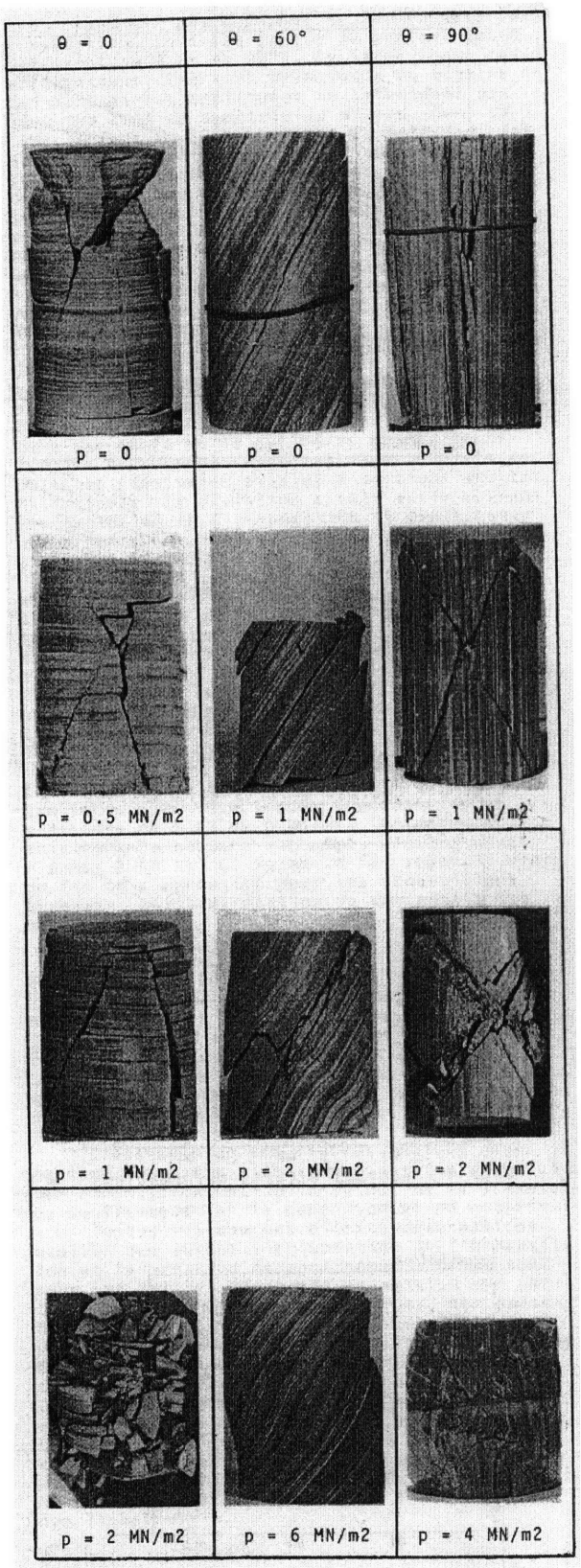

Figure 3.28 Failed Specimens of Diatomite (from Allirot and Boehler, 1979)

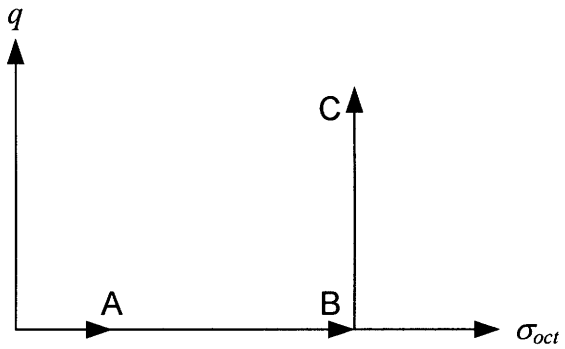

Figure 3.29 Typical Total Stress Path of Aristorenas's Tests (Aristorenas, 1992)

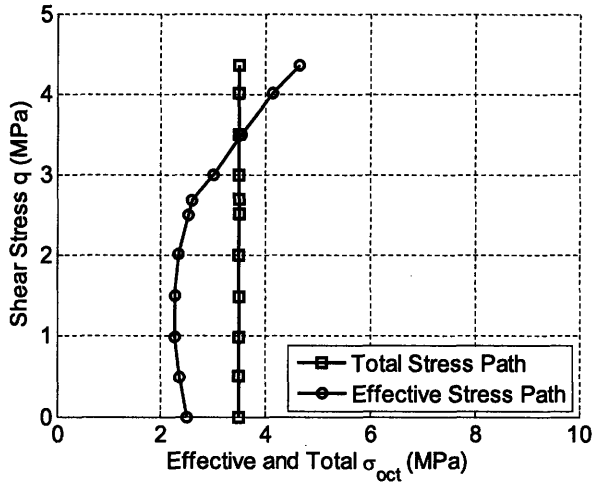

(a) Total and Effective Stress Paths

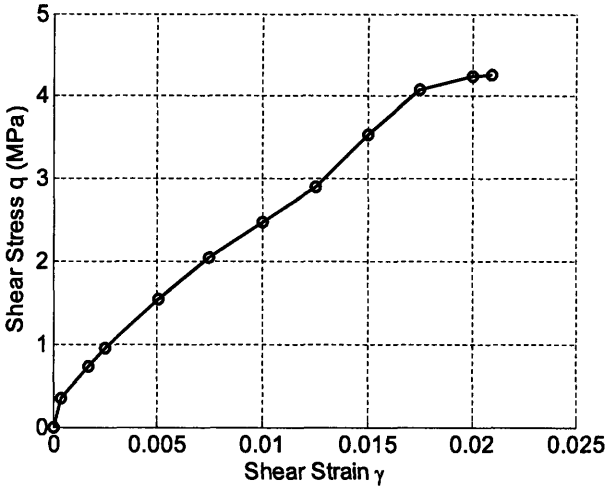

(b) Shear Stress-Strain Relationship

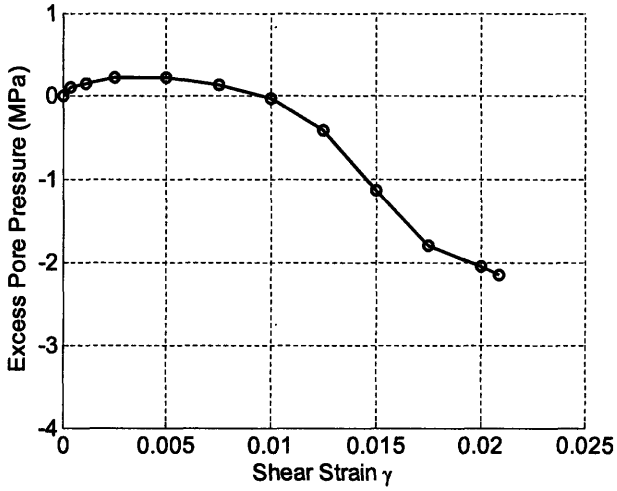

(c) Excess Pore Pressure

Figure 3.30 Sample Test Results for Specimen 23-10 in Pure Shear Undrained Compression (from Aristorenas, 1992)

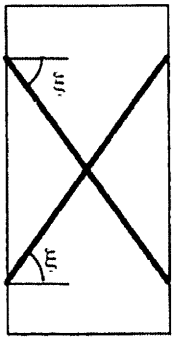

Mode A

Multiple conjugate shear failure planes
at an inclination of ξ

n = number of planes

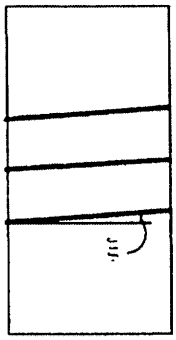

Mode B

Multiple fracture planes
at an inclination of ξ

n = number of planes

Figure 3.31 Two Failure Modes Observed (from Aristorenas, 1992)

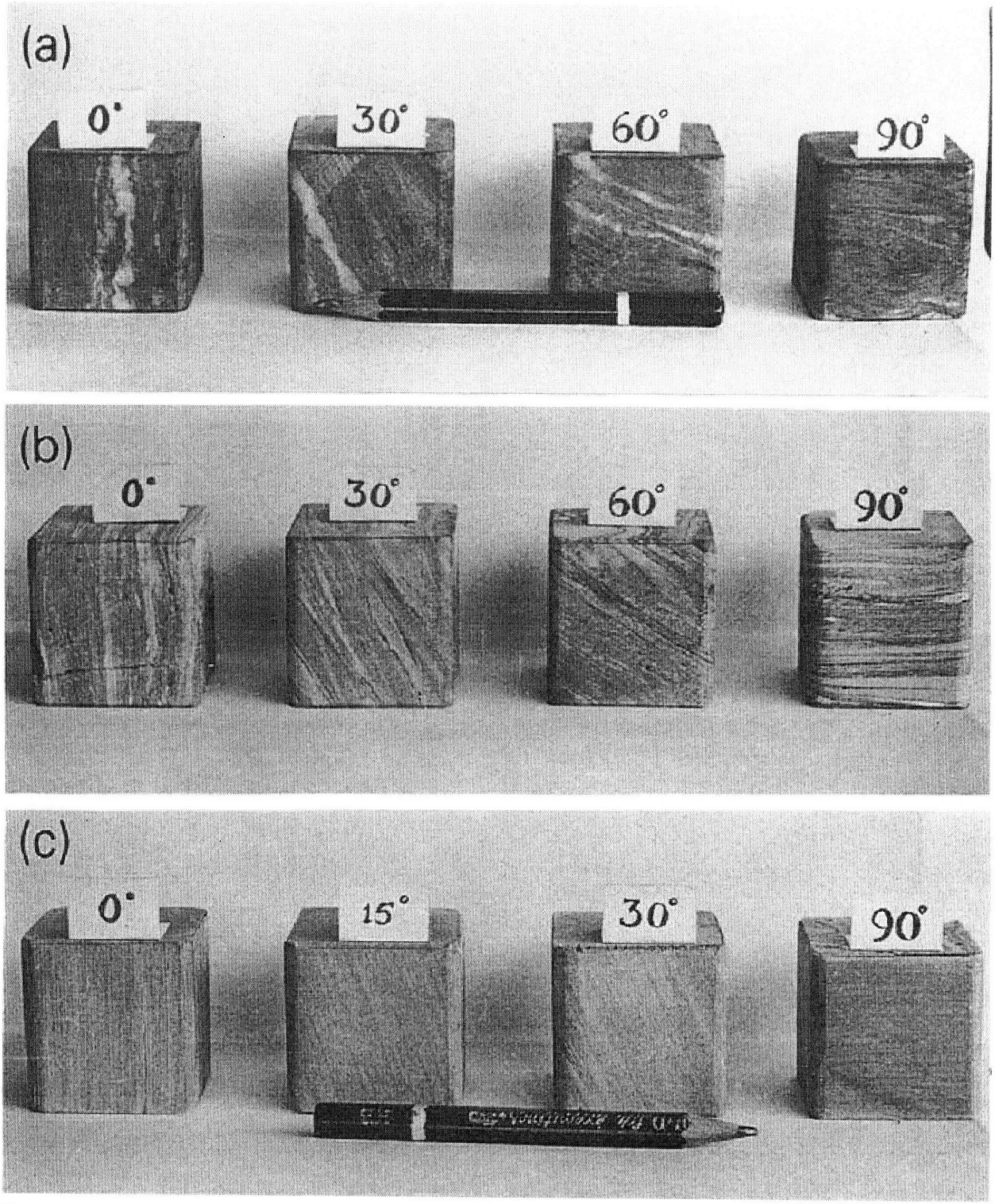

Figure 3.32 Specimens for Triaxial Tests: (a) Quartzitic phyllite, (b) carbonaceous phyllite, and (c) micaceous phyllite. (from Ramamurthy et al., 1993)

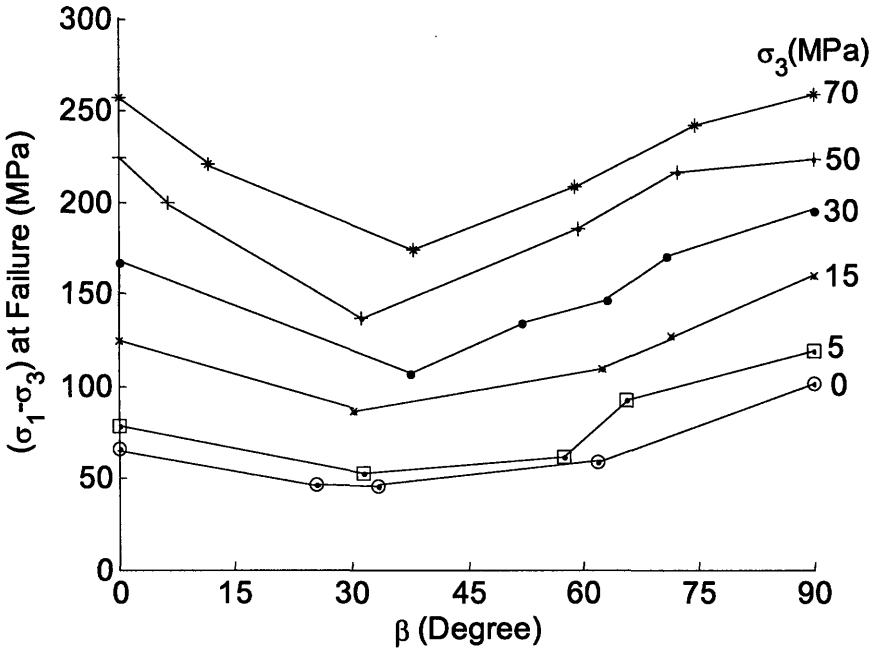

Figure 3.33 Triaxial Strength of Quartzitic Phyllite (data from Ramamurthy et al., 1993)

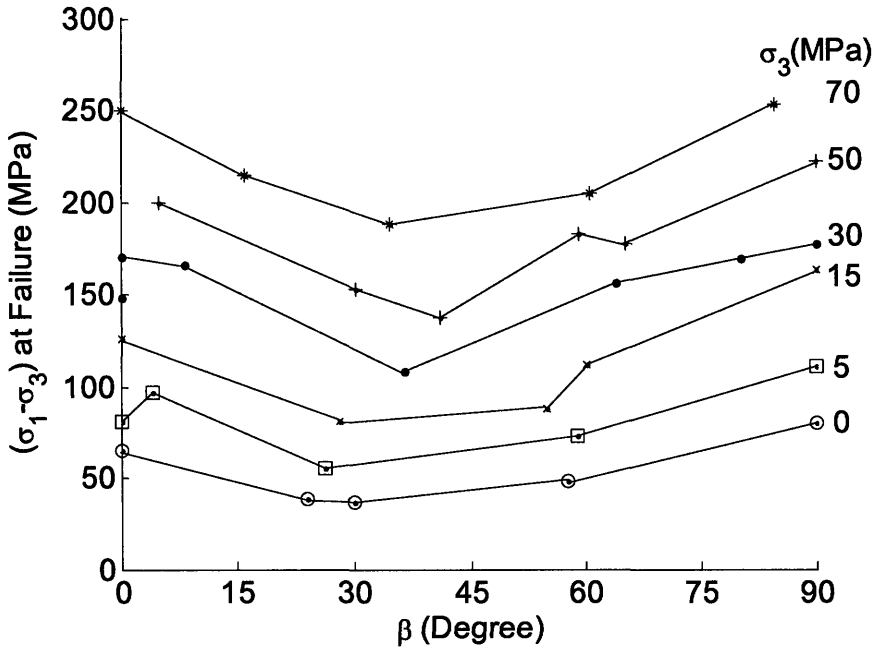

Figure 3.34 Triaxial Strength of Carbonaceous Phyllite (data from Ramamurthy et al., 1993)

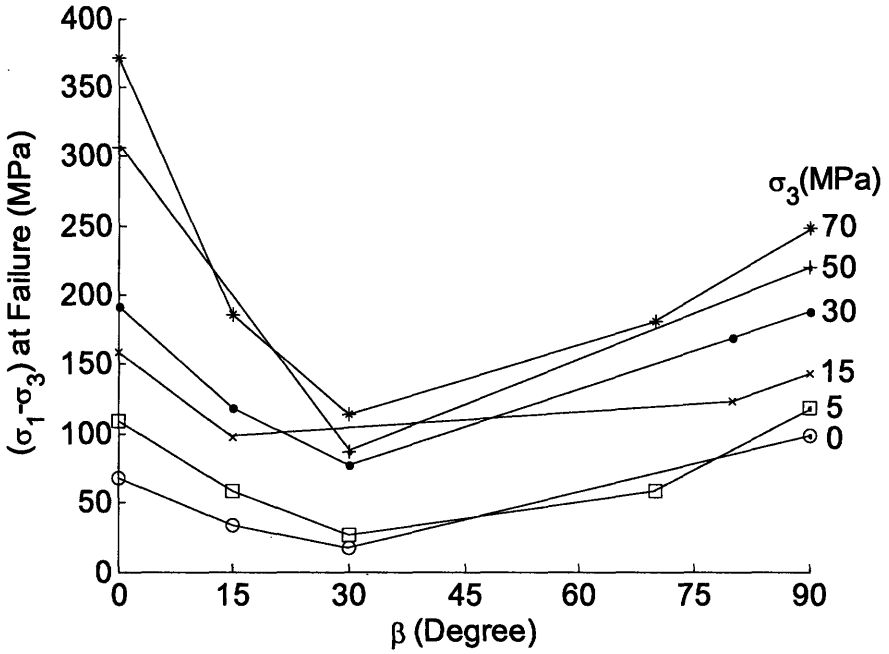

Figure 3.35 Triaxial Strength of Micaceous Phyllite (data from Ramamurthy et al., 1993)

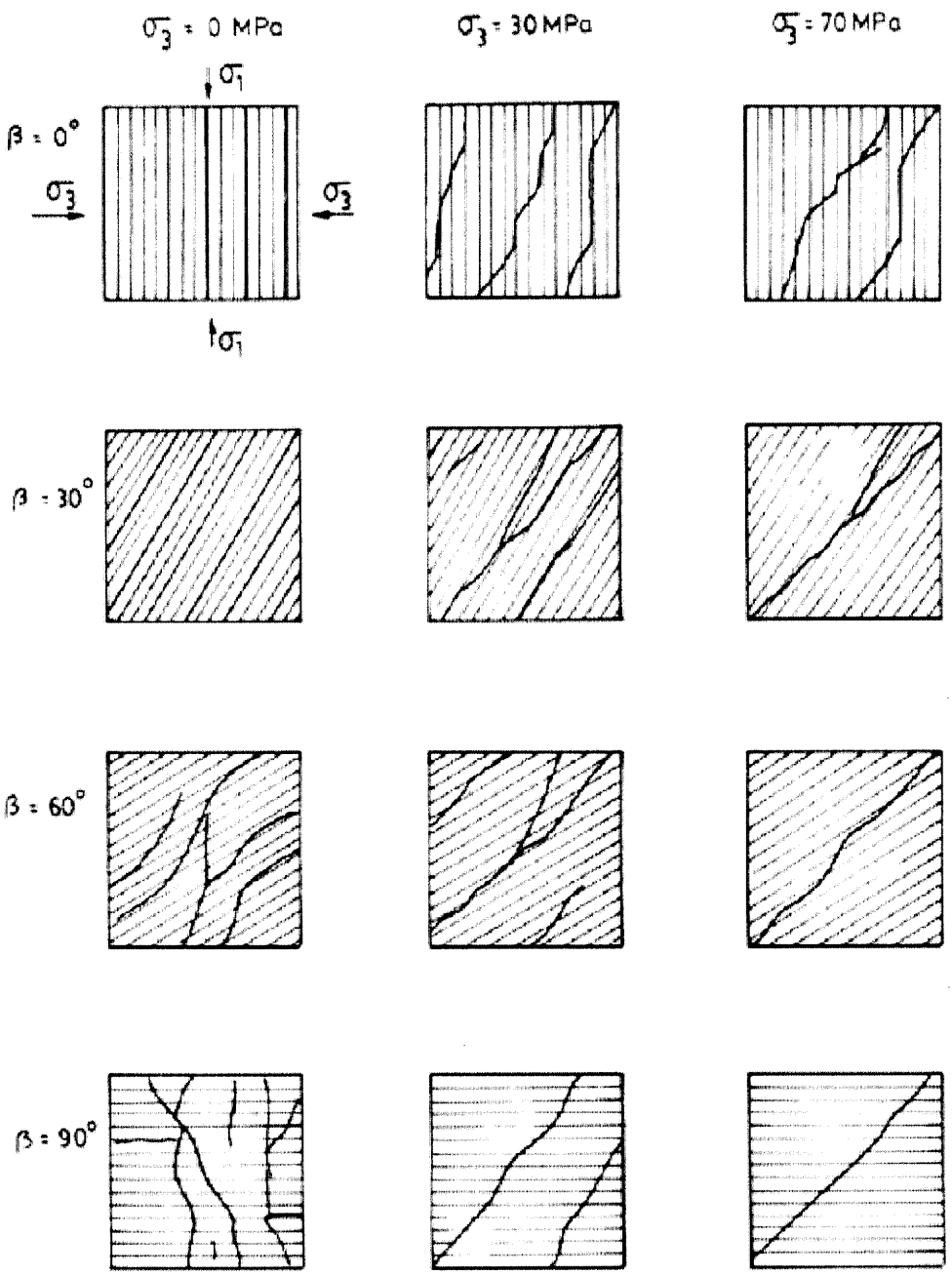

Figure 3.36 Failure Modes of Triaxial Compression Specimens of Phyllites (from Ramamurthy et al., 1993)

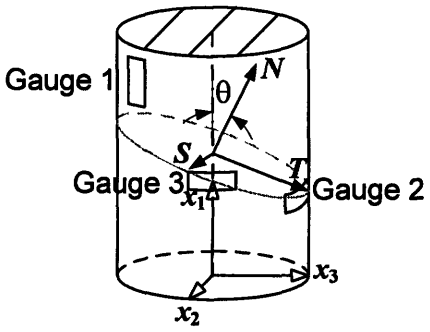

Figure 3.37 Strain Gauge Configuration (from Niandou, 1994)

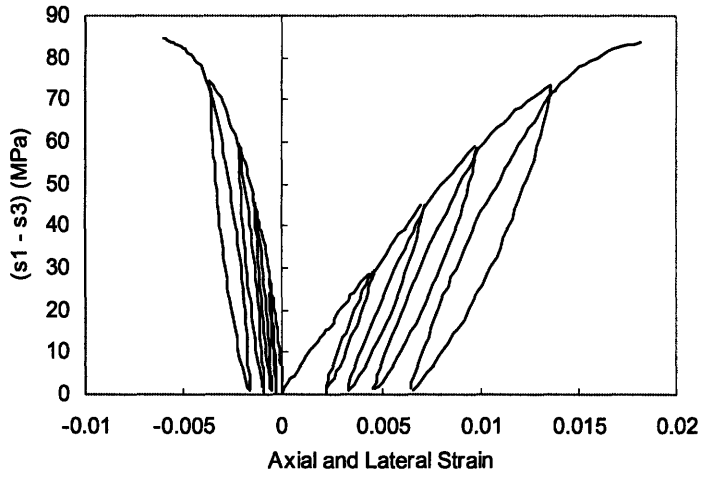

(a) Axial and Lateral Strains Measured by Strain Gauges

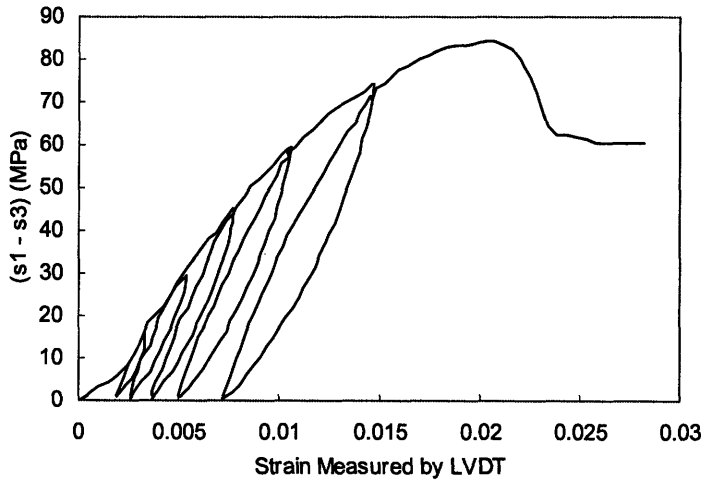

(b) Axial Strain Measured by LVDT

Figure 3.38 Sample Stress Strain Curves with $\beta = 90°$ and $\sigma_3 = 30$ MPa (data from Niandou, 1994)

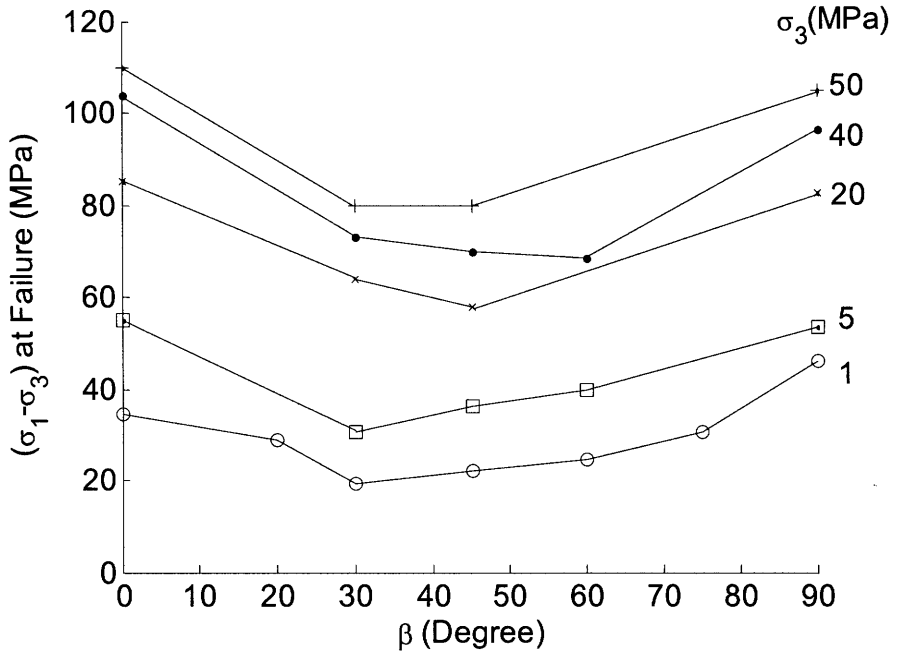

Figure 3.39 Triaxial Strength of Tournemire Shale (data from Niandou, 1994)

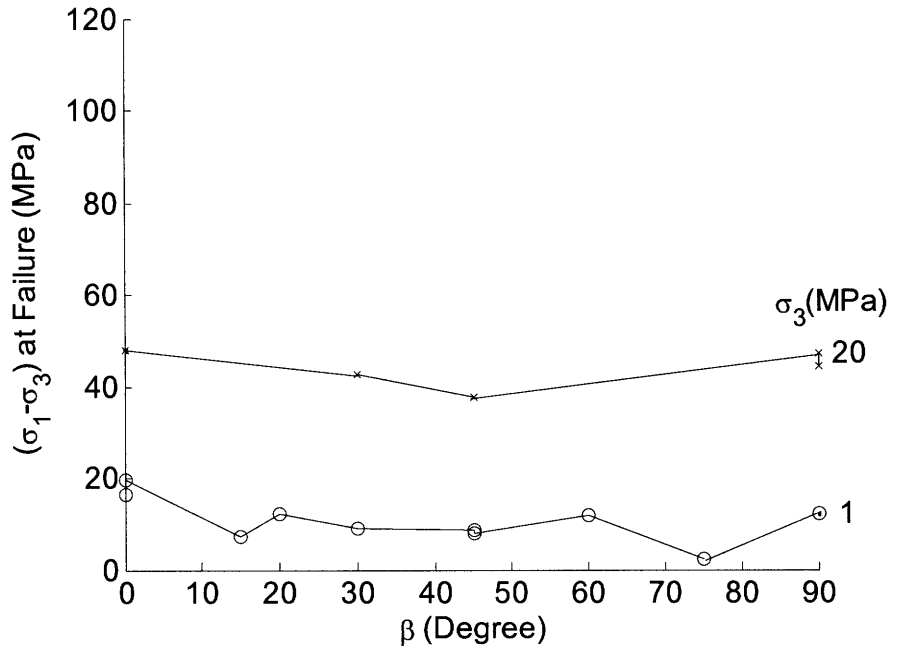

Figure 3.40 Post-Peak Strength of Tournemire Shale Specimens (data from Niandou, 1994)

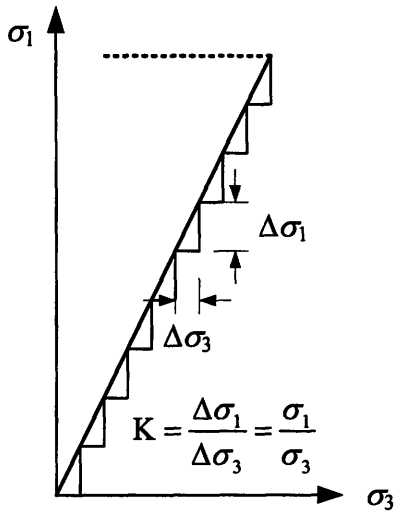

Figure 3.41 Stepwise Loading Path to Approximate Proportional Loading

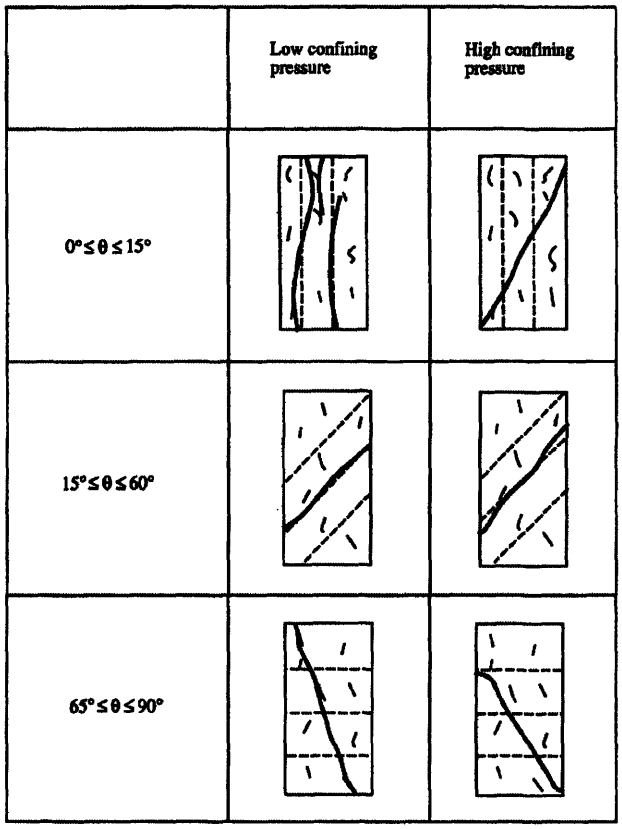

Figure 3.42 Sketch of Failure Modes Observed from Tournemire Shale Specimens (from Niandou, 1997)
Note: $\theta = \pi/2 - \beta$

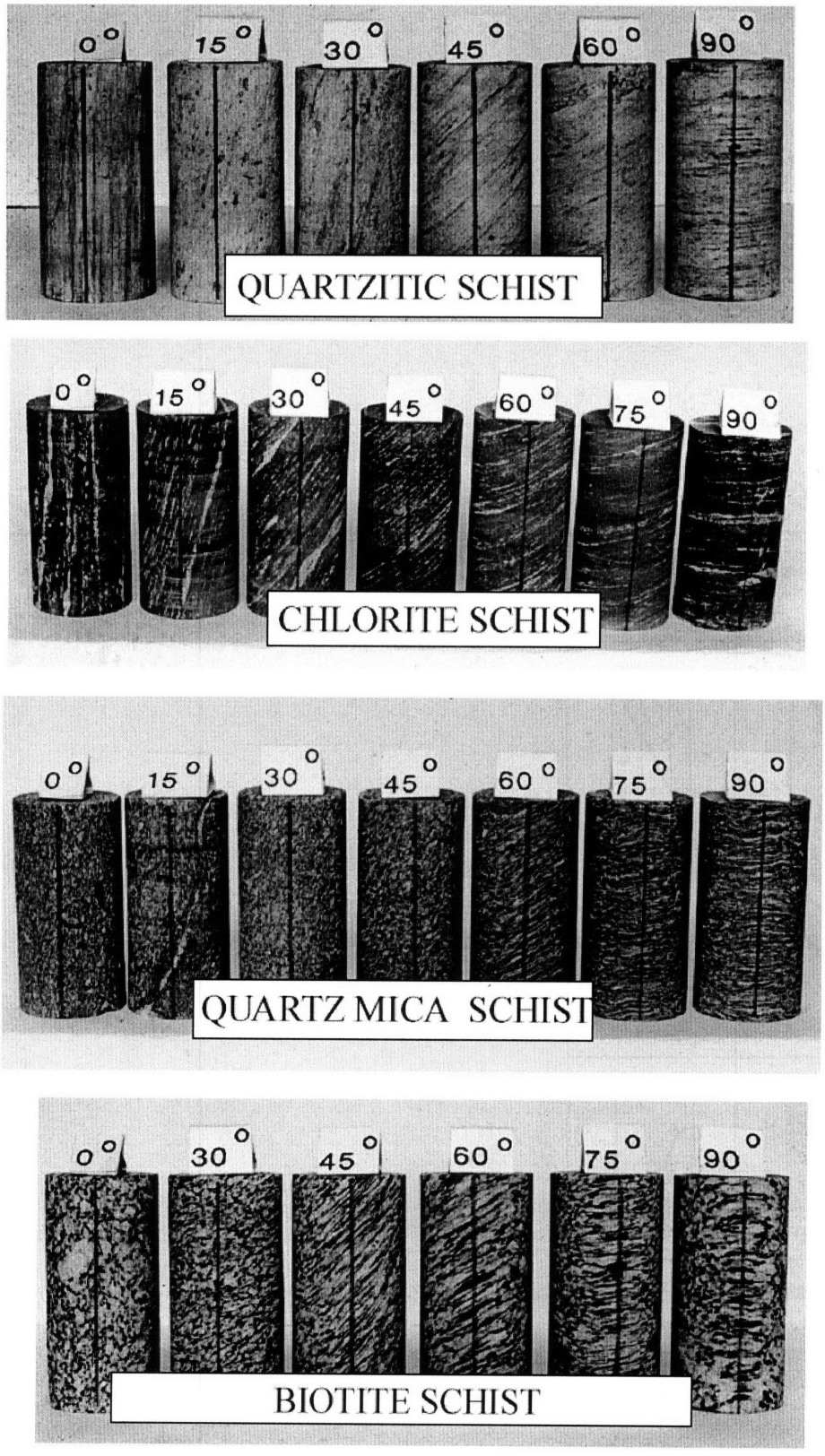

Figure 3.43 Himalaya Schist Specimens (from Nasseri, 2003)

Note: Vertical lines on specimens are probably reference lines for measuring orientation.

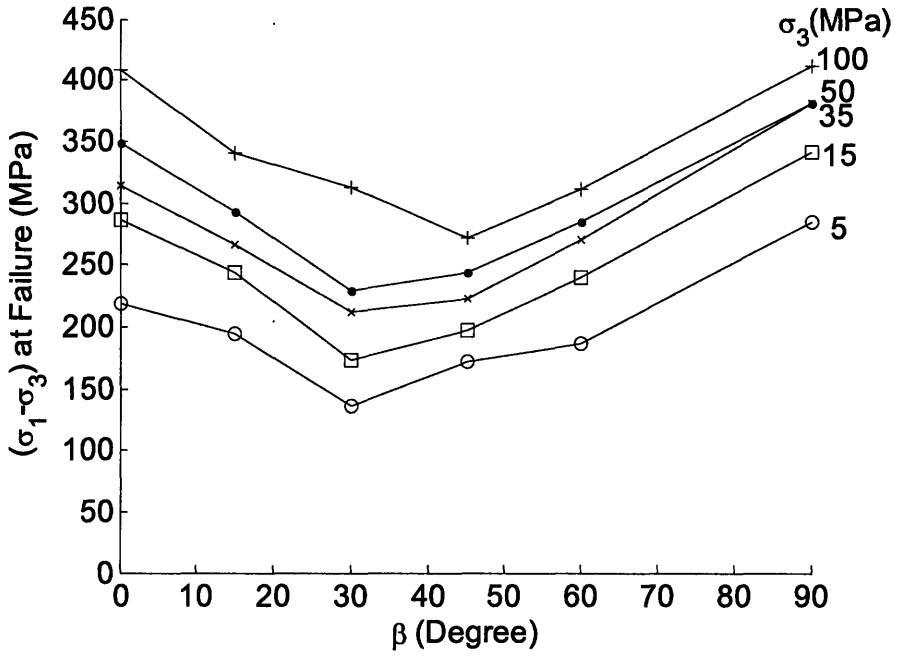

Figure 3.44 Triaxial Strength of Quartzitic Schist (data from Behrestaghi, 1996)

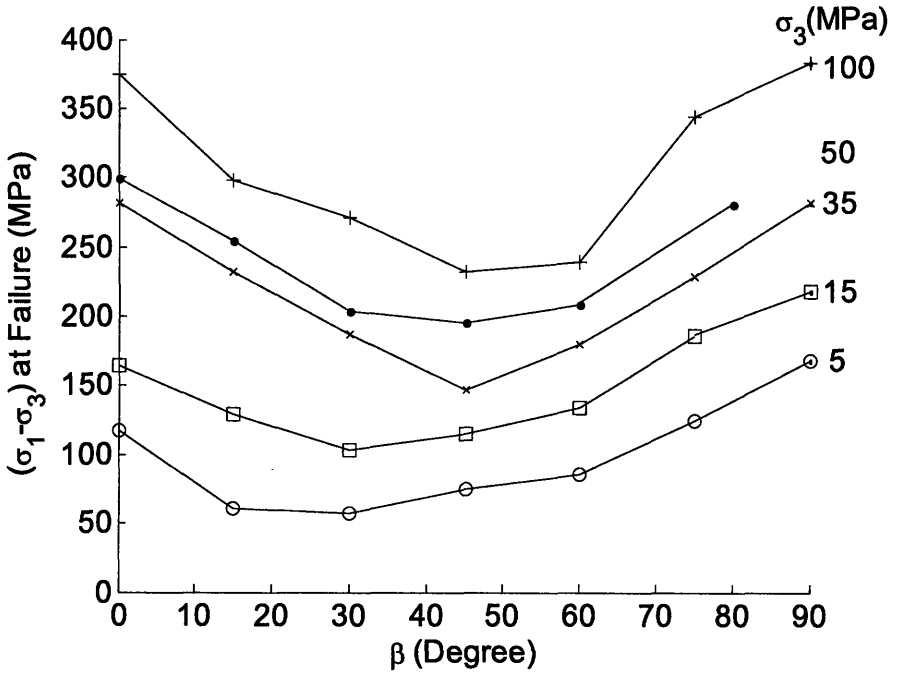

Figure 3.45 Triaxial Strength of Chlorite Schist (data from Behrestaghi, 1996)

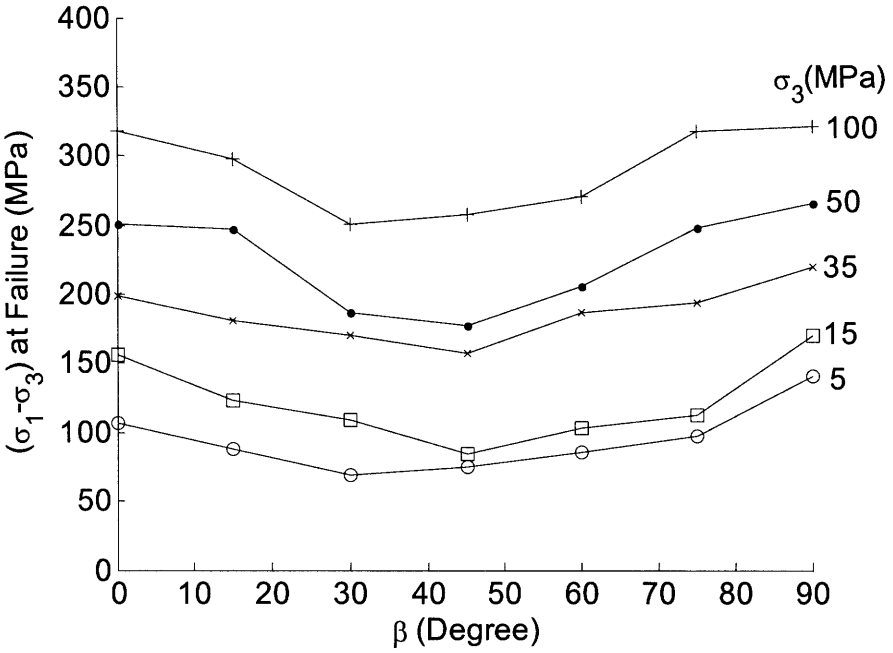

Figure 3.46 Triaxial Strength of Quartz Mica Schist (data from Behrestaghi, 1996)

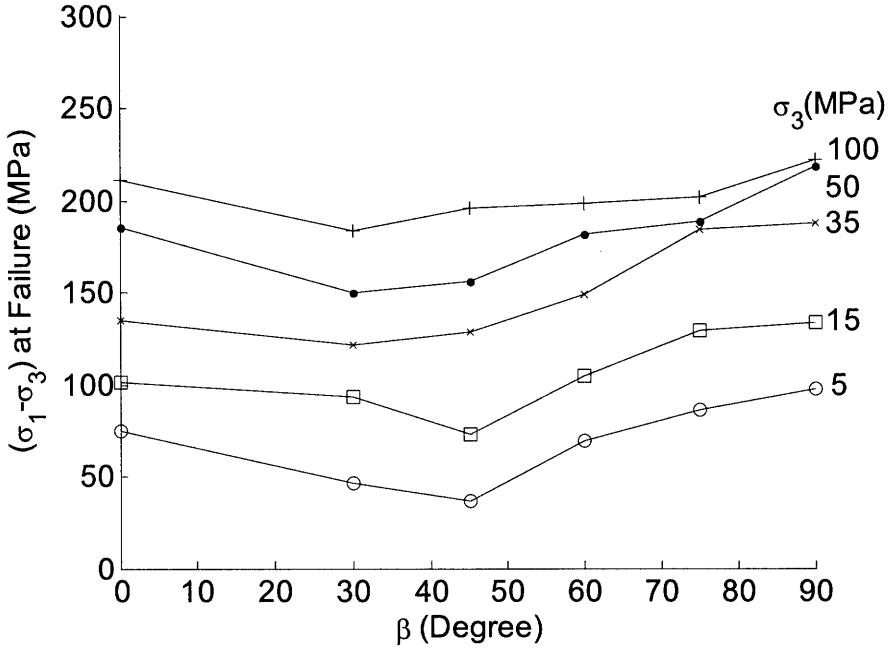

Figure 3.47 Triaxial Strength of Biotite Schist (data from Behrestaghi, 1996)

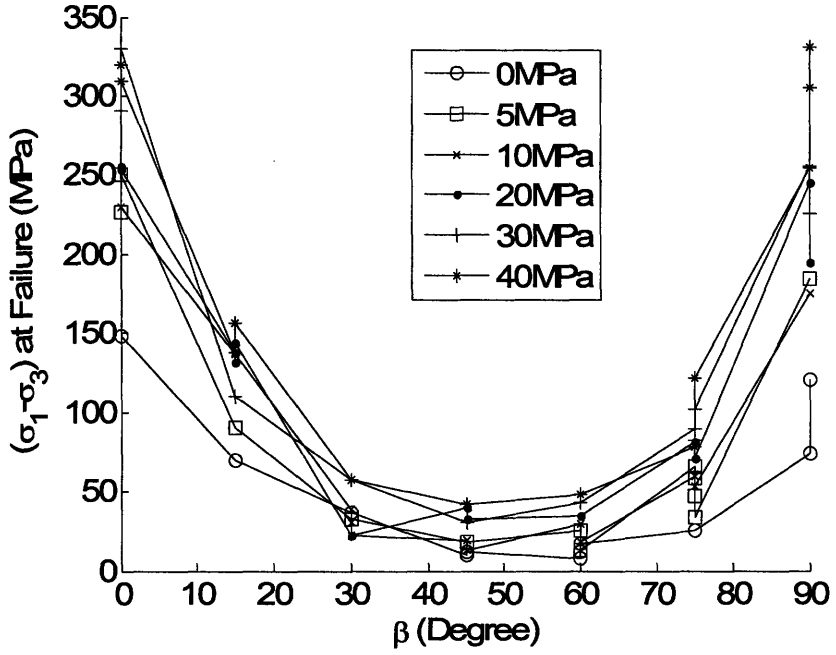

(a) Raw Data

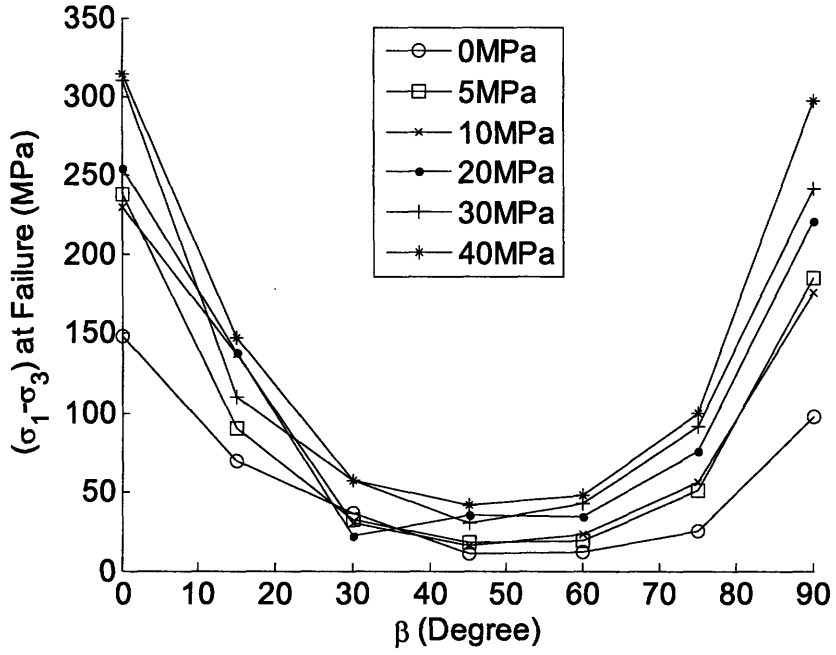

(b) Averaged Data

Figure 3.48 Triaxial Strength of Angers Schist (data from Duveau et al., 1998)

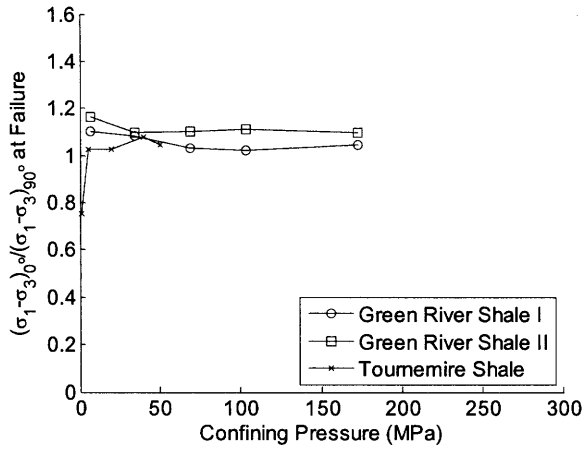

(a) Shale

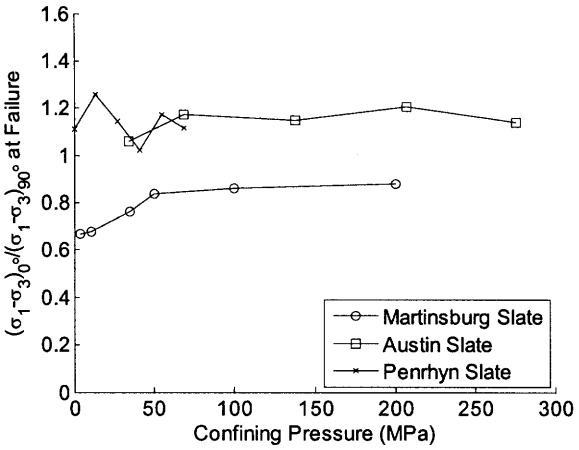

(b) Slate

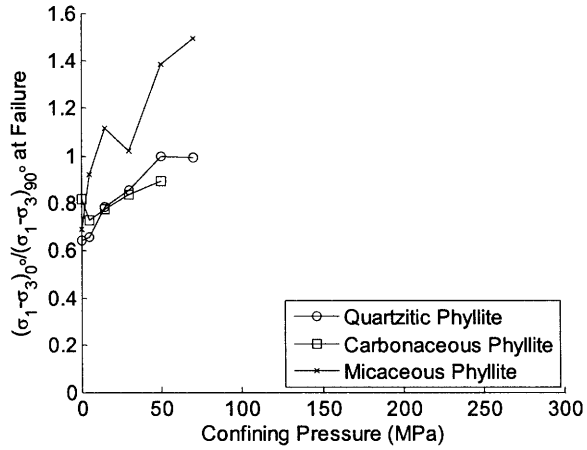

(c) Phyllite

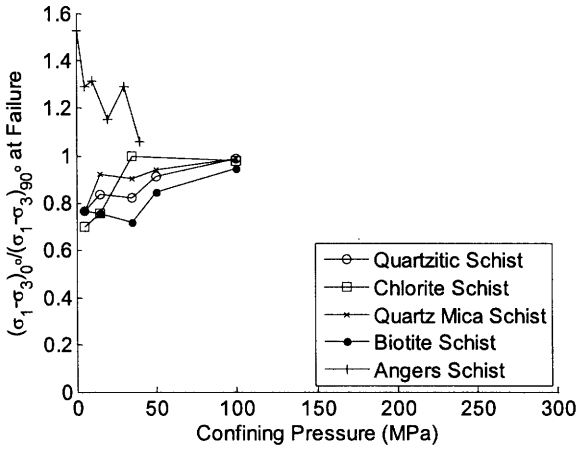

(d) Schist

Figure 3.49 The Unevenness Ratio for Anisotropic Rocks

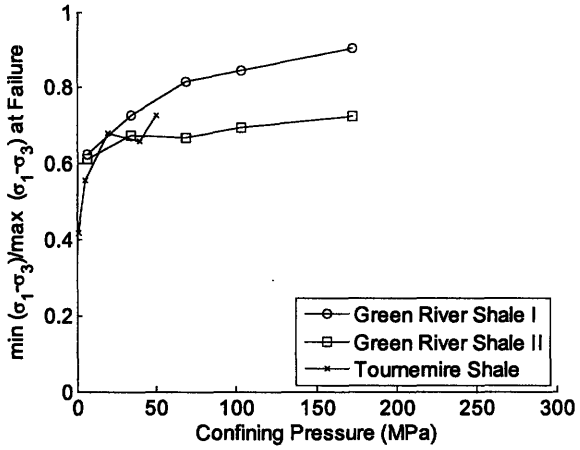

(a) Shale

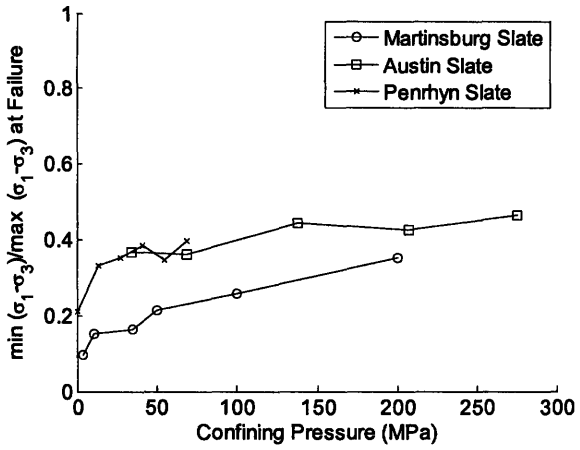

(b) Slate

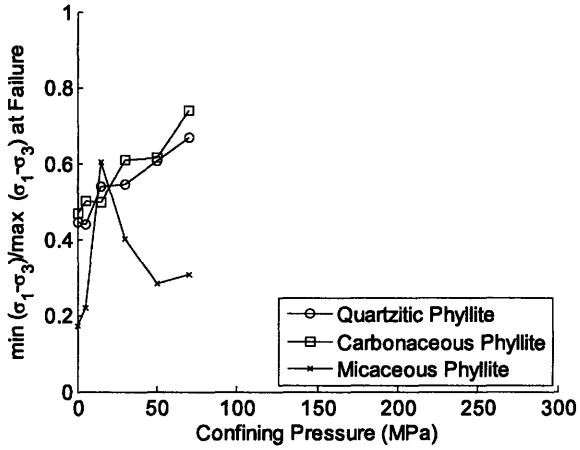

(c) Phyllite

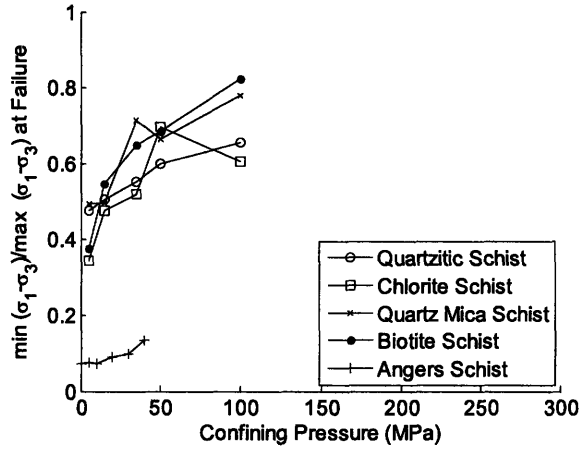

(d) Schist

Figure 3.50 The Depth Ratio for Anisotropic Rocks

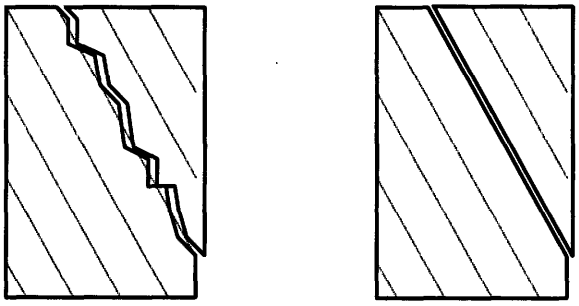

(a) Non-Planar (b) Planar

Figure 3.51 Failure along the Isotropic Plane with Non-Planar and Planar Shear Faults

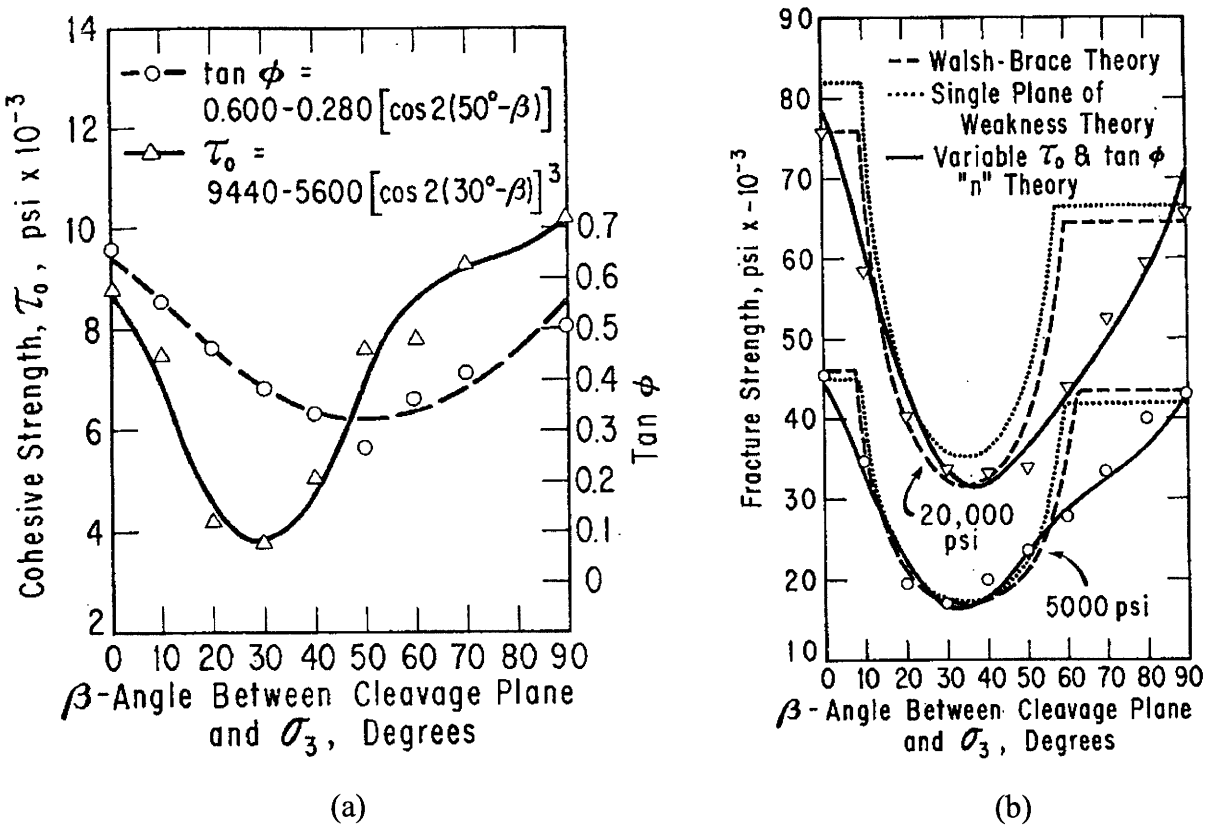

(a) (b)

Figure 3.52 Application of the Empirical Criterion by McLamore and Gray on the Austin Slate (from McLamore and Gray, 1967)

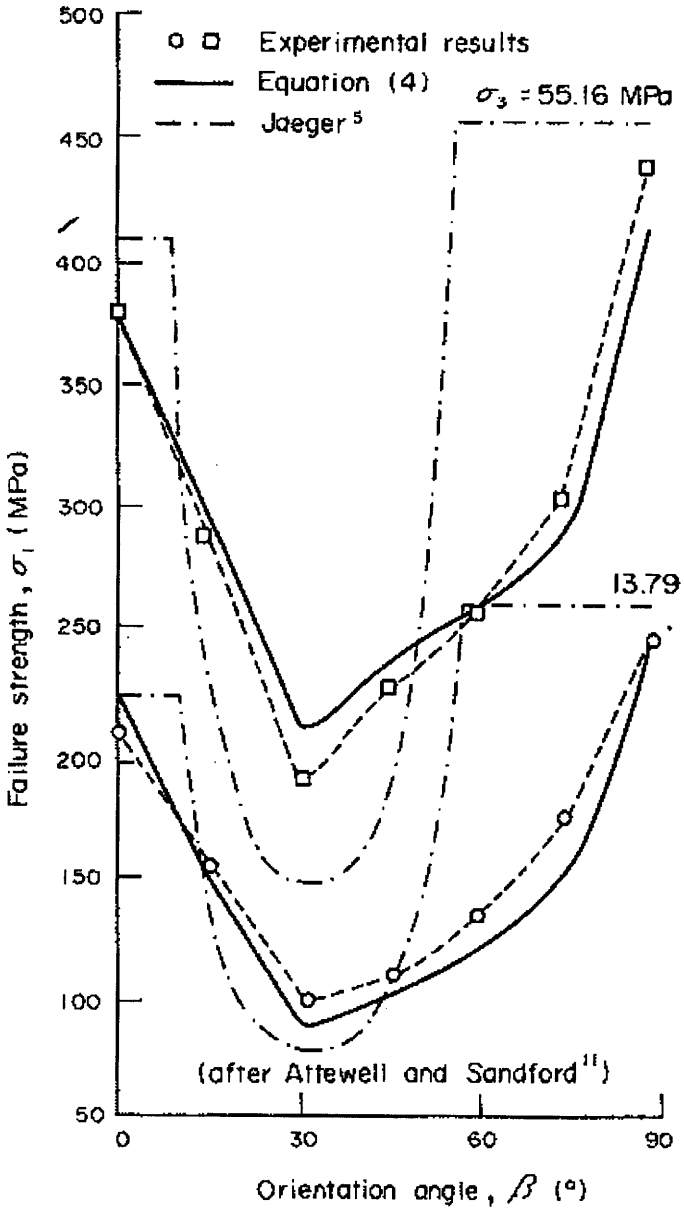

Figure 3.53 Application of the Theory by Ramamurthy et al. on Penrhyn Slate (from Ramamurthy, 1983)

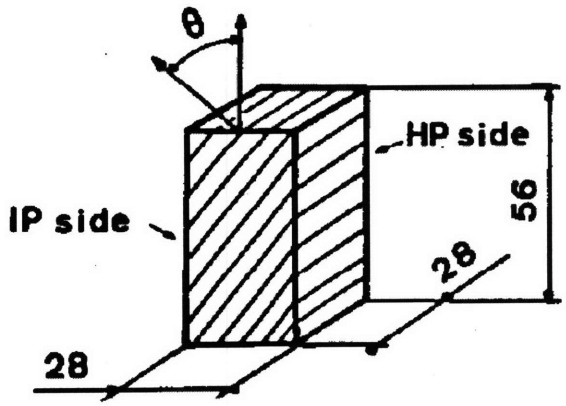

Figure 3.54 Specimen Dimension of Glass-Fiber Reinforced Composite, Units in mm (modified from Boehler and Raclin, 1985)

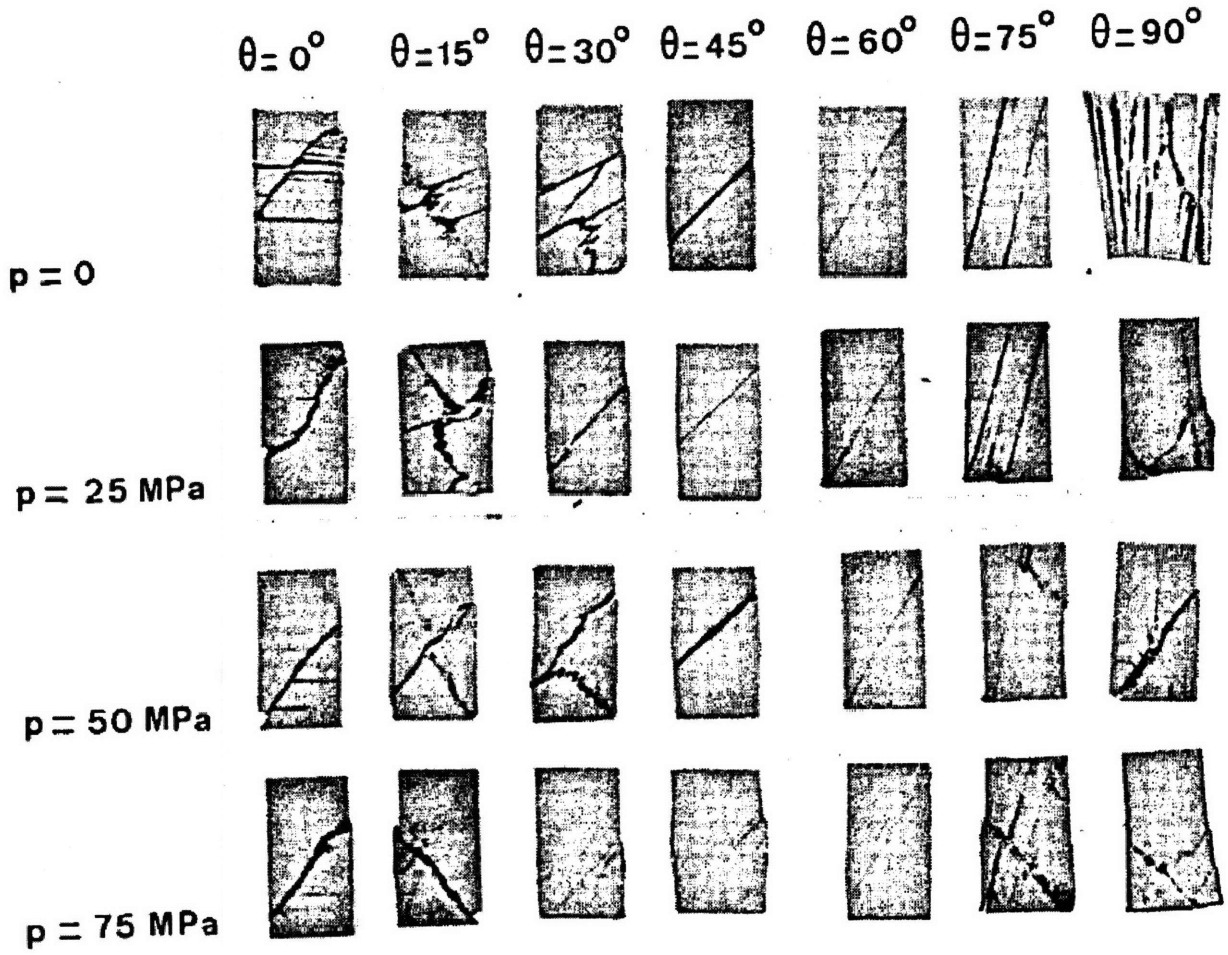

Figure 3.55 Failed Specimens of Glass-Fiber Reinforced Composite (from Boehler and Raclin, 1985)

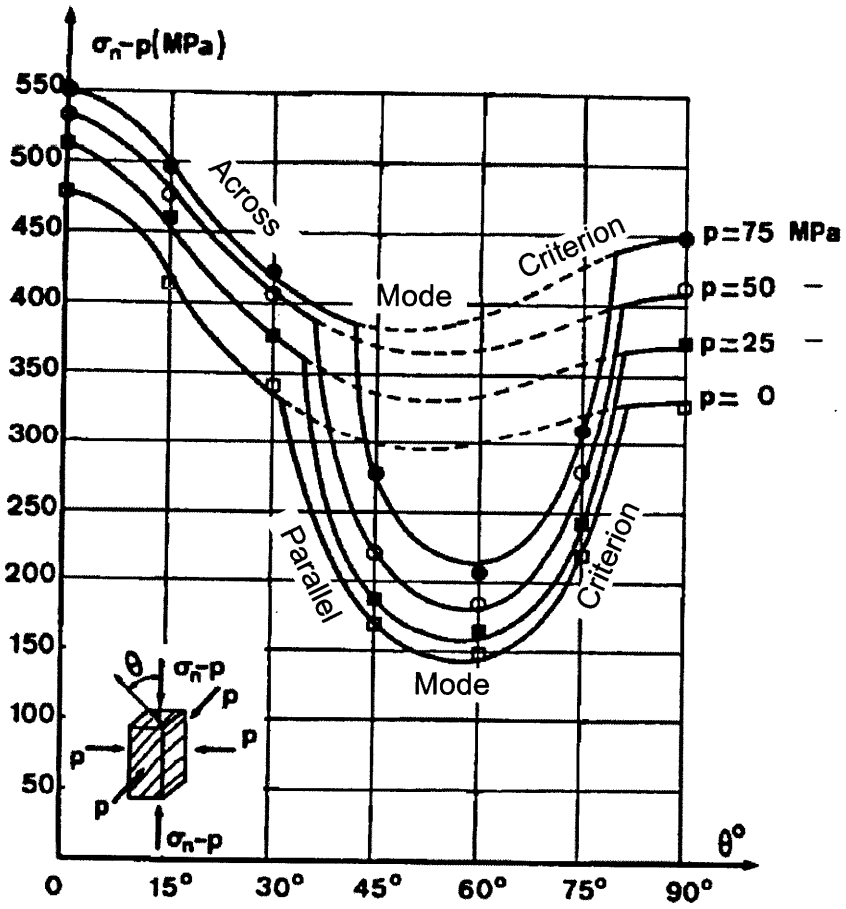

Figure 3.56 Comparison of Measured and Predicted Strength (modified from Boehler and Raclin, 1985)
Note: Solid lines show the lower predicted strength of the "parallel mode" and the "across mode" criteria. When the "across mode" criterion produces higher strength, it is shown with a dashed line.

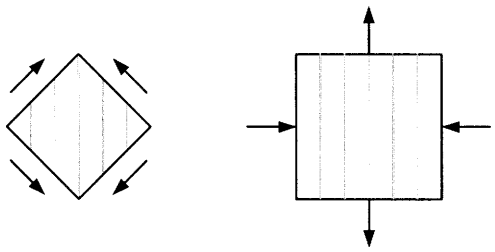

(a) Left: Pure Shear Stress State; Right: Equivalent Deviatoric Normal Stress State

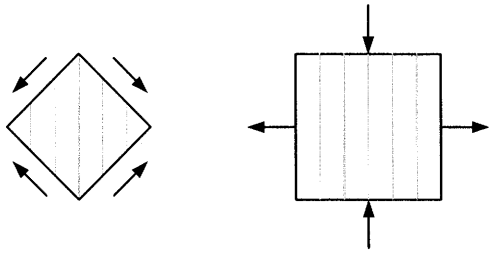

(b) Left: Pure Shear Stress State; Right: Equivalent Deviatoric Normal Stress State

Figure 3.57 Pure Shear Stress States with Same Magnitude but Different Directions of Shear Stresses

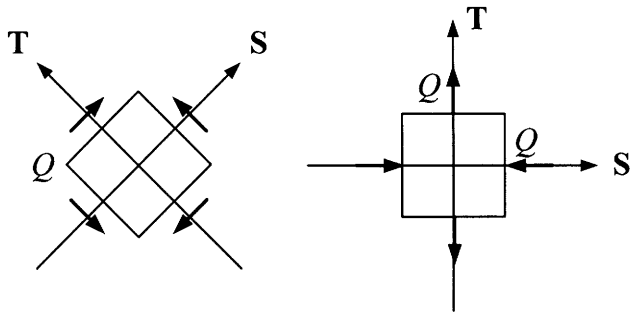

Figure 3.58 Equivalence of a Pure Shear Stress (Left) and Deviatoric Normal Stress (Right)

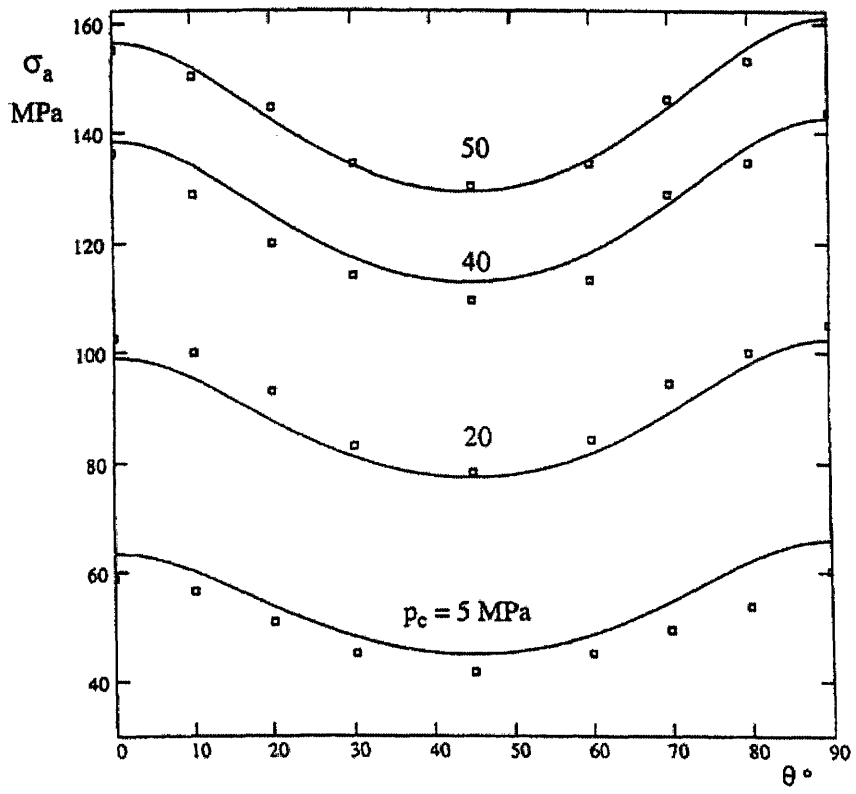

Figure 3.59 Application of the AMS Criterion on Tournemire Shale (from Cazacu, 1999) Note: $\theta = \pi/2 - \beta$

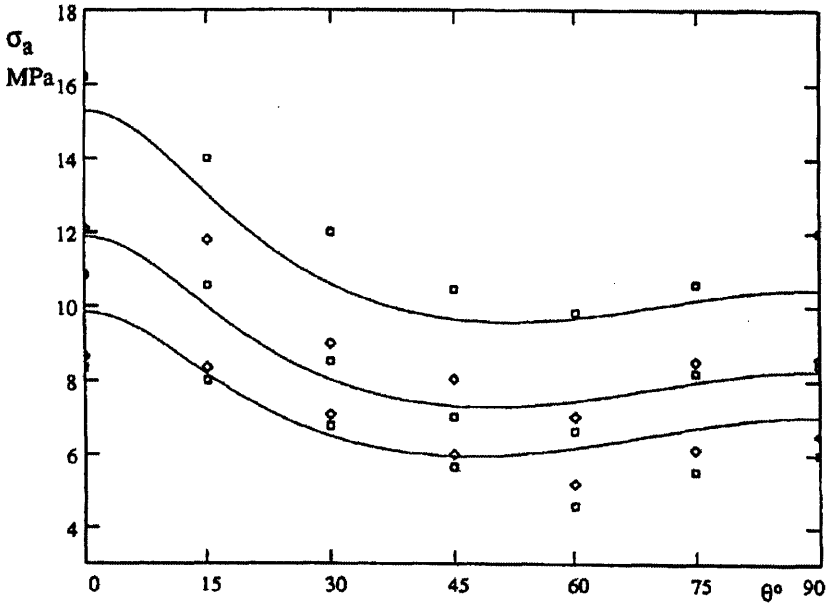

Figure 3.60 Application of the AMS Criterion on Diatomite (from Cazacu, 1998) Note: $\theta = \pi/2 - \beta$

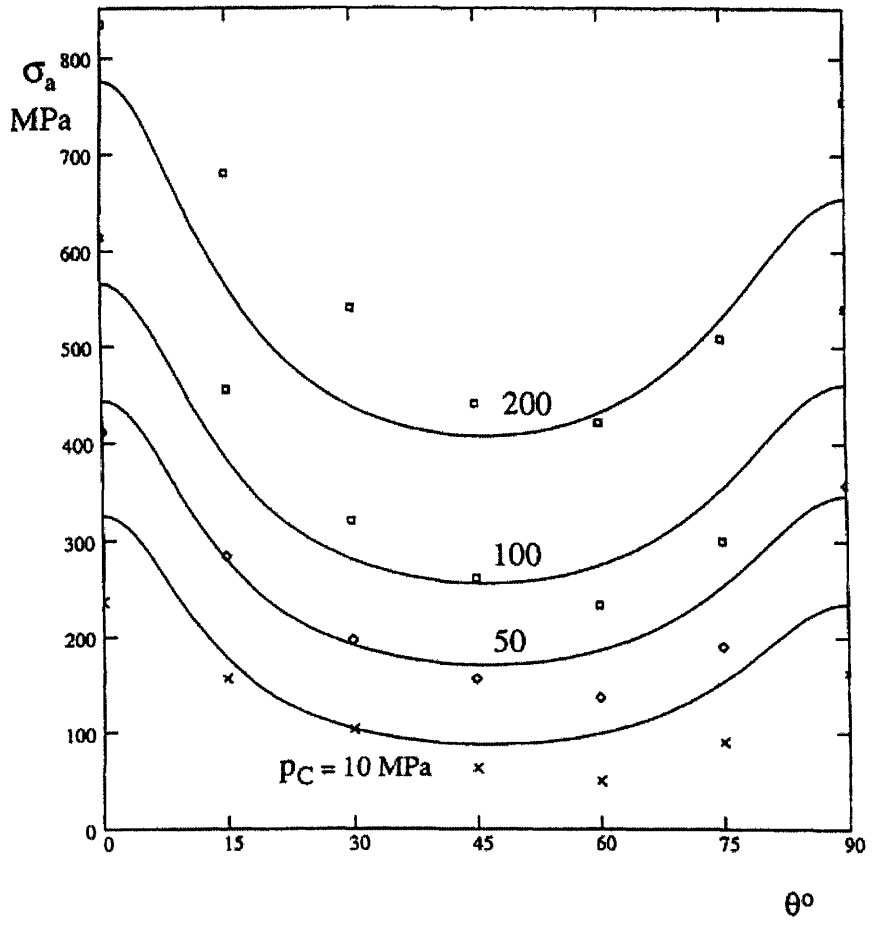

Figure 3.61 Application of the AMS Criterion on Martinsburg Slate (from Cazacu, 1999) Note: $\theta = \pi/2 - \beta$

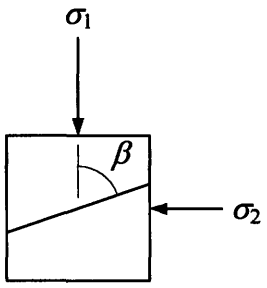

Figure 3.62 Isotropic Rock Body with One Set of Joints

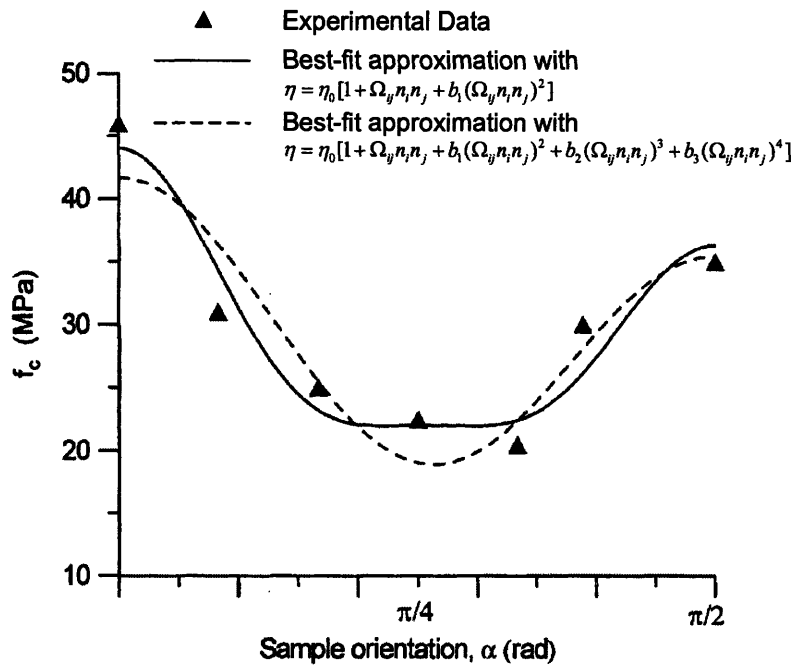

Figure 3.63 Fitting of Uniaxial Compression Strength of Tournemire Shale (modified from Pietruszczak et al., 2002)

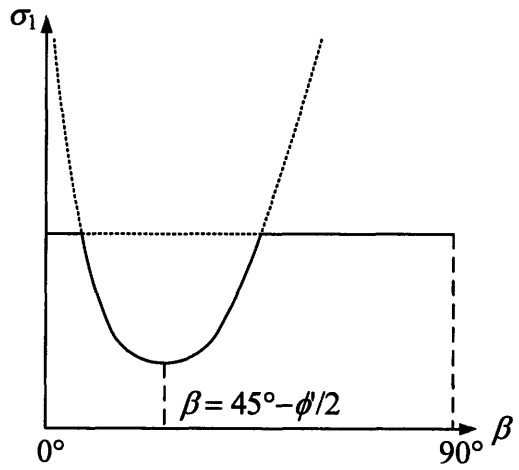

Figure 3.64 Failure Stress Predicted by Jaeger (1960)

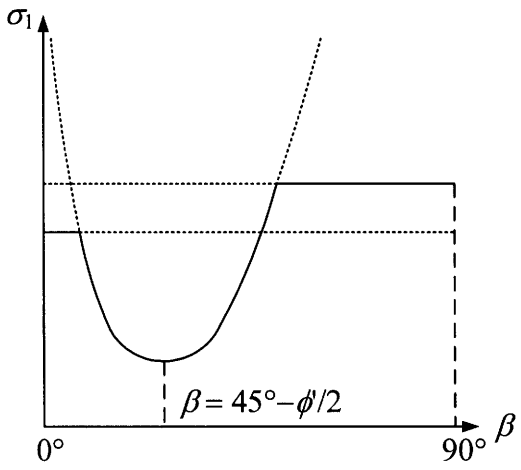

Figure 3.65 Failure Stress Predicted by Duveau and Shao (1998)

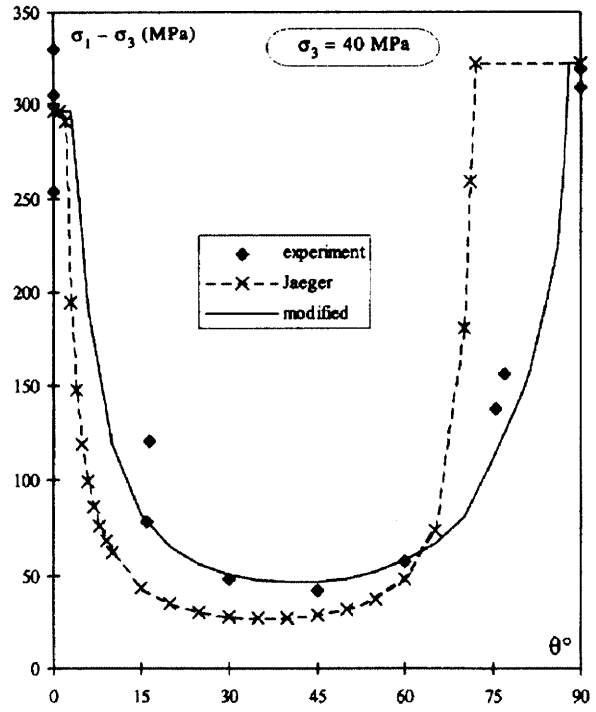

Figure 3.66 Comparison of the Experimental Data on Angers Schist and the Prediction of Duveau and Shao (1998)

4 A New Approach to Anisotropic Failure Criteria

The previous chapter has described laboratory measurements of the shear strength of anisotropic rocks, together with a series of failure criteria that have been proposed to characterize anisotropic shear strength. It has been shown that there are several different ways to generate anisotropic failure criteria. In terms of continuous functions, polynomials of order two (e.g. the AMS criterion) can describe "U" shaped curves that characterize the shear strength of transversely isotropic rocks in conventional triaxial tests. There are certain difficulties in formulating anisotropic failure criteria that use higher order polynomials. On the one hand, there are so many cubic terms of the stress components, as shown by Tsai and Wu (1971), that they become impractical. On the other hand, failure criteria of anisotropic rock are usually a function of all six stress components. Geometrically, they are surfaces in a six dimensional space, whose shapes cannot be directly imagined and understood. The shapes are even more complicated with higher order terms. In contrast, the failure surface of isotropic failure criteria can be directly observed in the principal stress space, which greatly facilitates the formulation of failure criteria. To the author's knowledge, polynomials of higher orders have not been applied to represent anisotropic rock strength.

In this chapter, a new approach for constructing anisotropic failure criteria is proposed. It makes the visualization of anisotropic failure criteria in a three dimensional space possible. Desirable features of anisotropic failure surfaces are identified geometrically. Mathematical expressions that can generate these features are identified by studying the geometry of existing criteria. Isotropic failure criteria can be extended to anisotropy by incorporating these expressions.

In order to visualize the failure surface in a three dimensional space, a *Material Normal Stress System* (MNSS) is proposed to describe the failure of both isotropic and anisotropic materials. As a new system to visualize the failure phenomena, the representation of failure for isotropic and anisotropic materials in MNSS is very different from that in the principal stress system. It will be shown first how this system can help to visualize the coupling between the structure orientation and the stress tensor. As the name implies, this system only captures the normal stresses. Each point in this space can represent numerous stress states, with different shear components. Hence, other conditions must be enforced to eliminate this ambiguity.

One way to do this is to assume that the orientation of the three principal stresses does not change with regard to the material coordinate system. This is exactly the case in the conventional

and true triaxial tests on anisotropic rock. With this assumption, stress paths of these tests can be drawn in the MNSS. Conventional triaxial tests will be examined in this context. The direction of the stress path changes with the orientation of the specimen, even for the same principal stress increment. It will also be shown that isotropic materials fail along a straight line which is located on a π-plane in the MNSS.

An alternate approach to eliminate ambiguity is to assume the same shear stresses for all points in this space. By doing this, failure surfaces become three dimensional surfaces in the MNSS, whose geometry varies with shear stress level. Isotropic failure criteria, including the Drucker-Prager and the Matsuoka-Nakai criteria, are then examined in the MNSS. The geometry of their failure surfaces in the MNSS is visualized, first with all zero shear stresses and then with non-zero shear stresses. The mathematical expressions of both failure criteria are then examined, and the effect of each term on the failure surface geometry is discussed. It is found that the two key ingredients in formulating a failure criterion in the MNSS are: the bounding failure surface with all zero shear stresses and the variation of its geometry with non-zero shear stresses. Combining the representation of stress path and the representation of failure surfaces, failure of the material can be predicted in the MNSS.

Based on the study of anisotropic rock failure in conventional triaxial tests, the desirable geometry features of an anisotropic failure surface are then proposed. The Matsuoka-Nakai failure criterion is extended to anisotropy, based on the study of failure surface geometry of isotropic failure criteria in the MNSS. Anisotropy is introduced in both its bounding failure surface, and the variation of its geometry with non-zero shear stresses. Correspondingly, two new parameters are introduced in the formulation. Each parameter controls a certain geometric feature of the anisotropic π-plane cross-section. A parametric study is then provided to illustrate the effect of these parameters on the conventional triaxial strength. Finally, the Anisotropic Matsuoka-Nakai criterion is applied to some of the data sets compiled in Section 3.1.

In the following discussion, two coordinate systems are frequently referred to, that are consistent with those used in Chapter 3. One is the material system **STN**, in which **S**, **T** and **N** are principal directions of anisotropy. In the case of transverse isotropy, **N** is taken as the normal to the isotropic planes, while **S** and **T** are two directions in the isotropic plane. In this system, the stress tensor generally has six independent components: σ_s, σ_t, σ_n σ_{tn}, σ_{ns}, σ_{st} (Figure 4.1 (a)). The other coordinate system $\mathbf{x_1x_2x_3}$ is set up based on principal directions of stress, so that σ_1 is in the $\mathbf{x_1}$ direction and so on. In this system, the stress tensor has only three components, which are the principal stresses σ_1, σ_2, σ_3. All shear stresses are zero.

4.1 Material Normal Stress System

For isotropic material, a strength criterion can usually be expressed as a function of stresses and

a few material parameters. Isotropic failure surfaces can usually be visualized in the three-dimensional principal stress space. Likewise, an anisotropic failure criterion is the function of the material stresses and material parameters. Since there are six components of the material stresses, it is impossible to visualize all of them in a three dimensional system. One way to solve this problem is to introduce the Material Normal Stress System, which is the stress space formed by only the material normal stresses $\sigma_s\sigma_t\sigma_n$ (Figure 4.1 (a)). The state of the material normal stresses can be described by a point (σ_s, σ_t, σ_n) in the MNSS.

Similar to the principal stress space, the hydrostatic line and the π-plane can be defined in the MNSS (Figure 4.1 (b)). Along the hydrostatic line, $\sigma_s = \sigma_t = \sigma_n$. The π-plane is a plane that is perpendicular to the hydrostatic line (i.e. plane ABC). Another plane that is useful for later discussion is the plane where $\sigma_s = \sigma_t$ (i.e. plane AOD). This plane is defined as the triaxial plane of the MNSS (compare with the triaxial plane with $\sigma_2 = \sigma_3$ in the principal stress system). In a triaxial test where **N** is in the axial direction of the triaxial cell ($\beta = 90°$), the stress state of the specimen is located on this plane since $\sigma_s = \sigma_t$ always holds in this test. This plane passes through both the σ_n axis and the hydrostatic line. Therefore, the projection of this plane on the π-plane is a straight line, which coincides with the projection of σ_n on the π-plane (Figure 4.1 (c)). The σ_s and σ_t axes are symmetric with regard to this plane.

A polar coordinate system (r ,θ ,Z) can be established, where the Z axis is the hydrostatic line and (r ,θ) are on the π-plane (Figure 4.1 (c)). Both Z and r can be expressed in terms of the material normal stresses.

$$Z = \frac{\sigma_s + \sigma_t + \sigma_n}{\sqrt{3}} = \frac{I_1}{\sqrt{3}} \tag{4.1}$$

Therefore, Z is associated with the first stress invariant and describes the average confining pressure in the material. r is the distance from a stress point (σ_s, σ_t, σ_n) to the hydrostatic line in the π-plane:

$$r = \sqrt{\frac{1}{3}\left[(\sigma_s - \sigma_t)^2 + (\sigma_t - \sigma_n)^2 + (\sigma_n - \sigma_s)^2\right]} = \sqrt{2J_{2n}} \tag{4.2}$$

where J_{2n} is the part of J_2 that can be represented by normal stresses only. It is worth noting that J_{2n} is not a stress invariant, although J_2 is. Correspondingly, J_{2s} will be used to represent the part of the J_2 related to the shear stresses only, which is expressed by:

$$J_{2s} = \sigma_{st}^2 + \sigma_{tn}^2 + \sigma_{ns}^2 \tag{4.3}$$

so that $J_2 = J_{2n} + J_{2s}$. θ is the angle between a radial direction and the projection of σ_n on the π-plane, which is expressed by:

$$\tan\theta = \frac{\sqrt{3}(\sigma_t - \sigma_s)}{2\sigma_n - \sigma_s - \sigma_t} \tag{4.4}$$

θ is also not a stress invariant. Finally, the normal stresses can be expressed as functions of (r, θ, Z):

$$\sigma_s = \frac{Z}{\sqrt{3}} - \frac{\sqrt{6}}{3} r \sin(\frac{\pi}{6} + \theta)$$
$$\sigma_t = \frac{Z}{\sqrt{3}} - \frac{\sqrt{6}}{3} r \sin(\frac{\pi}{6} - \theta) \qquad (4.5)$$
$$\sigma_n = \frac{Z}{\sqrt{3}} + \frac{\sqrt{6}}{3} r \cos\theta$$

The radial dimensions $r(\theta)$ will be denoted r_θ. The point at failure along this direction will be denoted R_θ, and called the *radius* of the π-plane cross-section in this direction. Similar to the principal stress space, stress paths along r_0, r_{60}, ... r_{300} (shown in Figure 4.1 (c)) represent conventional triaxial tests. However, in the MNSS, the isotropic plane orientation is also specified. For example, r_0, r_{120} and r_{240} represent the triaxial compression test with **N**, **T** and **S** being the axial direction, respectively. For a transversely isotropic material, $R_{120} = R_{240}$ due to material symmetry.

This system seems to be very similar to the principal stress space and its polar representation reported in Chapter 2. However, all the stresses in this space are material normal stresses instead of principal stresses. In the principal stress space, r and θ in the π-plane are both stress invariants. In this system, however, both of them are not stress invariants since only the normal stresses are considered.

4.2 Coupling of the Structure and Stress in MNSS

In the principal stress space, one point stands for a certain set of principal stresses, whose orientation with regard to the **STN** system is not explicitly specified. The material structure therefore cannot be considered in this space. In the MNSS, however, the same principal stresses correspond to different points depending on the material structure orientation. Figure 4.2 shows a general case where the principal directions of anisotropy **STN** do not coincide with the principal directions of stress $\mathbf{x_1x_2x_3}$. In the following discussion, the magnitude and the direction of the principal stresses are kept constant. For the time being, it is assumed that $\sigma_1 > \sigma_2 > \sigma_3$, all of which are compressive stresses.

The Mohr circles of this stress state are shown in Figure 4.3. When the **STN** system is rotated, the material normal stresses (σ_s, σ_t, σ_n) will be changed accordingly. Assuming that the vector **N** can be represented by $[N_1, N_2, N_3]$ in the $\mathbf{x_1x_2x_3}$ system, then σ_n can be calculated by:

$$\sigma_n = \mathbf{N} \cdot \boldsymbol{\sigma} \cdot \mathbf{N} = [N_1, N_2, N_3] \begin{bmatrix} \sigma_1 & 0 & 0 \\ 0 & \sigma_2 & 0 \\ 0 & 0 & \sigma_3 \end{bmatrix} \begin{bmatrix} N_1 \\ N_2 \\ N_3 \end{bmatrix} = \sigma_1 N_1^2 + \sigma_2 N_2^2 + \sigma_3 N_3^2 \qquad (4.6)$$

σ_s and σ_t can be similarly obtained. The stresses on the **ST** plane, **TN** plane and **NS** plane all fall

in the shaded area in Figure 4.3 (see, for example, Zoback, 2007). The following conclusions can be made regarding the material normal stresses:

- The magnitude of any one of the material normal stresses must be between σ_3 and σ_1. This conclusion is quite straightforward by examining the shaded area in Figure 4.3.
- The point (σ_s, σ_t, σ_n) always remains on the π-plane with $Z=(\sigma_1+\sigma_2+\sigma_3)/\sqrt{3}$ (shown by the dashed line triangle in Figure 4.4 (a)). This is because $\sigma_s+\sigma_t+\sigma_n = I_1$, which is the first invariant of the stress tensor.
- If the **N** direction is kept constant, the rotation of the **ST** directions causes the point (σ_s, σ_t, σ_n) to travel along a straight line, which has the equation $\sigma_s+\sigma_t$ = constant. If the **N** direction is constant, then $\sigma_n = \sigma_1 N_1^2+\sigma_2 N_2^2+\sigma_3 N_3^2$ must also be constant. Therefore, $\sigma_s+\sigma_t = (\sigma_1+\sigma_2+\sigma_3)-\sigma_n$ is a constant. Geometrically, this line is parallel to the (σ_s, σ_t) plane, and forms a 45° angle with regard to both σ_s and σ_t axes (for example, line MN in Figure 4.4 (a) and (b)). This conclusion also holds if **T** or **S** is held constant, and the other two directions are rotated.

With these conclusions, it is then easy to understand that the material normal stress point (σ_s, σ_t, σ_n) remains in a hexagon in the π-plane, $Z=(\sigma_1+\sigma_2+\sigma_3)/\sqrt{3}$, for any orientation of the **STN** system with regard to the $\mathbf{x_1x_2x_3}$ system. Figure 4.4 illustrates this statement. Figure 4.4 (a) shows a three dimensional view of this hexagon. Figure 4.4 (b) shows its projection onto the (σ_s, σ_t) plane. Figure 4.4 (c) shows the plan view of this hexagon, and how the rotation of **STN** system determines the location of (σ_s, σ_t, σ_n). As an example, assume that initially $\sigma_s = \sigma_2$, $\sigma_t = \sigma_3$, and $\sigma_n = \sigma_1$. The stress point (σ_s, σ_t, σ_n) is at point A shown in Figure 4.4. If **N** is kept constant and **ST** are rotated, the point (σ_s, σ_t, σ_n) follows line AB until it reaches point B, where $\sigma_s = \sigma_3$, $\sigma_t = \sigma_2$, and $\sigma_n = \sigma_1$. Based on the previous analysis, line AB is parallel to the (σ_s, σ_t) plane and forms a 45° angle to both σ_s and σ_t axes. At this point, if **S** is kept constant (currently in the $\mathbf{x_3}$ direction) and **TN** are rotated, point (σ_s, σ_t, σ_n) marches from point B to point D. Line BD is parallel to the (σ_t, σ_n) plane and forms a 45° angle to both σ_t and σ_n axes. When (σ_s, σ_t, σ_n) reaches point N, if direction **N** is again kept constant and **ST** are rotated, then point (σ_s, σ_t, σ_n) follows the line MN. Line MN is parallel to line AB, but is inside the hexagon. By observation, it can be concluded that:

- At the vertices of this hexagon, the principal directions of anisotropy **STN** coincide with the principal directions of stress $\mathbf{x_1x_2x_3}$.
- Along the sides of this hexagon, only one of the principal directions of anisotropy coincides with one of the principal directions of stress.
- Within this hexagon, none of the principal directions of anisotropy coincides with the principal directions of stress.

To summarize, one particular principal stress state (σ_1, σ_2, σ_3) corresponds to a hexagonal locus in the MNSS. This hexagonal locus is defined in the π-plane with $Z=(\sigma_1+\sigma_2+\sigma_3)/\sqrt{3}$. The location of the corresponding point (σ_s, σ_t, σ_n) in this hexagon depends on the relative orientation of the principal directions of anisotropy to the principal directions of stress. Compared with the principal stress space, where (σ_1, σ_2, σ_3) is only represented with one point, the MNSS describes the coupling between the material structure and the stress.

4.3 Conventional Triaxial Tests in the MNSS

The conventional triaxial compression test is the most common laboratory test on anisotropic rocks, as shown in the previous chapter. In the special case of a conventional triaxial stress state, $\sigma_1 \geq \sigma_2 = \sigma_3$. From Figure 4.4 (b), it can be seen that point A and B must coincide and the length of line AB reduces to zero. In fact, the hexagon is reduced to a right triangle. Figure 4.5 shows the three dimensional view and the projection of the triangle onto the (σ_s, σ_t) plane. In the case where all three principal stresses are equal, there must be $\sigma_s=\sigma_t=\sigma_n$, the triangle is further reduced to a point on the hydrostatic line. A cylindrical specimen is usually used in these tests. In a very general configuration, none of the principal directions of anisotropy coincides with any of the principal stress directions (Figure 4.6 (a)).

During the test, the principal directions of both anisotropy and stress are unchanged. In a typical conventional triaxial compression test, the specimen is first loaded isotropically to a certain confining pressure σ_3. In this process, there must always be $\sigma_s=\sigma_t=\sigma_n$, so that the stress path follows the hydrostatic line in the MNSS. Then σ_1, the axial stress, is either increased or decreased to shear the specimen to failure, so that $\Delta\sigma_1 \neq 0$, and $\Delta\sigma_3 = 0$ for any load increment. The increment of the material normal stresses can be calculated by:

$$\Delta\sigma_s = \Delta\sigma_1 S_1^2; \Delta\sigma_t = \Delta\sigma_1 T_1^2; \Delta\sigma_n = \Delta\sigma_1 N_1^2 \tag{4.7}$$

in which the components of **S**, **T** and **N** are represented in the principal stress system $\mathbf{x_1x_2x_3}$. Obviously, $\Delta\sigma_s:\Delta\sigma_t:\Delta\sigma_n = S_1^2: T_1^2: N_1^2$ and the stress path must follow a straight line in the MNSS. This stress path in a conventional triaxial compression test is shown in Figure 4.7 (a). The segment OP_0 represents the isotropic loading. Shearing starts from point P_0 and proceeds to point P_1 at time t_1, P_2 at time t_2, etc. The representation of the stress state changes from the point P_0, to the smaller triangle $A_1B_1C_1$ at time t_1, then to the larger triangle $A_2B_2C_2$ at time t_2. As discussed before, each of these triangles is in a π-plane with $Z=(\sigma_1(t)+2\sigma_3)/\sqrt{3}$.

The locations of the stress points P_i at time t_i in the corresponding triangles are specified by the orientation of **STN** system relative to the $\mathbf{x_1x_2x_3}$ system. In the previous chapters, the orientation

of isotropic plane is described by the angle β between the isotropic planes and the axial direction. This simple representation is possible because the **S** direction and the $\mathbf{x}_2$ direction are assumed to always coincide (Figure 4.6 (b)). In this case, the stress point $\mathbf{P}_i$ always falls on the side $\mathbf{A}_i\mathbf{B}_i$ of the stress triangles in Figure 4.7 (b). The relationship between the material normal stresses and the principal stresses are:

$$\begin{aligned} \sigma_s &= \sigma_3 \\ \sigma_t &= \sigma_3 \sin^2\beta + \sigma_1 \cos^2\beta \\ \sigma_n &= \sigma_3 \cos^2\beta + \sigma_1 \sin^2\beta \end{aligned} \tag{4.8}$$

With a load increment $\Delta\sigma_1$, there must be:

$$\Delta\sigma_s = 0; \Delta\sigma_t = \Delta\sigma_1 \cos^2\beta; \Delta\sigma_s = \Delta\sigma_1 \sin^2\beta \tag{4.9}$$

Geometrically, the stress paths follow straight lines which are parallel to the (σ_t, σ_n) plane, with the slope $\Delta\sigma_n/\Delta\sigma_t = \sin^2\beta / \cos^2\beta$. Since all the stress paths start from the point $\mathbf{P}_0$, they are located in one plane (plane $\mathbf{P}_0\mathbf{A}_i\mathbf{B}_i$ in Figure 4.7 (b)), whose equation is $\sigma_s = \sigma_3$. This is actually the plane traversed by line $\mathbf{A}_i\mathbf{B}_i$ along the growth of the stress triangle. The stress paths of $\beta = 0°$ to 90° with 15° interval are shown in Figure 4.7 (b). The projections of these stress paths on the π-plane are shown in Figure 4.7 (c). In the π-plane, the distance of a stress point to the origin is determined by J_{2n}, according to Equation (4.2). The growing length of the stress paths, therefore, can be physically identified with the increasing material distortion due to normal material stresses.

The preceding analysis does not involve any material property. Therefore, it applies to both isotropic and anisotropic materials. A material coordinate system can also be established for an isotropic material. For example, **N** can be taken as the vertical direction when the specimen was in the ground, while **S** and **T** are in horizontal directions. Specimens can be cut so that the axial direction is different from the in-situ vertical direction. Because the failure of isotropic specimens does not depend on orientation, all specimens fail at the same σ_{1f} given the same confining pressure σ_3. As a result, the stress paths at any β must end at the same stress triangle, in the π-plane with $Z = (\sigma_{1f} + 2\sigma_3)/\sqrt{3}$. Geometrically, the failure of an isotropic specimen in a conventional triaxial test with specific confining pressure σ_3 can be represented by a straight line, which is the side **AB** of the failure stress triangle. This line will be called the *Isotropic Failure Line.*

If the material under discussion is an anisotropic material, its behavior in the conventional triaxial compression test can be similarly described. It has been shown that the conventional triaxial strength variation with β for anisotropic rocks can be described by "U" shaped curves with unequal ends (Figure 4.8). Two local maxima are reached at $\beta = 0°$ and $\beta = 90°$. In this case, an imaginary isotropic material can be defined, whose strength is independent of β, and is the same as the anisotropic strength at β = 90° (the horizontal line in Figure 4.8). It has just been

shown that the imaginary isotropic material fails along the side AB of the failure stress triangle (shown in Figure 4.9 (a)), whose location Z is determined by the strength at $\beta = 90°$. At a specific β, the anisotropic material follows the same stress path as the imaginary isotropic material, but fails before or after the stress path reaches line AB, depending on whether the anisotropic strength is smaller or larger than the imaginary isotropic strength. Therefore, the "U" shaped line shown in Figure 4.8 maps into the MNSS to form the curved locus shown in Figure 4.9. This curve will be termed the *Anisotropic Failure Curve*. Since all stress paths are in the same plane $\sigma_s = \sigma_3$, the anisotropic failure curve must also be in the plane P_0AB.

Since the MNSS only captures the normal stress components, it does not have enough information to fully describe the stress state at one point. Each point (σ_s, σ_t, σ_n) in this space can represent numerous stress states, depending on how shear stresses are determined. In the previous discussion about the triaxial tests, shear stresses are implicitly specified. The magnitude and the directions of the principal stresses are known, together with the principal directions of anisotropy. In this case, the normal and shear stresses in the material coordinate system can be uniquely determined. While plotting the stress paths, only the normal stress components are considered. The material shear stresses can be expressed by:

$$\sigma_{st} = 0; \sigma_{tn} = \frac{\sigma_1 - \sigma_3}{2} \sin 2\beta; \sigma_{ns} = 0 \tag{4.10}$$

Obviously, σ_{tn} increases linearly with σ_1, under a specific confining pressure σ_3 and isotropic plane orientation β. At each point along a stress path, therefore, the shear stresses are different. In the following sections, in which the failure criteria are discussed, shear stresses will be explicitly specified, so that they are the same for any point (σ_s, σ_t, σ_n).

4.4 Drucker-Prager Criterion in the MNSS

In order to predict the failure of anisotropic materials in the MNSS, it is necessary to study how to represent failure criteria in the MNSS. A relatively simple isotropic model, the Drucker-Prager criterion, will be studied first. As discussed previously, a material coordinate system **STN** is set up on an isotropic material that obeys the Drucker-Prager criterion.

The Drucker-Prager criterion can be written in invariant form as:

$$\sqrt{2J_2} = kI_1 + c \tag{4.11}$$

where c stands for the cohesion when the material is sheared with zero octahedral stress, while k specifies the pressure dependence. By squaring both sides of Equation (4.11), dividing the invariant J_2 into components J_{2n} and J_{2s}, and using Equations (4.1) and (4.2), the polar representation of Drucker-Prager criterion in the MNSS is obtained:

$$R^2 = \left(\sqrt{3}kZ + c\right)^2 - 2\left(\sigma_{st}^2 + \sigma_{tn}^2 + \sigma_{ns}^2\right) \tag{4.12}$$

R and Z are expressions of σ_s, σ_t, σ_n, the normal stresses in the **STN** system. σ_{st}, σ_{tn}, σ_{ns} are the shear stresses in the **STN** system.

In the first case, zero shear stresses are specified, such that $\sigma_{st} = \sigma_{tn} = \sigma_{ns} = 0$. This condition is explicitly imposed on all points in the MNSS. In this case, Equation (4.12) reduces to:

$$R_B = \sqrt{3}kZ + c \tag{4.13}$$

This failure surface is termed the *bounding failure surface*, because it is the largest failure surface that the Drucker-Prager criterion describes in the MNSS. Accordingly, R_B is used to represent its radius on the π-plane. Equation (4.13) represent a cone in the MNSS (Figure 4.10 (a)), whose radius varies linearly with pressure level (i.e. it describes a linear pressure dependence) and whose π-plane cross-section is a circle. The geometry of Drucker-Prager failure surface in the MNSS is the same as it is in the principal stress space. This is because the normal material stresses are the principal stresses when shear stresses are all zero. Physically, this corresponds to true triaxial tests where the principal stresses are applied in the principal directions of anisotropy (i.e. **S**, **T**, and **N**).

When any of the shear stresses are not zero, it can be directly obtained from Equation (4.12) that:

$$R = \sqrt{(\sqrt{3}kZ + c)^2 - 2(\sigma_{st}^2 + \sigma_{tn}^2 + \sigma_{ns}^2)} \tag{4.14}$$

Since R also does not depend on θ, the π-plane cross-section is still circular. However, R is always smaller than R_B at the same Z level (Figure 4.10 (b)). As the magnitude of shear stresses increases, the ratio R/R_B reduces. The variation of R with Z is obtained by taking the derivative of Equation (4.14) to Z:

$$\frac{dR}{dZ} = \frac{\sqrt{3}k}{\sqrt{1 - \dfrac{2(\sigma_{st}^2 + \sigma_{tn}^2 + \sigma_{ns}^2)}{(\sqrt{3}kZ + c)^2}}} \tag{4.15}$$

Clearly, dR/dZ is always larger than dR_B/dZ, which is a constant $\sqrt{3}k$. At a given level of Z, the difference is larger for larger shear stresses. At constant shear stresses, the difference is larger for smaller Z values. When Z approaches infinity, dR/dZ approaches $\sqrt{3}k$. The failure surface of Drucker-Prager criterion with non-zero shear stress is shown in Figure 4.10 (b). Since dR/dZ depends on Z, this relationship describes a nonlinear pressure dependence. Note that the r in the MNSS system is defined as $\sqrt{2J_{2n}}$, which is different from its definition $\sqrt{2J_2}$ in the principal stress system. As shown in Equation (4.11), $\sqrt{2J_2}$ obviously depends linearly on I_1. Therefore, the Drucker-Prager criterion describes a linear pressure dependence in the principal stress system, while there is a non-linear pressure dependence in the MNSS system.

Since this criterion is an isotropic criterion, it must predict that the material fails at the same σ_{1f},

regardless of the orientation β. In fact, if Equations (4.8) and (4.10) are substituted into Equation (4.12), the terms with β will cancel out. The predicted σ_{1f} values are:

$$\sigma_{1f} = \frac{(2+6k^2) \pm 3\sqrt{6}k}{2-3k^2}\sigma_3 \tag{4.16}$$

at confining pressure σ_3. They are, indeed, independent to β:

To summarize, the representation of the Drucker-Prager criterion in the MNSS is composed of two parts: 1) a bounding failure surface with radius R_B (Equation (4.13)), and 2) the variation of its size with shear stress magnitude. The bounding failure surface is reached for all zero shear stresses ($\sigma_{st} = \sigma_{tn} = \sigma_{ns} = 0$). As such, it is entirely a function of material normal stresses. This is the largest failure surface in the MNSS for the Drucker-Prager criterion. The shape of the bounding failure surface is the same as its shape in the principal stress space. Physically, the bounding failure surface describes the failure of specimens in true triaxial tests, where the principal stresses are applied in the principal directions of anisotropy **S**, **T** and **N**. The size reduction is controlled by the magnitude of the shear stresses. For isotropic models, they must be such that the failure surface always meets the stress paths along the side AB of the failure stress triangle, as shown in Figure 4.7.

The concept of stress paths and of failure surfaces can be combined to predict material failure. Figure 4.11 (a) and (b) show the conventional triaxial compression tests on specimens with β = 90° and 0°, respectively. As shown in Figure 4.7, the stress paths of these two shear modes are in the OA and OB directions. Because $\sigma_{st} = \sigma_{tn} = \sigma_{ns} = 0$ always holds in these tests, the bounding failure surface always applies. Therefore, failure occurs at point A and point B, respectively, for these two shear modes. For 0° < β <90°, as shown in Figure 4.11 (c), the stress path OM is between OA and OB, depending on the value of β, as shown in Figure 4.7. However, in this scenario shear stress σ_{tn} is not zero, and it increases with σ_1 (Equation (4.10)). The failure surface then shrinks with increasing shear stress σ_{tn}, until it finally meets the stress path at point M. Point M is the point where failure occurs, and it is located on line AB.

Clearly, the normal and shear stresses play separate roles in the MNSS. In a conventional triaxial test, each loading step drives the stress path farther away from the hydrostatic line. The radius of the current stress point on the π-plane is determined by Equation (4.2), which is solely a function of material normal stresses. At the same time, shear stresses also increase (in a general scenario like Figure 4.11 (c)) according to Equation (4.10). With this increase of shear stress, the failure surface shrinks. At one point, the stress path meets the failure surface and failure occurs. The normal stresses therefore control the stress path, and the shear stresses control the variation of failure surface size.

4.5 Matsuoka-Nakai Criterion in the MNSS

In Chapter 2, it was concluded that the π-plane cross-section described by the LMN dependence, combined with a pressure dependence function $R_0(Z)$, captures the failure behavior of isotropic rock in a polyaxial stress state. The LMN dependence describes a group of curved right triangles whose shapes are entirely defined by one shape factor β_s. Both the Lade criterion and the Matsuoka-Nakai criterion have this type of π-plane cross-section. In this section, the Matsuoka-Nakai criterion will be analyzed in the MNSS system. This criterion will be developed into an anisotropic criterion, based on the results of this section.

The Matsuoka-Nakai criterion is expressed in the invariant form as:

$$I_2 I_1 - kI_3 = 0 \tag{4.17}$$

The invariants in this equation can be expressed as functions of the material stresses: σ_s, σ_t, σ_n, σ_{st}, σ_{tn}, σ_{ns}. The three normal stresses can in turn be expressed by R, θ and Z with Equation (4.5). After regrouping the terms, the Matsuoka-Nakai criterion can finally be expressed by R, θ, Z and the material stresses:

$$-\frac{1}{3\sqrt{6}}R^3\cos 3\theta + \frac{1-3k}{2\sqrt{3}}R^2 Z = \frac{1-9k}{3\sqrt{3}}Z^3 - \frac{1-3k}{\sqrt{3}}(\sigma_{st}^2+\sigma_{tn}^2+\sigma_{ns}^2)Z - \frac{2}{\sqrt{6}}(\sigma_{st}^2 r_n + \sigma_{tn}^2 r_s + \sigma_{ns}^2 r_t) + 2\sigma_{st}\sigma_{tn}\sigma_{ns} \tag{4.18}$$

in which r_n, r_s and r_t are defined as:

$$r_n = \frac{1}{\sqrt{6}}(2\sigma_n - \sigma_s - \sigma_t); r_t = \frac{1}{\sqrt{6}}(2\sigma_t - \sigma_n - \sigma_s); r_s = \frac{1}{\sqrt{6}}(2\sigma_s - \sigma_t - \sigma_n) \tag{4.19}$$

Clearly, these quantities are associated with the stress deviator. Geometrically, these quantities are determined by the location of a stress point (σ_s, σ_t, σ_n) on the π-plane. Defining the r_n, r_s and r_t axes to be the projection of the σ_n, σ_s, and σ_t axes on the π-plane respectively, as shown in Figure 4.13, these quantities can be obtained by projecting the stress point onto the three axes (r_n, r_s and r_t) on the π-plane.

When all shear stresses are zero, Equation (4.18) is simplified to:

$$-\frac{1}{3\sqrt{6}}R^3\cos 3\theta + \frac{1-3k}{2\sqrt{3}}R^2 Z = \frac{1-9k}{3\sqrt{3}}Z^3 \tag{4.20}$$

The three dimensional representation of the failure surface is shown in Figure 4.14 (a). It is the same as the failure surface of the Matsuoka-Nakai criterion in the principal stress space. The geometry of this surface was described in previous chapters. A few important aspects will be restated here. Equation (4.20) describes a conic shape failure surface. This failure surface specifies a linear pressure dependence, with:

$$R_0 = \frac{3\sqrt{1-10k+9k^2}+(1-9k)}{\sqrt{2}}Z; R_{180} = \frac{3\sqrt{1-10k+9k^2}-(1-9k)}{\sqrt{2}}Z \tag{4.21}$$

The triaxial plane cross-section of this failure surface is shown in Figure 4.14 (c), where both

$R_0(Z)$ and $R_{180}(Z)$ are straight lines. Its π-plane cross-section is shown in Figure 4.14 (b), which is a curved right triangle described by the LMN dependence. The size of the curved right triangle at a certain octahedral stress level can be determined by (R_0+R_{180}). The shape of the triangle is determined by:

$$\beta_s = R_{180} / R_0 = \frac{3\sqrt{1-10k+9k^2}-(1-9k)}{3\sqrt{1-10k+9k^2}-(1-9k)} \tag{4.22}$$

It is also important to note that this criterion is a one-parameter criterion. The only parameter k defines the shape of the π-plane cross-section and the linear pressure dependence of the triaxial plane cross-section. k is associated with friction angle of a material by:

$$k = \frac{1}{9}\left(1-\frac{8\sin^2\phi}{9-\sin^2\phi}\right) \tag{4.23}$$

This is because the Matsuoka-Nakai failure surface matches the Mohr-Coulomb criterion in conventional triaxial compression and extension tests.

When any of the shear stresses are not zero, Equation (4.18) specifies the size and shape of the failure surface. Due to the complexity of this expression, a numerical example is shown here to illustrate how the size and shape of the surface vary with shear stresses. It will be assumed that the friction angle of the material is $\phi = 30°$, so that $k = 0.0857$. In order to further simplify the problem, it is assumed that only one of the shear stresses σ_{tn} is non-zero. The failure surface at σ_{tn} = 0, 0.1, 0.2, 0.3 are shown in Figure 4.15. Clearly, the failure surface shrinks as the shear stress increases. It is important to note that the size reduction of the failure surface is different in different directions. With non-zero σ_{tn}, the size reduction is the largest for R_{240}, while it is the smallest for R_{60}. Due to this direction dependent size reduction, the shape of the failure surface distorts during its size reduction.

This distortion can be physically explained through a simple thought experiment. Since the Matsuoka-Nakai failure criterion matches the Mohr-Coulomb criterion in conventional triaxial states, the strength R_{240} and R_{60} can also be determined by Mohr-Coulomb criterion with the same friction angle and zero cohesion. As shown in Figure 4.14 (b), R_{240} represents the strength of a conventional triaxial compression test, with **S** being the axial direction; while R_{60} represents the strength of a conventional triaxial extension test, with **S** being the axial direction. Figure 4.16 shows a specimen with friction angle $\phi = 30°$ and zero cohesion. A conventional triaxial test is first performed with **S** being the axial direction. The confining pressures are assumed to be $\sigma_t = \sigma_n$ = 10MPa. With the Mohr-Coulomb criterion, one obtains σ_s at failure to be 30MPa in triaxial compression and 3.3MPa in triaxial extension, as shown by the solid Mohr circles in Figure 4.16. Now the shear stress σ_{st} is increased to 2MPa. The principal stresses in the **TN** plane are 8MPa and 12MPa, based on the dotted Mohr Circle. If σ_s is again changed to bring the specimen to failure, the dashed Mohr circles apply and the specimen fails at 24MPa in compression and 4MPa in extension. Comparing with the strengths at σ_{tn} = 0, the conventional triaxial

compression strength is reduced by 6MPa, while the extension strength is increased by 0.7MPa only. This explains why the failure surface shrinks significantly in the R_{240} direction but only slightly in the R_{60} direction at non-zero σ_{tn} (Figure 4.15). Clearly, the distortion of failure surface with non-zero shear stress is a necessary consequence of the frictional nature of the material.

It is worth examining Equation (4.18), to see how the non-uniform size reduction is generated mathematically. The size and shape of the failure surface depend on the right hand side of Equation (4.18). At all zero shear stresses, the right hand side is $\frac{1-9k}{3\sqrt{3}}Z^3$. Non-zero shear stresses changes the size and shape of the failure surface by modifying this term. The term $-\frac{1-3k}{\sqrt{3}}(\sigma_{st}^2+\sigma_{tn}^2+\sigma_{ns}^2)Z$ in (4.18) is always negative, and it does not depend on θ. Geometrically, it reduces the size of the bounding failure surface, but the reduced surface still possesses six-fold symmetry. As shown in Figure 4.17, this term reduces the bounding failure surface from the solid line to the dashed line. The term $-\frac{2}{\sqrt{6}}\sigma_{tn}^2 r_s$, on the other hand, can be positive or negative. To the left of the $r_s = 0$ line, this term is negative and it causes the size of the failure surface to reduce. To the right of this line, this term is positive and the size of the failure surface increases. This term is 0 on the line $r_s = 0$, therefore the reduced surface (dashed surface in Figure 4.17) and the distorted surface (smaller solid surface in Figure 4.17) intersect. Since this term depends linearly on r_s, it is called a *linear shape distortion*. When there are more than one non-zero shear stresses, the shape distortion is described by $-\frac{2}{\sqrt{6}}(\sigma_{st}^2 r_n+\sigma_{tn}^2 r_s+\sigma_{ns}^2 r_t)$, which simply adds up the contribution of different shear stresses.

The Matsuoka-Nakai criterion has a more complicated failure geometry than Drucker-Prager. However, both have similar representations in the MNSS system. The only difference is that non-zero shear stresses control not only the size reduction, but also the shape distortion of the Matsuoka-Nakai failure surface.

4.6 An Anisotropic Matsuoka-Nakai Criterion for Transversely Isotropic Rocks

4.6.1 General Considerations

Based on the preceding discussion of the Drucker-Prager criterion and the Matsuoka-Nakai criterion in the MNSS, it can be concluded that the representation of a failure criterion in the MNSS has two essential components: the bounding failure surface, which is entirely a function of material normal stresses, and how its size and shape vary with non-zero shear stresses. Earlier

in this chapter, it has been observed that "U" shaped curves with unequal end points are obtained when the strengths of transversely isotropic rocks are plotted against isotropic plane orientation β. In order to describe the failure behavior of anisotropic rocks, therefore, these observations must be incorporated in an anisotropic failure criterion.

Bounding Failure Surface for Anisotropic Material

The bounding failure surface describes failure under true triaxial stresses, where the principal stresses are in the principal material directions (i.e. directions **S**, **T** and **N**). Conventional triaxial tests with $\beta = 0°$ and 90°, as shown in Figure 4.11 (a) and (b), are two special cases. They correspond to the two shoulders of the "U" shaped curves.

The bounding failure surface is conceptually illustrated in Figure 4.18 (a). The conventional triaxial strength of the rock specimens with $\beta = 90°$ and $\beta = 0°$ but at various confining pressure can be described by the functions $R_0(Z)$ and $R_{120}(Z)$, respectively. Geometrically, they can be represented by the intersections of the bounding failure surface with plane (r_0, Z) and (r_{120}, Z), as shown in Figure 4.18 (a). Figure 4.18 (b) shows the planes (r_0, Z) and (r_{120}, Z) overlapped. σ_n is in the (r_0, Z) plane, and its orientation with regard to the Z axis can be described by Θ:

$$\Theta = \arctan\sqrt{2} \approx 54.74° \tag{4.24}$$

σ_t is in the (r_{120}, Z) plane, but with the same orientation. Therefore, σ_n and σ_t coincide in the overlapped view. If a conventional triaxial test is performed with $\beta = 90°$, the stress path should be parallel to σ_n direction. The length of the stress path at failure is $(\sigma^n_{1f} - \sigma_3)$, where σ_3 is the confining pressure and σ^n_{1f} is the axial stress at failure. The same statements are also true for a conventional triaxial test performed with $\beta = 0°$. When overlapped, a stress path in the (r_{120}, Z) plane must be parallel to one that is in the (r_0, Z) plane. If a conventional triaxial test with $\beta = 90°$ and one with $\beta = 0°$ are performed at the same confining pressure, then their stress paths start from the same point along the Z axis (point **O′** in Figure 4.18). Since these two tests have different strengths, their lengths to failure must be different and they must end at different points on the overlapped plane (shown in Figure 4.18 as point **A** for $\beta = 90°$ and point **B** for $\beta = 0°$). This means that the functions $R_0(Z)$ and $R_{120}(Z)$ must be different. Consequently, the π-plane cross-section of the bounding failure surface for an anisotropic material can have a different radius in $\theta = 0°$ and $\theta = 120°$, and will lose the six-fold symmetry that is characteristic of isotropic failure surfaces.

Variation of Bounding Failure Surface Geometry for Anisotropic Material

The representation of failure for isotropic and anisotropic materials has been discussed earlier. It is concluded that the failure of isotropic materials must always be along one side of the failure stress triangle, as shown in Figure 4.7. The failure of an anisotropic material can be represented by a "U" shaped curve in the MNSS, as shown in Figure 4.9.

The failure of an anisotropic material and the corresponding imaginary isotropic material are plotted in Figure 4.19, where the imaginary isotropic material has a constant strength that matches the anisotropy material strength at point A, which corresponds to the failure of a specimen with $\beta = 90°$, as shown in Figure 4.11 (a). Failure of the anisotropic material is represented by a solid curve AND, and that of the imaginary isotropic material by a dashed line AB. Suppose there is an isotropic failure criterion that can predict the strength of the imaginary isotropic material, the geometry variation of its failure surface with non-zero shear stress must be such that it always meets the stress paths along line AB, as illustrated by point M in Figure 4.19. If an anisotropic criterion is to be built based on this isotropic criterion, the geometry variation must be modified so that the failure surface meets the same stress path along the anisotropic failure curve, in this case point N along curve AND.

Based on the above discussions, two modifications must be made to extend the Matsuoka-Nakai criterion to anisotropy:

- Its bounding failure surface must be modified to eliminate the six-fold symmetry.
- The variation of its bounding failure surface geometry with non-zero shear stresses must be modified so that it meets the stress paths along the anisotropic failure curve in the MNSS.

Before extending the Matsuoka-Nakai criterion to anisotropy, its pressure dependence and Lode angle dependence will first be separated. With this separation, the π-plane cross-section can be manipulated without worrying about the triaxial plane cross-section. Equation (4.18) is first normalized by R_0 in Equation (4.21), and then the parameter k is substituted by β_s according to Equation (4.22). The normalized form of the Matsuoka-Nakai criterion is:

$$\begin{aligned}-(1-\beta_s)R'^3\cos 3\theta+\left(1-\beta_s+\beta_s^2\right)R'^2 &= \beta_s^2-2(1-\beta_s+\beta_s^2)(\sigma_{st}'^2+\sigma_{tn}'^2+\sigma_{ns}'^2)\\ &\quad -6(1-\beta_s)(\sigma_{st}'^2 r_n'+\sigma_{tn}'^2 r_s'+\sigma_{ns}'^2 r_t')+6\sqrt{6}(1-\beta_s)\sigma_{st}'\sigma_{tn}'\sigma_{ns}'\end{aligned} \tag{4.25}$$

If the pressure dependence is described by a non-linear function $R_0(Z)$, then the normalized quantities are simply defined by $R' = R/R_0(Z)$, etc. When all shear stresses are zero, this equation is identical to the LMN dependence. It defines π-plane cross-sections that have curved triangular shape, with $R'_0 = R'_{120} = R'_{240} = 1.0$ and $R'_{60} = R'_{180} = R'_{300} = \beta_s$ (refer to Figure 2.23).

4.6.2 Extension of the Bounding Failure Surface

For anisotropic rocks, two pressure dependence functions $R_0(Z)$ and $R_{120}(Z)$ can be different. As shown previously, $R_0(Z)$ describes the conventional triaxial compression strength where N is the axial direction, which corresponds to $\beta = 90°$. $R_{120}(Z)$ describes conventional triaxial compression strength where T is the axial direction, which corresponds to $\beta = 0°$. A detailed example has been shown in Chapter 2 on how to obtain $R_0(Z)$ based on the conventional triaxial compression tests. The same technique can be used to obtain $R_0(Z)$ and $R_{120}(Z)$ for anisotropic

rocks, based on conventional triaxial compression tests performed with $\beta = 90°$ and $\beta = 0°$, respectively. The difference of these two strengths at the same Z level can be described by the ratio $R_{120}(Z)/R_0(Z)$. This ratio will be used to specify the shape of the π-plane cross-section of the anisotropic Matsuoka-Nakai criterion.

Normalized values of $R_{120}(Z)$ and $R_0(Z)$ will be used in the following discussion, because $R'_{120}(Z)/R'_0(Z) = R_{120}(Z)/R_0(Z)$. When the ratio $R'_{120}(Z)/R'_0(Z)$ is different from 1, the shape of the π-plane cross-section must be distorted accordingly. In the isotropic Matsuoka-Nakai criterion, shape distortion is controlled by the linear term $-\frac{2}{\sqrt{6}}(\sigma_{st}^2 r_n + \sigma_{tn}^2 r_s + \sigma_{ns}^2 r_t)$. The mechanism of this linear shape distortion is shown in Figure 4.17. It turns out that the linear shape distortion can be used to provide the desired features. Due to material symmetry for a transversely isotropic material, the distorted π-plane cross-section must be symmetric with regard to the projection of σ_n axis on the π-plane, which is the r_n axis (refer to Figure 4.13). Therefore, only the linear term of r_n can be included. Based on the same mechanism, a generalized linear form of r_n is proposed in its normalized form, which reads:

$$A(Z)\beta_s^2(r'_{n0} - r'_n) \tag{4.26}$$

This term can be added to the right side of Equation (4.25) to generate the desired shape distortion. If this term is positive, it increases the right hand side of Equation (4.25) and the size of the π-plane cross-section is increased. If this term is negative, then the size of the π-plane cross-section is decreased. r'_{n0} is a reference level of r'_n. At this level, Equation (4.26) becomes zero and the original shape intersects with the distorted shape. A is a factor whose sign and magnitude control how much the original shape is distorted with regard to r'_{n0}. The effect of this term on the shape of the π-plane cross-section is illustrated in Figure 4.20, where the original π-plane cross-section with six fold symmetry is shown with a dashed line, and the distorted shape is shown by a solid line. When $A > 0$, the shape shrinks above r'_{n0} and expands below it, as shown in Figure 4.20 (a). For $A < 0$, the effect is reversed (Figure 4.20 (b)). Clearly, the distorted shapes have $R'_{120}(Z)/R'_0(Z) \neq 1$. By carefully selecting the value of A, the desired $R'_{120}(Z)/R'_0(Z)$ value can be obtained. The parameter A is made a function of Z, because the ratio $\frac{(\sigma_1 - \sigma_3)_{0°}}{(\sigma_1 - \sigma_3)_{90°}}$, which indicates how unequal the ends of a "U" shaped curve are, varies with confining pressure (Figure 3.49). Finally, β_s^2 is added in Equation (4.25) to control its dependence on β_s.

Although theoretically r'_{n0} can take any value, it is most convenient to choose either $r'_{n0} = 1.0$ or $r'_{n0} = -0.5$. $r'_{n0} = 1.0$ corresponds to $R'_0 = 1.0$, while $r'_{n0} = -0.5$ corresponds to R'_{120} and $R'_{240} = 1.0$ on the original normalized π-plane cross-section. Figure 4.21 through Figure 4.23 plot the effect of Equation (4.26) on the original π-plane cross-sections with β_s ranging from 0.6 to 0.8. There are two subplots in each plot: subplot (a) is for $r'_{n0} = 1.0$, and subplot (b) is for $r'_{n0} = -0.5$. For each combination of β_s and r'_{n0}, A is taken to be between –0.5 and 0.5 at 0.05 intervals. In all the plots, the shape with the thick black line is the original shape with six-fold symmetry, which

corresponds to $A = 0$. The shapes with solid thin black lines are for $A = \pm 0.1, \pm 0.2, \cdots, \pm 0.5$, while the shapes with dotted thin black lines are for $A = \pm 0.05, \pm 0.15, \cdots, \pm 0.45$.

Discussion on Subplot (a)'s in which $r'_{n0} = 1.0$

Figure 4.21 (a), Figure 4.22 (a) and Figure 4.23 (a) all have $r'_{n0} = 1.0$, but with different values of β_s. The distorted shapes intersect the original shape at $R'_0 = 1.0$. When A increases from 0, it can be seen from the subplot (a)'s that the failure surfaces expanded downwards. However, the bottom of the failure surface is approaching a triangle with the increase of A, as shown by dashed lines in Figure 4.21 (a) and Figure 4.22 (a). This limits how far the failure surface can be expanded (e.g. limits the possible value of $R'_{120}(Z)/R'_0(Z)$ that can be described), and poses restrictions on the possible values A can take. For smaller β_s values, the original π-plane cross-section is closer to a right triangle. Therefore, this restriction is more significant for $\beta_s = 0.6$ than for $\beta_s = 0.8$. The limiting values are as follows:

- $\beta_s = 0.6$, limit of $A \approx 0.076$, maximum $R'_{120}(Z)/R'_0(Z) \approx 1.207$;
- $\beta_s = 0.7$, limit of $A \approx 0.349$, maximum $R'_{120}(Z)/R'_0(Z) \approx 1.637$;
- $\beta_s = 0.8$, limit of A is larger than 0.5, $R'_{120}(Z)/R'_0(Z) = 1.485$ for $A = 0.5$;

For $A < 0$, the bottom of the distorted shape shrinks into the original shape, and it gets more rounded with decreasing A. There is no restriction on values of $A < 0$. The A values and corresponding $R'_{120}(Z)/R'_0(Z)$ values for $r'_{n0} = 1.0$ are tabulated in Table 4.1, and plotted in Figure 4.24 (a).

Discussion on Subplot (b)'s in which $r'_{n0} = -0.5$

The results in Figure 4.21 (b), Figure 4.22 (b) and Figure 4.23 (b) correspond to the case where $r'_{n0} = -0.5$. The distorted shapes intersect the original shape at $R'_{120} = 1.0$ and $R'_{240} = 1.0$. When A decreases from 0, the failure surface expands in the $\theta = 0°$ direction, with a more pointed apex as A decreases. In this case, the top of the distorted shape approaches the top of a triangle, which is shown as dashed lines in Figure 4.21 (b) and Figure 4.22 (b). Therefore, the restriction on A is in the negative part, as listed below:

- $\beta_s = 0.6$, limit of $A \approx -0.070$, minimum $R'_{120}(Z)/R'_0(Z) = 0.837$;
- $\beta_s = 0.7$, limit of $A \approx -0.296$, minimum $R'_{120}(Z)/R'_0(Z) = 0.620$;
- $\beta_s = 0.8$, limit of A is smaller than -0.5, $R'_{120}(Z)/R'_0(Z) = 0.634$ for $A = -0.5$;

For $A > 0$, the top of the distorted shape shrinks into the original shape, and it gets more rounded. Thus there is no restriction on the magnitude of A. The A values and corresponding $R'_{120}(Z)/R'_0(Z)$ values for $r'_{n0} = -0.5$ are tabulated in Table 4.2, and plotted in Figure 4.24 (b). For this group of distorted π-plane cross-sections, obviously R'_0 is different from 1 while $R'_{120} = R'_{240} = 1$. Therefore, the normalized quantities must be normalized against $R_{120}(Z)$, instead of $R_0(Z)$.

4.6.3 Extension of Geometry Variation with Non-Zero Shear Stresses

It has been shown in Figure 4.19 that the failure surface must meet the stress path on the anisotropic failure curve AND, instead of the isotropic failure line AB. Along the stress path shown in Figure 4.19, the anisotropic material fails earlier than the imaginary isotropic material. The geometry variation with non-zero shear stresses of the isotropic Matsuoka-Nakai criterion must be modified so that the predicted failure point is at point N instead of at point M. It is possible to change both the shape distortion and size reduction to obtain this feature. To keep the formulation simple, however, only the uniform size reduction will be modified.

In the original Matsuoka-Nakai criterion, the uniform size reduction of the failure surface is controlled by the term $-\frac{1-3k}{\sqrt{3}}(\sigma_{st}^2+\sigma_{tn}^2+\sigma_{ns}^2)Z$. The term involving σ_{st} must not be changed, because σ_{st} is in the isotropic plane and its effect on failure should be described by an isotropic criterion. The term involving σ_{tn} must be changed, because it is the only non-zero shear stress in a conventional triaxial compression test, and as such it must be the shear stress that controls anisotropic size reduction. Any change on σ_{tn} must be also made on σ_{ns}, due to material symmetry. Based on these considerations, the following term is proposed:

$$-K(Z)(\sigma_{tn}'^2+\sigma_{ns}'^2) \tag{4.27}$$

K is a positive parameter, while $\sqrt{\sigma_{tn}'^2+\sigma_{ns}'^2}$ is the normalized resultant shear stress on the isotropic plane. Clearly, this term is always smaller than zero when there is non-zero shear stress on the isotropic plane. When this term is added to the right hand side of Equation (4.25), it speeds up the size reduction of the failure. The failure surface then meets the stress path earlier compared with the isotropic case, and the required anisotropy is then predicted. The larger K is, the faster the size reduces with non-zero shear stress and the corresponding AND curve deviates farther from the isotropic failure line AB (Figure 4.19). The depth of the "U" shaped curve in Figure 4.8 is clearly correlated with the value of $K(Z)$.

4.6.4 The Anisotropic Matsuoka-Nakai (AMN) Criterion

Incorporating both the linear shape distortion of the bounding failure surface and the anisotropic size reduction, the final expression for the normalized anisotropic π-plane cross-section becomes:

$$\begin{aligned}-(1-\beta_s)R'^3\cos 3\theta+\left(1-\beta_s+\beta_s^2\right)R'^2 &= \beta_s^2-2(1-\beta_s+\beta_s^2)(\sigma_{st}'^2+\sigma_{tn}'^2+\sigma_{ns}'^2)\\ &-6(1-\beta_s)(\sigma_{st}'^2r_n'+\sigma_{tn}'^2r_s'+\sigma_{ns}'^2r_t')+6\sqrt{6}(1-\beta_s)\sigma_{st}'\sigma_{tn}'\sigma_{ns}'+A(Z)\beta_s^2(r_{n0}'-r_n')-K(Z)(\sigma_{tn}'^2+\sigma_{ns}'^2)\end{aligned} \tag{4.28}$$

Equation (4.28), together with the two pressure dependence functions $R_0(Z)$ and $R_{120}(Z)$, completes the formulation of AMN criterion. Both the bounding failure surface and the geometry variation are modified to incorporate anisotropic features. These anisotropic features of the AMN criterion will be termed the *bounding failure surface anisotropy* and the *geometry variation anisotropy* from now on.

Figure 4.25 shows the bounding failure surface of the AMN criterion in the MNSS and its π-plane cross section at a certain Z level. Functions $R_0(Z)$ and $R_{120}(Z)$ determine how the size of the π-plane cross-section varies with pressure level. They can be obtained through conventional triaxial compression tests on specimens with $\beta = 90°$ (to obtain $R_0(Z)$) and $\beta = 0°$ (to obtain $R_{120}(Z)$). For the π-plane cross-section at a certain Z, the lengths of R_0 and R_{120} of this π-plane cross-section (i.e. length of OA and OC in Figure 4.25) are determined through $R_0(Z)$ and $R_{120}(Z)$. Compared with isotropic materials, where there is only one pressure dependence function, there are two pressure dependence functions for a transversely isotropic material.

Once $R'_{120}(Z)/R'_0(Z)$ is known, the shape of the π-plane cross-section at this Z level depends on the value of r'_{n0} and β_s. The parameter A can be determined from Figure 4.24 based on the value of $R'_{120}(Z)/R'_0(Z)$ and r'_{n0}. Therefore, the parameter A is transparent to the end user of the model. In an ideal situation, r'_{n0} and β_s must be obtained through true triaxial tests on the anisotropic rock, where the principal stresses are in the principal material directions **S**, **T** and **N**. The anisotropic π-plane cross-section is symmetric to the projection of the σ_n axis, but does not possess the six-fold symmetry at $R'_{120}(Z)/R'_0(Z)$ different from 1. Therefore, true triaxial tests must be performed so that data points cover the entire range of ABCD in Figure 4.25, or half of the π-plane cross-section. The π-plane cross-section obtained from the experiments can then be compared with the shapes shown in Figure 4.21 through Figure 4.23, to determine the most suitable r'_{n0} and β_s. In the case of an isotropic material, only one-sixth of the π-plane cross-section (section AB for example) needs to be covered by experimental results, and β_s is the only parameter that describes the shape of the π-plane cross-section.

Parameter K determines the extra size reduction of the bounding failure surface, which is added to the isotropic size reduction. This parameter determines the depth of the "U" shaped curve, which is obtained through a series of triaxial compression tests with varying β but with the same confining pressure. Therefore, K should be calibrated based on a series of "U" shaped curves at various confining pressures.

Once all parameters are obtained, computer programs can be written to implement the AMN criterion. While implementing this failure criterion, it is frequently necessary to judge whether a stress point is inside or outside of the failure surface. Therefore, a failure function is defined based on Equation (4.28):

$$f(r',\theta;\sigma'_{st},\sigma'_{tn},\sigma'_{ns}) = -(1-\beta_s)r'^3\cos 3\theta + \left(1-\beta_s+\beta_s^2\right)r'^2 - \beta_s^2 + 2(1-\beta_s+\beta_s^2)(\sigma'^2_{st}+\sigma'^2_{tn}+\sigma'^2_{ns})$$
$$+ 6(1-\beta_s)(\sigma'^2_{st}r'_n + \sigma'^2_{tn}r'_s + \sigma'^2_{ns}r'_t) - 6\sqrt{6}(1-\beta_s)\sigma'_{st}\sigma'_{tn}\sigma'_{ns} - A(Z)\beta_s^2(r'_{n0}-r'_n) + K(Z)(\sigma'^2_{tn}+\sigma'^2_{ns}) \quad (4.29)$$

Equation (4.28) is equivalent to $f = 0$. If $f < 0$ for a given stress point, then this point is inside the failure surface, and it is safe. Otherwise the point is either on or outside of the failure surface, and failure occurs.

4.7 Parametric Study

A parametric study will be shown here to illustrate how the parameters of the AMN model affect the conventional triaxial strength. In Chapter 2, the pressure dependence function $R_0(Z)$ has been thoroughly discussed for isotropic rocks. A numerical example was presented to illustrate how $R_0(Z)$ can be obtained from conventional triaxial compression tests. In the case of anisotropic rocks, $R_0(Z)$ shows the pressure dependence in the **N** direction, while $R_{120}(Z)$ shows the pressure dependence in **S** and **T** directions. The procedures presented in Chapter 2 can still be used to obtain $R_0(Z)$ and $R_{120}(Z)$ for anisotropic rocks. Therefore, in this parametric study, only the three parameters involved in Equation (4.28) will be discussed. These parameters are r'_{n0}, β_s, and K. The effect of these parameters on the predicted conventional triaxial compression strength will be calculated for a number of different combinations of these parameters. It has been shown that Equation (4.28) must be used together with a pressure dependence function. In order to make the calculations possible, the pressure dependence function of Chichibu Green Schist (Equation (4.37)) will be used.

The parameters r'_{n0} and β_s, together with $R'_{120}(Z)/R'_0(Z)$, define the shape of the normalized π-plane cross-section of the bounding failure surface. The parameter K, on the other hand, defines how the geometry of the bounding failure surface varies with non-zero shear stresses. Eight different combinations of the parameters are assumed, as shown in Table 4.3.

The anisotropic bounding failure surfaces for these combinations are first studied. Figure 4.26 (a) shows the bounding failure surfaces for $R'_{120}(Z)/R'_0(Z) = 0.9$, $\beta_s = 0.6$, and for r'_{n0} = both -0.5 and 1.0. Figure 4.26 (b) shows similar results but with $\beta_s = 0.8$. The bounding failure surfaces with $R'_{120}(Z)/R'_0(Z) = 1.1$ and different combinations of β_s and r'_{n0} are shown in Figure 4.27. It can be seen that for the same $R'_{120}(Z)/R'_0(Z)$ and β_s, the shapes determined by $r'_{n0} = -0.5$ and $r'_{n0} = 1.0$ are close to each other. Therefore, as long as the limit of the shapes are not exceeded, the choice of $r'_{n0} = -0.5$ and $r'_{n0} = 1.0$ should give similar results on the material strength. It is also shown that larger β_s results in more rounded shapes, which is consistent with the role of β_s on the isotropic π-plane cross-section. The parameter K does not have any effect on the shape of the bounding failure surface, and it is irrelevant here.

The predicted conventional triaxial compression strengths are then plotted against the isotropic

plane orientation, for these eight combinations. Figure 4.28 (a) plots the triaxial strengths with $R'_{120}(Z)/R'_0(Z) = 0.9$, $\beta_s = 0.6$, and $r'_{n0} = 1.0$. The three curves correspond to $K = 0$, 0.8 and 1.6, respectively. The following observations are made:

Observation 1: When $K = 0$, the strength monotonically increases from $\beta = 0°$ to $\beta = 90°$. This variation of strength is solely generated by the anisotropy of the bounding failure surface.
Observation 2: The depth of the "U" shaped curves increase with K. The rate of increase is faster from 0 to 0.8 than from 0.8 to 1.6.

Figure 4.28 (b) plots similar results but for $r'_{n0} = -0.5$. Comparing corresponding curves in Figure 4.28 (a) and (b), the effect of r'_{n0} on the strength can be observed:

Observation 3: When $K = 0$, the strength with $r'_{n0} = -0.5$ and that with $r'_{n0} = 1.0$ are very close to each other, which is consistent with the observations on the shape of their π-plane cross-sections.
Observation 4: For K larger than 0, the minimum strength predicted with $r'_{n0} = -0.5$ is slightly smaller than the minimum strength predicted with $r'_{n0} = 1.0$.

The effect of r'_{n0} on the predicted strength, therefore, is very small for the parameters considered here.

Figure 4.29 shows similar results as those in Figure 4.28, the only difference is that $\beta_s = 0.8$. Observations 1 through 4 are still true in Figure 4.29. The following additional observations are made by comparing Figure 4.29 with Figure 4.28:

Observation 5: At the same K value, the depth of the "U" shaped curve is smaller for $\beta_s = 0.8$ than for $\beta_s = 0.6$. Therefore, the effect of K on the depth of the "U" shaped curves decreases with increasing β_s.
Observation 6: The strength difference between the case $r'_{n0} = -0.5$ and $r'_{n0} = 1.0$ is even smaller for $\beta_s = 0.8$. Therefore, it seems that the effect of r'_{n0} decreases with increasing β_s.
Observation 7: The minimum strength is obtained at β smaller than 45°. This is also true in Figure 4.28, but is less evident there.

Figure 4.30 and Figure 4.31 are similar to Figure 4.28 and Figure 4.29, with the only difference being $R'_{120}(Z)/R'_0(Z) = 1.1$. Some of the previous observations must be changed for $R'_{120}(Z)/R'_0(Z) = 1.1$:
Observation 1: When $K = 0$, the strength monotonically *decreases* from $\beta = 0°$ to $\beta = 90°$. This variation of strength is solely generated by the anisotropy of the bounding failure surface.
Observation 2: Not changed.
Observation 3: Not changed.
Observation 4: For K larger than 0, the minimum strength predicted with $r'_{n0} = -0.5$ is

somewhat *larger* than the minimum strength predicted with $r'_{n0} = 1.0$.
Observation 5: Not changed.
Observation 6: Not changed.
Observation 7: The minimum strength is obtained at β somewhat *larger* than 45°. This is also true in Figure 4.30, but is less evident there.

Based on this parametric study, it is clear that the AMN criterion has the ability to describe the strength of transversely isotropic rocks in conventional triaxial tests.

4.8 Application of the AMN Criterion

The Anisotropic Matsuoka-Nakai criterion can be applied to different anisotropic rocks, to predict their strength in conventional and true triaxial tests. It has been found that there are different failure modes involved in the conventional triaxial tests. For example, single or multiple sliding along the isotropic planes, kink banding, shear faulting across the isotropic planes, etc. It is only natural that one criterion cannot be used to describe all these failure phenomena. In this research, it is assumed that anisotropic rocks fail in two different modes: along and across the isotropic planes. The AMN criterion will be applied only to shear faulting across the isotropic planes. When the rock fails along the isotropic planes, the shear behavior along the isotropic plane then must take over. This philosophy is consistent with Boehler and Raclin (1985), where the behavior of a chopped strand mat laminate is modeled with a "Parallel Mode" criterion and an "Across Mode" criterion (refer to Section 3.2.2.1). Therefore, in order to explain the strength of anisotropic rocks in conventional triaxial tests, two failure criteria will be simultaneously used: the AMN criterion and the shear criterion along the isotropic plane.

Throughout this section, the Coulomb criterion will be assumed to be applicable to the isotropic planes:

$$\tau_n = \sigma_n \tan\phi + c \tag{4.30}$$

The frictional criterion along the isotropic plane can be obtained by plotting the normal and shear stresses along the isotropic plane. It was observed that many anisotropic rocks tend to fail through their bedding planes at β around 30° to 40°. Therefore, the normal and shear stresses on the isotropic plane at this orientation usually define the Coulomb envelope.

In this section, the AMN criterion and the Coulomb criterion will be applied to two different anisotropic rocks: the Martinsburg slate and the Chichibu Green Schist. The conventional triaxial strength will be predicted for the Martinsburg slate, and the true triaxial strength will be predicted for the Chichibu Green Schist.

4.8.1 Martinsburg Slate

The conventional triaxial strength of the Martinsburg Slate as reported by Donath (1964) was plotted in Figure 3.3 and tabulated in Table B.1 in Appendix B.

Obtaining the Coulomb Envelope

Based on the axial stress σ_1 at failure and the confining pressure σ_3, the normal and shear stress on the isotropic plane at failure can be obtained by the following equations:

$$\sigma_n = \sigma_3 \cos^2\beta + \sigma_1 \sin^2\beta; \tau_n = \frac{\sigma_1 - \sigma_3}{2}\sin 2\beta; \tag{4.31}$$

σ_n and τ_n can be calculated for every test in Table B.1. These τ_n are plotted against σ_n in Figure 4.32. For the orientations with β = 15°, 30°, 45°, and 60°, the τ_n against σ_n curves are close to straight lines, and they plot very close to each other. The τ_n against σ_n curves for β = 0°, 75°, 90° plot below the other curves. Based on the observations of Donath (1964), most specimens with β = 15° to 60° fail along the isotropic planes. Therefore, they define the Coulomb envelope of the isotropic plane of Martinsburg slate. Of these envelopes, the one with β = 45° seems to be the topmost. A straight line is thus fitted through the τ_n against σ_n data points for β = 45°, which will be used as the Coulomb envelope (Figure 4.32). The equation for this line is:

$$\tau_n = 0.3396\sigma_n + 130.7 \text{ (bar)} \tag{4.32}$$

The cohesion of the isotropic plane of this rock, therefore, is 130.7 bar. Its friction angle can be calculated to be around 19°.

Obtaining Pressure Dependence Functions $R_0(Z)$ and $R_{120}(Z)$

In order to obtain $R_0(Z)$, the σ_1 at failure measured from specimens with β = 90° are collected. For each data point, R_0 and Z are calculated based on the following equations:

$$\begin{aligned} R_0 &= \sqrt{\frac{1}{3}\left[(\sigma_s - \sigma_t)^2 + (\sigma_t - \sigma_n)^2 + (\sigma_n - \sigma_s)^2\right]} = \sqrt{\frac{2}{3}}(\sigma_1 - \sigma_3); \\ Z &= \frac{\sigma_s + \sigma_t + \sigma_n}{\sqrt{3}} = \frac{\sigma_1 + 2\sigma_3}{\sqrt{3}}; \end{aligned} \tag{4.33}$$

In order to obtain $R_{120}(Z)$, the σ_1 at failure measured from specimens with β = 0° are collected. For each data point, R_{120} and Z are calculated based on the following equations:

$$\begin{aligned} R_{120} &= \sqrt{\frac{1}{3}\left[(\sigma_s - \sigma_t)^2 + (\sigma_t - \sigma_n)^2 + (\sigma_n - \sigma_s)^2\right]} = \sqrt{\frac{2}{3}}(\sigma_1 - \sigma_3); \\ Z &= \frac{\sigma_s + \sigma_t + \sigma_n}{\sqrt{3}} = \frac{\sigma_1 + 2\sigma_3}{\sqrt{3}}; \end{aligned} \tag{4.34}$$

The R_0 and R_{120} values are then plotted against corresponding Z values in Figure 4.33. These data can be fitted with power law functions, so that:

$$R_0(Z) = 14.287Z^{0.6662}; R_{120}(Z) = 9.2491Z^{0.7063}; \quad (4.35)$$

For this specific rock there is $R'_{120}(Z)/R'_0(Z) < 1$. The variation of the ratio $R'_{120}(Z)/R'_0(Z)$ with Z as calculated from the fitted functions is plotted in Figure 4.34.

Obtaining Parameters r'_{n0}, β_s, and K

Since there are no true triaxial test data available for this rock, it is impossible to know the exact shape of the anisotropic π-plane cross-section. Therefore, it is assumed that $r'_{n0} = 1.0$ and $\beta_s = 0.7$ is applicable to this rock. Based on Figure 4.24, the formulation of the AMN criterion can describe $R'_{120}(Z)/R'_0(Z)$ up to 1.637 at $\beta_s = 0.7$. The observed $R'_{120}(Z)/R'_0(Z)$ for Martinsburg slate is always less than 1. Therefore, the shape limit of the formulation for $r'_{n0} = 1.0$ and $\beta_s = 0.7$ as shown in Figure 4.22 (a) will not be a problem with these assumed r'_{n0} and β_s values.

Finally, K must be obtained by matching the "U" shaped curves. This can be achieved simply by trial and error. If K is too small, then the predicted "U" shaped curve will be shallower than the experimental curve. It K is too large, then the predicted "U" shaped curve will be deeper than the experimental curve. After this trial and error process, K is determined to be 1.8 for Martinsburg slate.

Based on these parameters, the conventional strength of Martinsburg slate at various confining pressures and different isotropic plane orientations is calculated. The predicted strength is compared with the measured strength in Figure 4.35. Note that the axial stress at failure is plotted, instead of the stress difference. Both the strength calculated by the AMN criterion and that by the Coulomb criterion are plotted. The true failure strength is taken as the lower of the two, and plotted as solid lines in Figure 4.35. When the AMN strength is larger than the Coulomb strength, the AMN strength is plotted by dashed lines. It seems that failure is controlled by the Coulomb criterion for β roughly between 10° and 60°, which is consistent with the observations of Donath (1964), that most specimens with β = 15° to 60° fail along the isotropic planes. For other β values, failure seems to be controlled by the AMN criterion. In general, the agreement seems to be very good.

4.8.2 Chichibu Green Schist

The experimental results on Chichibu Green Schist were reported by Mogi (2007), and they were summarized in Chapter 3. In these tests, the specimens were sheared in four different modes (Figure 4.36), under conventional triaxial stress and true triaxial stress. Conventional triaxial tests were performed on specimens with $\beta = 30°$ and $\beta = 90°$, with confining pressures 0, 25, 50 and 75MPa. These results are plotted in Figure 4.37. The strength of $\beta = 90°$ is higher because it is always at one end of the "U" shaped curves at different confining pressures. All true triaxial

tests were performed with σ_3 = 50MPa, and the results are plotted in Figure 4.38.

Obtaining the Coulomb Envelope

In order to obtain the Coulomb envelope of Chichibu Green Schist, the normal and shear stresses on the bedding planes are calculated and plotted in Figure 4.39 for all of the tests, except those with Mode IV where the shear stress is always 0 on the isotropic planes. In Figure 4.39, the solid symbols are for conventional triaxial tests, while the empty ones are for true triaxial tests. Since the conventional triaxial tests were performed with $\beta = 30°$, it is reasonable to assume that most of these specimens fail along the bedding plane. Indeed, in Figure 4.39 they fall in a narrow band between the two dashed lines, which can be considered to be the Coulomb envelope of this rock. Some of the true triaxial tests also fall in this band, and thus may also fail through the bedding planes. Finally, the Coulomb envelope is assumed to be in the middle of the band:

$$\tau_n = 0.6575\sigma_n + 17 \tag{4.36}$$

Therefore, the cohesion along the bedding planes is around 17MPa, and the friction angle is around 33°.

Obtaining Pressure Dependence Functions $R_0(Z)$ and $R_{120}(Z)$

Following the procedures shown in Section 2.4.2, the conventional triaxial strength of $\beta = 90°$ can be used to obtain the pressure dependence function $R_0(Z)$:

$$R_0(Z) = 5.2988Z^{0.7032} \tag{4.37}$$

Since no triaxial test was performed with $\beta = 0°$, it is impossible to fit function $R_{120}(Z)$ directly from experimental data. It will be assumed that $R_{120}(Z) = R_0(Z)$ for this rock, which is explained below.

Obtaining Parameters r'_{n0}, β_s, and K

In order to obtain the shape of the π-plane cross-section for the bounding failure surface, the true triaxial tests of Mode IV are normalized with $R_0(Z)$ (Equation (4.37)) and plotted in Figure 4.40. The solid line in Figure 4.40 shows the shape defined by the LMN dependence with $\beta_s = 0.75$. It seems that the original shapes without distortion can be used to fit the π-plane cross-section very well. Therefore, $\beta_s = 0.75$ is assumed, and the original non-distorted π-plane cross-section is assumed to apply (i.e. $R'_{120}(Z)/R'_0(Z) = 1.0$, which means that $R_{120}(Z) = R_0(Z)$). Since no shape distortion is necessary, the value of r'_{n0} is irrelevant. Based on these considerations, the value of K is then obtained through trial and error to be $K = 1.5$.

This set of parameters is then used to predict the strength of Chichibu green schist in true triaxial tests. The predictions are shown as solid lines in Figure 4.41. The predicted true triaxial strength

of Chichibu green schist is shown by four solid lines. The left end of each line stands for the condition where $\sigma_2 = \sigma_3 = 50$MPa. These lines show how the failure axial stress σ_1 varies with the increase of σ_2 at different shear modes, until $\sigma_2 = \sigma_1$ at the right ends of the lines. At each σ_2 value, the strength predicted by the Coulomb criterion and that by the AMN criterion are both calculated, and the smaller one is taken as the real strength. With reasonable scatter, the behavior of Chichibu Green Schist in true triaxial tests is well captured, for all of the test modes.

The predicted failure mode of this rock is not immediately clear. Figure 4.42 shows the strength predicted by both the Coulomb criterion and the AMN criterion, for different modes. In Mode I, it is evident from Figure 4.42 (a) that the Coulomb strength is lower than the AMN strength for all the σ_2 values. In this test mode, therefore, it is predicted that all specimens fail along the isotropic planes. Also, the Coulomb strength does not change with σ_2. This is because the isotropic planes dip into σ_3 direction in this mode, and the normal and shear stresses on the isotropic plane are independent to σ_2.

Figure 4.42 (b) shows the Coulomb and AMN strength of Mode II specimens. At lower σ_2 values, the Coulomb strength is smaller. However, the Coulomb strength increases very quickly with increasing σ_2, and it is larger than the AMN strength at larger σ_2 values. Therefore, the failure of the specimens in the mode is along the isotropic plane for smaller σ_2, and across the isotropic plane for larger σ_2.

Figure 4.42 (c) shows the two strengths for Mode III specimens. The variation of these strengths is similar to that of Mode II. However, in this case the Coulomb strength increases even faster with σ_2, and thus failure along the isotropic planes only occurs when σ_2 is very close to σ_3.

According to these calculations, it is evident that failure strength and failure mode of an anisotropic rock subject to true triaxial stress are controlled by both the stress and the isotropic plane orientation. Unfortunately, a systematic summary of the observation of failure modes cannot be found in the literature to verify the predicted failure modes, and its variation with σ_2 level.

4.8.3 Application to Other Rocks

The AMN criterion combined with the Coulomb criterion is also applied to other transversely isotropic rocks that have been collected in this research. Section 3.1 offers a complete description of these transversely isotropic rocks and their experimental results. Except for Chichibu Green Schist, there are only conventional triaxial test results available for other rocks. Therefore, the same procedures are followed as outlined in Section 4.8.1 for Martinsburg slate data set. The parameters for the AMN criterion and the Coulomb criterion are compiled in Table 4.4. The predicted strengths are compared with the measured strengths in Figure 4.43 through Figure

4.47.

Figure 4.43 compares the predicted and measured strengths for shales, including the Green River Shale I, Green River Shale II, and Tournemire Shale. For Green River Shale I and II (Figure 4.43 (a) and (b)), the strengths predicted by both the AMN criterion and the Coulomb criterion are shown. The strength predicted by the AMN criterion forms the two shoulders of the "U" shaped curves. For β around 30°, the strengths predicted from the Coulomb criterion are smaller than those of the AMN criterion, and the AMN strengths are shown with dashed lines. Within the range of β values where the Coulomb strengths are lower, the differences between Coulomb strengths and the AMN strengths are not significant for these two shales. For Tournemire shale, the predicted strengths in Figure 4.43 (c) are solely predicted from the AMN criterion, and the agreement is very good. These observations may indicate that shales are closer to a continuous material than to a discontinuous material.

Figure 4.44 compares the predicted and measured strengths for slates, including the Austin Slate, the Martinsburg Slate, and the Penrhyn Slate. It is also observed that for β values around 30°, the Coulomb strength is smaller than the AMN strength. However, the differences between the Coulomb strength and the AMN strength are much larger than those of shales. The ranges of β where Coulomb strengths are smaller are generally larger too. Compared with shale, slates seem to be closer to a discontinuous material. This is physically grounded, since slates can be separated into slabs following their cleavage planes. The cleavage planes are therefore close to a set of joints.

Figure 4.45 compares the predicted and measured strengths for phyllites, including the Carbonaceous Phyllite, the Micaceous Phyllite, and the Quartzitic Phyllite. It is difficult to make a unique statement for these three phyllites about the relative magnitude of the Coulomb strength and the AMN strength. For Carbonaceous phyllite (Figure 4.45 (a)), the difference between the Coulomb strengths and the AMN strengths are not very significant, which is quite similar to the case of shales. For Micaceous phyllite (Figure 4.45 (b)), the difference seems to be large and the ranges of β where the Coulomb strength is smaller than the AMN strength is comparable to those of slates. For Quartzitic phyllite (Figure 4.45 (b)), the differences between the Coulomb strengths and the AMN strengths are quite significant. However, the range of β where the Coulomb strength is smaller is not as large as slates. It is therefore difficult to decide whether phyllites are closer to a continuous or to a discontinuous material. Each phyllite must be studied individually.

Figure 4.46 compares the predicted and measured strengths for schists, including the Angers Schist, the Biotite Schist, the Chlorite Schist, the Quartz Mica Schist, and the Quartzitic Schist. For the Angers Schist and the Biotite Schist (Figure 4.46 (a) and (b)), the strengths are predicted with only the AMN criterion. Although the Coulomb parameters are also obtained and listed in Table 4.4, it is found that reasonable agreement is obtained with the AMN criterion alone. For the Chlorite Schist and the Quartz Mica Schist (Figure 4.46 (c) and (d)), the differences between the

Coulomb strength and the AMN strength when the Coulomb strength is lower are very small. In fact, the agreement between the predicted and the measured strength will not be affected even if only the AMN criterion were used. For the Quartzitic Schist (Figure 4.46 (e)), the differences between the Coulomb strength and the AMN strength is larger than the other schist, but still not as large as the slates. Therefore, it is reasonable to conclude that schists are closer to continuous materials.

Figure 4.47 compares the predicted and measured strengths for diatomite. Since there is only one data set available, it is hard to make any general conclusions.

Table 4.1 Variation of R'_{120}/R'_0 with A for different β_s values at r'_{n0} = 1.0 (Refer to Figure 4.24 (a) for Plot)

$\beta_s = 0.6$		$\beta_s = 0.7$		$\beta_s = 0.8$	
A	R'_{120}/R'_0	A	R'_{120}/R'_0	A	R'_{120}/R'_0
-0.500	0.491	-0.500	0.534	-0.500	0.562
-0.450	0.532	-0.450	0.578	-0.450	0.607
-0.400	0.574	-0.400	0.621	-0.400	0.651
-0.350	0.617	-0.350	0.665	-0.350	0.695
-0.300	0.661	-0.300	0.710	-0.300	0.738
-0.250	0.706	-0.250	0.755	-0.250	0.781
-0.200	0.754	-0.200	0.801	-0.200	0.825
-0.150	0.806	-0.150	0.848	-0.150	0.868
-0.100	0.862	-0.100	0.897	-0.100	0.912
-0.050	0.925	-0.050	0.947	-0.050	0.956
0	1.000	0	1.000	0	1.000
0.050	1.103	0.050	1.056	0.050	1.045
0.076	1.207	0.100	1.115	0.100	1.090
Limit	Limit	0.150	1.180	0.150	1.136
		0.200	1.252	0.200	1.182
		0.250	1.335	0.250	1.230
		0.300	1.441	0.300	1.278
		0.349	1.637	0.350	1.328
		Limit	Limit	0.400	1.379
				0.450	1.431
				0.500	1.485

Table 4.2 Variation of R'_{120}/R'_0 with A for different β_s values at $r'_{n0} = -0.5$ (Refer to Figure 4.24 (b) for Plot)

$\beta_s = 0.6$		$\beta_s = 0.7$		$\beta_s = 0.8$	
A	R'_{120}/R'_0	A	R'_{120}/R'_0	A	R'_{120}/R'_0
				-0.500	0.634
				-0.450	0.666
				-0.400	0.699
		Limit	Limit	-0.350	0.732
		-0.296	0.620	-0.300	0.766
		-0.250	0.718	-0.250	0.801
		-0.200	0.782	-0.200	0.838
Limit	Limit	-0.150	0.839	-0.150	0.876
-0.070	0.837	-0.100	0.893	-0.100	0.915
-0.050	0.902	-0.050	0.946	-0.050	0.957
0	1.000	0	1.000	0	1.000
0.050	1.079	0.050	1.055	0.050	1.046
0.100	1.153	0.100	1.111	0.100	1.094
0.150	1.225	0.150	1.169	0.150	1.144
0.200	1.297	0.200	1.229	0.200	1.198
0.250	1.370	0.250	1.292	0.250	1.254
0.300	1.446	0.300	1.359	0.300	1.315
0.350	1.524	0.350	1.429	0.350	1.379
0.400	1.605	0.400	1.502	0.400	1.447
0.450	1.690	0.450	1.581	0.450	1.520
0.500	1.780	0.500	1.664	0.500	1.598

Table 4.3 Combination of Parameters Used in the Parametric Study

Case #	$R'_{120}(Z)/R'_0(Z)$	β_s	r'_{n0}	K
1	0.9	0.6	1.0	0, 0.8, 1.6
2	0.9	0.6	–0.5	0, 0.8, 1.6
3	0.9	0.8	1.0	0, 0.8, 1.6
4	0.9	0.8	–0.5	0, 0.8, 1.6
5	1.1	0.6	1.0	0, 0.8, 1.6
6	1.1	0.6	–0.5	0, 0.8, 1.6
7	1.1	0.8	1.0	0, 0.8, 1.6
8	1.1	0.8	–0.5	0, 0.8, 1.6

Table 4.4 Model Parameters for Different Transversely Isotropic Rocks

Rock Name and Unit	Coulomb Criterion	AMN Criterion			
		$R_0(Z)$	$R_{120}(Z)$	β_s	K
Green River Shale I (psi)	τ=0.5823σ+6317	$74.16Z^{0.5907}$	$91.97Z^{0.5736}$	0.7	0.1
Green River Shale II (psi)	τ=0.3363σ+4634	0.3605Z+10445	0.379Z+11669	0.7	0.2
Tournemire Shale (MPa)	τ=0.4093σ+8.027	$6.898Z^{0.5072}$	$4.739Z^{0.5953}$	0.7	0.8
Austin Slate (psi)	τ=0.2716σ+6474	$119.4Z^{0.5446}$	$71.08Z^{0.5995}$	0.7	1.4
Martinsburg Slate (bar)	τ=0.3396σ+130.7	$14.29Z^{0.6662}$	$9.249Z^{0.7068}$	0.7	1.8
Penrhyn Slate (psi)	τ=0.4488σ+2489	0.7844Z+9915	0.7617Z+8724	0.7	1.6
Carbonaceous Phyllite (MPa)	τ=0.5913σ+12.08	$5.187Z^{0.6657}$	$4.316Z^{0.6859}$	0.7	0.5
Micaceous Phyllite (MPa)	τ=0.4264σ+9.866	$6.857Z^{0.6087}$	$3.063Z^{0.7862}$	0.7	1.2
Quartzitic Phyllite (MPa)	τ=0.5079σ+14.94	$6.844Z^{0.6136}$	$3.866Z^{0.7141}$	0.7	0.4
Angers Schist (MPa)	τ=0.7424σ+15.31	$4.036Z^{0.7471}$	$5.557Z^{0.7}$	0.7	9.6
Biotite Schist (MPa)	τ=0.4405σ+20.36	$7.653Z^{0.5726}$	$5.326Z^{0.6197}$	0.7	0.8
Chlorite Schist (MPa)	τ=0.6513σ+17.76	$7.650Z^{0.624}$	$4.022Z^{0.7357}$	0.7	0.8
Quartz Mica Schist (MPa)	τ=0.5892σ+19.67	$7.357Z^{0.6112}$	$5.085Z^{0.673}$	0.7	0.8
Quartzitic Schist (MPa)	τ=0.4925σ+41.76	$27.60Z^{0.422}$	$12.16Z^{0.5547}$	0.7	0.8
Diatomite (MPa)	τ=0.6111σ+0.936	$1.708Z^{0.7816}$	$2.59Z^{0.4798}$	0.7	0.3

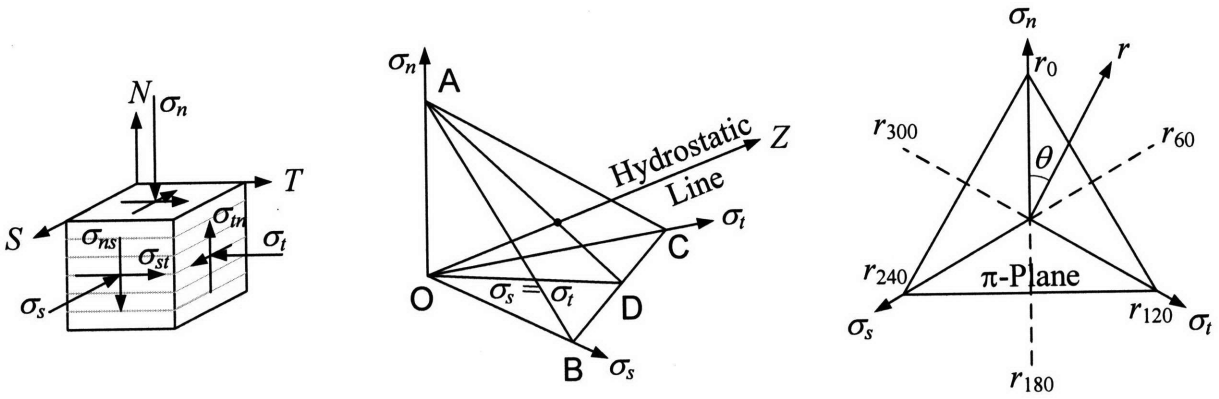

(a) **STN** Coordinate System (b) Hydrostatic Line and Triaxial Plane (c) π-Plane

Figure 4.1 Material Normal Stress Space

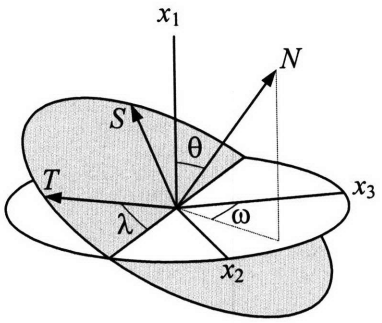

Figure 4.2 Relative Orientation of Material Structure and Stress Tensor

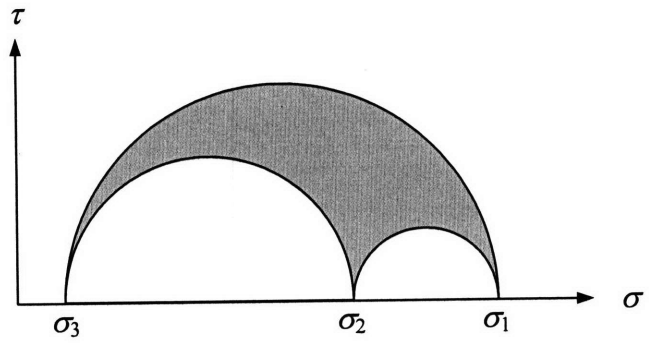

Figure 4.3 Mohr Circles of Principal Stress State (σ_1, σ_2, σ_3)

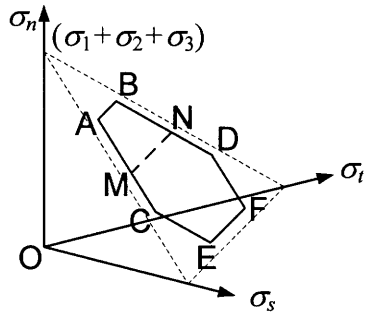

(a) 3D View of the Hexagon

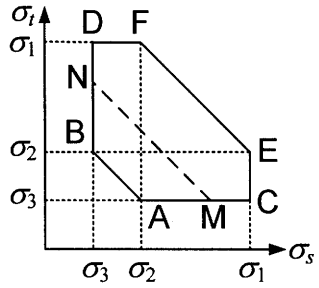

(b) Projection on (σ_s,σ_t) Plane

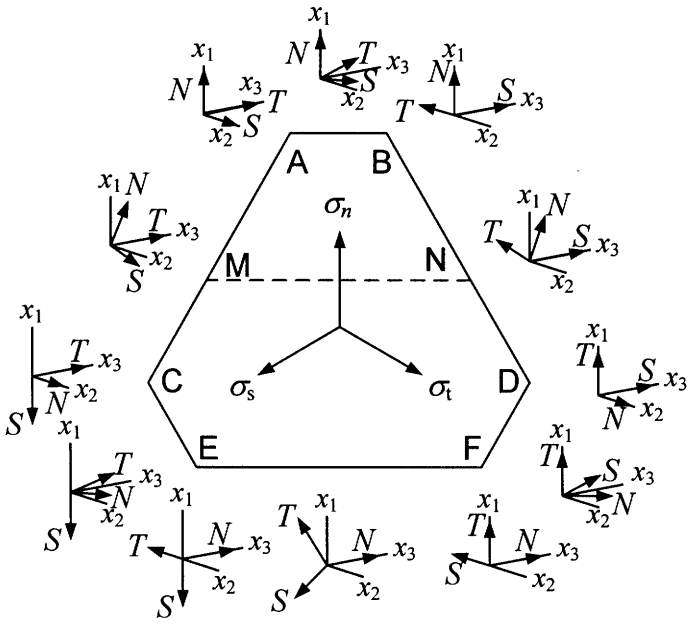

(c) Plane View of the Hexagon

Figure 4.4 Representation of True Triaxial Stress in MNSS

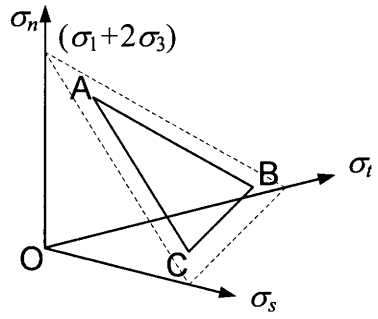

(a) 3D View of the Right Triangle

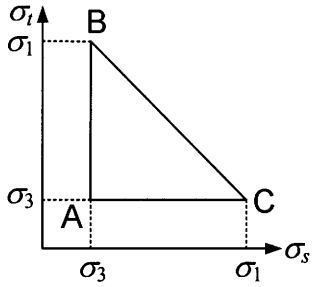

(b) Projection on (σ_s,σ_t) Plane

Figure 4.5 Representation of Conventional Triaxial Stress in MNSS

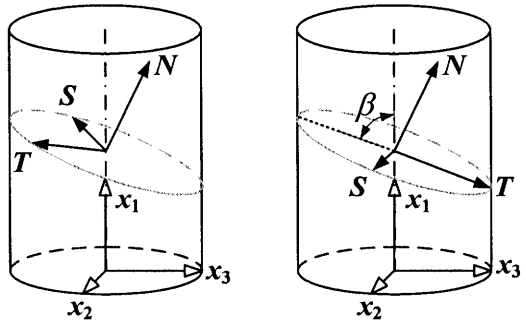

(a) General Case (b) S and x_2 Coincide

Figure 4.6 Orientation of Isotropic Planes in a Cylindrical Specimen

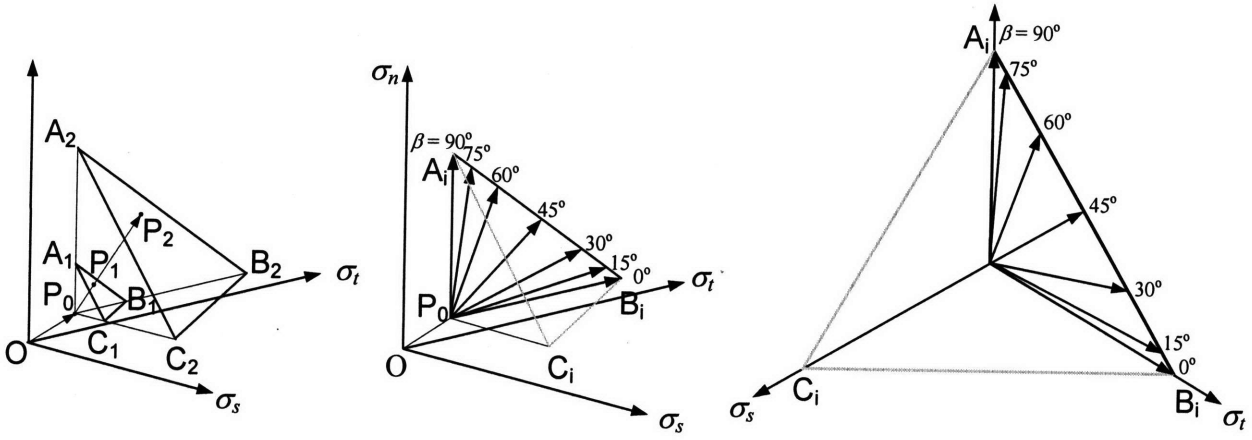

(a) General Case (b) S and $\mathbf{x_2}$ coincide (c) π-Plane Representation

Figure 4.7 Stress Paths of Conventional Triaxial Compression Test

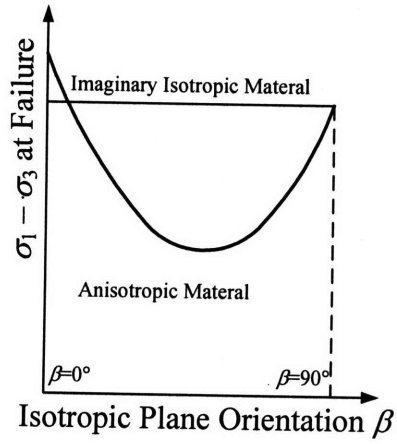

Figure 4.8 Failure of Anisotropic Rock in Conventional Triaxial Compression Test

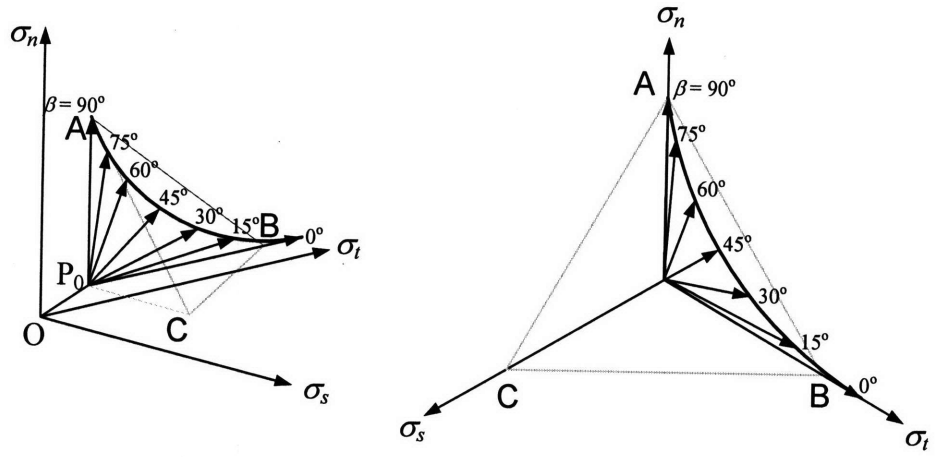

(a) 3D View (b) π-Plane Representation

Figure 4.9 Failure of Anisotropic Material in MNSS

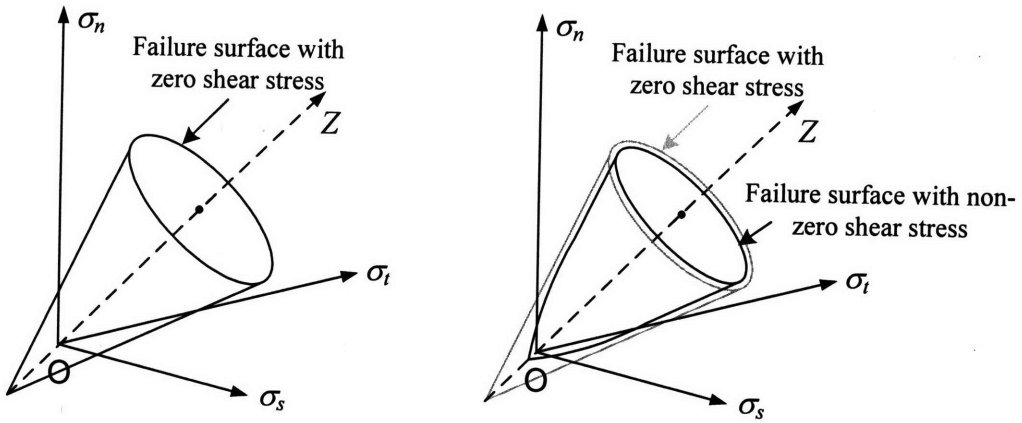

(a) Zero Shear Stress (b) Non-Zero Shear Stress

Figure 4.10 Failure Surface of Drucker-Prager Criterion in MNSS

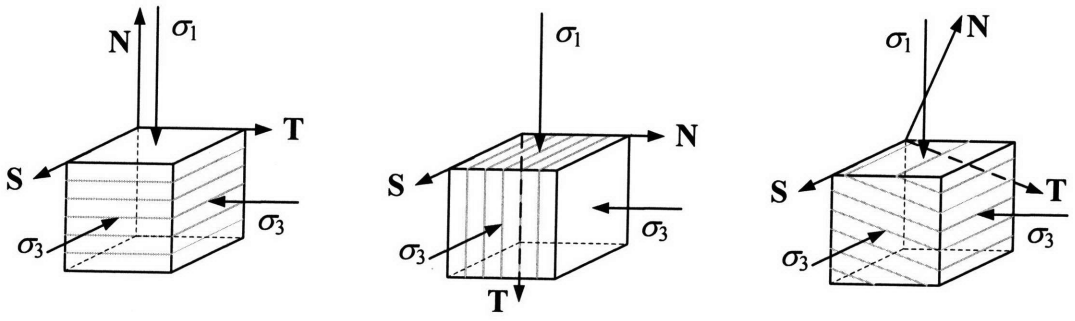

(a) $\beta = 90°$ (b) $\beta = 0°$ (c) β is between 0° and 90°

Figure 4.11 Different Isotropic Plane Orientations in a Conventional Triaxial Test

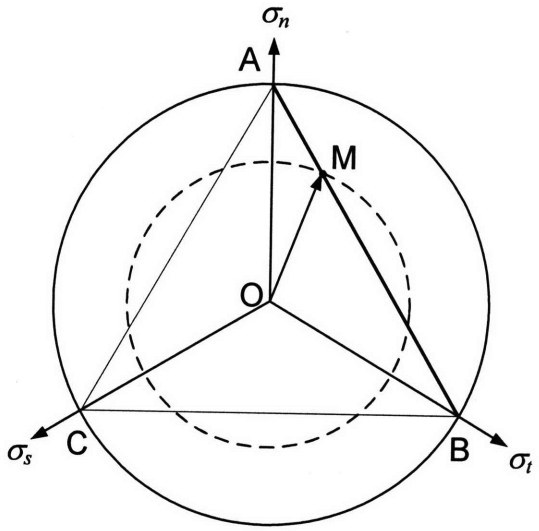

Figure 4.12 Prediction of Conventional Triaxial Strength by Drucker-Prager Criterion in MNSS

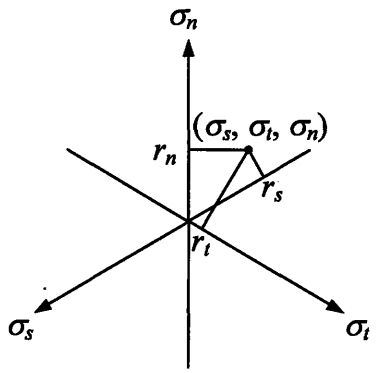

Figure 4.13 Determination of r_n, r_s, and r_t

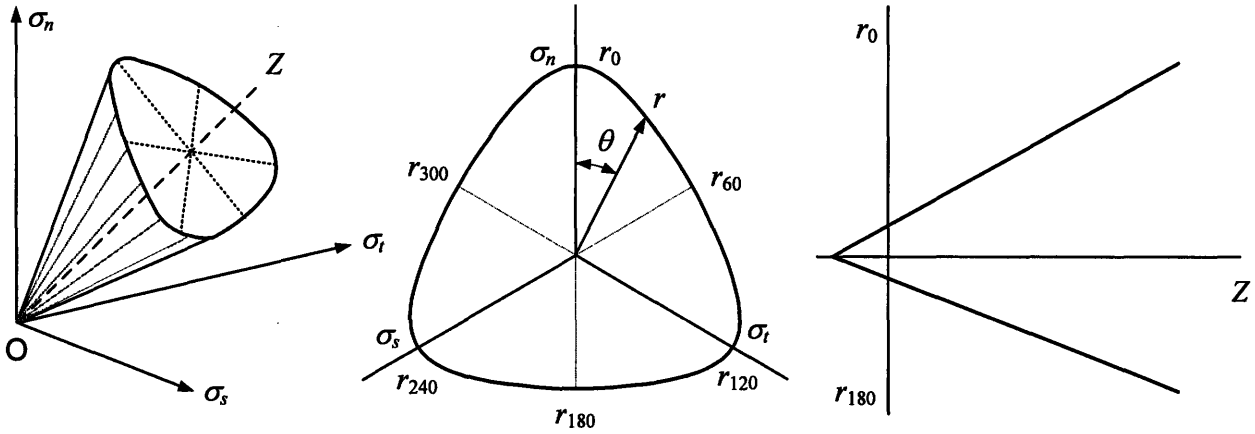

(a) 3D View (b) π-plane Cross-Section (c) Triaxial Plane Cross-Section

Figure 4.14 Matsuoka-Nakai Failure Surface with All Zero Shear Stresses

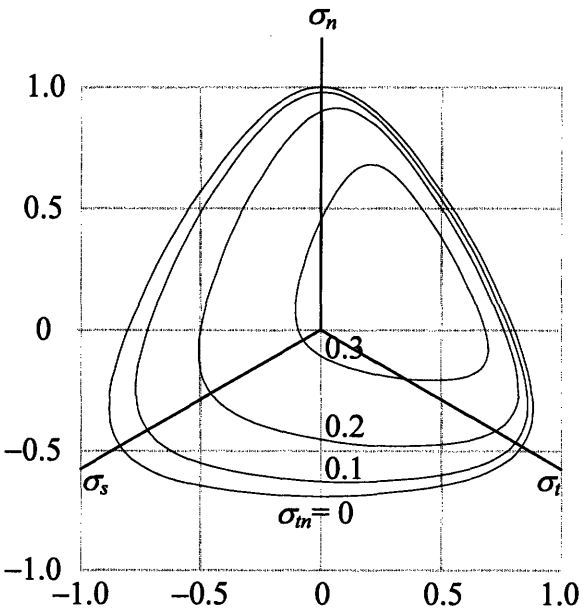

Figure 4.15 Matsuoka-Nakai Failure Surface with Increasing Shear Stress σ_{tn}

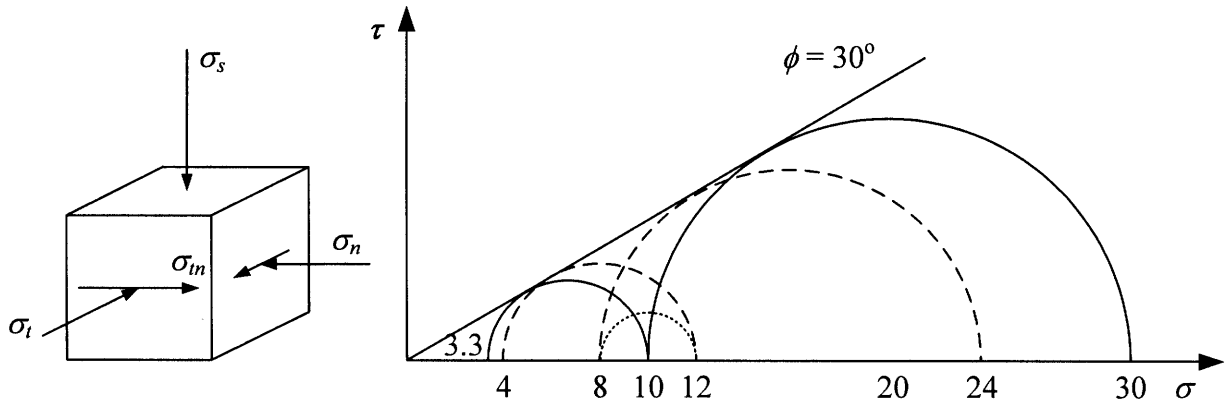

Figure 4.16 Explanation of the Shape Distortion of Matsuoka-Nakai Failure Surface

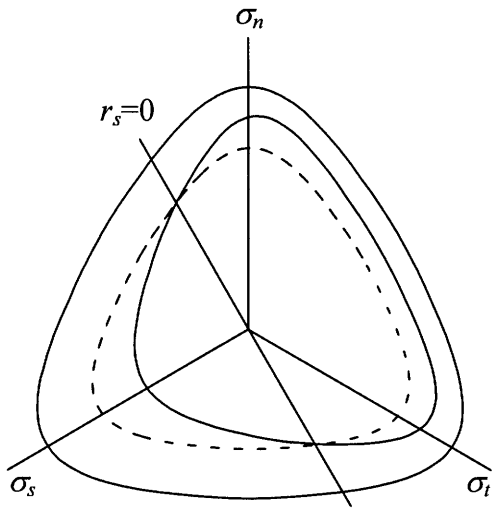

Figure 4.17 Separating the Size Reduction and Shape Distortion in the MNSS

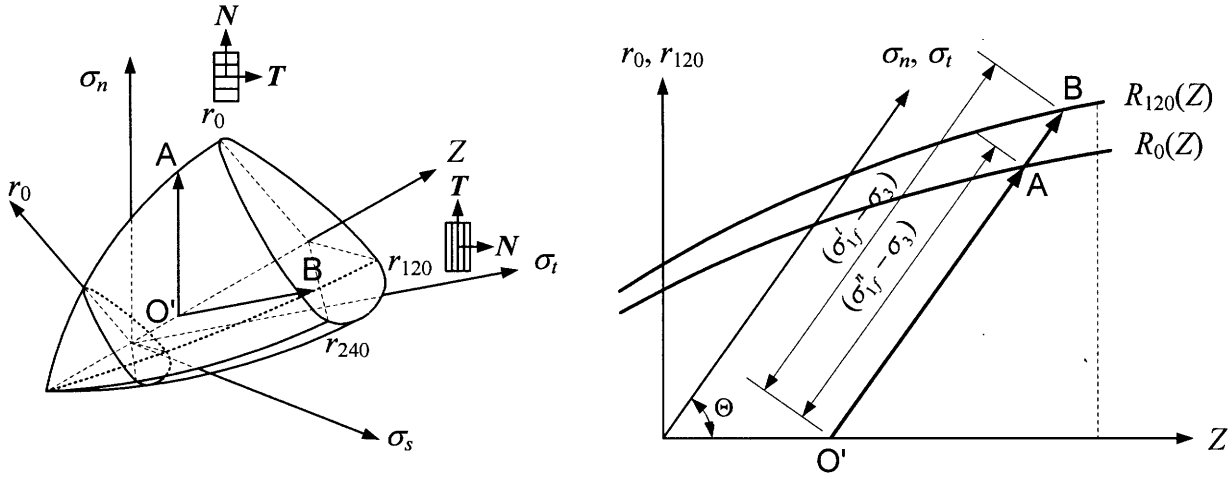

(a) 3D View of Bounding Failure Surface (b) Overlapped (r_0,Z) and (r_{120},Z) Planes

Figure 4.18 Bounding Failure Surface for an Anisotropic Material

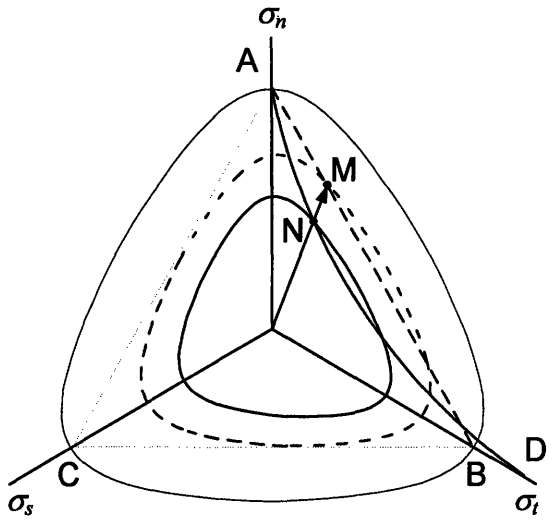

Figure 4.19 Variation of Failure Surface Geometry for an Anisotropic Material in the MNSS

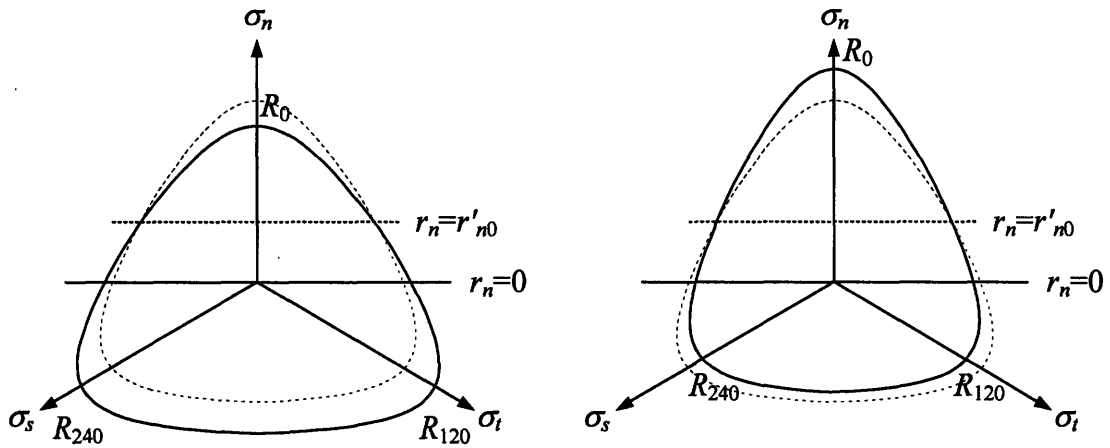

(a) Distorted Shape with $A > 0$ (b) Distorted Shape with $A < 0$

Figure 4.20 Creating Distorted π-plane Cross-Section of Matsuoka-Nakai Criterion in the MNSS Based on Linear Shape Distortion

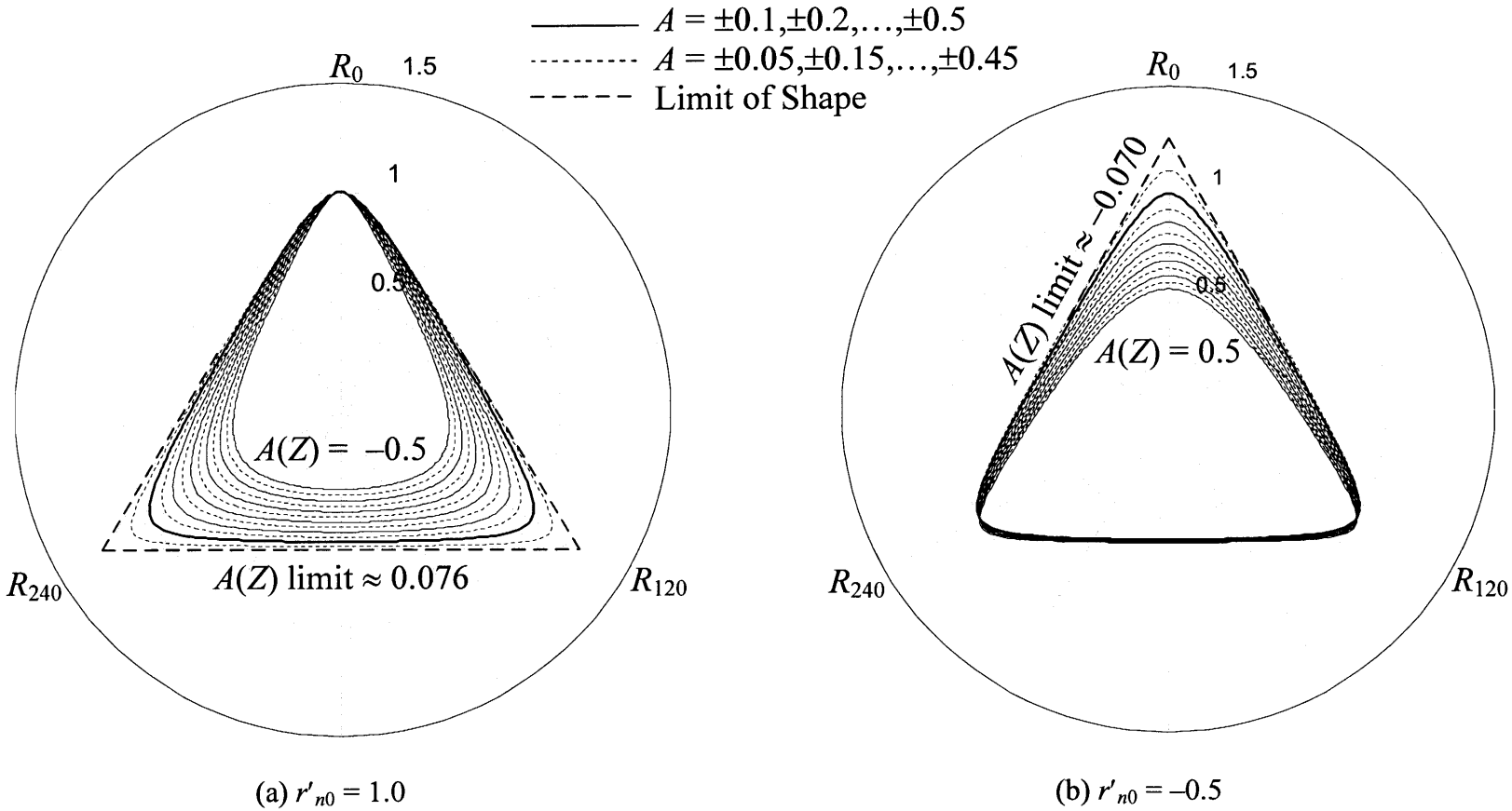

(a) $r'_{n0} = 1.0$

(b) $r'_{n0} = -0.5$

Figure 4.21 Distorted π-plane Cross-Sections at $\beta_s = 0.6$

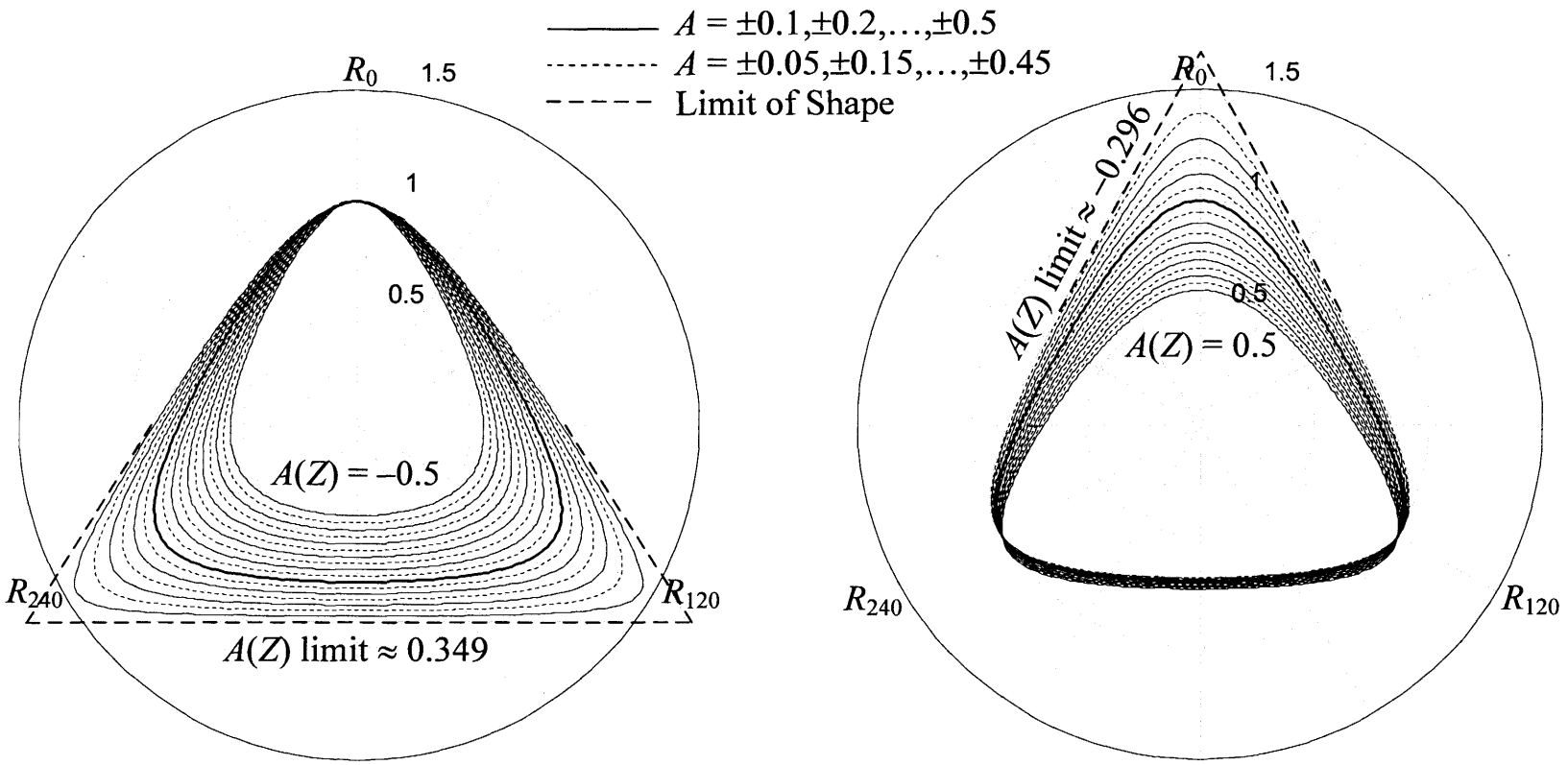

(a) $r'_{n0} = 1.0$

(b) $r'_{n0} = -0.5$

Figure 4.22 Distorted π-plane Cross-Sections at $\beta_s = 0.7$

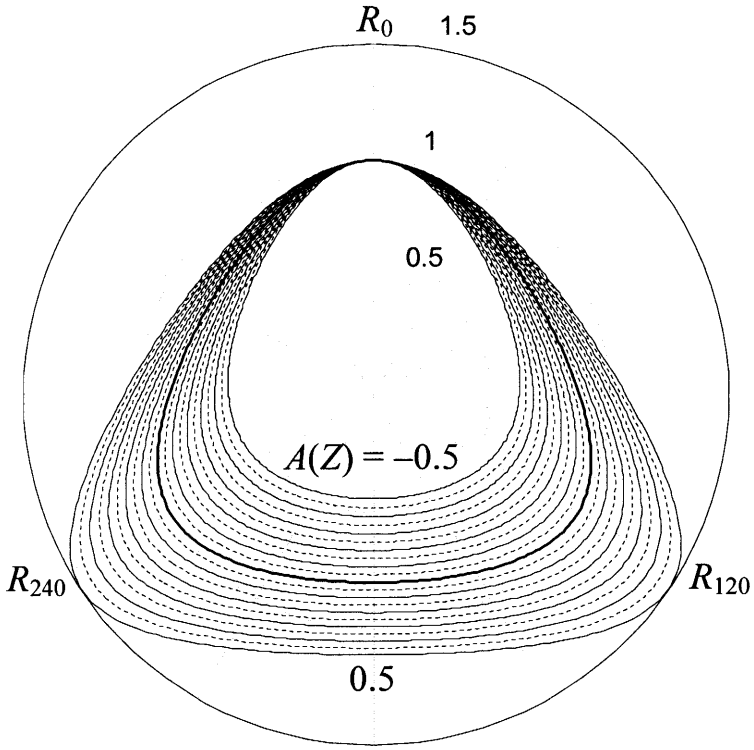

(a) $r'_{n0} = 1.0$

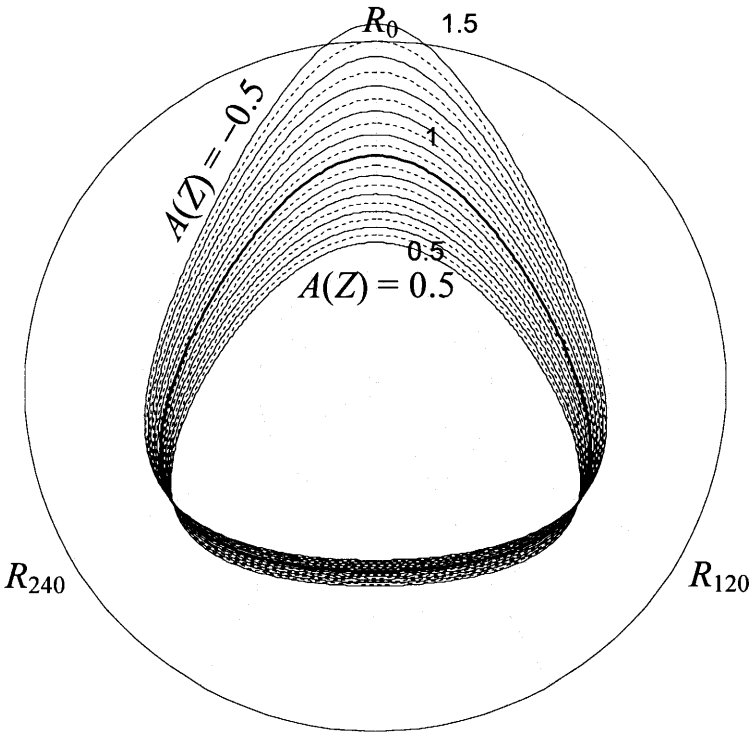

(b) $r'_{n0} = -0.5$

Figure 4.23 Distorted π-plane Cross-Sections at $\beta_s = 0.8$

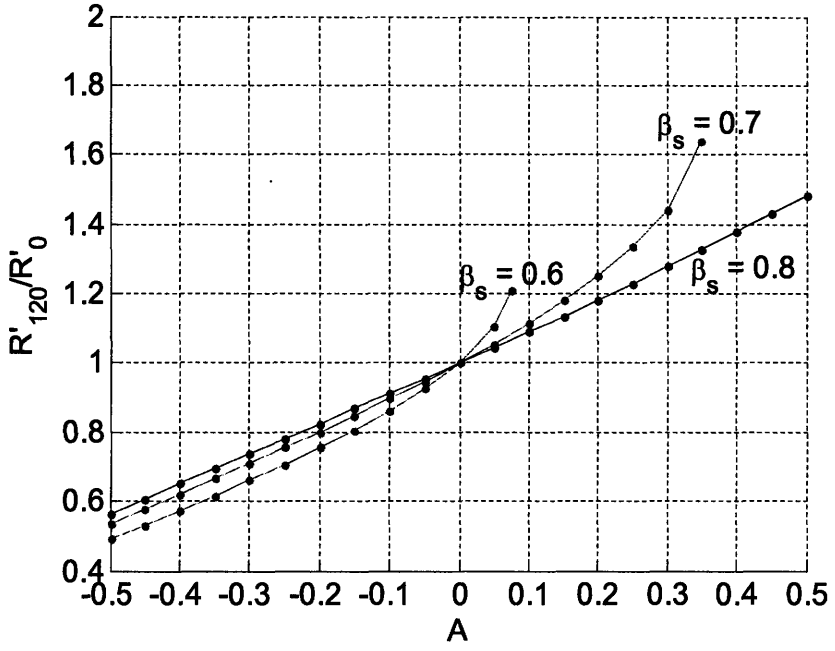

(a) $r'_{n0} = 1.0$

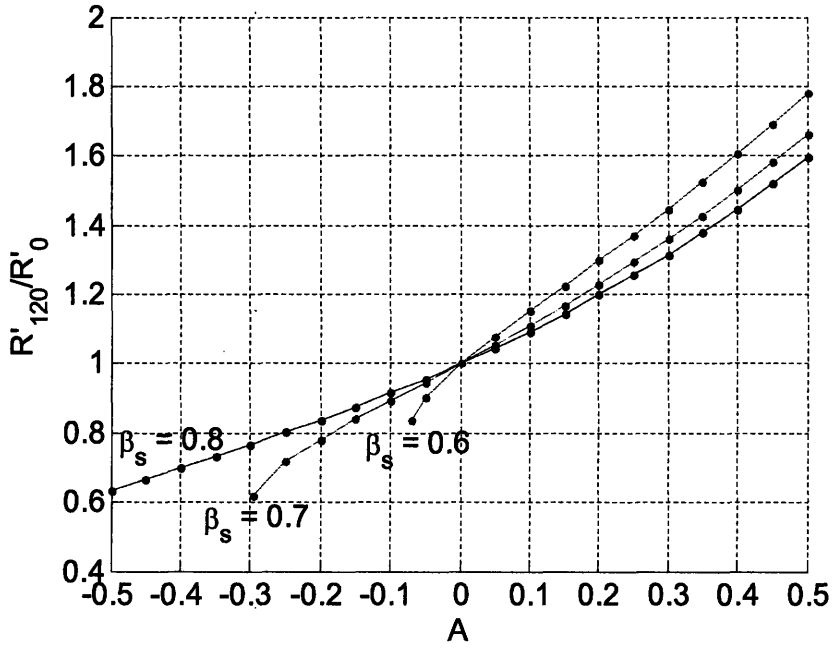

(b) $r'_{n0} = -0.5$

Figure 4.24 Variation of R_{120}/R_0 with A(Z) at Different r'_{n0} and β_s

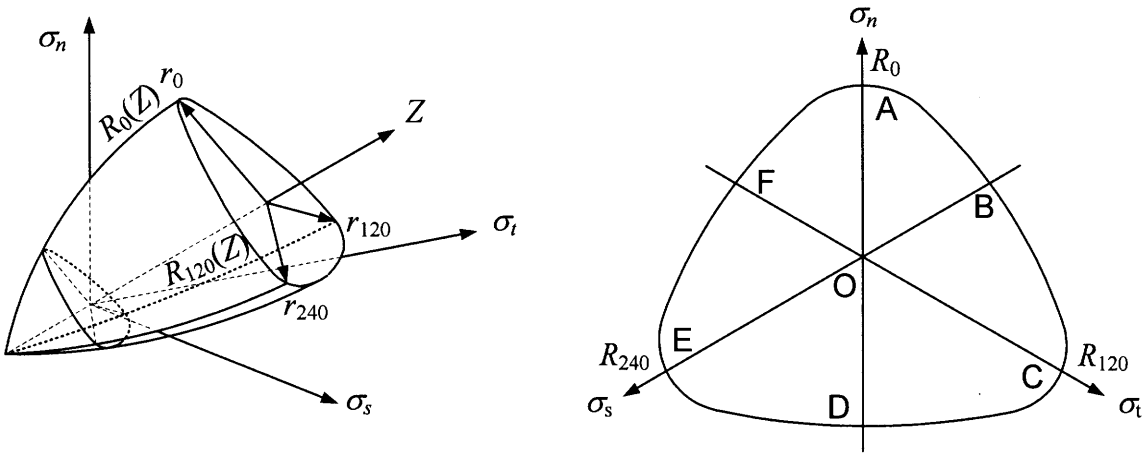

Figure 4.25 Bounding Failure Surface of the Anisotropic Matsuoka-Nakai Failure Criterion

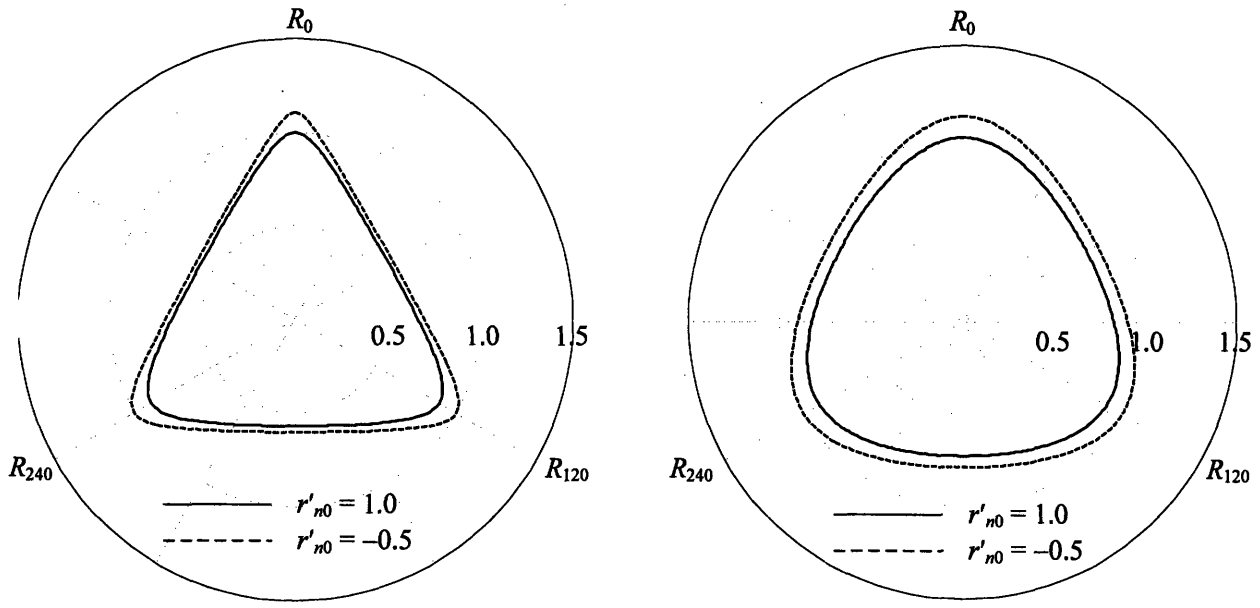

(a) $\beta_s = 0.6$ (b) $\beta_s = 0.8$

Figure 4.26 π-plane Cross-section of Bounding Failure Surface with $R'_{120}/R'_0 = 0.9$

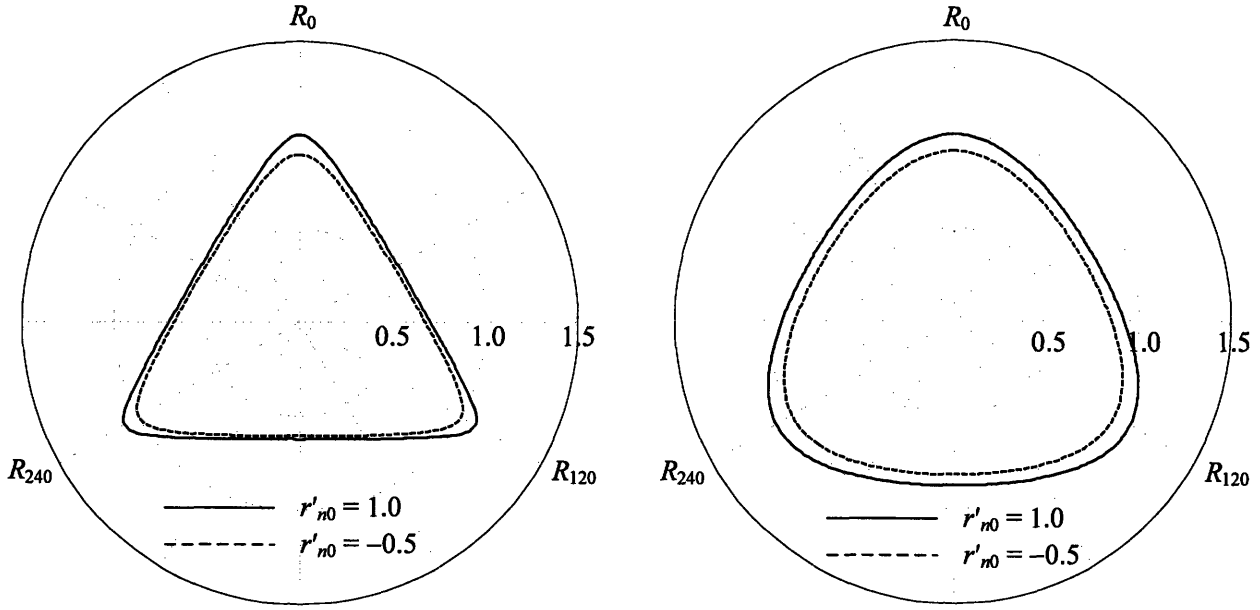

(a) $\beta_s = 0.6$ (b) $\beta_s = 0.8$

Figure 4.27 π-plane Cross-section of Bounding Failure Surface with $R'_{120}/R'_0 = 1.1$

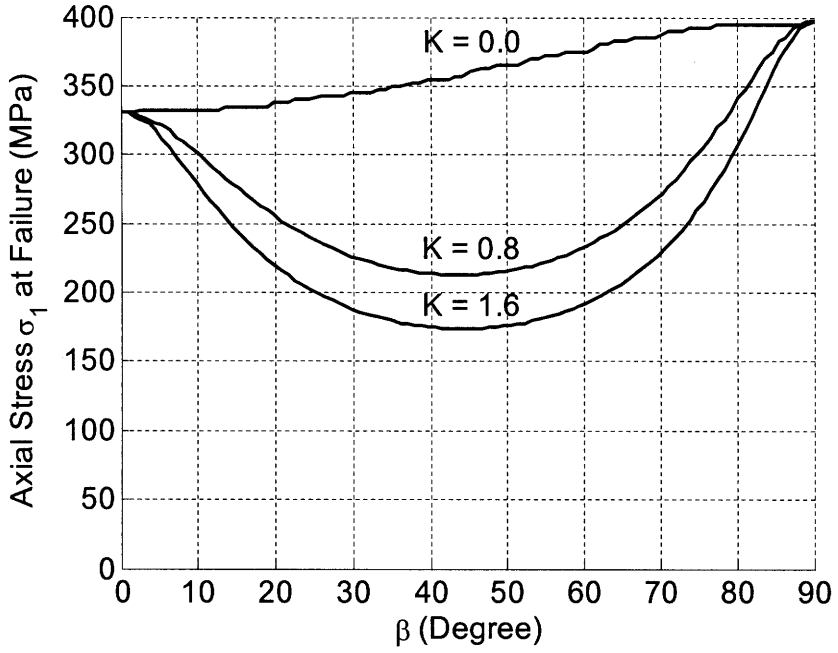

(a) $r'_{n0} = 1.0$

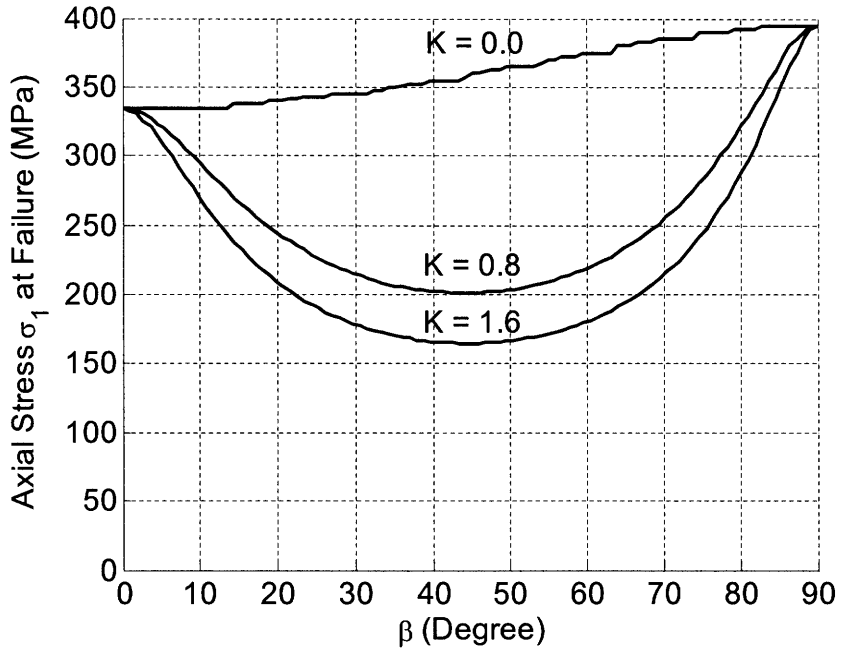

(b) $r'_{n0} = -0.5$

Figure 4.28 Predicted Triaxial Strength at $R'_{120}/R'_0 = 0.9$, $\beta_s = 0.6$

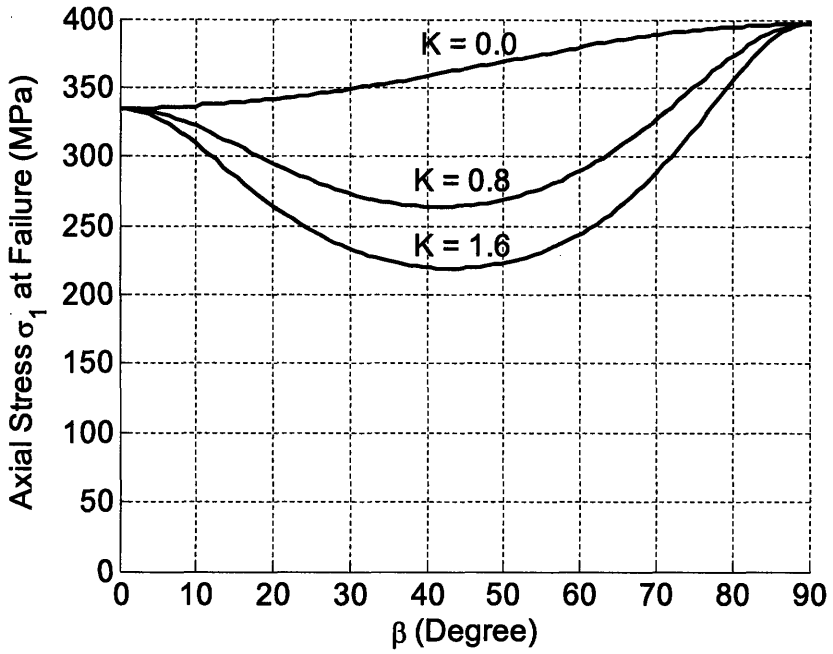

(a) $r'_{n0} = 1.0$

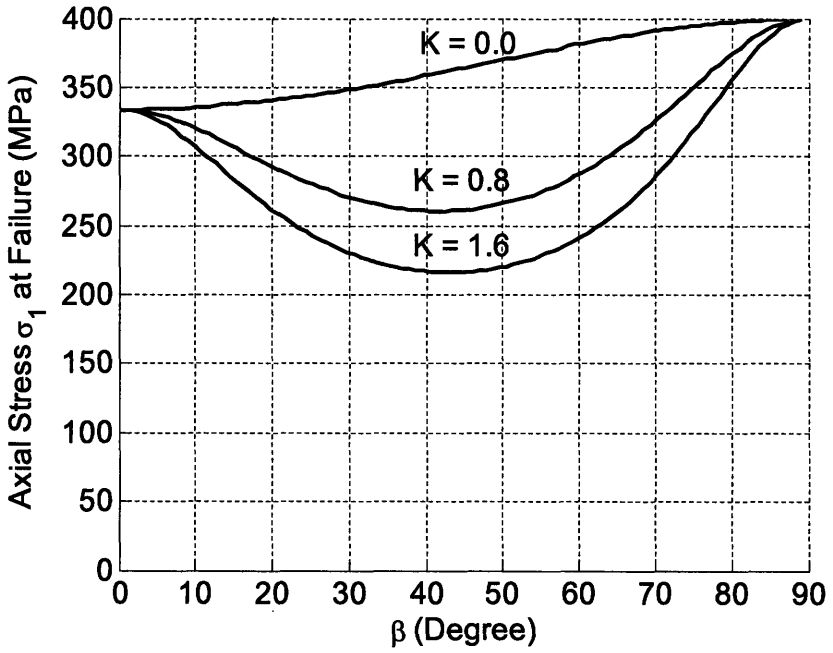

(b) $r'_{n0} = -0.5$

Figure 4.29 Predicted Triaxial Strength at $R'_{120}/R'_0 = 0.9$, $\beta_s = 0.8$

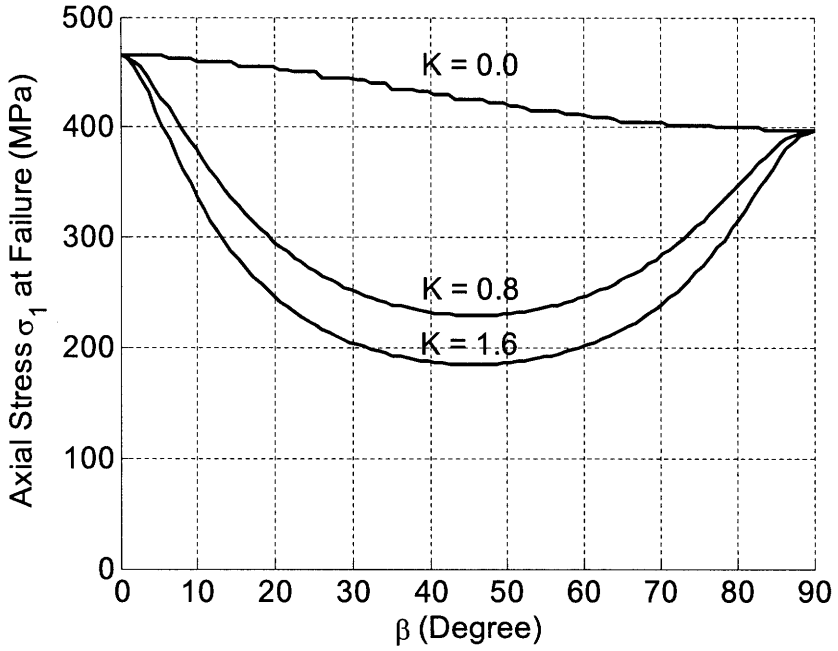

(a) $r'_{n0} = 1.0$

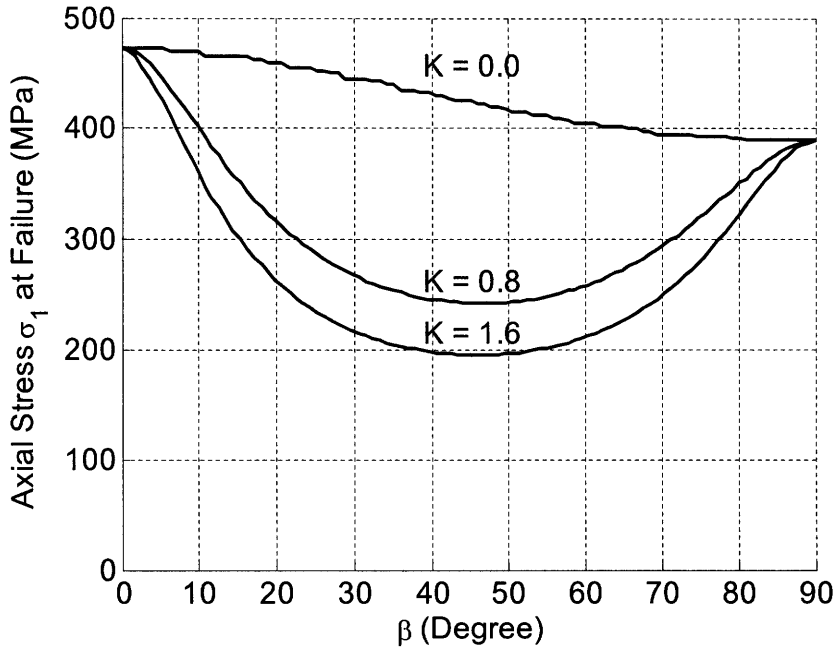

(b) $r'_{n0} = -0.5$

Figure 4.30 Predicted Triaxial Strength at $R'_{120}/R'_0 = 1.1$, $\beta_s = 0.6$

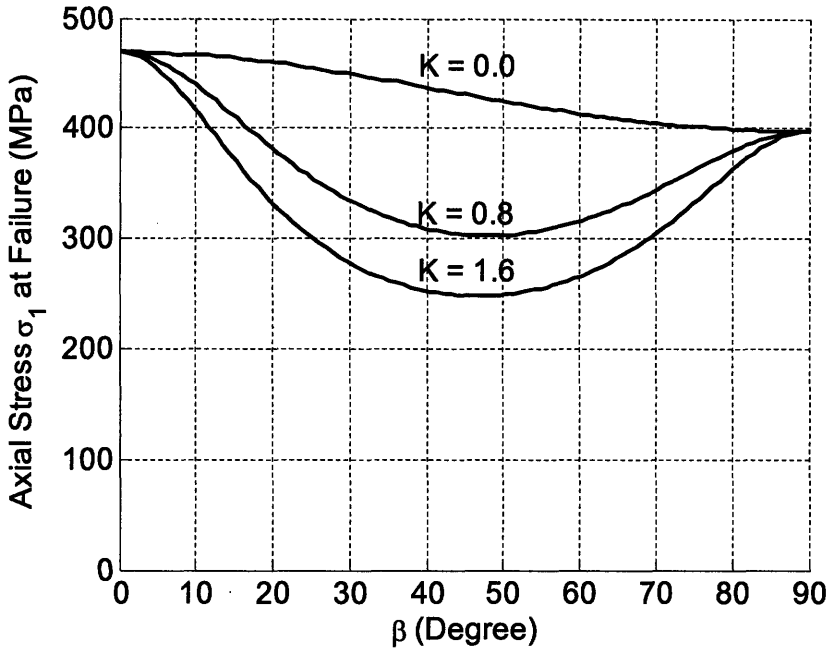

(a) $r'_{n0} = 1.0$

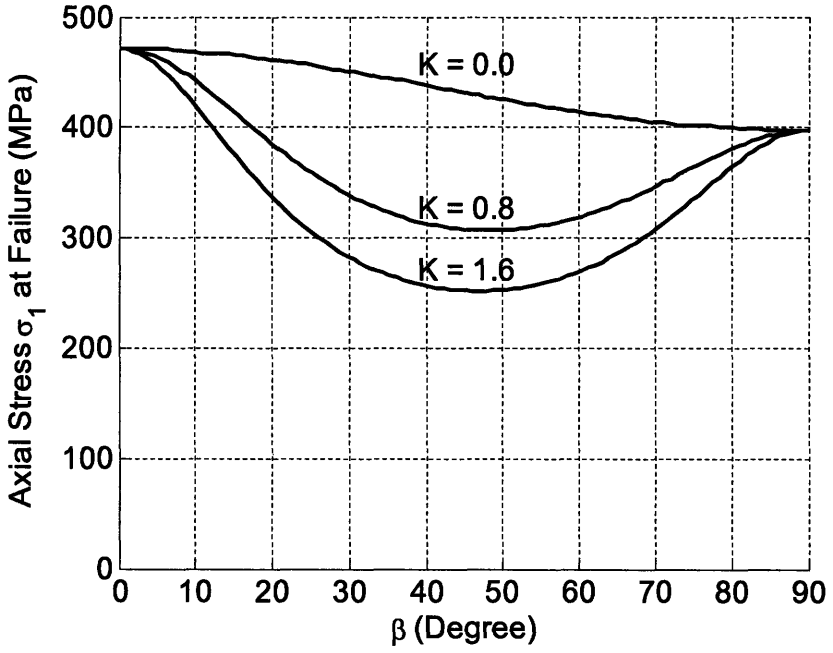

(b) $r'_{n0} = -0.5$

Figure 4.31 Predicted Triaxial Strength at $R'_{120}/R'_0 = 1.1$, $\beta_s = 0.8$

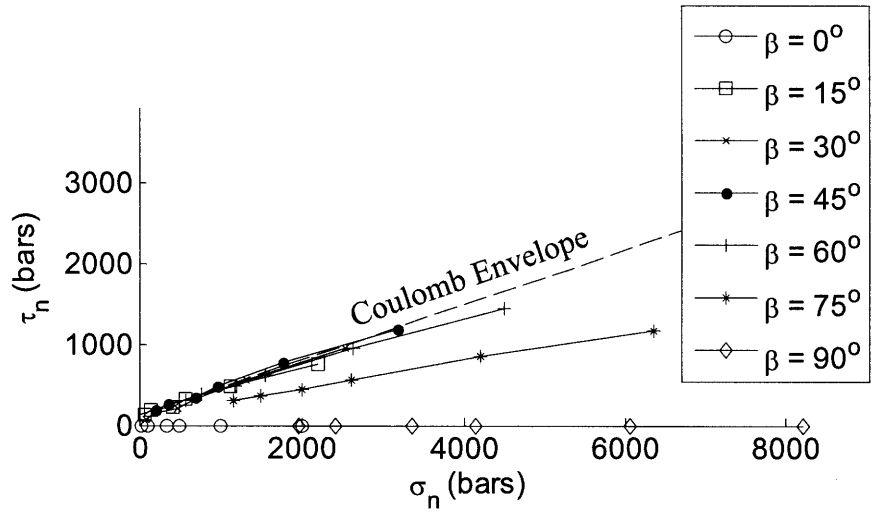

Figure 4.32 Linear Shear Criterion of Martinsburg Slate

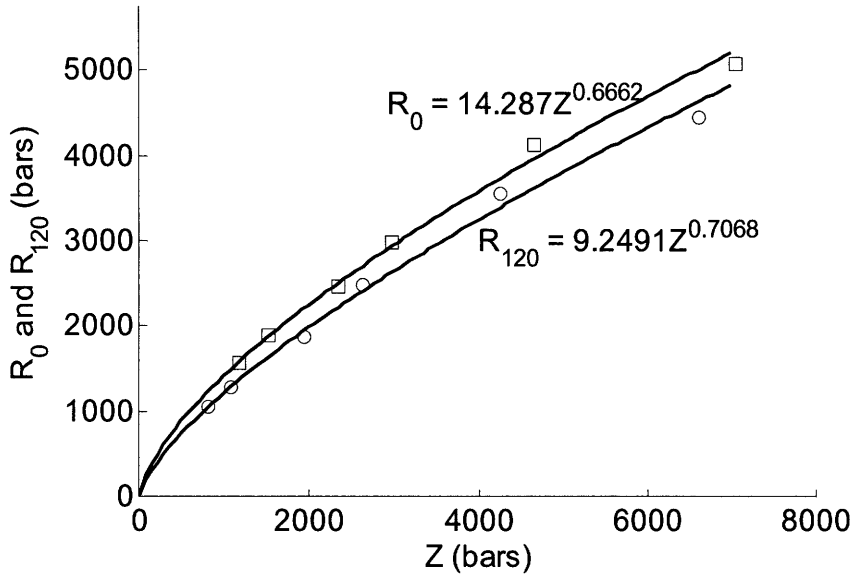

Figure 4.33 $R_0(Z)$ and $R_{120}(Z)$ for Martinsburg Slate

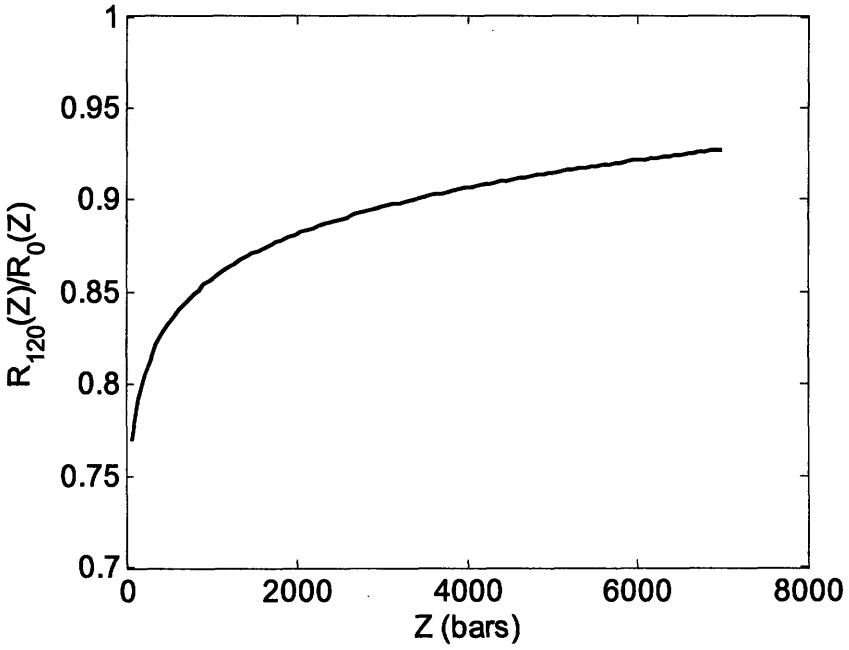

Figure 4.34 $R_{120}(Z)/R_0(Z)$ for Martinsburg Slate

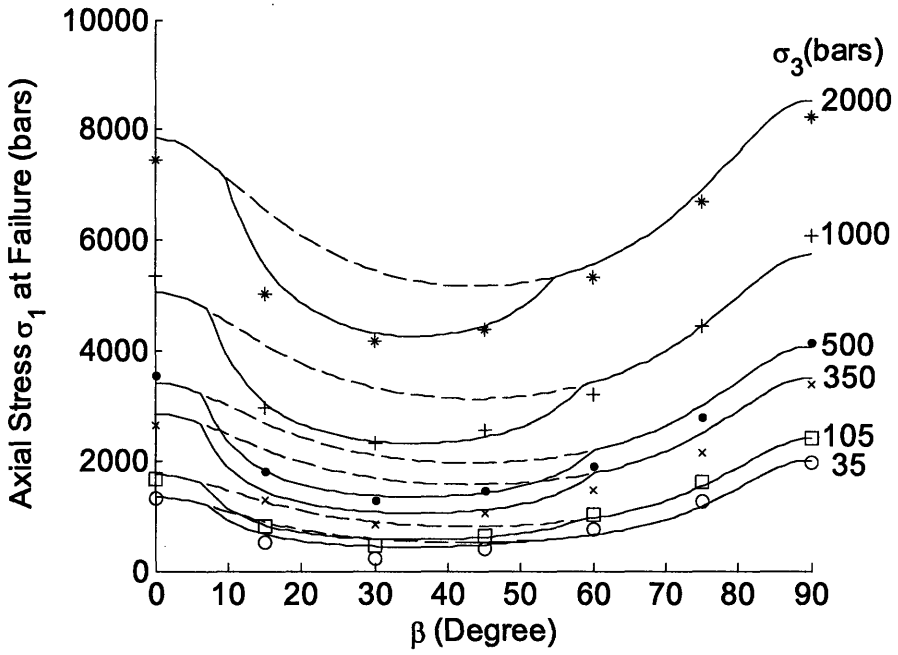

Figure 4.35 Comparison of Measured and Predicted Strength for Martinsburg Slate

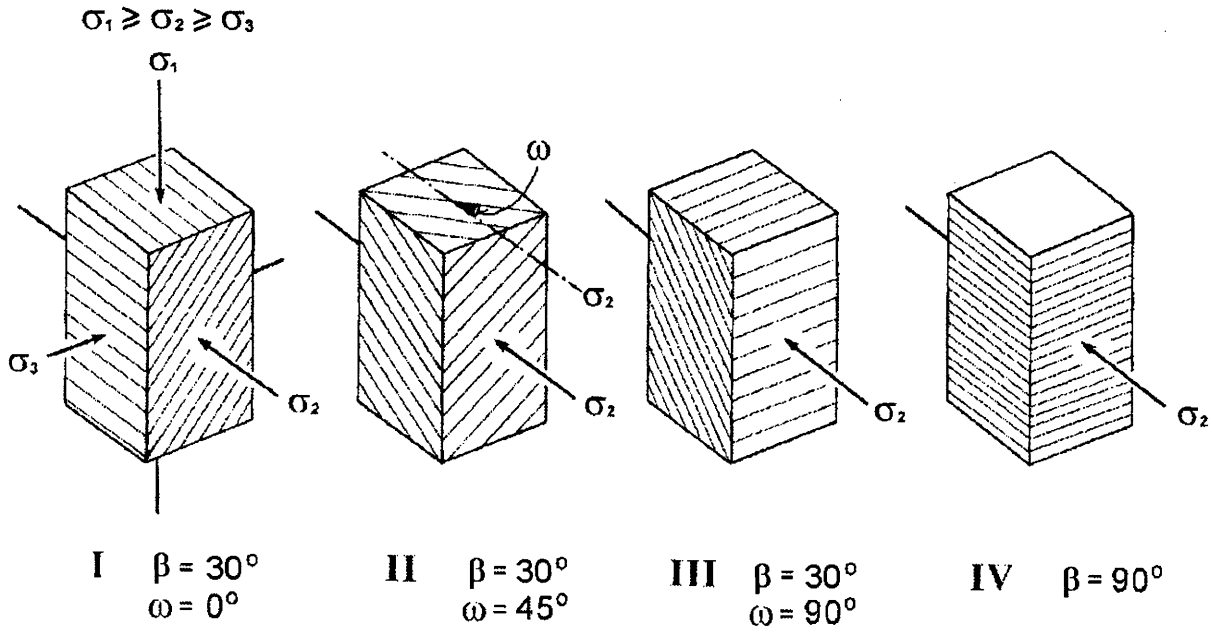

Figure 4.36 Four Different Test Modes for Chichibu Green Schist (from Mogi, 2007)

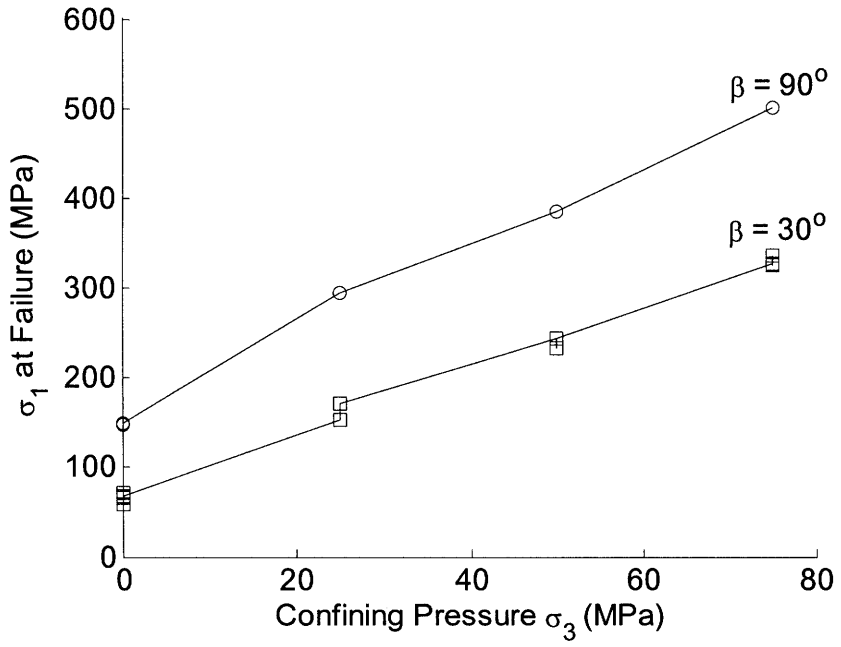

Figure 4.37 Conventional Triaxial Tests on Chichibu Green Schist (data from Mogi, 2007)

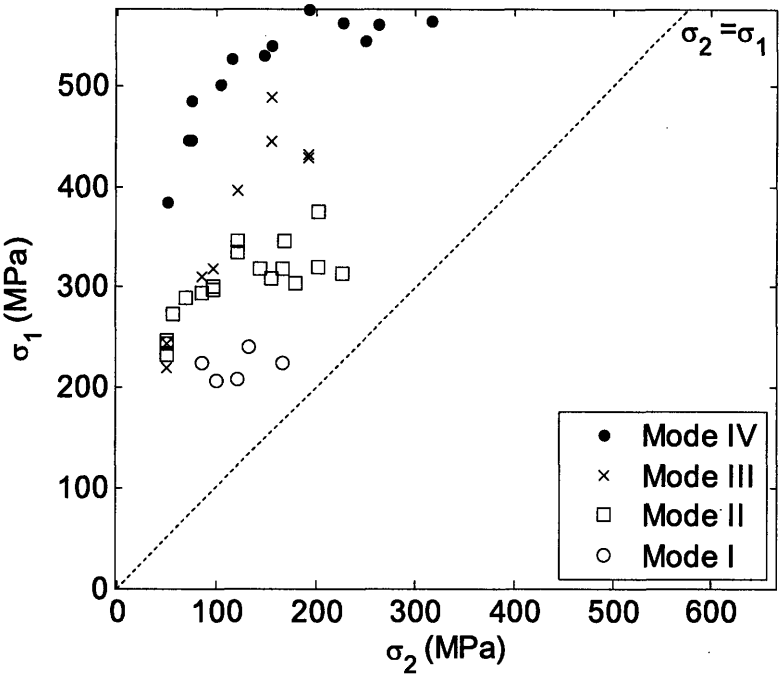

Figure 4.38 True Triaxial Tests on Chichibu Green Schist with σ_3 = 50 MPa (data from Mogi, 2007)

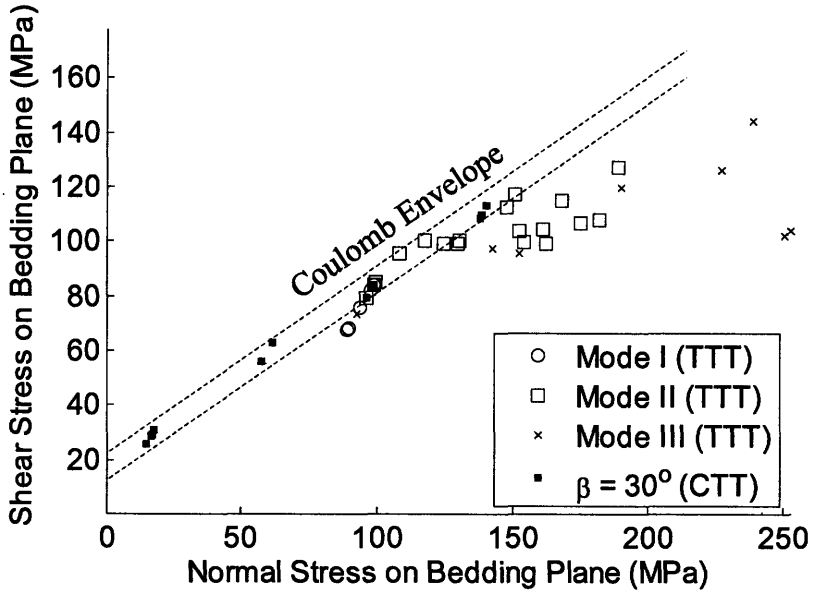

Figure 4.39 The Friction Envelope for Chichibu Green Schist (CTT: Conventional Triaxial Tests, TTT: True Triaxial Tests)

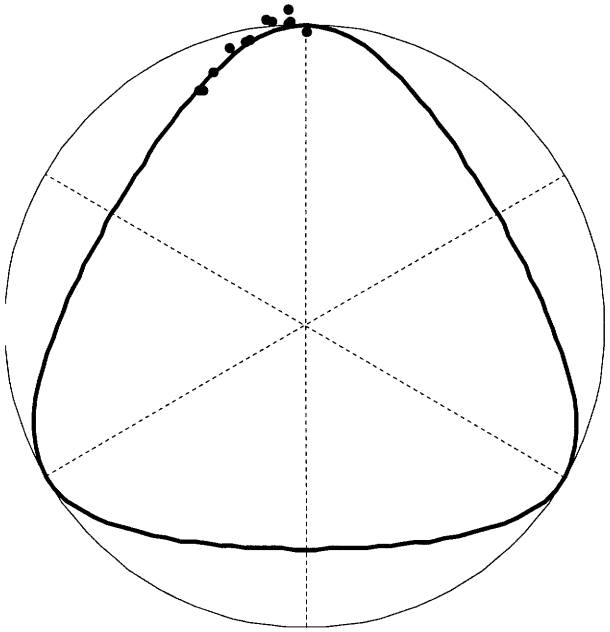

Figure 4.40 Normalized Bounding Failure Surface π-Plane Cross-Section for Chichibu Green Schist (β_s = 0.75, R_{120}/R_0 = 1.0)

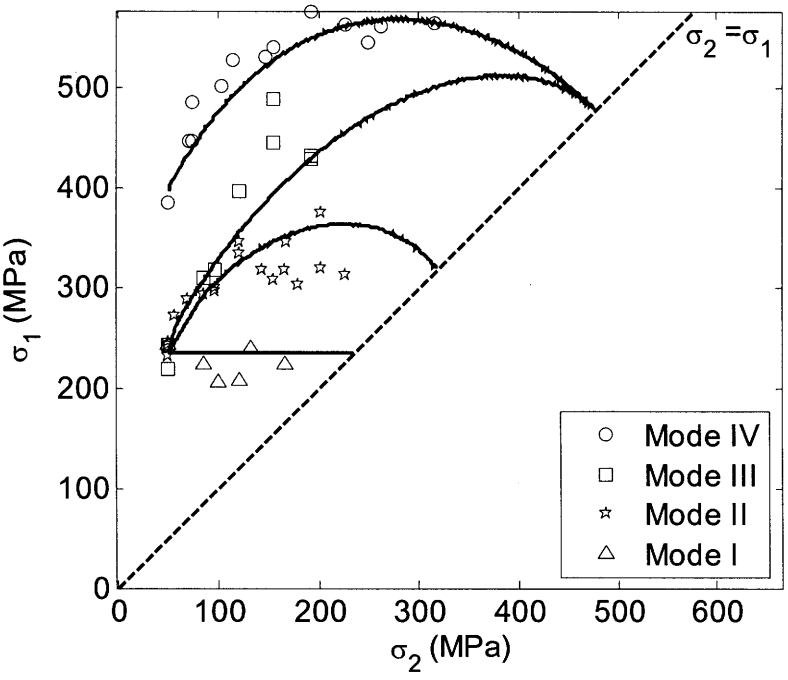

Figure 4.41 Comparison of Predicted and Experimental Strength of Chichibu Green Schist

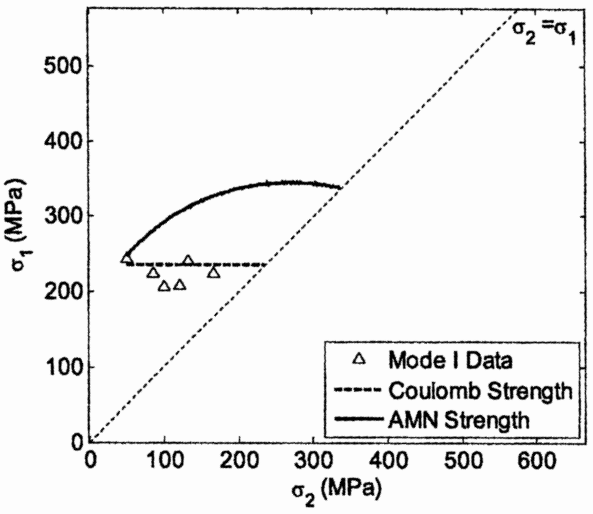

(a) Mode I

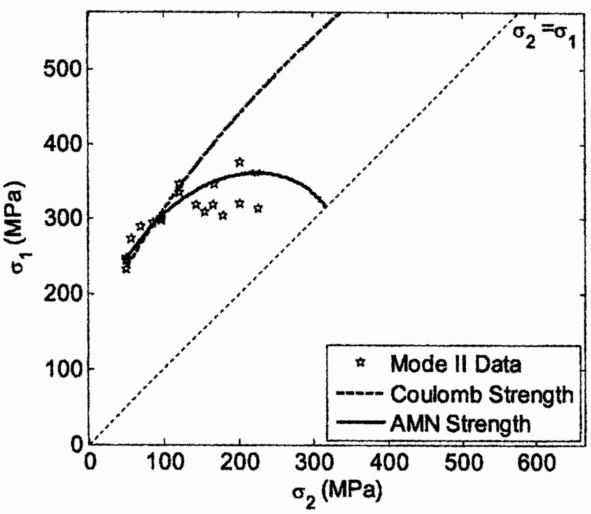

(b) Mode II

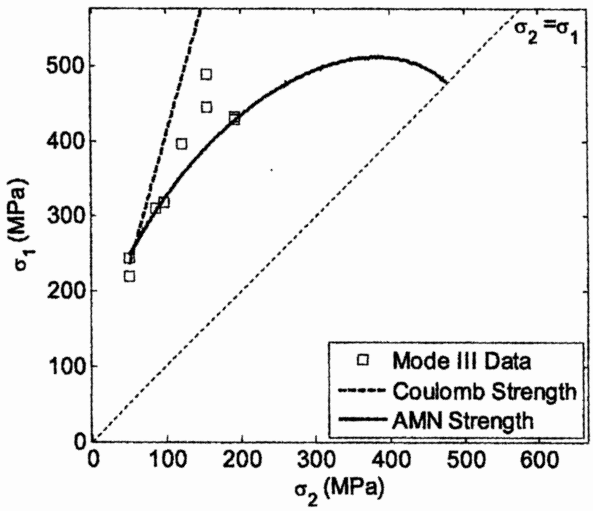

(c) Mode III

Figure 4.42 Strength Predicted by Coulomb Criterion and AMN Failure Criterion for Different Modes

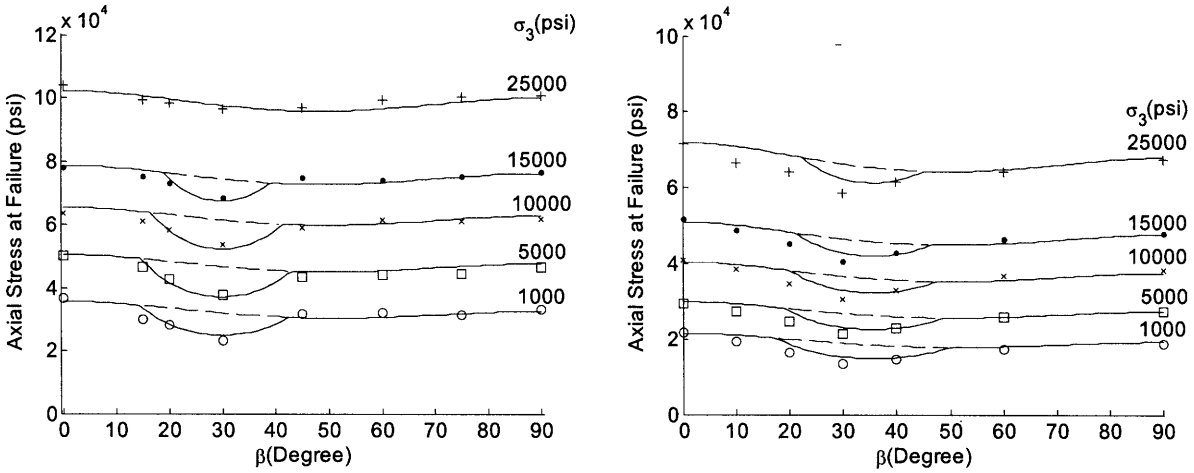

(a) Green River Shale I

(b) Green River Shale II

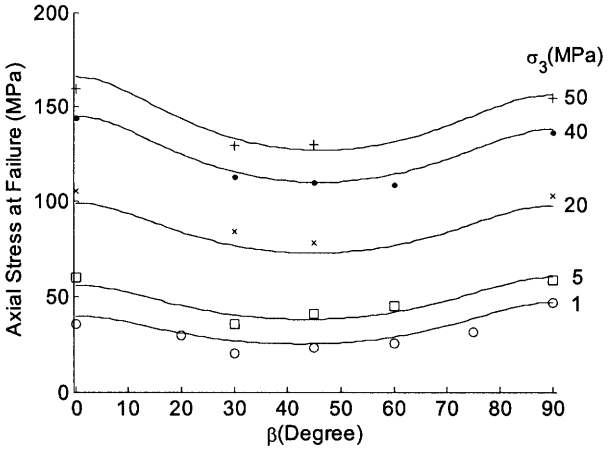

(c) Tournemire Shale

Figure 4.43 Comparison of Measured and Predicted Strength for Shales

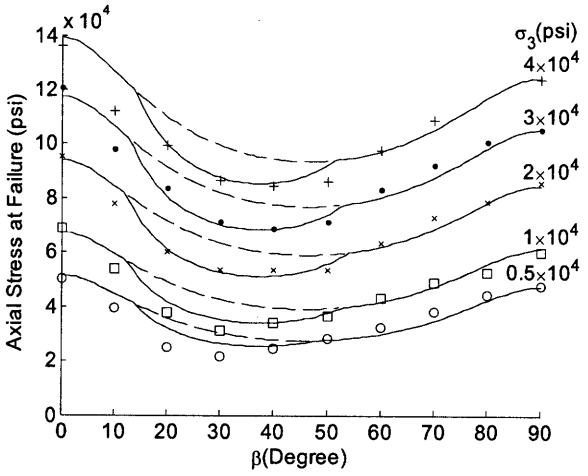

(a) Austin Slate

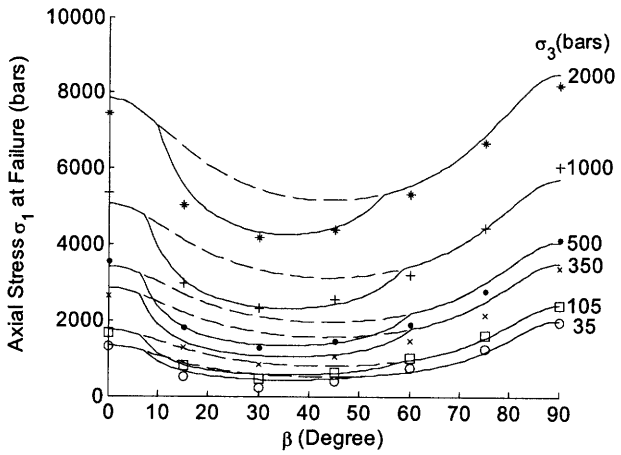

(b) Martinsburg Slate

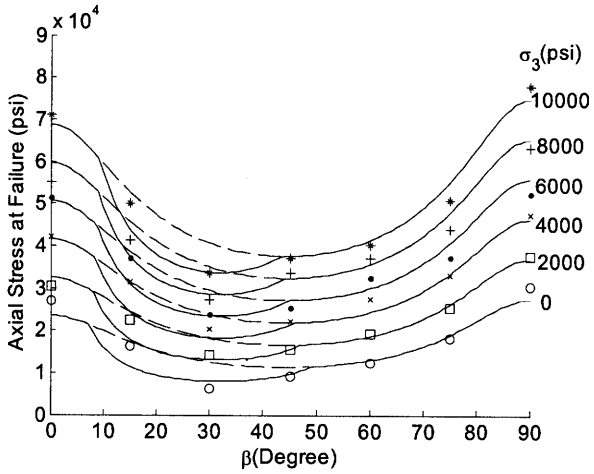

(c) Penrhyn Slate

Figure 4.44 Comparison of Measured and Predicted Strength for Slates

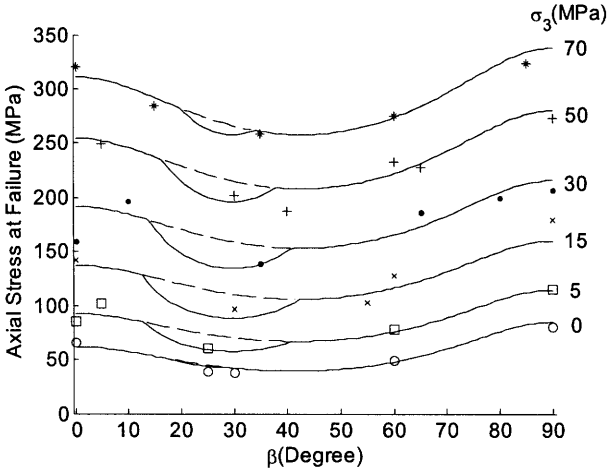

(a) Carbonaceous Phyllite

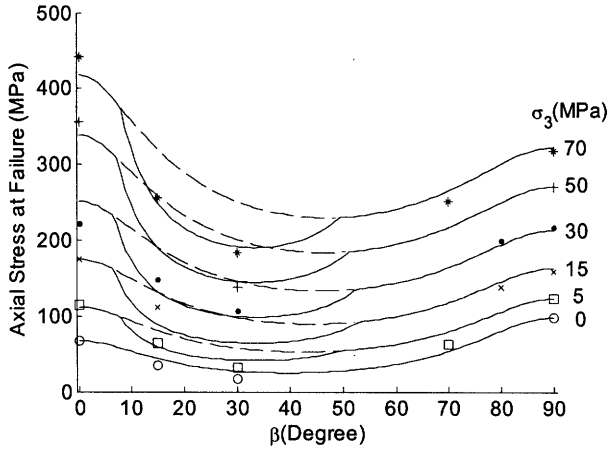

(b) Micaceous Phyllite

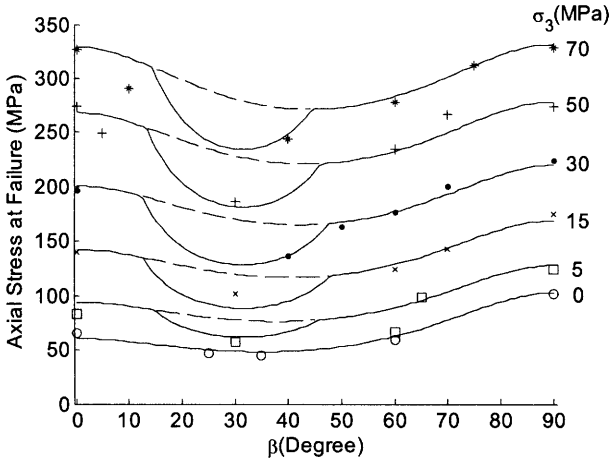

(c) Quartzitic Phyllite

Figure 4.45 Comparison of Measured and Predicted Strength for Phyllites

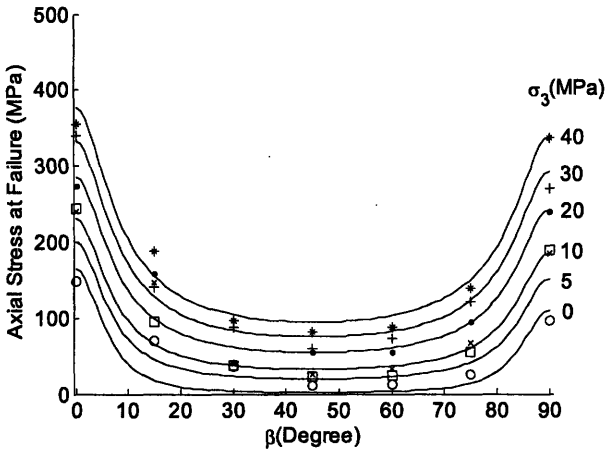

(a) Angers Schist

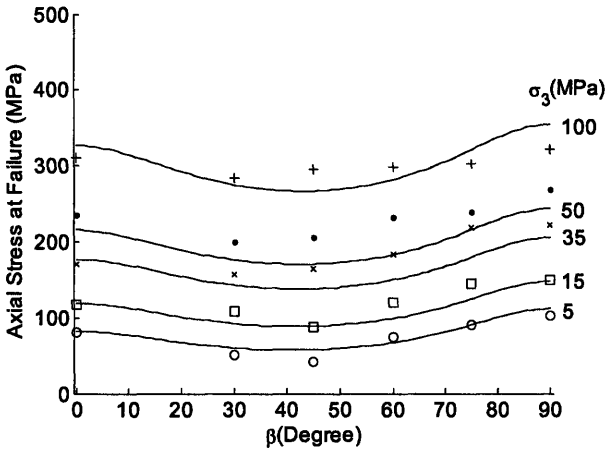

(b) Biotite Schist

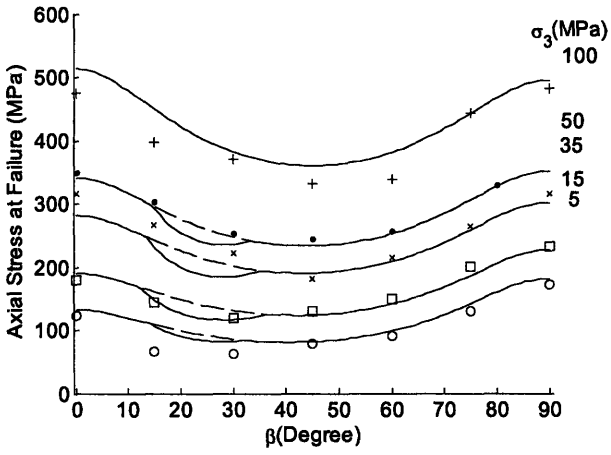

(c) Chlorite Schist

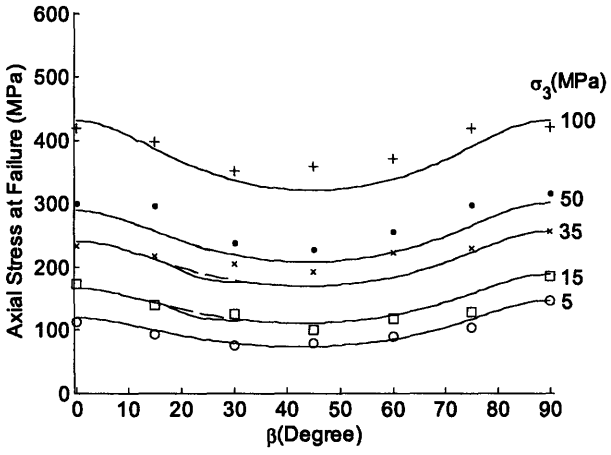

(d) Quartz Mica Schist

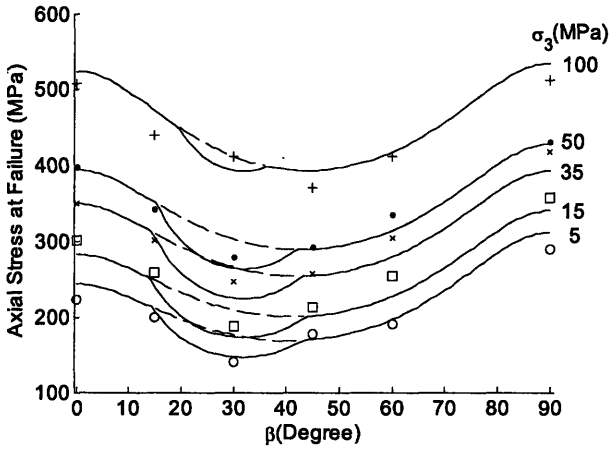

(e) Quartzitic Schist

Figure 4.46 Comparison of Measured and Predicted Strength for Schists

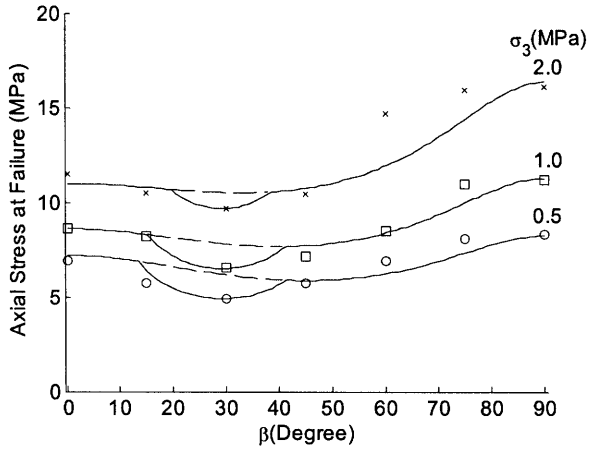

Figure 4.47 Comparison of Measured and Predicted Strength for Diatomite

5 Application of the AMN Criterion in the Borehole Stability Problem

A new anisotropic criterion, the anisotropic Matsuoka-Nakai criterion was proposed in Chapter 4. It has been applied to interpret the experimental result on anisotropic rocks, both for conventional and true triaxial tests. The agreement between the predictions and the experimental results are generally very good. In this chapter, the AMN criterion will be applied to analyze the problem of borehole stability.

Before the criterion can be applied, the stress distribution around a borehole in anisotropic rock must be obtained. In order to do so, the theory outlined by Lekhnitskii (1963) and Amadei (1983) for a cylindrical hole in homogeneous, linearly elastic, anisotropic medium will be applied. A computer program was developed to implement this theory. The AMN criterion will be applied to the stresses obtained from the program, and the stability of borehole will be studied.

5.1 Problem Statement

It is assumed that the borehole is drilled within Chichibu green schist to a depth of 4000m. The total density of the rock is assumed to be 2.5t/m^3. The total vertical stress can then be obtained to be σ_V = 100MPa (assuming g = 10m/s^2). The formation pore pressure, p_f, is assumed to be hydrostatic, so that p_f = 40MPa. The larger total horizontal stress is denoted σ_H, which is assumed to be $\sigma_H = 0.85\sigma_V$ = 85MPa. The smaller total horizontal stress is denoted σ_h, and it is assumed to be $\sigma_h = 0.7\sigma_V$ = 70MPa. Assuming that the Terzaghi's law of effective stress applies, the in-situ effective stresses are:

$$\sigma'_V = 60\text{MPa}, \sigma'_H = 45\text{MPa}, \sigma'_h = 30\text{MPa} \tag{5.1}$$

The mud pressure inside the borehole is denoted p_m. The effective mud pressure is defined as:

$$p' = p_m - p_f \tag{5.2}$$

which is the pressure applied on the rocks. Finally, the radius of the borehole is assumed to be:

$$a = 1.0\text{m} \tag{5.3}$$

The effective mud pressure that prevents the borehole from collapsing will be calculated based on the AMN criterion. The mode of failure of the borehole collapsing will also be studied.

5.2 Coordinate Systems

Three different coordinate systems are involved (Figure 5.1 (a)) in the borehole stability problem in a transversely isotropic medium: 1) the global coordinate system **XYZ**, 2) the local borehole frame **xyz**, and 3) the material coordinate system **STN**.

The global coordinate system can be arbitrarily selected. In this research, it will be specified that **Z** is in vertical direction, while **X** and **Y** are in horizontal directions. The local borehole frame **xyz** is based on the orientation of the borehole, where **z** defines the axis of the borehole, while **x** and **y** form the local normal cross-section. The orientation of **z** axis in the **XYZ** system is described by two angles: the inclination β and the azimuth α, as shown in Figure 5.2 on a unit sphere. β is defined as the angle between the **Z** axis and the **z** axis, and α the angle between the projection of **z** onto **XY** plane and the **X** axis. The material system **STN** has been widely used in previous chapters to describe the behavior of anisotropic rock. For the case of a transversely isotropic rock, **N** is normal to the isotropic planes, while **S** and **T** form the isotropic plane. The orientation of **N** relative to the global coordinate system is also expressed by the inclination and the azimuth (refer to Figure 5.2). In the following discussion, α_z and β_z are used to specify the azimuth and the inclination of the borehole, while α_n and β_n those of the transversely isotropic rock.

In order to illustrate the orientation of **z** and **N** in the global coordinate system in a two dimensional manner, the projection of the upper unit hemisphere onto the horizontal plane is used. Figure 5.3 shows the projection of the latitude and meridian lines on the upper hemisphere onto the horizontal plane. For illustration purpose, the latitude lines of $\beta = 0°$ (which is the north pole), 30°, 60°, 90° (which is the equator) are shown. The meridional lines of $\alpha = 0°$, 90°, 180°, and 270° are shown, with $\alpha = 0°$ being the positive **X** direction. The orientation of the material and the borehole will be shown on the two dimensional projection.

Also shown in Figure 5.3 is the orientation of in-situ stresses. It is assumed that σ_h is in the X direction, σ_H in the Y direction, and σ_V in the Z direction. Therefore:

$$\sigma'_{XX} = \sigma'_h = 30\text{MPa}; \sigma'_{YY} = \sigma'_H = 45\text{MPa}; \sigma'_{ZZ} = \sigma'_V = 60\text{MPa}; \tag{5.4}$$

5.3 Calculation of Stresses around the Borehole

In order to assess the stability of the borehole, the effective stresses induced by drilling the borehole must first be calculated. The problem of an anisotropic homogeneous body bounded internally by a cylindrical surface of arbitrary cross-section has been discussed by Lekhnitskii (1963) and Amadei (1983). Solutions were provided on the distribution of stresses, strains, and displacements around the cylindrical surface. The solutions of stress distribution are applied in

this research to calculate the drilling induced stress.

In the most general form of their solution, there is only one assumption regarding the boundary conditions, that the surface forces and body forces do not vary along the axis of the borehole.

Amadei (1983) also discussed the forms of the solution with certain simplifications. In this research, the implementation is based on a simplified version of the solution with the following additional assumptions: 1) The cylindrical hole has a circular cross-section; 2) There is a uniform internal pressure applied along the surface of the hole. Body forces are supposed to be absent; and 3) Generalized plane strain condition exists such that all components of stress, strain, displacement, body and surface forces must be identical in all planes perpendicular to the axis of the borehole. It should be noted that the assumptions on surface and body forces are consistent with the generalized plane strain condition. Under this assumption, the only zero strain is ε_z, which is the normal strain in the axis direction of the borehole.

Based on these assumptions, the problem of introducing a hole with internal pressure into an anisotropic linear elastic medium subject to far-field stresses is then decomposed into the superposition of three sub-problems:

1. The far-field stress is applied to an anisotropic linear elastic medium with no opening.
2. The hole is introduced into the medium. Existing stresses are relieved to zero around the surface of the hole.
3. The surface of the hole is uniformly pressurized with the internal pressure.

Due to the assumption of the generalized plane strain condition, sub-problem 2 and 3 introduce zero longitudinal strain ε_z.

A MATLAB program was written to implement the solution of Amadei (1983). The following input parameters are necessary for the calculation:

1. Orientations of the coordinate systems: α_z and β_z for the borehole system, α_n and β_n for the material system.
2. Anisotropic elastic parameters of rock: E_n, E_s, ν_{st}, ν_{ns}, G_{ns}. These parameters define the following elastic relationship for a transversely isotropic rock:

$$\begin{bmatrix} \varepsilon_s \\ \varepsilon_t \\ \varepsilon_n \\ \gamma_{tn} \\ \gamma_{ns} \\ \gamma_{st} \end{bmatrix} = \begin{bmatrix} \frac{1}{E_s} & -\frac{\nu_{st}}{E_t} & -\frac{\nu_{ns}}{E_n} & 0 & 0 & 0 \\ -\frac{\nu_{st}}{E_t} & \frac{1}{E_t} & -\frac{\nu_{ns}}{E_n} & 0 & 0 & 0 \\ -\frac{\nu_{ns}}{E_n} & -\frac{\nu_{ns}}{E_n} & \frac{1}{E_n} & 0 & 0 & 0 \\ 0 & 0 & 0 & \frac{1}{G_{ns}} & 0 & 0 \\ 0 & 0 & 0 & 0 & \frac{1}{G_{ns}} & 0 \\ 0 & 0 & 0 & 0 & 0 & \frac{1}{G_{st}} \end{bmatrix} \begin{bmatrix} \sigma_s \\ \sigma_t \\ \sigma_n \\ \sigma_{tn} \\ \sigma_{ns} \\ \sigma_{st} \end{bmatrix} \tag{5.5}$$

Since the strain energy of an elastic material must always be positive, the elastic parameters must satisfy the following conditions:

$$E_s > 0, E_n > 0, G_{ns} > 0, -1 \le \nu_{st} \le 1, \frac{E_s}{E_n}(1-\nu_{st}) - 2\nu_{sn}^2 \ge 0 \tag{5.6}$$

where $\nu_{sn} = \frac{E_s}{E_n}\nu_{ns}$. Note that these parameters are in the local material coordinate system **STN**.

3. The far effective field stress in the **XYZ** system.
4. The radius of the borehole a, the mud pressure p_m, and the formation pore pressure p_f.

Based on these information, the program gives the effective stress components at any point around the borehole.

The solutions from Lekhnitskii (1963) and Amadei (1983) are briefly summarized in Appendix C of this thesis. Only the part of the solutions that is implemented with the MATLAB code is presented. The MATLAB code that calculates the stress distribution around the borehole is listed in Appendix D.

5.4 Strength and Stiffness Parameters

Since the formation rock is assumed to be Chichibu green schist, the strength parameters are the same as those reported in Section 4.8.2, with a Coulomb criterion describing failure along the isotropic planes, and AMN criterion describing failure across the isotropic planes.

The elastic parameters can be obtained only from the stress-strain curves. Mogi (2007) reported the stress-strain curves from true triaxial tests for different test modes (see Figure 3.20 for different test modes). Figure 5.4 shows the stress-strain curves of five tests on Mode I specimens, where σ_3 = 50MPa and σ_2 = 50, 85, 100, 133, and 166MPa. Figure 5.5 shows the stress-strain curves of five tests on Mode III specimens, with σ_3 = 50MPa and σ_2 = 50, 86, 97, 121, and

155MPa. Figure 5.6 shows the stress-strain curves of five true triaxial tests on Mode IV specimens, where σ_3 = 50MPa and σ_2 = 50, 71, 75, 227, and 316MPa.

For a specimen with isotropic plane orientation β, the Young's Modulus in the axial direction is defined as:

$$E_\beta = \frac{d\sigma_1}{d\varepsilon_1} \tag{5.7}$$

which can be obtained by measuring the slope of the initial elastic part of the stress-strain curves. It can be seen from Figure 5.4 and Figure 5.5 that the isotropic plane orientations for both Mode I and III are 30°. Therefore, both Figure 5.4 and Figure 5.5 give the Young's Modulus E_{30}. By averaging the initial slope of these stress-strain curves, one obtains E_{30} = 34.0GPa for Mode I specimens and E_{30} = 37.9 for Mode III specimens. Finally, E_{30} is taken as the average of the two, which is 36.0GPa. The Young's Modulus E_{90}, which is E_n in Equation (5.5), can be obtained from the stress-strain curves in Figure 5.6. The initial slope of these curves are measured and averaged, and one obtains $E_{90} = E_n$ = 29.3GPa.

For a transversely isotropic material, the Young's Modulus for a specimen with isotropic plane β can be expressed by (see, for example, Amadei 1983):

$$\frac{1}{E_\beta} = \frac{\sin^4\beta}{E_n} + \frac{\cos^4\beta}{E_s} + \frac{\sin^2(2\beta)}{4}\left(\frac{1}{G_{sn}} - \frac{2\nu_{sn}}{E_s}\right) \tag{5.8}$$

The shear modulus G_{sn} is not reported for Chichibu green schist. Therefore, its value has to be estimated by:

$$\frac{1}{G_{sn}} = \frac{1}{E_s} + \frac{1}{E_n} + \frac{2\nu_{sn}}{E_s} \tag{5.9}$$

Substitute Equation (5.9) to (5.8), the following result can be obtained:

$$\frac{1}{E_\beta} = \frac{\sin^4\beta}{E_n} + \frac{\cos^4\beta}{E_s} + \frac{\sin^2(2\beta)}{4}\left(\frac{1}{E_s} + \frac{1}{E_n}\right) \tag{5.10}$$

Substitute β = 30°, E_β = 36.0GPa, and E_n = 29.3GPa into Equation (5.10), it is solved that E_s = 38.9GPa. The Poisson's ratios are assumed to be: ν_{st} = 0.25 and ν_{ns} = 0.2. To summarize, the elastic parameters are:

$$E_n = 29.3\text{GPa},\ E_s = 38.9\text{GPa},\ G_{sn} = 13.6\text{GPa},\ \nu_{st} = 0.25,\ \nu_{ns} = 0.2$$

5.5 Effective Mud Pressure against Borehole Collapsing

In order to prevent failure of the wellbore, the mud pressure inside the borehole must be large enough to prevent yield from occurring in the surrounding rock mass. The effective mud pressure below which the borehole collapses is called the *critical mud pressure*, and will be denoted p'_c. The smaller the critical mud pressure, the less support the borehole needs. Hence, borehole

stability can be evaluated from the critical mud pressure that corresponds to the onset of failure in the rock. The intention of this calculation is to determine the critical mud pressure for a given material orientation and borehole orientation.

Seven material orientations have been chosen for this study, denoted material orientation I through VII. The orientation of direction **N** in these material orientations are shown in Figure 5.7 by ⊗ symbols. The inclination β_n and azimuth α_n of these seven material orientations are also listed in Figure 5.7.

For each material orientation, many different borehole orientations are calculated. These borehole orientations are shown as black dots in Figure 5.8. The borehole orientations are arranged in a grid with intervals $\Delta\alpha_z = 10°$ and $\Delta\beta_z = 10°$. Altogether, there are 36×9 = 324 borehole orientations whose critical mud pressures are calculated for each material orientation shown in Figure 5.7. For each borehole orientation, the effective mud pressure p' inside the borehole is increased until there is no failure at any point around the borehole. This p' corresponds to the critical mud pressure p'_c for this particular borehole orientation.

Figure 5.9 (a) through (c) are pseudocolor plots of the variation of p'_c with borehole orientation, at Material Orientations I, II and III respectively (refer to Figure 5.7 for Material Orientations). The orientation of **N** in these material orientations is still shown with ⊗ symbols. The scale is shown to the right most of the plot. To the blue end of the scale, the effective mud pressure is 0MPa (corresponding mud pressure in the borehole is $p_m = p_f = 40$MPa). To the red end of the scale, the effective mud pressure is 20MPa (corresponding mud pressure in the borehole is $p_m = p_f$ +20MPa = 60MPa). The upper hemisphere projections in Figure 5.9 are placed according to Figure 5.3, so that σ_h is in the left-right direction, while σ_H is in the up-down direction.

Figure 5.9 (a) shows the distribution of critical mud pressure p'_c when the isotropic planes are horizontal. It is clearly shown that the critical mud pressure is larger when the borehole orientation is closer to parallel to the isotropic planes (i.e. closer to horizontal direction). When the borehole orientation is moving toward the vertical direction (i.e. toward the normal direction of the isotropic planes), the critical mud pressure decreases (between 0MPa to 2MPa for a large area surrounding the **N** orientation). If the borehole is horizontal, the critical mud pressure depends on the azimuth of the borehole. When the borehole is aligned with σ_h ($\alpha = 0°$ and 180°), the critical mud pressure is larger, and it is between 8MPa to 10MPa according to the plot. When the borehole is aligned with σ_H ($\alpha = 90°$ and 270°), the critical mud pressure is between 0MPa to 2MPa, which is much smaller. A horizontal borehole is indifferent to the material anisotropy because it is parallel to the isotropic planes. The variation of mud pressure with borehole azimuth, therefore, must be caused by the stress anisotropy within the isotropic plane.

The orientation of the **N** direction in Figure 5.9 (b) is $\beta_z = 45°$ and $\alpha_z = 0°$, so that it is 45° inclined toward σ_h direction. The isotropic plane intersects the upper hemisphere in a half circle,

whose projection onto the horizontal plane is represented by the dashed line in the plot. In an area close to the dashed line, the critical mud pressure is elevated. This again shows that a borehole tends to be unstable if it is close to parallel to the isotropic planes, and more support from the mud is necessary. The critical mud pressure is smaller if the borehole orientation is closer to the normal direction. The lowest critical mud pressure is again obtained in an area surrounding the isotropic plane normal, which is between 0MPa to 2MPa. When the borehole is parallel to the isotropic planes, the critical mud pressure is between 18MPa to 20MPa at $\beta_z = 90°$ and $\alpha_z = 90°$ (i.e. when the borehole axis is aligned with σ_H direction), and it is between 6MPa to 8MPa at $\beta_z = 45°$ and $\alpha_z = 180°$ (i.e. 45° between σ_V direction and σ_h direction). The difference is a result of stress anisotropy.

In Figure 5.9 (c), the isotropic plane normal direction coincides with the σ_h direction, hence it is horizontal and the isotropic planes are vertical. Once again, one observes that the critical mud pressure is higher for borehole orientations that are close to parallel to the isotropic planes. In this case, it is between 14MPa to 16MPa at $\beta_z = 90°$ and $\alpha_z = 90°$ (i.e. when the borehole axis is aligned with σ_H direction), and between 6MPa to 8MPa at $\beta_z = 0°$ (i.e. when the borehole axis is aligned with σ_V direction).

To summarize, the following observations can be made based on Figure 5.9:

Observation 1: If the borehole orientation is close to the direction normal to the isotropic planes, the borehole tends to be stable with no or little support from the mud. If the borehole is close to parallel to the isotropic planes, then the critical mud pressure becomes higher, and the borehole tends to be unstable.
Observation 2: The critical mud pressure is also affected by the far-field stress anisotropy. As a result, when the borehole is parallel to the isotropic planes, the critical mud pressure still varies with the borehole orientation within the isotropic plane.

Figure 5.10 and Figure 5.11 show similar results for Material Orientations I, IV, V and Material Orientation I, VI, VII, respectively. Similar observations as just made apply to these plots, too.

5.6 Failure Contours of Boreholes

Figure 5.9 through Figure 5.11 in the previous section only illustrate the critical mud pressure marking the onset of failure in the rock. However, they do not show the mechanism of incipient borehole collapse for p' smaller than the critical mud pressure. In this section, calculations are performed to illustrate this.

In order to show how failure occurs around a certain borehole, it is necessary to define failure functions. For the Coulomb criterion, a failure function F_C is defined as:

$$F_C = \frac{(\tau_n)_{mob} - (\tau_n)_{max}}{(\tau_n)_{max}} \tag{5.11}$$

where $(\tau_n)_{mob}$ is the mobilized shear strength on the isotropic planes, while $(\tau_n)_{max}$ is the maximum shear strength on the isotropic planes. Their definitions are shown in Figure 5.12. With this definition, if $F_C \geq 0$ then failure occurs according to the Coulomb criterion. A failure function F_A is defined for the AMN criterion, which is the same as function f in Equation (4.29). If $F_A \geq 0$, then failure occurs according to the AMN criterion.

The failure function distributions are calculated for a borehole embedded in the rock with Material Orientation I (vertical **N** direction and horizontal isotropic planes) and aligned in σ_h direction (i.e. $\beta_z = 90°$, $\alpha_z = 0°$), as shown in Figure 5.13. The orientation of the isotropic planes and the far-field stress on the cross-section of the borehole are shown in Figure 5.14. During the calculation, p' is reduced from a large value until $F_C = 0$ or $F_A = 0$ is reached. Based on the calculation, failure occurs according to the Coulomb criterion at $p' = 6.1$MPa (corresponding to a mud pressure in the borehole $p_m = p_f + 6.1$MPa = 46.1MPa). At this point, the failure function F_C is plotted in Figure 5.15. It can be seen that $F_C = 0$ is obtained at four locations around the borehole wall, where failure initiates according to the Coulomb criterion. These four locations are symmetric with regard to the horizontal and vertical directions. Therefore, the location of these four points around the borehole wall can be determined by the angle between the top two failure locations. In this case, this angle is 67°.

At $p' = 6.1$MPa, there is still $F_A < 0$. If, on the other hand, it is assumed that failure is controlled by the AMN criterion, then p' must be further reduced to induce failure. It is found that when p' is reduced to 4.4MPa (corresponding to mud pressure in the borehole $p_m = p_f + 4.4$MPa = 44.4MPa), $F_A = 0$ is obtained at four locations around the borehole wall (Figure 5.16). With the AMN criterion, the angle between the top two failure locations is 101.4°. Due to the complex mathematical expression of the AMN criterion, it is not intuitively clear why this angle is larger for the AMN criterion than for the Coulomb criterion.

With the previous analysis, it is evident that with either the Coulomb criterion or the AMN criterion, failure initiates at four locations around the borehole wall. The only difference between Figure 5.15 and Figure 5.16 is the exact location of these four points. This is consistent with the double-lobed failure pattern that is often observed in the boreholes drilled in bedded rocks (for example, see Zoback 2007).

5.7 Summary

In this chapter, the AMN criterion, together with the Coulomb criterion, is applied to the borehole stability problem. The results about critical mud pressure can be used as the rule of thumb of drilling in a transversely isotropic rock, i.e. less mud support is necessary if a well is

closer to the normal direction of the isotropic planes. Both the AMN criterion and the Coulomb criterion can predict the four-lobed failure style that has been observed on wells in transversely isotropic rocks. These results also indicate that the AMN criterion and its combination with the Coulomb criterion are physically grounded, and can be used to solve real problems.

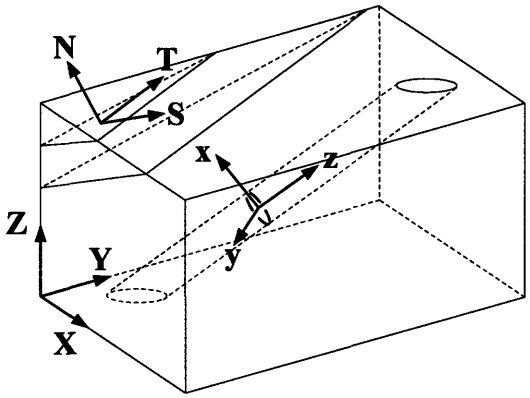

Figure 5.1 Three Coordinate Systems in the Borehole Stability Problem

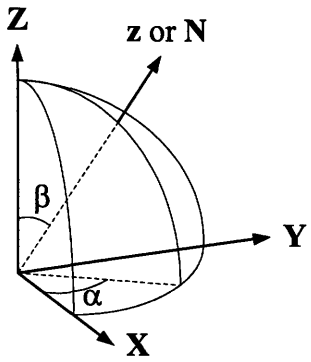

Figure 5.2 Inclination β and Azimuth α

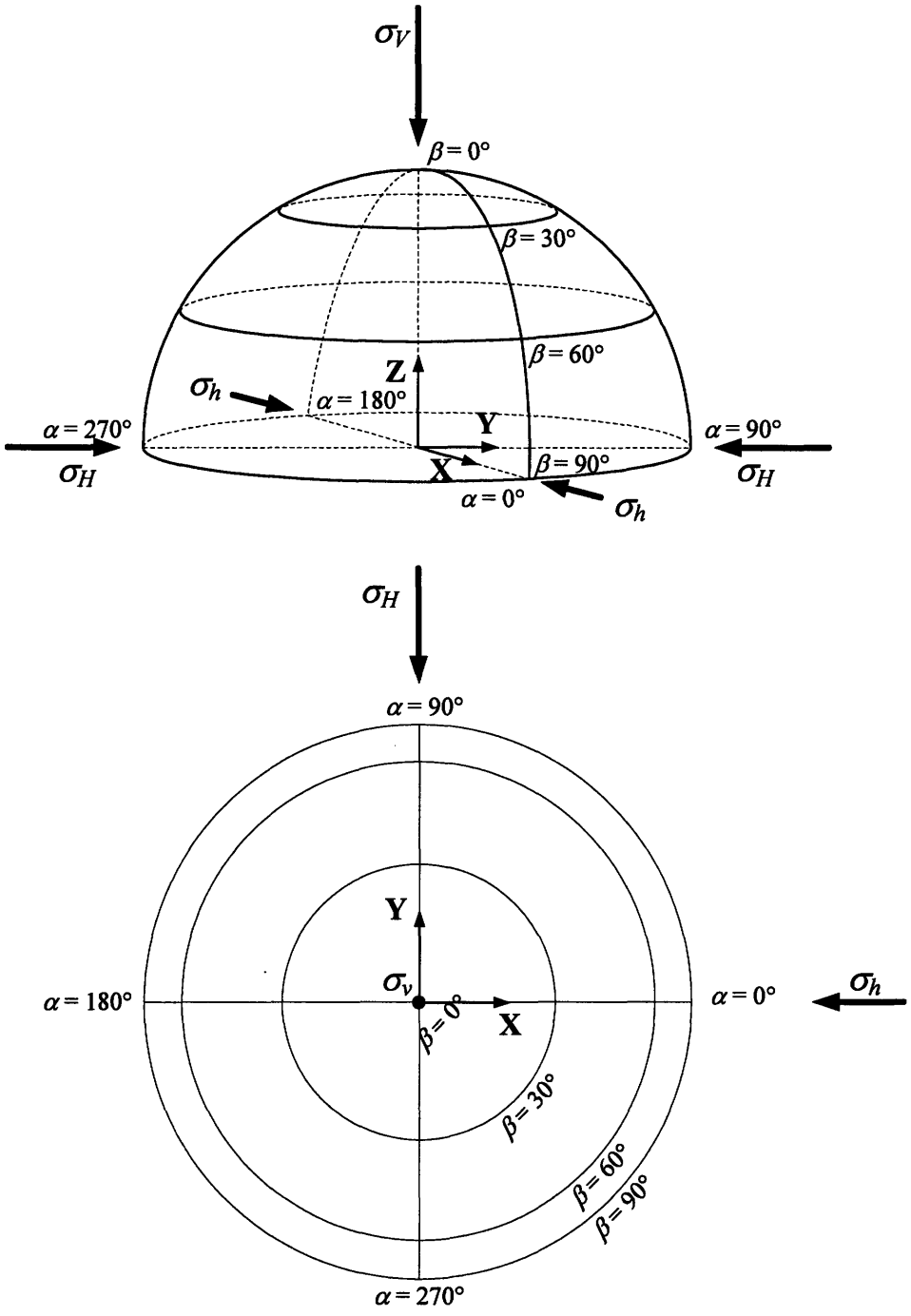

Figure 5.3 Projection of the Upper Hemisphere

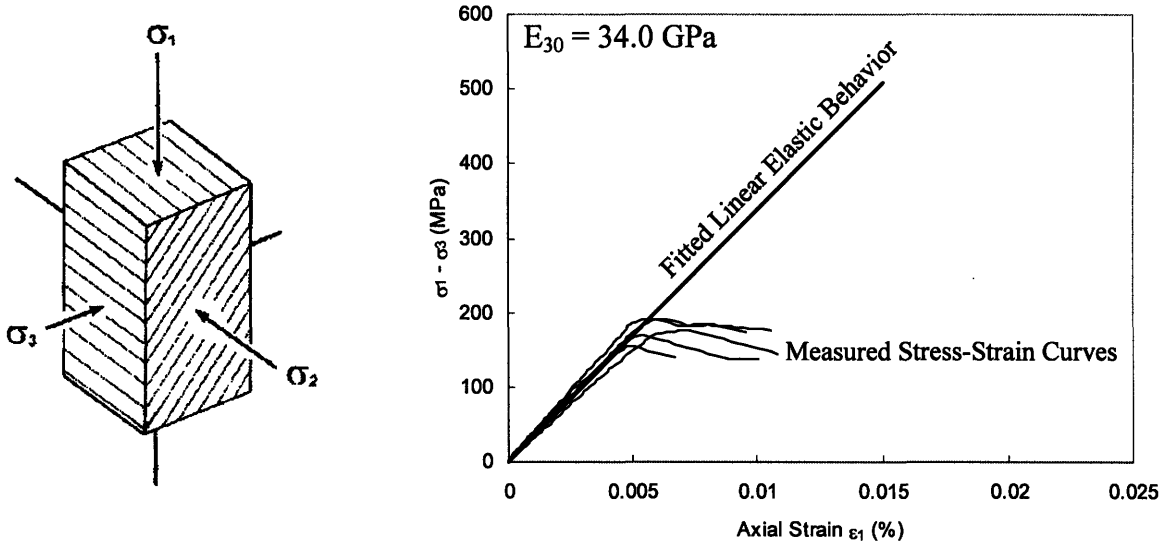

(a) Mode I Specimen (b) Stress-Strain Curves

Figure 5.4 Stress-Strain Curves of Five Mode I Specimens (data from Mogi, 2007)

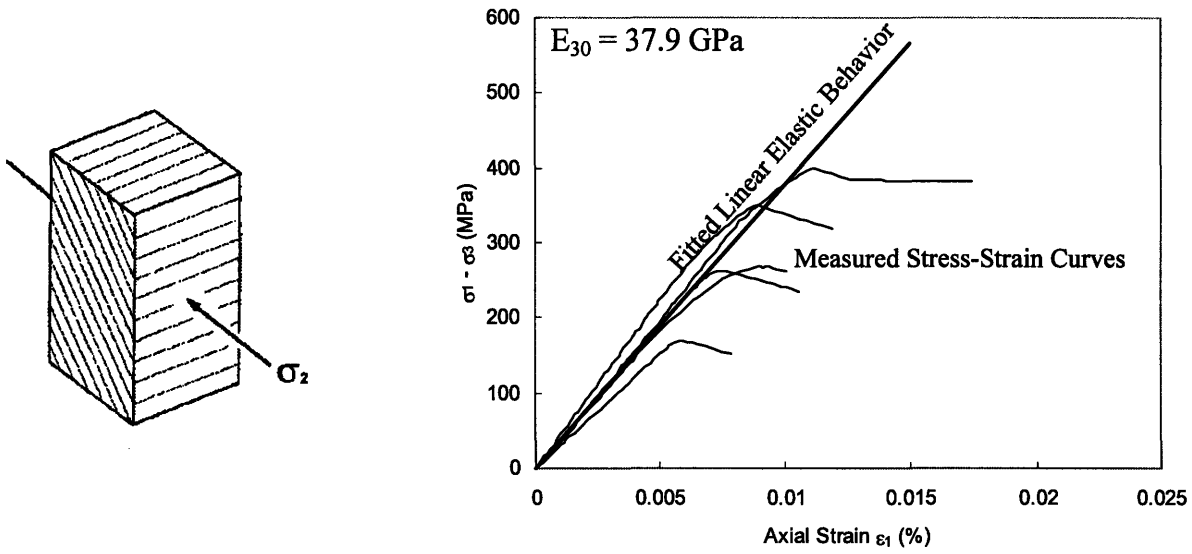

(a) Mode III Specimen (b) Stress-Strain Curves

Figure 5.5 Stress-Strain Curves of Five Mode III Specimens (data from Mogi, 2007)

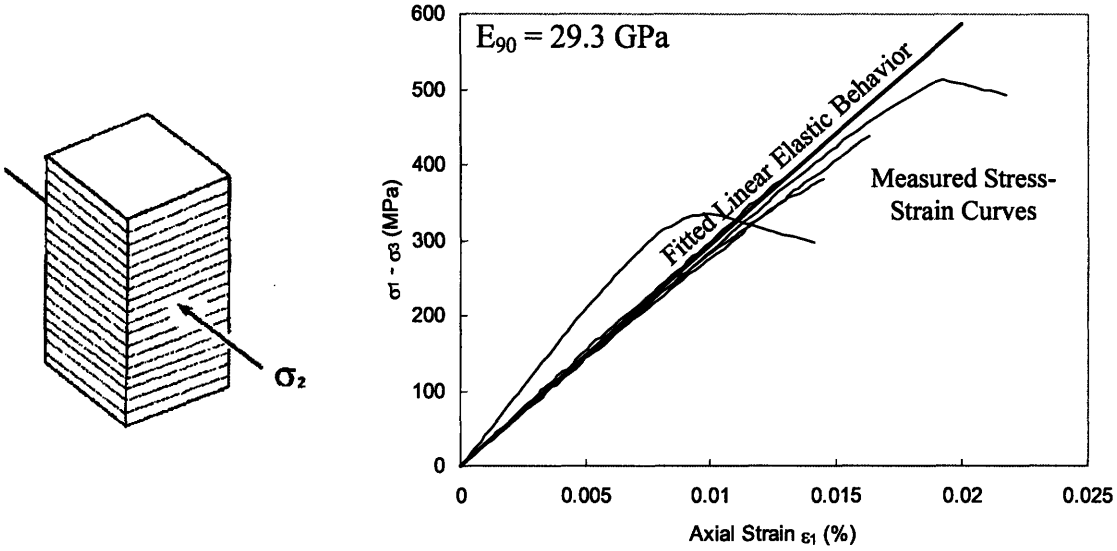

(a) Mode IV Specimen (b) Stress-Strain Curves

Figure 5.6 Stress-Strain Curves of Five Mode IV Specimens (data from Mogi, 2007)

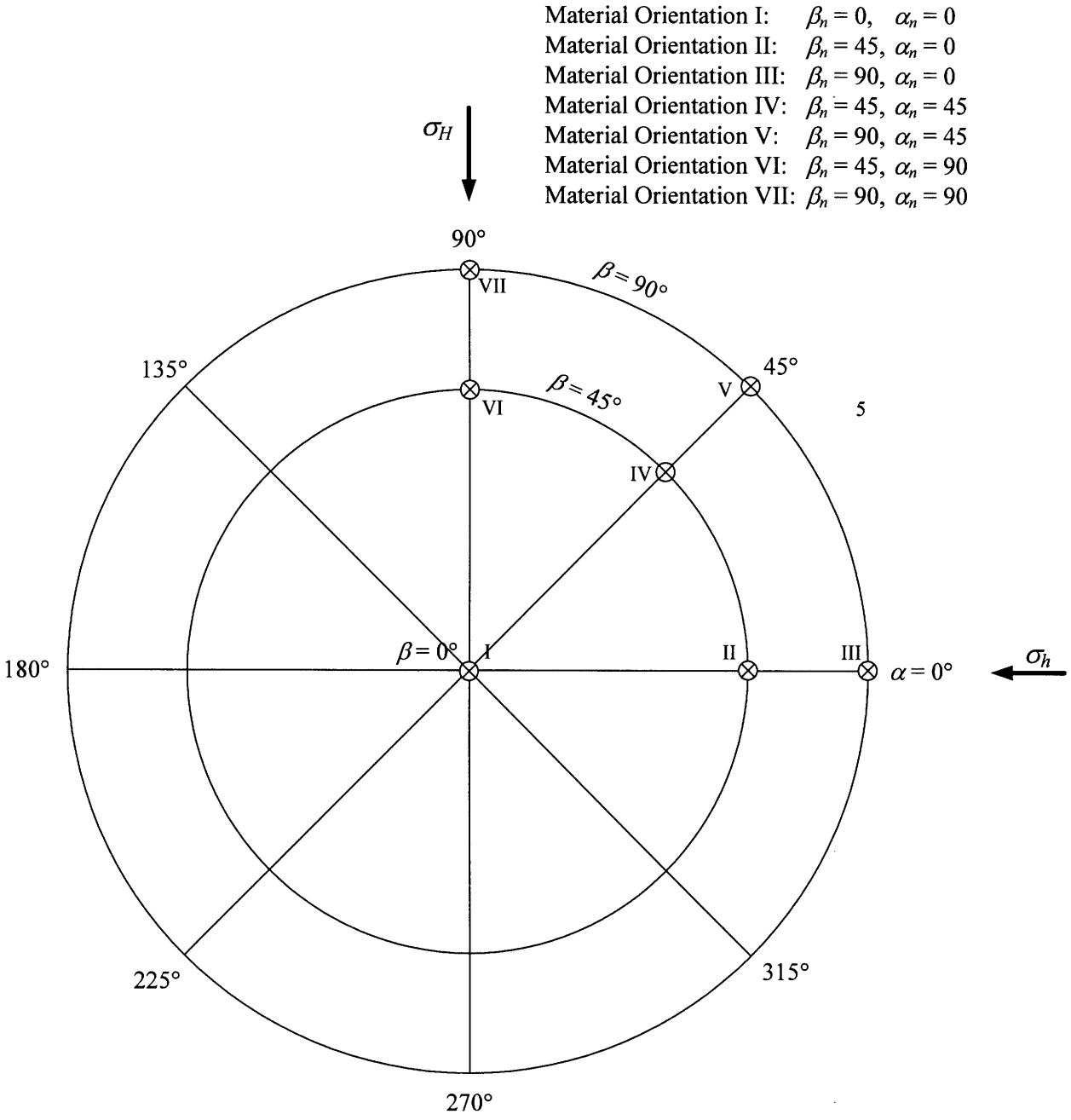

Figure 5.7 The Seven Material Orientations Shown on the Projection of the Upper Hemisphere

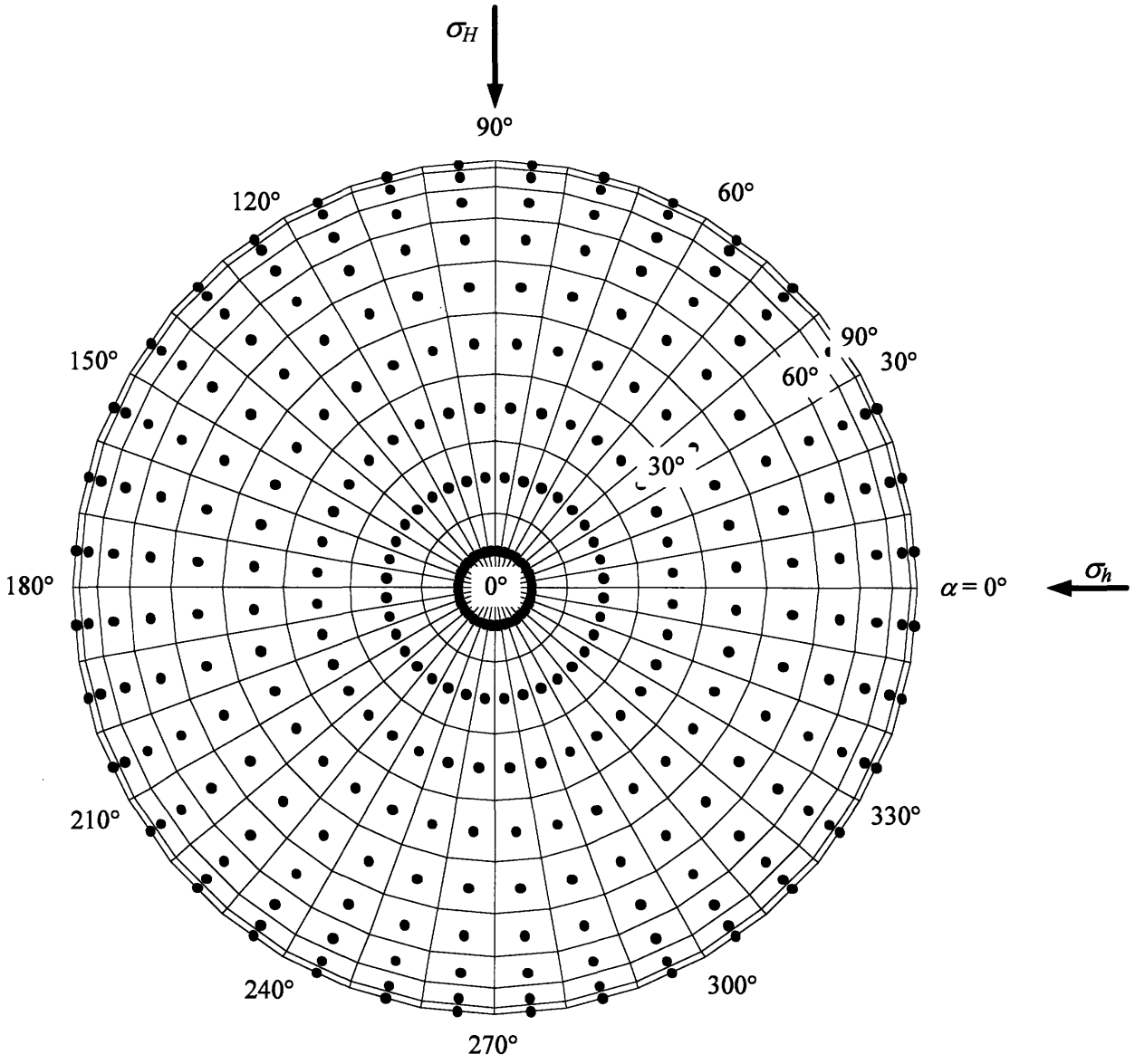

Figure 5.8 The Borehole Orientation Calculated in Each Case

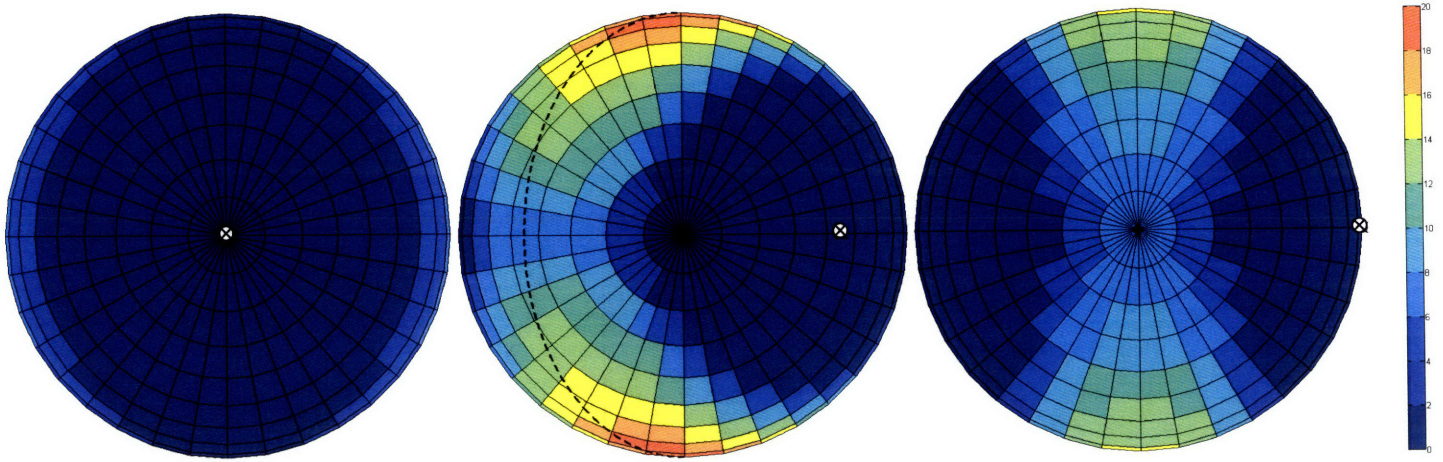

(a) Material Orientation I (b) Material Orientation II (c) Material Orientation III

Figure 5.9 Critical Mud Pressure p'_c Distributions for Material Orientation I, II and III

Note: The ⊗ symbol marks the orientation of **N**. The dashed line marks the trace of isotropic plane on upper hemisphere.

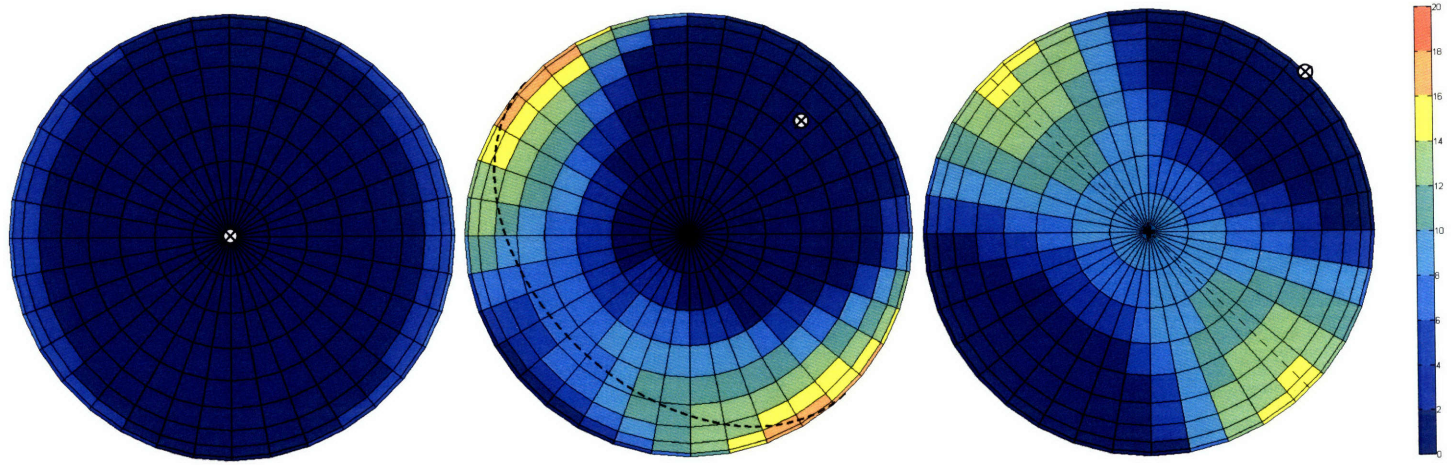

(a) Material Orientation I (b) Material Orientation IV (c) Material Orientation V

Figure 5.10 Critical Mud Pressure p'_c Distributions for Material Orientation I, IV, and V

Note: The ⊗ symbol marks the orientation of **N**. The dashed line marks the trace of isotropic plane on upper hemisphere.

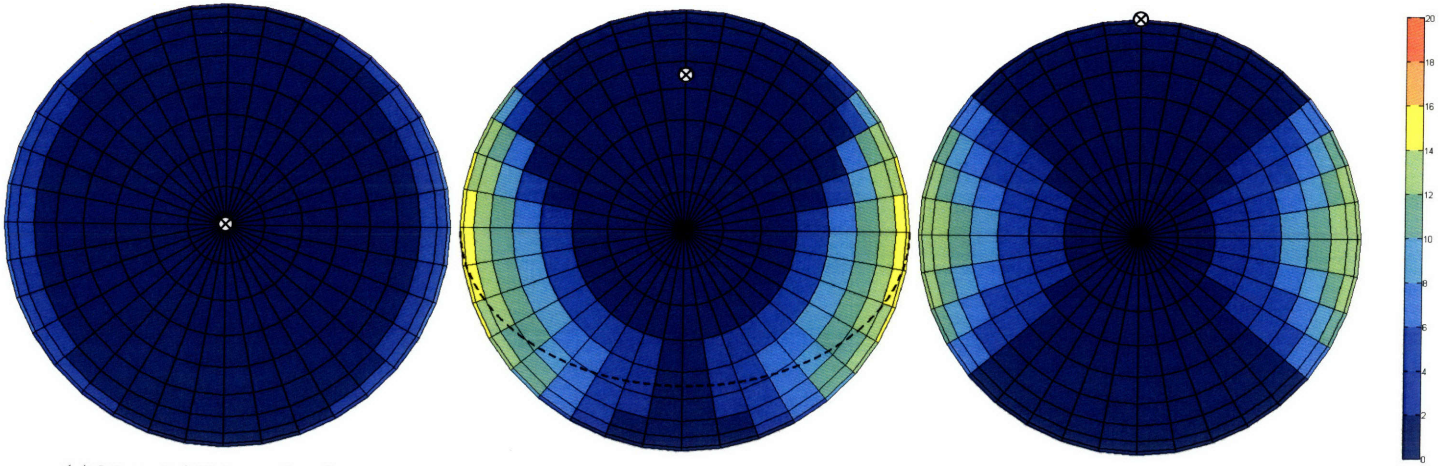

(a) Material Orientation I (b) Material Orientation VI (c) Material Orientation VII

Figure 5.11 Critical Mud Pressure p'_c Distributions for Material Orientation I, VI, and VII

Note: The ⊗ symbol marks the orientation of **N**. The dashed line marks the trace of isotropic plane on upper hemisphere.

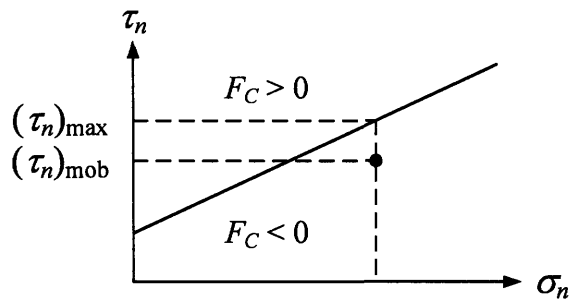

Figure 5.12 Definition of Failure Function for Coulomb Criterion

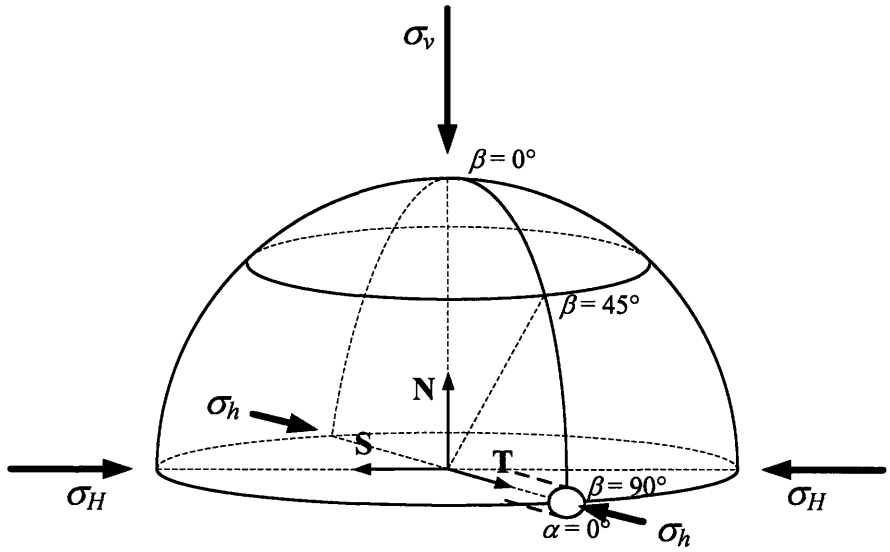

Figure 5.13 Orientation of the Borehole (β = 90° and α = 0°) Whose Failure Functions are Calculated

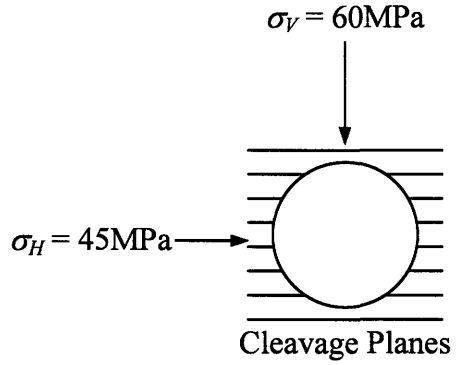

Figure 5.14 Illustration of the Borehole with β = 90° and α = 0°

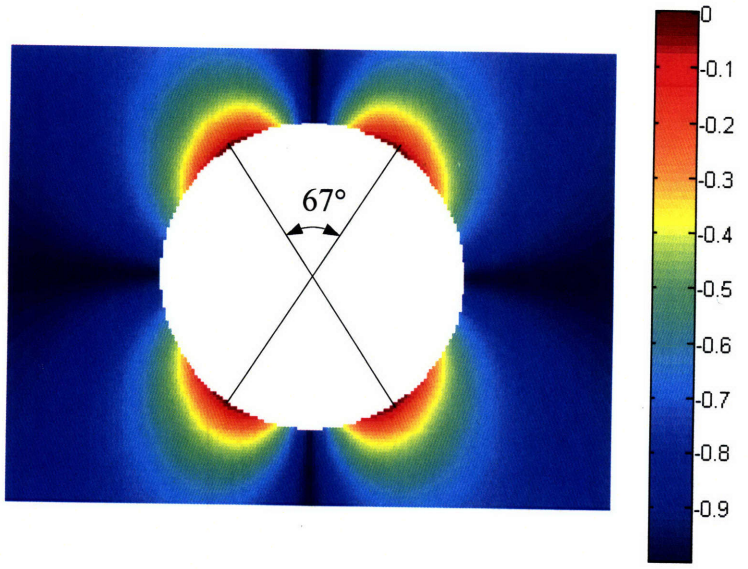

Figure 5.15 Coulomb Failure Function at p′ = 6.1MPa for a Borehole with $\beta = 90°$ and $\alpha = 0°$

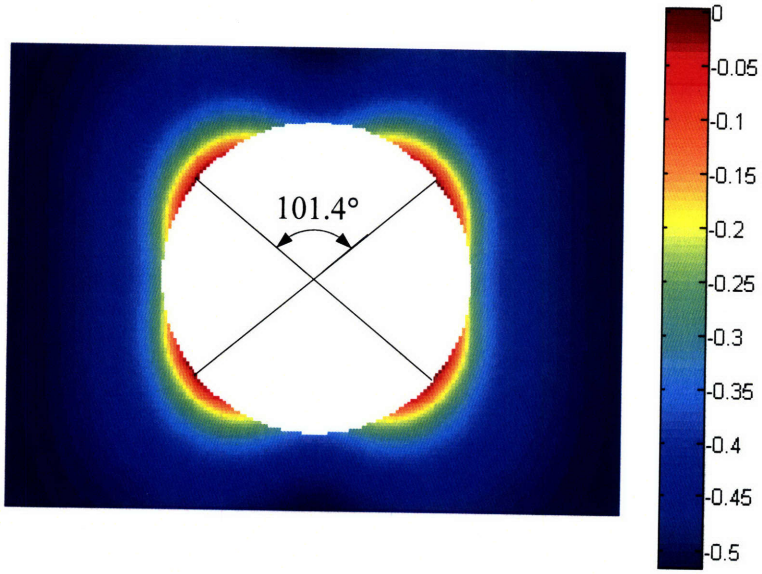

Figure 5.16 AMN Failure Function at p′ = 4.4MPa for a Borehole with $\beta = 90°$ and $\alpha = 0°$

6 Summary, Conclusions and Recommendations

6.1 Summary

The goal of this research is to provide a way to characterize the failure of transversely isotropic rocks under true triaxial stress states. While reviewing the literature, it was found that existing anisotropic models, for example the Tsai and Wu criterion (Tsai and Wu, 1971), the Anisotropic Mises-Schleicher criterion (Cazacu, 1998, 1999), etc. were only validated against data from conventional triaxial tests. Therefore, a new failure criterion for transversely isotropic rocks under true triaxial stress states is proposed and validated in this thesis. For this purpose, the following tasks have been fulfilled:

1. Data sets of true triaxial experiments on more or less isotropic rocks are first compiled and analyzed. Some of the isotropic failure criteria that characterize rock strength under true triaxial stress states are then presented and reviewed.

2. Experimental results on transversely isotropic rocks are also collected, most of which are from conventional triaxial tests. The most comprehensive true triaxial test data are reported by Mogi (2007), on Chichibu green schist. This set of data is later used to validate the proposed model. Existing anisotropic criteria are categorized and reviewed.

3. A new approach, the Material Normal Stress System, is proposed, which helps to visualize anisotropic failure surfaces, and facilitates the development of anisotropic failure criteria. The observations on isotropic rock failure under true triaxial stress state, and those on transversely isotropic rock failure under conventional triaxial stress state are expressed in the system as geometrical characteristics of the failure surface. These geometrical features are incorporated into the failure surface of the Matsuoka-Nakai criterion, which produces the Anisotropic Matsuoka-Nakai criterion. The Anisotropic Matsuoka-Nakai criterion should be used to capture the continuous component of strength anisotropy, while the Coulomb criterion should be used to describe the discontinuous component of strength anisotropy. This combination is then validated against the conventional triaxial test data of different rock types and the true triaxial test data (i.e. Chichibu green schist data set only) of transversely isotropic rocks. It seems that this combination of criteria is capable of capturing the failure of transversely isotropic rocks under both conventional and true triaxial stress states.

4. The Anisotropic Matsuoka-Nakai criterion combined with the Coulomb criterion is then applied to the problem of borehole stability. It is assumed that a borehole is drilled at 4000m depth in Chichibu green schist, whose stress-strain behavior is described by transversely

isotropic elasticity. The necessary mud support to keep the borehole from collapsing (critical mud pressure) is calculated as a function of the orientation of the isotropic planes and the borehole axis. For a certain borehole orientation, the failure modes at the onset of failure as predicted by the combination of the Anisotropic Matsuoka-Nakai and the Coulomb criterion are discussed. The critical pressures and the failure modes as calculated are consistent with the observations made in real wellbore failures.

6.2 Conclusions

The following conclusions can be drawn:

1. The failure of more or less isotropic rocks can be described by a continuous failure surface in the principal stress space. For many rocks, the shape of the π-plane cross-section of this failure surface can be formulated by the LMN (Lade, Matsuoka-Nakai) dependence, which describes a group of curved triangular shapes. There is only one parameter (β_s) in the formulation of the LMN dependence, which specifies the roundness of the curved triangles. When β_s varies from 0.5 to 1.0, the shape described by the LMN dependence varies from a right triangle to a circle. Based on the data fitting of the true triaxial test results of many different rocks, it seems that β_s does not vary significantly with the pressure level, i.e. the shape of the π-plane cross-section does not change significantly along the hydrostatic line.

2. In order to provide greater flexibility to the model, it is recommended to describe the failure surface by two cross-sections. The triaxial cross-section of the failure surface, which is a meridian cross-section, defines how the conventional triaxial strength increases with the average confining pressure. The shape of the π-plane cross-section, which is a normal cross-section, describes the variation of its radius with the Lode angle. For example, the closer the shape is to a circle (β_s approaching 1.0), the smaller the variation of its radius with the Lode angle. Physically, this approach corresponds to the separation of the pressure dependence and the Lode angle dependence.

3. The strength of anisotropic rocks in conventional triaxial tests is a function of both the isotropic plane orientation β and the confining pressure σ_3. Specimens with $\beta = 0°$ have isotropic planes parallel to the axial direction. Specimens with $\beta = 90°$ have isotropic planes perpendicular to the axial direction. For a particular β, the strength increases with confining pressure σ_3. For a particular σ_3, the strength variation with β can be described by a "U" shaped curve, which has local maxima at $\beta = 0°$ and 90°, and reaches its minimum for β around 30° to 40°. The two maxima of the "U" shaped curve (at $\beta = 0°$ and 90°) are usually not equal (i.e. specimens with isotropic planes parallel to the axial direction usually have a different strength than those with isotropic planes perpendicular to the axial direction). The geometry of this "U" shaped curve can be captured by the unevenness ratio and the depth ratio. These ratios seem to be related to the lithology of the rocks.

4. Several different failure modes have been observed for transversely isotropic rocks in conventional triaxial tests.
   - For small confining pressures, the failure is brittle. Specimens can fail by tensile splitting when the isotropic planes are close to the axial direction. Shearing along or across the isotropic planes or a mixture of both may also occur.
   - For large confining pressures, failure is usually ductile. A kink band may develop, usually for steeply inclined isotropic planes. Slipping along multiple isotropic planes or shear faulting across the isotropic planes may also occur.

5. In a material coordinate system **STN**, where **N** is the normal to the isotropic planes while **S** and **T** form the isotropic plane, the stress has six components: three normal components σ_s, σ_t, σ_n, and three shear components σ_{tn}, σ_{ns}, σ_{st}. Existing anisotropic failure criteria can usually be expressed in terms of all six components. It seems that the criteria expressed as quadratic polynomials of the stress components have the ability to describe the "U" shaped curves that characterize the conventional triaxial compression strength of transversely isotropic rocks. To the author's knowledge, however, these criteria have only been validated against conventional triaxial test data.

6. Isotropic failure criteria can usually be expressed by corresponding failure surfaces in the principal stress space. The failure behavior described by these criteria can thus be directly visualized and understood. This greatly facilitates the development of isotropic failure criteria. On the contrary, anisotropic failure criteria are the functions of all six stress components, hence cannot be directly visualized in three-dimensional space. This is believed to pose great difficulty in understanding and further developing the existing anisotropic criteria. In order to solve this problem, the Material Normal Stress System is proposed.

7. Similar to the principal stress space, which is the space formed by the three principal stresses (σ_1, σ_2, σ_3), the Material Normal Stress System is a space that is formed by the three normal stress components, (σ_s, σ_t, σ_n). For a certain set of principal stresses, the normal stresses vary when the orientation of the **STN** coordinate system changes with regard to the principal stress directions. Therefore, the Material Normal Stress System can capture the coupling between the material orientation and the principal stress orientation. A certain principal stress state (σ_1, σ_2, σ_3), described by one point in the principal stress space, corresponds to a hexagonal locus on the π-plane in the Material Normal Stress System. The exact location of the point (σ_s, σ_t, σ_n) within this hexagon is determined by the relative orientation of the **STN** coordinate system with regard to the principal stress directions.

8. A conventional triaxial stress state (i.e. $\sigma_2 = \sigma_3$) corresponds to a right triangle on the π-plane in the Material Normal Stress System. In a conventional triaxial test at a certain confining pressure, the stress path is a straight line in the Material Normal Stress System.

The failure points of an isotropic material in conventional triaxial tests with the same confining pressure but different specimen orientation fall on one straight line, which forms one side of the failure stress triangle (termed the isotropic failure line). The failure of transversely isotropic rock in conventional triaxial compression tests, on the other hand, is described by a curve in the Material Normal Stress System, which is called the anisotropic failure curve.

9. Since the Material Normal Stress System only describes the three normal stresses, anisotropic failure criteria involving all six stress components can be visualized in the MNSS. Based on the discussion of two isotropic failure criteria, the Drucker-Prager criterion and the Matsuoka-Nakai criterion, it is found that a failure criterion in the Material Normal Stress Space can be described by two components: the bounding failure surface at all zero shear stresses ($\sigma_{tn} = \sigma_{ns} = \sigma_{st} = 0$), and the variation of its geometry with non-zero shear stresses. Physically, the bounding failure surface describes the failure of the anisotropic material under true triaxial stress conditions, where the principal stress directions and the material directions (**S**, **T** and **N**) coincide. For isotropic failure criteria, their bounding failure surfaces have the same geometry as their failure surfaces in the principal stress space. With non-zero shear stresses, the shape of the bounding surface usually distorts, and its size usually reduces. Shape distortion with non-zero shear stresses seems to be a necessary consequence of the frictional behavior (i.e. pressure dependence of strength). Therefore, it should be incorporated in any criteria that describe the failure of soils and rocks.

10. Based on the observation of failure of isotropic rocks under true triaxial tests, the isotropic Matsuoka-Nakai criterion is chosen to be the foundation for developing a new anisotropic failure criterion. This criterion is selected because its π-plane cross-section can be described by the LMN (Lade, Matsuoka-Nakai) dependence, which is known to capture the strength of isotropic rocks under true triaxial stress states. Based on the observation of failure of transversely isotropic rocks in conventional triaxial tests, anisotropy must be introduced into two different aspects of the original Matsuoka-Nakai criterion. For the bounding failure surface, anisotropy is introduced by using a distorted π-plane cross-section that does not possess the six-fold symmetry. Such a failure surface can predict different strengths at $\beta = 0°$ and $\beta = 90°$. The variation of failure surface geometry with non-zero shear stresses must also be changed so that the shrunk failure surface meets the stress path on the anisotropic failure curve instead of the isotropic failure line. The "U" shaped variation of strength with β can be generated by this modification. The proposed criterion is named the Anisotropic Matsuoka-Nakai criterion. It can be seen that the Material Normal Stress System greatly facilitates the development of the Anisotropic Matsuoka-Nakai criterion. In this system, the behavior of isotropic rocks and the behavior of transversely isotropic rocks can be represented by geometrical features of the failure surface, and combined in a straightforward way.

11. In the Anisotropic Matsuoka-Nakai criterion, three parameters are used to describe the shape of its bounding failure surface in the π-plane cross-section and its variation with non-zero shear stresses.
    - β_s is from the original LMN dependence, which describes the roundness of the π-plane cross-section.
    - A controls the distortion of the π-plane, and therefore controls the difference between the strength at $\beta = 0°$ and the strength at $\beta = 90°$.
    - K controls the size reduction of the π-plane cross-section with increasing non-zero shear stress. Higher K values produce deeper "U" shaped curves.

12. The proposed Anisotropic Matsuoka-Nakai criterion can capture the continuous component of the strength anisotropy of transversely isotropic rocks, where the specimen fails across the isotropic planes. If the specimen fails along the isotropic planes (i.e. the isotropic planes behave like macroscopic joints), the strength anisotropy is of the discontinuous type, and can be characterized by the Coulomb criterion. The Anisotropic Matsuoka-Nakai criterion, together with the Coulomb criterion, has been applied to interpret the experimental results reported in the literature. It seems that the combination of these two criteria makes it possible to describe the failure of transversely isotropic rocks under true triaxial stress states.

13. While applying the combination of criteria to different transversely isotropic rocks tested in conventional triaxial tests, it is found that the relative importance of the Anisotropic Matsuoka-Nakai criterion and the Coulomb criterion for characterizing strength anisotropy varies with rock type (e.g. shales, slates, phyllites, schists, etc.). This relative importance reveals where a certain type of rock is located within the transition from a continuous type of strength anisotropy to a discontinuous type of strength anisotropy. Based on the brief analysis of fifteen different rocks, it seems that slates are closer to the discontinuous end, shales and schists are closer to the continuous end. No general conclusions can be made for phyllites, based on the limited data currently available.

14. The critical mud pressure, below which borehole collapse occurs, is most significantly affected by the orientation of the borehole with regard to the orientation of the isotropic planes of the rock. If the borehole orientation is closer to the normal of the isotropic planes, the borehole tends to be safer and less mud support is necessary. If the borehole is more or less parallel to the isotropic planes, the borehole is prone to failure, and more mud support is necessary. The critical mud pressure is also affected by far-field anisotropic stress conditions. Due to the complexity of the problem, it is difficult to draw a general conclusion on the effect of stress anisotropy.

15. The failure of a borehole embedded in a transversely isotropic rock starts at four locations around the borehole, which creates a double-lobed failure mode. This is consistent with the observations made on real borehole failures, and serves as further support of the validity of

the proposed criterion.

6.3 Recommendations

The predictive power of the Anisotropic Matsuoka-Nakai criterion combined with the Coulomb criterion is confirmed by their application to the conventional triaxial strength data of fifteen different rocks, to the true triaxial strength of Chichibu green schist, and to the problem of borehole stability. As a newly proposed model, however, more work is necessary before it is widely applied and accepted.

1. The combination of the Anisotropic Matsuoka-Nakai criterion and the Coulomb criterion has only been validated with the true triaxial strength of Chichibu green schist. This is because the data on true triaxial tests of transversely isotropic rocks are rarely found in the literature. In order to further validate this combination of criteria, more experimental data are necessary. It is suggested that a true triaxial test program should be performed on different types of transversely isotropic rocks (e.g. shales, phyllites, slates, schists, etc.), and the criterion should be calibrated against all these data. A database of typical values of the model parameters for different rocks should be set up.

2. It would be very interesting to understand the underlying mechanism for the discontinuous and continuous components of strength anisotropy, and to try to explain the observed relative importance of the two components for certain types of rocks. For some transversely isotropic rocks, it may be easier to understand why they are closer to the continuous or to the discontinuous strength anisotropy. For example, slates have well developed cleavage planes which act like discontinuities if failure occurs along them. Therefore, the discontinuous component of strength anisotropy (i.e. failure by Coulomb criterion) is more important for slates than for shales and schists, where failure along the foliation surfaces in bedding planes may not occur. For other rock types, however, explanations based on their lithology, mineralogy, etc. are still desirable. For example, the strength anisotropy of some phyllites seems to have more continuous characteristics than others. Further research may discover possible mechanisms underlying these observations.

3. The Anisotropic Matsuoka-Nakai criterion combined with the Coulomb criterion is applied to the borehole stability problem in this thesis. The stiffness law used there is transversely isotropic elasticity. A failure criterion combined with an elastic constitutive law only applies up to the first occurrence of failure, which produces a lower bound to the problem. Real failures are much more complicated. For example, plastic strains may develop before failure occurs, which cannot be captured by a linear elastic law. After the first occurrence of failure, the stress can be redistributed so that the failure zone may propagate, resulting in a progressive failure. This is also not captured in the present analysis. In order to describe

these real phenomena, more realistic constitutive laws may have to be used together with the proposed failure criteria, which are capable of describing the plastic deformation. Advanced numerical methods may also be necessary.

4. Finally, the Anisotropic Matsuoka-Nakai criterion may also be applicable for other geo-materials that are transversely isotropic, for example, varved clay. Considering that the Matsuoka-Nakai criterion was originally proposed to describe soil behavior, this is entirely possible. However, failure may not be as clearly defined for soil as it is defined for rock, since large deformations usually occur, and the stress-strain curves may not have a noticeable peak.

Reference

1) Al-Ajmi, A.M. and Zimmerman, R.W. 2005. Relationship between the parameters of the Mogi and Coulomb failure criterion. *Int. J. Rock Mech. Min. Sci.*, Vol. 42, No. 3, 431–439.
2) Al-Ajmi, A.M. and Zimmerman, R.W. 2006. Stability analysis of vertical boreholes using the Mogi-Coulomb failure criterion. *Int. J. Rock. Mech. Min. Sci.*, Vol: 43, 1200-1211
3) Allirot, D., Boehler, J.P. and Sawczuk, A. 1977. Irreversible deformations of an anisotropic rock under hydrostatic pressure. *Int. J. Rock Mech. Min. Sci. & Geomech. Abstr.*, Vol. 14, 77-83
4) Allirot, D. and Boehler, J.P. 1979. Evolution des Propriétés Mécaniques d'une roche stratifiée sous pression de confinement. *Proceedings of the 4th International Societies Rock Mechanics*, Vol. I, 15-22
5) Allirot, D., Boehler, J.P. and Sawczuk, A. 1981. Pressure-induced evolution of anisotropies in stratified rock. *Studia Geotechnica et Mechanica*, Vol. III, No. 2-4, 59-74
6) Amadei, B. 1983. Rock anisotropy and the theory of stress measurements. Springer, Heidelberg
7) Aristorenas, G.V. 1992. Time dependent behavior of tunnels excavated in shale. PhD. Thesis. Massachusetts Institute of Technology
8) Attewell, P.B. and Sandford, M.R. 1974. Intrinsic shear strength of a brittle, anisotropic rock – I Experimental and mechanical interpretation. *Int. J. Rock Mech. Min. Sci. & Geomech. Abstr.*, Vol. 11, 423-430
9) Attewell, P.B. and Sandford, M.R. 1974. Intrinsic shear strength of a brittle, anisotropic rock – II Textural data acquisition and processing. *Int. J. Rock Mech. Min. Sci. & Geomech. Abstr.*, Vol. 11, 431-438
10) Attewell, P.B. and Sandford, M.R. 1974. Intrinsic shear strength of a brittle, anisotropic rock – III Textural interpretation of failure. *Int. J. Rock Mech. Min. Sci. & Geomech. Abstr.*, Vol. 11, 439-451
11) Aubertin, M. and Simon, R. 1996. A multiaxial failure criterion that combines two quadric surfaces. *Rock mechanics: tools and techniques*, 1729-1736
12) Aubertin, M. Li, L. and Simon, R. 2000. A multiaxial stress criterion for short- and long-term strength of isotropic rock media. *Int. J. Rock. Mech. Min. Sci.*, Vol. 37, 1169-1193
13) Bardet, J.P. 1990. Lode dependences for isotropic pressure-sensitive elastoplastic materials. *J. Appl. Mech. (ASME)*, Vol. 57, No. 3, 498-506
14) Barton, N. 1976. Rock mechanics review: The shear strength of rock and rock joints. *Int. J. Rock Mech. Min. Sci. & Geomech. Abstr.*, Vol. 13, 255-279
15) Behrestaghi, M.H.N., Seshagiri Rao, K. and Ramamurthy, T. 1996. Engineering geological and geotechnical responses of schistose rocks from dam project areas in India. *Engineering Geology*, Vol. 44, 183-201
16) Bellward, P. 1990. A contribution to the design of tunnels in argillaceous rock. Ph.D. Thesis. Massachusetts Institute of Technology

17) Boehler, J.P. 1987. Applications of Tensor Functions in Solid Mechanics, CISM Courses and Lectures, No. 292, Springer-Verlag
18) Boehler, J.P. and Delafin, M. 1982. Failure criteria for unidirectional fiber-reinforced composites under confining pressure. *Proceedings of the Euromech Colloquium 115: Mechanical behavior of anisotropic solids*, 449-470
19) Boehler, J.P. and Raclin, J. 1985. Failure criteria for glass-fiber reinforced composites under confining pressure. *J. Sturct. Mech.*, Vol. 13, No. 3&4, 371-393
20) Boehler, J.P. and Sawczuk, A. 1976. Application of representation theorems to describe yielding of transversely isotropic solids, *Mech. Res. Comm.*, Vol. 3, 277-283
21) Boehler, J.P. and Sawczuk, A. 1977. On yielding of oriented solids. *Acta Mechanica*, Vol. 27, 185-206
22) Böker, R. 1915. Die Mechanik der bleibenden Formänderung in Kristallinisch aufgebauten Körpern. *Ver. Dtsch. Ing. Mitt. Forsch.*, Vol. 175, 1-51
23) Borecki, M. and Kwaśniewski, M. 1981. Experimental and analytical studies on compressive strength of anisotropic rocks. *Proceedings of the 7th Plenary Scientific Session of the International Bureau of Rock Mechanics*, 23-49.
24) Cazacu, O., Cristescu, N.D., Shao, J.F., and Henry, J.P. 1998. A new anisotropic failure criterion for transversely isotropic solids. *Mechanics of Cohesive-Frictional Materials*, Vol. 3, 89-103
25) Cazacu, O. 1999. A paraboloid failure surface for transversely isotropic materials. *Mech. Mater.*, Vol. 31, 381-393
26) Chang, C. and Haimson, B. 2000. True triaxial strength and deformability of the German Continental Deep Drilling Program (KTB) deep hole amphibolite. *J. Geophys. Res.*, Vol. 105, No. B8, 18999-19013
27) Chang, C. 2004. Effect of intermediate principal stress on rock fractures. *Jour. Korean Earth Science Society*. Vol. 25, No. 1, 22-31
28) Chang, C. and Haimson, B. 2005. Non-dilatant deformation and failure mechanism in two Long Valley Caldera rocks under true triaxial compression. *Int. J. Rock. Mech. Min. Sci.*, Vol: 42, 402-414
29) Chang, C. and Haimson, B. 2007. Effect of fluid pressure on rock compressive failure in a nearly impermeable crystalline rock: Implication on mechanism of borehole breakouts. *Engineering Geology*, Vol. 89, 230–242
30) Colmenares, L.B. and Zoback, M.D. 2002. A statistical evaluation of intact rock failure criteria constrained by polyaxial tests data for five different rocks. *Int. J. Rock Mech. Min. Sci.*, Vol. 39, 695–729
31) Crawford, B.R., Smart, B.G.D., Main, I.G. and Liakopoulou-Morris, F. 1995. Strength characteristics and shear acoustic anisotropy of rock core subjected to true triaxial compression. *Int. J. Rock Mech. Min. Sci. & Geomech. Abstr.*, Vol. 32, No. 3, 189-200
32) Dafalias, Y.F. 1979. Anisotropic hardening of initially orthotropic materials. *Z. Angew. Math. Mech.*, Vol. 59, No. 9, 437-446
33) Dafalias, Y.F. 1987. An anisotropic critical state clay plasticity model. *Proceedings of the*

Constitutive Laws for Engineering Materials: Theory and Applications. Vol. I, 513-521
34) Desai, C.S. and Salami, M.R. 1987. A constitutive model and associated testing for soft rock. *Int. J. Rock Mech. Min. Sci. & Geomech. Abstr.*, Vol. 24, No. 5, 299-307
35) Dolley, T.P. 2000. Diatomite. *US Geological Survey Minerals Yearbook*. 25.1 – 25.4
36) Donath, F.A. 1961. Experimental study of shear failure in anisotropic rocks. *Geological Society of America Bulletin*, Vol. 72, 985-990
37) Donath, F.A. 1964. Strength variation and deformational behavior of anisotropic rocks. *State of Stress in the Earth's Crust: Proceedings of the International Conference*, American Elsevier Publishing Co., 281-298.
38) Donath, F.A., Schuler, K.W., and Tillerson, J.R. 1979. Apparatus effects in the determination of strength variation in anisotropic rock. *No. 295 – Comportement Méchanique des Solides Anisotropes, Colloques internationaux du CNRS*. 819-832
39) Donath, F.A. 1972. Effects of cohesion and granularity on deformational behavior of anisotropic rock. *Studies in Mineralogy and Precambrian Geology*, Vol. 135, 95-128
40) Drucker, D. C. and Prager, W. 1952. Soild mechanics and plastic analysis for limit design. *Quarterly of Applied Mathematics*, Vol. 10, No. 2, 157-165
41) Duveau, G. and Shao, J.F. 1998. A modified single plane of weakness theory for the failure of highly stratified rocks. *Int. J. Rock Mech. Min. Sci.*, Vol. 35, No. 6, 807-813
42) Duveau, G., Shao, J.F., and Henry J.P. 1998. Assessment of some failure criteria for strongly anisotropic geomaterials. *Mech. Cohes.-Frict. Mater.*, Vol. 3, 1-26
43) Egger P. 1982. Engineering problems caused by the anisotropic behavior of the rock mass. *Proceedings of the Euromech Colloquium 115: Mechanical behavior of anisotropic solids*, 887-900
44) Gol'denblat, I.I. and Kopnov, V.A. 1966. Strength of glass-reinforced plastics in the complex stress state. *Polymer. Mech.*, Vol. 1, No. 2, 54-59
45) Griffith, A. A. 1924. Theory of rupture. *Proc. 1st Int. Congr. Appl. Mech.*, 55–63
46) Gupta, D. and Zaman, M. 1999. Stability of boreholes in a geologic medium including the effects of anisotropy. *Applied Math. And Mech.*, Vol. 20, No. 8, 837-866
47) Haimson, B. and Chang, C. 2000. A new true triaxial cell for testing mechanical properties of rock, and its use to determine rock strength and deformability of Westerly granite. *Int. J. Rock Mech. Min. Sci.*, Vol. 37, 285-296
48) Haimson, B. and Chang, C. 2002. True triaxial strength of the KTB amphibolite under borehole wall conditions and its use to estimate the maximum horizontal in situ stress. *J. Geophys. Res.*, Vol. 107, No. B10, 2257
49) Haimson, B. 2003, Strength, Deformability, and Micromechanics of Brittle Fracture in a Crystalline Rock Under True Triaxial Compressive Stresses. *ISRM 2003 – Technology roadmap for rock mechanics*, 451-456
50) Haimson, B. 2006. True triaxial stresses and the brittle fracture of rock. *Pure Appl. Geophys.*, Vol. 163, 1101-1130
51) Handin, J. and Hager, R.V. 1957. Experimental deformation of sedimentary rocks under confining pressure: tests at room temperature on dry samples. *Bull. Am. Assoc. Petrol. Geol.*,

Vol. 41, 1-50
52) Handin, J., Heard, H.C. and Magouirk, J.N. 1967. Effects of the intermediate principal stress on the failure of limestone, dolomite, and glass at different temperatures and strain rates. *J. Geophy. Res.*, Vol. 72, No. 2, 611-640
53) Hill, R.1948. A theory of the yielding and plastic flow of anisotropic metals. *Proc. R. Soc. Lond.*, 193A, 281–297.
54) Hoek, E. 1964. Fracture of Anisotropic Rock. *J. South African Inst. Min. and. Met.*, Vol. 1, No. 10, 510-518
55) Hoek, E. and Brown, E.T. 1980. Empirical strength criterion for rock masses. *J. Geotech. Engrg. Div. ASCE 106*, 1013–1035
56) Hoek, E. and Brown, E.T. 1980. Underground excavations in rock. The Institute of Mining and Metallurgy, London
57) Hojem, J.P.M. and Cook, N.G.L. 1968. The design and construction of a triaxial and polyaxial cell for testing rock specimens. *South African Mech. Engr.*, Vol. 18, 57-61
58) Hoffman, O. 1967. The brittle strength of orthotropic materials. *J. Composite Materials*. Vol. 1, 200-206
59) Hoskins, E.R. 1969. The failure of thick-walled hollow cylinders of isotropic rock. *Int. J. Rock Mech. Min. Sci.*, Vol. 6, 99-125
60) Hunsche, U. and Albrecht, H. 1990. Results of true triaxial strength tests on rock salt. *Eng. Fract. Mech.*, Vol. 35, No. 4/5, 867-877
61) Jaeger, J.C. 1960. Shear failure of anisotropic rocks. *Geol. Mag.*, Vol. 97, I960, 65-72.
62) Kármán, T. von. 1911. Festigkeitsversuche unter allseitigem. *Druck. Z. Ver. Dtsch. Ing.*, Vol. 55, 1749-4757
63) Karr, D.G., Law, F.P. and Fatt, M.H. 1989. Asymptotic and quadratic failure criteria for anisotropic materials. *Int. J. Plast.*, Vol. 5, 303-336
64) Kim, M.K. and Lade, P.V. 1984. Modelling rock strength in three dimensions. *Int. J. Rock Mech. Min. Sci. & Geomech. Abstr.*, Vol. 21, 21-33
65) Kwaśniewski, M. 1983. Anisotropy of elasticity of rocks and its effect on the magnitude and distribution of stresses around underground openings. *Proceedings of the 8th Plenary Scientific Session of the International Bureau of Strata Mechanics: Application of Rock Mechanics to Planning and Design Prior to Mining*, 5–37
66) Kwaśniewski, M.A. 1993. Mechanical behavior of anisotropic rocks. *Comprehensive rock engineering: Principles, practice and projects*, Vol. 1, 285–312
67) Lade, P.V. 1977. Elasto-plastic stress-strain theory for cohesionless soil with curved yield surfaces. *Int. J. Solids Struct.*, Vol. 13, 1019-1035
68) Lade, P.V. 1982. Three-parameter failure criterion for concrete. *J. Eng. Mech. Div. (ASCE)*. Vol. 108, 850-863
69) Lade, P.V. 1993. Rock strength criteria: the theories and the evidence. *Comprehensive rock engineering: Principle, practice, and projects*, Vol. 1, 255–284
70) Lekhnitskii, S.G. 1963. Theory of elasticity of an anisotropic elastic body. Holden-Day Inc. San Francisco

71) Lundborg, N. 1972. A statistical theory of the polyaxial compressive strength of materials. *Int. J. Rock Mech. Min. Sci.*, Vol. 9, 617-624
72) Matsuoka, H. and Nakai, T. 1974. Stress-deformation and strength characteristics of soil under three different principal stresses. *Proc. of JSCE.*, No. 232, 59-70
73) Matsuoka, H. and Nakai, T. 1982. A new failure criterion for soils in three-dimensional stresses. *Proceedings of the IUTAM Conference on Deformation and Failure of Granular Materials*, 253-263
74) McClintock, F.A. and Walsh, J.B. 1962. Friction on Griffith cracks in rocks under pressure. *Proceedings of the 4th U.S. National Congress on Applied Mechanics*, 1015-1021
75) McLamore, R. and Gray, K.E. 1967. The mechanical behavior of anisotropic sedimentary rocks. *Trans. Am. Soc. Mech. Eng. Series B*, Vol. 89, 62–76
76) Michelis, P. 1985. A true triaxial cell for low and high pressure experiments. *Int. J. Rock Mech. Min. Sci. & Geomech. Abstr.*, Vol. 22, No. 3, pp 183-188
77) Michelis, P. 1987. True triaxial cyclic behavior of concrete and rock in compression. *Int. J. Plast.*, Vol. 3, 249-270
78) Mogi, K. 1967. Effect of the intermediate stress on rock failure. *J. Geophys. Res.*, Vol. 72, 5117-5131
79) Mogi, K. 1969. On a new triaxial compression test of rocks. *Abstr. 1969 Meeting Seismol. Soc. Japan*, 3.
80) Mogi, K. 1970. Effect of the triaxial stress system on rock failure. *Rock Mech. In Japan. ISRM National Group of Japan*, Vol. 1, 53-55
81) Mogi, K. 1971. Fracture and flow of rocks under high triaxial compression, *J. Geophys. Res.*, Vol. 76, 1255–1269
82) Mogi, K. 2007. Experimental rock mechanics. Taylor & Francis Group, London, UK
83) Mróz, Z. and Maciejewski, J. 2002. Failure criteria of anisotropically damaged materials based on the critical plane concept. *Int. J. Numer. Anal. Meth. Geomech.*, Vol. 26, 407-431
84) Murrell S.A.F. 1963. A criterion for brittle fracture of rocks and concrete under triaxial stress, and the effect of pore pressure on the criterion, *Proceedings of Fifth U.S. Symposium on Rock Mech.*, 563-577.
85) Nasseri, M.H., Rao, K.S. and Ramamurthy, T. 1997. Failure mechanism in schistose rocks. *Int. J. Rock Mech. Min. Sci.*, Vol. 34, No. 3-4, Paper No. 219
86) Nasseri, M.H., Rao, K.S. and Ramamurthy, T. 2003. Anisotropic strength and deformational behavior of Himalayan schists. *Int. J. Rock Mech. Min. Sci.*, Vol. 40, 3-23
87) Niandou, H. 1994. Etude du comportement rhéologique et modélisation de l'argilite de Tournemire: Applications á la stabilité d'ouvrages souterrains. Doctoral thesis (in French), Université de Lille
88) Niandou, H., Shao, J.F., Henry, J.P., Fourmaintraux, D. 1997. Laboratory investigation of the mechanical behavior of Tournemire shale. *Int. J. rock Mech. Min. Sci.*, Vol. 34, No. 1, 3-16
89) Nova, R. 1980. The failure of transversely isotropic rocks in triaxial compression. *Int. J. Rock Mech. Min. Sci. & Geomech. Abstr.*, Vol. 17, 325-332
90) Nova, R. and Sacchi, G. 1982. A generalized failure condition for orthotropic solids.

Proceedings of the Euromech Colloquium 115: Mechanical behavior of anisotropic solids, 623-641

91) Nova, R. 1986. An extended cam clay model for soft anisotropic rocks. *Comput. Geotech.*, Vol. 2, 69-88

92) Olszak, W. and Urbanowski, W. 1956. The plastic potential and the generalized distortion energy in the theory of non-homogeneous anisotropic elastic-plastic bodies. *Arch. Mech. Stos*, Vol. 8, No. 4, 671-694

93) Oku, H. Haimson, B. and Song, S.-R. 2007. True triaxial strength and deformability of the siltstone overlying the Chelungpu fault (Chi-Chi earthquake), Taiwan. *Geophys. Res. Lett.*, Vol. 34, L09306

94) Ong, S.H. and Roegiers, J.-C. 1993. Influence of anisotropies in borehole stability. *Int. J. Rock Mech. Min. Sci. & Geomech. Abstr.*, Vol. 30, No. 7, 1069-1075

95) Ong, S.H. 1994. Borehole stability. Ph.D. Thesis, University of Okalhoma

96) Pariseau, W.G. 1972. Plasticity theory for anisotropic rocks and soils. *Proceedings of the 10th Symposium on Rock Mechanics (AIME)*, Vol. 1, 267-295

97) Pietruszczak, S., Lydzba, D., and Shao, J.F. 2004. Description of creep in inherently anisotropic frictional materials. *J. Eng. Mech.*, Vol. 130, No. 6, 681-690

98) Pietruszczak, S. and Mróz, Z. 2000. Formulations of anisotropic failure criteria incorporating a microstructure tensor. *Comput. Geotech.*, Vol. 26, 105–112

99) Pietruszczak, S. and Mróz, Z. 2001. On failure criteria for anisotropic cohesive-frictional materials. *Int. J. Numer. Anal. Meth. Geomech.*, Vol. 25, 509-524

100) Pietruszczak, S. and Pande, G.N. 2001. Description of soil anisotropy based on multi-laminate framework. *Int. J. Numer. Anal. Meth. Geomech.*, Vol. 25, 197-206

101) Pietruszczak, S., Lydzba, D., and Shao, J.F. 2002. Modelling of inherent anisotropy in sedimentary rocks. *Int. J. Solids Struct.*, Vol. 39, 637–648.

102) Ramamurthy, R. 1993. Strength and modulus responses of anisotropic rocks. *Comprehensive rock engineering principles, practice and projects*, Vol. 1, 313–329

103) Ramamurthy, T., Venkatappa Rao, G. and Singh, J. 1993. Engineering behavior of phyllites. *Engineering Geology*, Vol. 33, 209-225

104) Rogers T.G. 1990. Yield criteria, flow rules, and hardening in anisotropic plasticity. *Proceedings of the IUTAM/ICM Symposium on Yielding, Damage, and Failure of Anisotropic Solids*, 53-79

105) Schuler, K.W. and Tillerson, J.R. 1976. A preliminary analysis of stress nonuniformities in triaxial tests of bedded rocks. *Technical Report*, SAND-76-0526, Sandia Labs.

106) Singh, B., Goel, R.K. Mehrotra, V.K., Garg, S.K. and Allu, M.R. 1998. Effect of intermediate principal stress on strength of anisotropic rock mass. *Tunnelling and Underground Space Technology*, Vol. 13, No. 1, 71-79

107) Smart, B.G.D. 1995. A true triaxial cell for testing cylindrical rock specimens. *Int. J. Rock Mech. Min. Sci. & Geomech. Abstr.*, Vol. 32, No. 3, 269-275

108) Song, I. and Haimson, B. Polyaxial strength criteria and their use in estimating in-situ stress magnitudes from borehole breakout dimensions. *Int. J. Roc Mech. & Min. Sci.*, Vol. 34,

No. 3-4, Paper No. 116

109) Spencer, A.J.M. 1982. The formulation of constitutive equation for anisotropic solids. *Proceedings of the Euromech Colloquium 115: Mechanical behavior of anisotropic solids*, 2–26

110) Takahashi, M. and Koide, H. 1989. Effect of the intermediate principal stress on strength and deformation behavior of sedimentary rocks at the depth shallower than 2000m. *Proc. of Int. Symp. on Rock at Great Depth*, Pau, 19-26

111) Tsai, S.W. and Wu, E.M. 1971. A general theory of strength for anisotropic materials. *J. Composite Materials*, Vol. 5, 58-80

112) Tsai, S.W. 1982. Strength ratios of orthotropic materials. *Proceedings of the Euromech Colloquium 115: Mechanical behavior of anisotropic solids*, 435-448

113) von Mises, R. 1913. Mechanik der Festen Korper im plastisch deformablen Zustand. *Gottin. Nacher. Math. Phys.*, Vol. 1, 582–592.

114) Walsh, J.B. and Brace, W.F. 1964. A fracture criterion for brittle anisotropic rock. *Journ. Geoph. Res.*, Vol. 69, No. 16, 3449–3456

115) Wang, R. and Kemeny, J.M. 1995. A new empirical failure criterion for rock under polyaxial compressive stresses. *Proc. 35th US Symp. Rock Mechanics*. 453-458

116) Wawersik, W.R., Carlson, L.W., Holcomb, D.J. and Williams, R.J. 1997. New method for true-triaxial rock testing. *Int. J. Roc Mech. Min. Sci.*, Vol. 34, No. 3-4, Paper No. 330

117) Weibull, W. 1939. A statistical theory of the strength of materials. *Proc. R. Sw. Acad. Engng. Sci.* 151, 5-45

118) Wiebols, G.A. and Cook, N.G.W. 1968. An energy criterion for the strength of rock in polyaxial compression. *Int. J. Roc Mech. Min. Sci.*, Vol. 5, 529-549

119) Zhang, L. and Zhu, H. 2007. Three-dimensional hoek-brown strength criterion for rocks. *J. Geotech. Geoenv. Eng.*, Vol. 133, No. 9, 1128-1135

120) Zhou, S. 1994. A program to model the initial shape and extent of borehole breakout. *Comput. Geotech.*, Vol. 20, No. 7/8, 1143-1160

Appendix A Data for Isotropic Rocks

In this appendix, the strength of more or less isotropic rocks under true triaxial stress is summarized for all the data sets. The mineralogy of these rocks (if available) is summarized at the end of each table, most of which is cited from the original literature word for word.

Table A.1 Thick-walled Cylinder Tests on Bowral Trachyte (Hoskins, 1969)

σ_3 (kb)	σ_2 (kb)	σ_1 (kb)	σ_3 (kb)	σ_2 (kb)	σ_1 (kb)
0	0	1.63	0.21	0.21	3.19
0	0.19	2.29			
0	0.34	2.53	0.35	0.35	4.07
0	0.46	3	0.35	1.31	5.35
0	0.77	3.3	0.35	2.28	6.13
0	0.97	3.51			
0	1.45	3.89	0.52	0.52	4.66
0	1.93	3.92	0.52	1	5.3
0	2.32	4.4	0.52	1.97	6.03
0	2.42	4.06			
0	2.7	3.39	0.69	0.69	5.17
0	2.9	3.62	0.69	1.69	6
0	2.76	3.38			
0	2.57	3.62	1.03	1.03	6.61
0	2.62	3.86			
0.16	0.35	3.4			
0.17	0.17	2.59			
0.17	0.46	3.47			
0.17	0.66	3.9			
0.17	1.14	4.69			
0.17	1.62	5.05			
0.17	2.59	5.52			
0.17	3.08	5.56			

Note:
"This is the commercial name for a rock that has been more accurately described by Joplin as an altered micro-syenite. It is an even-grained, isotropic igneous rock consisting predominantly of orthoclase and aegerine-augite 1 mm in grain size with minor amounts of quartz, calcite, and altered ferro-magnesian minerals."

Table A.2 Thick-walled Hollow Cylinder Tests on Carrara Marble (Hoskins, 1969)

σ_3 (kb)	σ_2 (kb)	σ_1 (kb)	σ_3 (kb)	σ_2 (kb)	σ_1 (kb)
0	0	0.8	0.35	0.35	2.13
0	0.46	1.54	0.35	2.17	3.78
0	0.93	2.03			
0	1.38	2.39	0.5	0.5	2.38
0	1.84	2.59			
0	2.3	2.82	0.69	0.69	3.18
0	2.71	2.75	0.69	1.67	3.97
0.07	0.07	1.11	1.03	1.03	4.11
0.07	0.44	1.63			
0.07	0.8	2.14			
0.07	1.72	3.02			
0.07	3.09	3.28			

Note:
"A uniform medium-to-fine-grained isotropic essentially pure calcite marble. The grain size varies from piece to piece of this material but a single block with average grain size of about 0.2 mm was used for all of the specimens in these experiments."

Table A.3 Thick-walled Hollow Cylinder Tests on Gosford Sandstone (Hoskins, 1969)

σ_3 (kb)	σ_2 (kb)	σ_1 (kb)	σ_3 (kb)	σ_2 (kb)	σ_1 (kb)
0	0	0.49	0.17	0.17	0.98
0	0.09	0.67	0.17	0.66	1.4
0	0.18	0.8	0.17	1.43	1.54
0	0.46	1.08	0.17	1.62	2.1
0	0.77	1.12	0.17	2.34	2.59
0	0.92	1.29			
0	1	1.16	0.35	0.35	1.67
0	1.21	1.37	0.35	1.31	2.26
0	0.73	1.45	0.35	2.28	2.67
0	1.14	1.47			
0	0.83	1.66	0.5	0.5	1.93
0	0.87	1.74			
			0.69	0.69	2.22
0.07	0.07	0.8	0.69	1.66	2.84
0.07	0.45	1.15			
0.07	0.62	1.42	1.04	1.04	2.78
0.07	0.8	1.53			
0.07	1.07	1.59			
0.07	1.33	1.85			
0.07	1.42	1.84			
0.07	1.62	1.85			
Note: "A very uniform, isotropic, fine-grained, weakly cemented, quartz sandstone with a sugary texture."					

Table A.4 Conventional Triaxial Tests on a Limestone (Hoskins, 1969)

$\sigma_3 = \sigma_2$ (kb)	σ_1 (kb)
0	1.97
0	2.3
0	2.17
0.17	2.85
0.35	3.46
0.5	3.87
0.5	3.86
0.69	4.07
0.69	4.16
1	4.79

Table A.5 Thick-walled Hollow Cylinder Tests on a Limestone (Hoskins, 1969)

σ_3 (kb)	σ_2 (kb)	σ_1 (kb)
0	0	2.06
0	0.59	2.88
0	0.98	3.24
0	1.46	3.4
0	1.95	3.78
0	3.41	4.15
0	3.9	4.43
Note: "a lithographic limestone (presumed to be Solnhofen)"		

Table A.6 Conventional Triaxial Tests on a Quartz-Dolomite Rock (Hoskins, 1969)

$\sigma_3 = \sigma_2$ (kb)	σ_1 (kb)
0	2.28
0	2.13
0	1.78
0.35	4.83
0.35	5.13
0.35	5.13
0.69	6.13
0.69	5.49
0.69	6.03
1.03	6.71
1.03	7.35
1.03	7.28

Table A.7 Thick-walled Hollow Cylinder Tests on a Quartz-Dolomite Rock (Hoskins, 1969)

σ_3 (kb)	σ_2 (kb)	σ_1 (kb)
0	0	2.14
0	0	4.27
0	0	1.55
0	0.17	3.94
0	0.17	3.1
0	0.17	3.7
0	0.5	4.42
0	0.5	4.22
0	0.5	4.64
0	0.84	5.3
0	0.84	4.6
0	0.84	4.95
0	1.67	5.7
0	1.67	6.04
0	1.67	6.02
0	3.34	7.85
0	3.34	7.1
0	3.34	7.1
Note: "from Mt Isa, Australia"		

Table A.8 Conventional Triaxial Tests on Apache Leap Tuff (Wang and Kemeny, 1995)

σ_3(MPa)	σ_2(MPa)	σ_1(MPa)
0	0	141.9
0	0	141.9
0	0	155.2
0	0	152.9
0	0	169.5
0	0	120.6
0	0	145.5
0	0	131.3
0	0	152.6
0	0	161.5
3.4	3.4	181.8
6.9	6.9	197
10.3	10.3	240.4
13.8	13.8	248.9
13.8	13.8	250
17.2	17.2	265.3
20.7	20.7	242.3
24.1	24.1	308.4
27.6	27.6	329.8
31	31	356.7
34.5	34.5	360.2
37.9	37.9	396.5
41.4	41.4	419.5
44.8	44.8	456.1
48.3	48.3	434.1
55.2	55.2	464.9

Table A.9 Thick Walled Hollow Cylinder Tests on Apache Leap Tuff (Wang and Kemeny, 1995)

σ_3(MPa)	σ_2(MPa)	σ_1(MPa)	σ_3(MPa)	σ_2(MPa)	σ_1(MPa)
0	14.8	164.7			
0	15.4	180.3	3.4	8.6	170.1
0	18.4	190.1	6.9	17.2	223.9
0	30.7	218.1	10.3	25.7	200.2
0	29.6	221.4	13.8	34.5	255.6
0	36.8	227.8	17.2	43.1	241.9
0	44.5	247.1	20.7	51.7	289.3
0	55.2	241.1	24.1	60.3	373.9
0	50.7	276.6	27.6	68.9	419.1
0	61.5	272.6			
0	59.3	286.6	6.9	8.6	170.9
0	73.5	286	10.3	12.9	242.3
0	79.9	333.7	13.8	17.2	201.7
0	92.3	341.3	17.2	21.5	260.1
0	110.3	325.9	20.7	25.9	244.8
0	88.9	349.6	24.1	30.2	328.8
			27.6	34.5	295.9
			31	38.8	340.3

Table A.10 True Triaxial Tests on Dunham Dolomite (Mogi, 2007)

σ_3(MPa)	σ_2(MPa)	σ_1(MPa)	σ_3(MPa)	σ_2(MPa)	σ_1(MPa)
0	0	(265)	105	105	682
0	0	(258)	105	167	778
			105	205	786
25	25	400	105	268	805
25	66	475	105	270	863
25	96	495	105	334	824
25	129	560	105	356	840
25	174	571	105	415	822
25	229	586			
25	272	545	125	125	725
			125	187	824
45	45	486	125	239	860
45	97	570	125	293	863
45	126	576	125	362	897
45	160	606	125	414	941
45	183	639	125	463	918
45	240	670	125	516	886
45	266	670			
45	294	622	145	145	*
			145	253	883
60	60	540	145	296	927
			145	324	923
65	65	568	145	349	922
65	117	638	145	392	1015
65	153	644	145	410	1002
65	208	687	145	455	952
65	262	685			
65	318	746	200	200	*
65	393	701			
85	85	620			
85	128	684			
85	153	719			
85	233	744			
85	306	773			
85	376	818			
85	445	793			

Note:
*: Ultimate stress was not determined in the test because of high ductility.
"This rock is highly homogeneous and isotropic".

Table A.11 True Triaxial Tests on Solnhofen Limestone (Mogi, 2007)

σ_3(MPa)	σ_2(MPa)	σ_1(MPa)	σ_3(MPa)	σ_2(MPa)	σ_1(MPa)
0	0	310	80	80	538
			80	126	572
20	20	397	80	150	577
20	51	417	80	208	647
20	92	413	80	225	591
20	165	453	80	283	677
20	206	460	80	298	665
20	233	465	80	378	650
			80	454	680
40	40	449			
40	40	446	105	105	*
40	80	486	105	185	*
40	113	499	105	293	711
40	193	530	105	341	*
40	274	547	105	439	*
40	315	535	105	528	*
			105	577	727
60	60	473			
60	87	517	120	120	*
60	102	537	120	294	*
60	113	530	120	362	*
60	164	576	120	450	*
60	197	550	120	533	*
60	275	553			
60	345	557			

Note:
*: Ultimate stress was not determined in the test because of high ductility.
This rock "is highly homogeneous and isotropic".

Table A.12 True Triaxial Tests on Yamaguchi Marble (Mogi, 2007)

σ_3(MPa)	σ_2(MPa)	σ_1(MPa)	σ_3(MPa)	σ_2(MPa)	σ_1(MPa)
0	0	82	55	55	*
			55	82	*
6	6	118	55	107	369
			55	138	388
12.5	12.5	140	55	167	390
12.5	26	179	55	200	396
12.5	28	177	55	231	390
12.5	45	196			
12.5	67	213	70	70	*
12.5	90	225	70	108	*
12.5	105	228	70	148	*
12.5	115	200	70	181	454
			70	214	464
25	25	189	70	243	440
25	39	209	70	268	462
25	48	240			
25	78	252	85	85	*
25	107	275	85	119	*
25	132	268	85	157	*
25	157	268	85	194	*
25	168	250	85	238	535
			85	274	537
40	40	243			
40	64	290	100	100	*
40	88	288	100	133	*
40	88	309	100	169	*
40	112	319	100	207	*
40	143	307	100	279	*
40	160	336			
40	177	321	150	150	*
40	208	341	150	150	*
			200	200	*
			200	200	*

Note:

*: Ultimate stress was not determined in the test because of high ductility.

"This rock a medium-grained calcite marble quarried at Mine, Yamaguchi

prefecture, Japan".

Table A.13 True Triaxial Tests on Mizuho Trachyte (Mogi, 2007)

σ_3(MPa)	σ_2(MPa)	σ_1(MPa)	σ_3(MPa)	σ_2(MPa)	σ_1(MPa)
0	0	100	75	75	368
			75	108	405
15	15	196	75	147	415
			75	210	438
30	30	259	75	279	440
			75	318	430
45	45	302	75	363	452
45	58	314			
45	67	327	100	100	437
45	90	341	100	126	463
45	138	350	100	171	493
45	204	359	100	256	497
45	281	368	100	354	522
45	323	353	100	384	510
60	60	341			
60	83	353			
60	133	386			
60	186	401			
60	212	403			
60	254	401			
60	306	381			

Note:
"This rock, quarried at Tomisaki, Gunma prefecture, Japan, is a moderately porous and fairly homogeneous silicate rock.".

Table A.14 True Triaxial Tests on Manazuru Andesite (Mogi, 2007)

σ_3(MPa)	σ_2(MPa)	σ_1(MPa)
0	0	140
16	16	349
20	20	364
20	20	381
20	67	470
20	124	516
20	186	538
40	40	552
40	75	577
40	112	632
40	126	669
40	206	653
40	278	626
70	70	671
70	101	735
70	152	735
70	193	808
70	275	812
70	313	801
70	375	833
100	100	806
110	110	875
130	130	881
Note: "This andesite quarried at Manazuru, Kanagawa prefecture, Japan, is a compact, light gray rock."		

Table A.15 True Triaxial Tests on Inada Granite (Mogi, 2007)

σ_3(MPa)	σ_2(MPa)	σ_1(MPa)	σ_3(MPa)	σ_2(MPa)	σ_1(MPa)
0	0	226	150	150	1138
0	0	232	150	150	1198
			150	164	1223
20	20	508	150	195	1279
20	44	556	150	215	1316
20	46	611	150	273	1332
20	74	643	150	309	1342
20	101	624	150	317	1275
20	127	607	150	365	1307
40	40	692	200	200	1301
40	63	722	200	200	1398
40	88	743	200	200	1438
40	120	802	200	200	1388
40	142	760	200	200	1334
40	147	791	200	216	1425
40	174	834	200	233	1441
			200	281	1545
70	70	841	200	309	1523
70	70	879	200	383	1554
			200	439	1587
100	100	1003			
100	100	1023	230	230	1497
100	138	1046			
100	148	1037			
100	199	1083			
100	239	1141			
100	291	1125			
100	336	1131			

Note:
"This biotite granite quarried at Inada, Ibaraki prefecture, Japan, is medium-grained and light gray in color."

Table A.16 True Triaxial Tests on Orikabe Monzonite (Mogi, 2007)

σ_3(MPa)	σ_2(MPa)	σ_1(MPa)	σ_3(MPa)	σ_2(MPa)	σ_1(MPa)
0	0	236	140	140	943
0	0	232	140	140	981
			140	205	1098
5	5	339	140	259	1144
			140	331	1161
20	20	504	140	424	1168
40	40	583	200	200	1107
40	40	571	200	235	1168
40	40	600	200	251	1244
40	59	636	200	298	1305
40	80	698	200	343	1352
40	101	673	200	401	1329
40	102	775	200	473	1358
40	121	739	200	537	1364
40	143	747			
40	168	777			
40	187	748			
80	80	718			
80	80	742			
80	80	794			
80	95	834			
80	108	810			
80	117	836			
80	135	854			
80	147	893			
80	182	889			
80	183	930			
80	216	906			
80	218	973			
80	281	926			
80	284	956			
80	311	966			

Table A.17 True Triaxial Tests on Shirahama Sandstone (Takahashi and Koide, 1989)

σ_3(MPa)	σ_2(MPa)	σ_1(MPa)	σ_3(MPa)	σ_2(MPa)	σ_1(MPa)
8	8	118.561	40	40	220.317
8	14.3883	110.129	40	40	231.959
8	25.401	129.764	40	40	216.087
8	40.169	131.959	40	59.8249	244.761
8	60.2195	132.594	40	69.8158	254.867
8	71.8512	126.306	40	79.8531	251.745
			40	99.3723	253.436
15	15	147.7	40	99.8385	270.899
15	28.4722	156.764	40	99.9223	247.09
15	40.0331	170.582	40	119.917	263.597
15	59.582	163.807	40	139.925	276.402
15	79.6382	162.855	40	159.522	255.87
15	85.4223	168.706	40	160.527	270.162
15	93.871	167.163			
			50	50	242.597
20	28.3941	178.986	50	50	224.079
20	40.5013	187.516	50	60.2503	273.864
20	48.9555	184.386	50	70.3267	259.631
20	60.0427	182.857	50	80.7689	291.433
20	69.5059	192.96	50	90.8901	264.502
20	82.1724	192.498	50	110.972	256.143
20	99.0903	183.593	50	130.456	267.886
20	100.136	186.244	50	150.973	285.984
			50	171.072	272.863
30	30	185.873	50	190.578	278.257
30	30	196.457			
30	30	180.056			
30	47.7754	219.829			
30	68.859	226.819			
30	87.3097	232.208			
30	108.425	230.203			
30	130.023	240.9			
30	148.547	225.654			
30	168.107	215.704			

Table A.18 True Triaxial Tests on Izumi Sandstone (Takahashi and Koide, 1989)

σ_3(MPa)	σ_2(MPa)	σ_1(MPa)
20	20	341.656
20	20	352.218
20	39.6713	441.146
20	39.794	429.516
20	50.1243	450.718
20	60.3925	377.812
20	78.1995	390.595
20	98.6258	455.204
20	110.346	444.692
20	120.576	475.411
20	139.019	427.925
20	149.606	424.809
50	50	552.229
50	50	560.682
50	71.0369	569.258
50	89.7653	594.734
50	99.7497	648.715
50	120.125	618.158
50	130.092	573.8
50	148.787	602.448
50	168.682	617.357

Table A.19 True Triaxial Tests on Yuubari Shale (Takahashi and Koide, 1989)

σ_3(MPa)	σ_2(MPa)	σ_1(MPa)
25	25	160.975
25	25	167.713
25	35	181.677
25	35	187.369
25	45	175.326
25	55	175.05
25	65	186.264
25	75	199.69
25	80	193.765
25	85	196.405
25	95	200.678
25	100	194.04
25	115	185.64
25	125	197.359
25	135	183.191
50	50	228.364
50	50	238.904
50	50	244.782
50	70	257.171
50	90	260.564
50	100	265.544
50	110	259.656
50	120	259.761
50	130	285.345
50	150	265.797
50	160	255.91

Table A.20 True Triaxial Tests on Horonai Sandstone (Takahashi and Koide, 1989)

	σ_3(MPa)	σ_2(MPa)	σ_1(MPa)		σ_3(MPa)	σ_2(MPa)	σ_1(MPa)
HOSS-I	5	5	117.303		50	129.481	362.946
	5	14.8585	121.52		50	169.811	320.448
	5	25.4717	122.908		50	169.811	327.52
	5	37.5	122.88		50	170.519	333.874
	5	51.6509	127.087		50	190.33	309.799
	5	73.5849	112.901		50	199.528	317.551
					50	210.849	328.125
	10	10	138.493				
	10	19.8113	154.017	HOSS-III	10	10.6132	234.604
	10	39.6226	140.543		10	43.1604	235.941
	10	60.1415	174.417		10	60.8491	250.74
	10	77.1226	172.963		10	63.6792	271.935
	15	15	137.774		20	22.6415	305.954
	15	28.3019	163.891		20	31.1321	316.534
	15	46.6981	185.049		20	39.6226	343.37
	15	70.0472	193.475		20	58.7264	351.805
	15	77.1226	176.497				
	15	83.4906	191.323				
	15	95.5189	194.828				
	15	116.745	189.831				
HOSS-II	15	24.7642	202.062				
	15	29.0094	211.239				
	15	30.42	252.23				
	15	39.6226	232.415				
	15	45.9906	228.16				
	15	58.7264	233.784				
	15	64.3868	243.665				
	15	79.2453	258.471				
	15	96.934	245.001				
	15	118.16	240.711				

Table A.21 True Triaxial Tests on Gosford Sandstone (Wawersik, 1997)

Deviatoric Stress Path	Load Angle	$I_1/3$	$\sqrt{J_2}$	σ_1	σ_2	σ_3
	θ (°)	(MPa)	(MPa)	(MPa)	(MPa)	(MPa)
$\sigma_2 = \sigma_3$, $I_1/3$ = constant	0	76.9	78.0	167.0	31.87	31.87
σ_3 = constant, proportional	21.0	77.0	63.4	145.3	65.54	20.11
σ_2 = constant, $I_1/3 \approx$ constant, pure shear	31.3	77.7	65.6	142.4	79.42	11.26
σ_3 = constant, plane strain	45.8	76.9	58.8	124.2	95.89	11.08
$\sigma_2 = \sigma_3$ = constant, CTC	0	78.8	80.6	171.9	32.27	32.27
σ_3 = constant, proportional	21.0	74.2	61.2	140.2	63.15	19.28
Note: The principal stress values are calculated from the three stress invariants, which are reported in Wawersik (1997).						

Table A.22 True Triaxial Tests on Westerly Granite (Haimson & Chang, 2000)

σ_3 (MPa)	σ_2(MPa)	σ_1(MPa)	σ_3(MPa)	σ_2(MPa)	σ_1(MPa)
0	0	201	60	60	747
0	40	306	60	90	811
0	60	301	60	114	821
0	80	317	60	180	860
0	100	304	60	249	861
2	2	231	77	77	889
2	18	300	77	102	954
2	40	328	77	142	992
2	60	359	77	214	998
2	80	353	77	310	1005
2	100	355			
			100	100	1012
20	20	430	100	165	1103
20	40	529	100	167	1147
20	60	602	100	216	1155
20	61	553	100	259	1195
20	62	554	100	312	1129
20	79	532			
20	100	575			
20	114	567			
20	150	601			
20	202	638			
38	38	605			
38	38	620			
38	57	700			
38	78	733			
38	103	720			
38	119	723			
38	157	731			
38	198	781			

Note:

Westerly granite "is a fine-medium grained Late-Pennsylvanian to Permian rock found mainly in the southeast corner of Rhode Island. Its important properties include very low porosity, high strength, almost complete isotropy, linear elasticity, and homogeneity".

Table A.23 True Triaxial Tests on KTB Amphibolite (Chang & Haimson, 2000)

σ_3(MPa)	σ_2(MPa)	σ_1(MPa)	σ_3(MPa)	σ_2(MPa)	σ_1(MPa)
0	0	158	100	100	790
0	0	160	100	100	868
0	0	176	100	160	959
0	40	272	100	200	1001
0	80	346	100	250	945
0	150	291	100	270	892
0	200	347	100	300	1048
0	230	267	100	350	1058
			100	440	1155
30	30	410	100	600	1118
30	60	479			
30	100	599	150	150	1147
30	200	652	150	200	1065
30	250	571	150	200	1112
30	300	637	150	250	1176
			150	250	1230
60	60	702	150	300	1431
60	90	750	150	350	1326
60	100	766	150	400	1169
60	155	745	150	450	1284
60	200	816	150	500	1265
60	250	888	150	640	1262
60	300	828			
60	350	887			
60	400	954			
60	450	815			

Note:

"The amphibolite samples used in our experimental study were prepared from core (234 mm diameter) extracted from the main KTB borehole at a depth of 6355-6360 m. Generally, it is a massive metamorphic rock, which at that depth has little or no foliation. We analyzed a thin section of the amphibolite using a point-counting method and derived its mineral composition as being 58% amphibole (mainly hornblende, average grain size 0.4 mm), 25% plagioclase (average grain size 0.2 mm), 5% garnet, 2% biotite, and 7% minor opaque minerals. The amphibole, which is the dominant mineral, is evenly distributed and randomly oriented."

Table A.24 True Triaxial Tests on Long Valley Hornfels (Chang & Haimson, 2005)

σ_3(MPa)	σ_2(MPa)	σ_1(MPa)
0	0	141.239
0	0	141.239
15	15	275.044
30	30	289.912
30	30	272.814
30	55.9367	321.293
30	96.0422	293.726
30	98.153	273.764
30	148.813	258.555
30	197.361	281.369
45	45	340.885
60	60	418.407
60	60	423.954
60	118.206	429.658
60	187.863	403.042
60	246.966	414.449
60	297.625	348.859
100	100	466.195
100	100	466.73
100	199.472	479.087
100	299.736	471.483
100	397.889	442.966

Note:

"The hornfels samples used in our experiments came from a depth range of 2256-2262 m, and displayed weakly defined banding, dipping 50°. Hornfels is an ultra-fine-grained crystalline rock that has been metamorphic under high temperature under hydrostatic pressure. This process has left the grains randomly oriented with no schistosity or planes of weakness, i.e. the rock can be considered isotropic. The uniaxial compressive strength is 152 MPa regardless of the orientation to the banding."

Table A.25 True Triaxial Tests on Long Valley Metapelite (Chang & Haimson, 2005)

σ_3(MPa)	σ_2(MPa)	σ_1(MPa)
0	0	183.65
0	48.8127	159.696
0	97.6253	173.004
30	65.9631	258.175
30	87.0712	318.061
30	143.799	312.738
60	149.077	505.703
60	238.786	509.696
60	341.689	419.202
100	100.264	552.281
100	296.834	644.106
100	349.604	582.89
100	497.361	589.544

Note:

"The metapelite samples came from core extracted at 2641-2644 m. Metapelite is a metamorphic rock derived from clay-rich sediments or sedimentary rocks, which is characterized by extremely small grain size. A set of clearly defined banding planes traversed the metapelite core at an average dip of 40°. The banding in the metapelite exhibited slight local curvature, which reflects a degree of ductile deformation during its formation. The metapelite exhibited clear anisotropy, with its UCS varying from 111 MPa to 308 MPa, depending on banding inclination."

Table A.26 True Triaxial Tests on Chelungpu Siltstone (Oku et al., 2007)

σ_3(MPa)	σ_2(MPa)	σ_1(MPa)	σ_3(MPa)	σ_2(MPa)	σ_1(MPa)
10	10	113.369	60	60	317.647
10	20	154.011	60	122.03	375.401
10	40	157.219	60	178.186	379.679
10	60	188.235	60	238.661	403.209
10	80	200	60	300	333.7
10	100	193.583	60	300	360.428
10	120	185.027			
			100	100	441.711
25	25	203.209	100	200	489.84
25	50	195.722	100	300	495.187
25	70	263.102	100	400	467.38
25	75	251.337			
25	100	251.337			
25	125	244.92			
25	150	260.963			
25	175	263.102			
25	200	270.588			
25	217.063	224.599			
40	40	262.032			
40	60	317.647			
40	80	271.658			
40	126.35	313.369			
40	160	304.813			
40	200	282.353			
40	220	298.396			

Note:

"The composition of tested siltstone was determined by using a point-counting method that yielded 68% quartz, 19.5% clay, 9.5% k-feldspar, and 3% biotite. The UCS is 79.5±2.2 MPa. From this initial study, the siltstone can be characterized as a very fine-grained, clay-rich, low-porosity, medium-strength, and highly deformable rock."

Appendix B Data for Transversely Isotropic Rocks

In this appendix, the strength of more or less isotropic rocks under true triaxial stress is summarized for all the data sets. The mineralogy of these rocks (if available) is summarized at the end of each table, most of which is cited from the original literature word for word.

Table B.1 Axial Stress σ_1 at Failure for Martinsburg Slate (Donath, 1964) (Unit: bar)

β	35bar	105bar	350bar	500bar	1000bar	2000bar
0°	1326.9	1668.5	2653.0	3552.0	5362.4	7457.3
15°	520.3	824.2	1294.0	1809.0	2955.0	5022.2
30°	219.0	457.4	843.0	1273.7	2307.3	4187.3
45°	395.3	633.9	1047.3	1459.6	2549.3	4382.3
60°	749.4	1006.5	1467.0	1916.4	3193.5	5326.1
75°	1253.2	1594.8	2139.2	2776.0	4446.1	6672.3
90°	1963.5	2417.3	3364.5	4141.7	6064.2	8215.4
Note: Martinsburg slate is Ordovician, from Bangor, Pennsylvania.						

Table B.2 Axial Stress at Failure for South African Slate (Hoek, 1964) (Unit: lb/in^2)

β	$\sigma_3/\sigma_1 = 0$	$\sigma_3/\sigma_1 = 0.113$	$\sigma_3/\sigma_1 = 0.171$
0°	17600	39200	55700
0°	21600	36000	49300
15°	6900	18300	34200
15°	8700	30000	39000
30°	4500	7300	8730
30°	4150	---	7840
45°	5540	13900	15000
45°	6560	11000	16300
60°	11850	24600	29600
60°	11600	19400	32400
75°	16000	31200	41400
75°	16600	31900	42900
90°	15600	30600	41700
90°	16100	---	39300
Note: Sample of this slate is from the Pretoria area.			

Table B.3 Axial Stress at Failure for Austin Slate (McLamore & Gray, 1967) (Unit: psi)

β	5000	10000	20000	30000	40000
0°	50243.5	68864.7	95243	120972.9	135999.6
10°	39360.5	54089.9	77873.3	98089.7	112143.4
20°	25072.4	37855.8	60179.8	83477.3	99315.1
30°	21648.5	31350.9	53351.1	71297	86486.2
40°	24387.6	34252.2	53332.9	68684.5	84522
50°	28261.6	36504.5	53477.4	71261.4	86288.7
60°	32621.7	43134.9	63512.9	83243.7	97621.5
70°	38279.7	48955.3	73063.1	92144.4	108630.2
80°	44585.2	52504.4	78558.3	100882.9	
90°	47649.2	60270.5	85513	105567	124161.8

Note:
"The slate used in this study was a fine-grained black slate. There were no discernible bedding planes within the material but cleavage was well developed. The material was obtained from a building site on the University of Texas campus. Attempts to determine the exact geological age and formation of the mother material were fruitless."

Table B.4 Axial Stress at Failure for Green River Shale I (McLamore & Gray, 1967) (Unit: psi)

β	1000	5000	10000	15000	25000
0°	36552.9	50090.2	63637.9	78085	103920.5
15°	30059.7	46566	61103.4	75191	99137
20°	28165.4	42692.2	58399.2	72936.4	98232.3
30°	23206.5	37733.3	53710.3	68337.9	96333.1
45°	31649.2	43387	58824	74891.2	96767.6
60°	32174	44091.9	61328.1	74336.1	99361.7
75°	31439	44346.5	60953.3	75310.8	100516.3
90°	33223.5	46671	61927.8	76645.2	100591.3

Note:
"Green River Shale is also commonly known as Colorado Oil Shale or just oil shale. In actuality, it is neither a shale nor an oil-bearing rock in the usual sense of the word. It is composed of fine-grained calcite and dolomite particles interbedded with a solid native high molecular weight organic material called kerogen. Upon retort in the 700-800 deg F range, Green River Shale yields a synthetic crude oil of about 30 deg API gravity."

"Green River Shale I was quite competent mechanically and failed in a brittle (shear) manner over the pressure range studied. Upon retort, samples of this material yielded 18-22 gal/ton of synthetic crude oil. Physically this material was light gray to light brown in appearance and was finely laminated."

"Obtained from the Bureau of Mines' demonstration mine near Rifle, Colo."

Table B.5 Axial Stress at Failure for Green River Shale II (McLamore & Gray, 1967) (Unit: psi)

β	1000	5000	10000	15000	25000
0°	21555.6	29444.5	40959.7	51666.5	71515.1
10°	19226.9	27368.3	38479.3	48782.4	66560.2
20°	16291.8	24635.4	34736.3	45393.1	64180.9
30°	13559.1	21498.5	30639.9	40437.9	58619.5
40°	14714.8	22755.5	32957.5	42957.5	61442.1
60°	17380.4	25723.9	36632.7	46531.9	64107.7
90°	18676.8	27272.7	38080.8	47929.3	67373.8

Note:

"Green River Shale is also commonly known as Colorado Oil Shale or just oil shale. In actuality, it is neither a shale nor an oil-bearing rock in the usual sense of the word. It is composed of fine-grained calcite and dolomite particles interbedded with a solid native high molecular weight organic material called kerogen. Upon retort in the 700-800 deg F range, Green River Shale yields a synthetic crude oil of about 30 deg API gravity."

"Green River Shale II was much darker in appearance and yielded 38-40 gal/ton of synthetic crude oil when retorted. Mechanically, the material behaved in a plastic manner and as a rule failed in shear only after considerable plastic strain."

"Obtained from the Bureau of Mines' demonstration mine near Rifle, Colo."

Table B.6 Conventional Triaxial Tests on Penrhyn Slate (Attewell & Sandford, 1974) (Unit: lb/in^2)

β	0	1000	2000	6000	8000	10000
0°	27167.4	29372.5	40012.5	51461.7	55104.9	70907.7
15°	16431.9	21485.1	29496.1	37001.6	41192.5	50203.4
30°	6353.68	13378.7	18541.5	29662	27170.6	
30°				23856		
45°	9092.33	14802.8	20403.8	25280.1	33414.7	36948.4
60°	12488.3	18308.3	25442.9	32510.2	37139.3	40125.2
75°	18403.8	24442.9	31139.3	37439.7	43931.1	50751.2
90°	30234.7	36383.4	45270.7	52557.1	63320.8	77918.6

Table B.7 Conventional Triaxial Tests on Chichibu Green Schist (Mogi, 2007) (Unit: MPa)

	σ_1	σ_2	σ_3
Mode I	59	0	0
	71	0	0
	154	25	25
	244	50	50
	328	75	75
Mode II	66	0	0
	68	0	0
	171	25	25
	233	50	50
	243	50	50
	244	50	50
	325	75	75
	336	75	75
Mode IV	147	0	0
	149	0	0
	294	25	25
	385	50	50
	501	75	75

Note:
"A macroscopically homogeneous green crystalline schist with a distinct, dense foliation, from Chichibu mountain, west of Tokyo was selected for the experiment."

Table B.8 True Triaxial Tests on Chichibu Green Schist (Mogi, 2007) (Unit: MPa)

	σ_1	σ_2	σ_3		σ_1	σ_2	σ_3
β=30°, ω=0°	244	50	50	β=30°, ω=90°	219	50	50
	225	85	50		244	50	50
	206	100	50		311	86	50
	208	121	50		318	97	50
	240	133	50		397	121	50
	225	166	50		445	155	50
					488	156	50
β=30°, ω=45°	233	50	50		428	192	50
	244	50	50		432	193	50
	247	50	50				
	273	56	50	β=90°	385	50	50
	290	70	50		446	71	50
	294	86	50		447	74	50
	300	97	50		486	75	50
	298	97	50		502	103	50
	346	121	50		528	115	50
	335	121	50		531	148	50
	318	144	50		540	156	50
	308	156	50		577	192	50
	319	167	50		563	227	50
	346	168	50		546	249	50
	304	180	50		562	262	50
	320	203	50		565	316	50
	376	203	50				
	313	227	50				

Table B.9 Axial Stress at Failure for Diatomite (Allirot & Boehler, 1979) (Unit: MPa)

β	0.5	1	2
0°	6.91007	8.67098	11.56234
15°	5.76294	8.25923	10.54732
30°	4.90478	6.5603	9.68854
45°	5.72797	7.14723	10.48547
60°	6.94596	8.4958	14.7245
75°	8.1105	10.97393	15.9416
90°	8.32844	11.2452	16.1594

Note:
"Diatomite is a chalk-like, soft, friable, earthy, very fine-grained, siliceous sedimentary rock, usually light in color (white if pure, commonly buff to gray in situ, and rarely black). It is very finely porous, very low in density (floating on water at least until saturated), and essentially chemically inert in most liquids and gases. (Dolley, 2000)"

Table B.10 Summary of Samples of Opalinus Shale (Aristorenas,1987)

Sample ID	Formation	Depth (m)	Water Content (%)	Void Ratio	Saturation (%)	Grain Density (g/cm^3)	Specific Weight	Liquid Limit (%)	Plastic Limit (%)
23-1	Opalinus	22	9.6	0.269	99.9	2.79	2.20	31.5	18.6
23-5	Opalinus	50	7.5	0.220	94.2	2.75	2.25	31.6	19.1
23-6	Opalinus	55	5.1	0.185	76.3	2.77	2.34	33.1	20.2
23-9	Lias	73	5.7	0.199	29.6	2.79	2.33	28.6	23.7
23-10	Lias	77	6.2	0.175	99.5	2.83	2.40	28.2	23.5
26B-4	Opalinus	38	5.7	0.168	92.4	2.73	2.34	32.7	22.4
26B-6	Opalinus	47	6.7	0.203	90.6	2.75	2.29	30.7	21.3
26B-8	Opalinus	58	6.4	0.184	98.0	2.80	2.36	31.4	21.7
ERZ4	Opalinus	21	8.9	0.323	78.2	2.35	2.15	36.7	25.5

Table B.11 Mineralogical Composition of Opalinus Shale (Aristorenas,1987)

Sample #	Quartz/Feldspar/Sulfides	Carbonate	Clay
23-1	40%	26%	34%
23-5	37%	6%	57%
23-6	9%	60%	31%
23-9	37%	12%	51%
23-10	53%	10%	37%
26B-4	46%	7%	47%
26B-6	43%	7%	50%
26B-8	43%	8%	49%
ERZ4	-	-	-

Table B.12 Conventional Triaxial Tests on Opalinus Shale Specimens (Aristorenas,1987)

Specimen ID	Shale Type	θ	Consolidation	Drainage Condition	Stress Path
23-1(UC)	Opalinus	0°	Isotropic	Undrained	Pure shear stress path
23-5(UC)	Opalinus	0°	Isotropic	Undrained	Pure shear stress path
23-6(UC)	Opalinus	0°	Isotropic	Undrained	Pure shear stress path
23-9(UC)	Lias α	0°	Isotropic	Undrained	Pure shear stress path
23-10(UC)	Lias α	0°	Isotropic	Undrained	Pure shear stress path
23-1(DC)	Opalinus	0°	Isotropic	Drained	Explained in text
23-5(DC)	Opalinus	0°	Isotropic	Drained	Explained in text
23-9(DC)	Lias α	0°	Isotropic	Drained	Explained in text
26B-6(DC)	Opalinus	0°	Isotropic	Drained	Pure shear stress path
26B-8(DC)	Opalinus	0°	K_A=0.5	Drained	Pure shear stress path
26B-4(UE)	Opalinus	0°	K_0=0.58	Undrained	Pure shear stress path
26B-6(UE)	Opalinus	0°	Isotropic	Undrained	Pure shear stress path
26B-8(UE)	Opalinus	0°	K_A=2.0	Undrained	Pure shear stress path
ERZ4(UE)	Opalinus	0°	K_0=0.68	Undrained	Pure shear stress path

3 Failure of Opalinus Shale Specimens (Aristorenas,1987)

n	σ'_{10} (MPa)	σ'_{30} (MPa)	σ'_{1f} (MPa)	σ'_{3f} (MPa)	Δu (MPa)	Mode	n	ξ (°)	Remarks
)	5.0	5.0	8.72	2.31	0.567	-	-	-	Specimen broke into several pieces at failure
)	1.3	1.3	6.82	0.21	–0.810	A	2	55	
)	1.3	1.3	6.11	0.74	–1.236	A	2	50	
)	2.5	2.5	8.88	1.24	–1.139	-	-	-	Specimen broke into several pieces at failure
C)	2.5	2.5	10.44	1.73	–2.05	A	2	70	
)	0.8	0.8	2.54	0.0231	0	A	2	55	
)	1.3	1.3	4.01	0.0335	0	A	1	50	
)	2.5	2.5	5.93	0.585	0	A	2	55	
C)	1.8	1.8	4.99	0.0869	0	A	2	60	
C)	3.15	1.575	6.15	0.121	0	A	1	60	
E)	1.764	1.023	0.145	3.44	–1.053	B	2	0	
E)	1.75	1.75	–0.0165	4.01	–1.303	B	3	0	
E)	1.002	2.004	0.486	3.48	–0.887	B	3	0	
E)	0.572	0.389	0.275	1.25	–0.490	A/B	1/1	50/0	Specimen had one shear plane and one fracture plane

$'_{30}$: Effective axial and lateral stress in the specimen after consolidation.

$'_{3f}$: Effective axial and lateral stress at failure.

s pore pressure due to shear.

ξ: See Figure 3.31 for illustration.

Table B.14 Conventional Triaxial Strength of Quartzitic Phyllite (Ramamurthy, 1993) (Unit: MPa)

beta	0	5	15	30	50	70
0	65.5856	83.5586	140.405	196.847	273.784	326.937
5					249.279	
10						290.901
25	46.8468					
30		57.6126	101.4865		186.216	
35	45.4054					
40				136.667		243.694
50				163.694		
60	59.4595	66.982	124.91	176.667	234.865	278.649
65		98.3333				
70			142.928	200.45	266.937	
75						312.523
90	101.622	124.64	175	224.955	273.784	329.099

Note:
"Dhundiara Group (Permo Triassic, 200-280 m.y.) Phyllitic texture. Dark colored groundmass is strongly foliated with concordant folded quartz veins of thickness varying from 0.5 to 5.0 mm. The relative abundance of quartz and feldspar (Q + F)= 75%. Other minerals present are chlorite, muscovite, biotite and Fe-oxide."

Table B.15 Conventional Triaxial Strength of Carbonaceous Phyllite (Ramamurthy, 1993) (Unit: MPa)

beta	0	5	15	30	50	70
0	65.1274	85.5997	142.376	178.246	249.7	320.075
0				200.555		
5		101.7916				
10				196.237		
15						284.453
25	38.5007	60.4123				
30	37.4213		96.6792		201.844	
35				138.666		258.186
40					187.811	
55			102.4363			
60	48.5757	77.6837	127.624		232.429	274.738
65				186.162	227.391	
80				199.475		
85						323.313
90	79.5202	115.465	178.718	207.391	272.729	

Note:
"Dhundiara Group (Permo Triassic, 200-280 m.y.) Very similar to QP. Light grey colored groundmass with nearly planer quartz and calcite veins. 'Pinch and swell' structure in the veins at places. Q + F = 60-70% and present in both groundmass and layers. Other minerals are chlorite, muscovite, biotite, calcite and Fe-oxide/sulfide. Wavy extinction of quartz in the veins (the rock is from a shear zone)."

Table B.16 Conventional Triaxial Strength of Micaceous Phyllite (Ramamurthy, 1993) (Unit: MPa)

beta	0	5	15	30	50	70
0	67.5719	114.563	175.241	222.58	356.486	441.162
15	34.3491	63.9658	112.0905	148.804	137.5204	255.428
30	17.0474	31.2243		107.373		184.052
70		62.8059				251.85
80			138.503	199.37		
90	97.9793	123.734	158.349	218.236	271.055	318.084

Note:
"Jutogh Group (Pre-Cambrian, > 350 m.y.) Light green colored rock with planer foliations. Silky sheen on fresh exposed surfaces. Veins are absent. Texture grades between schistose and slaty. Q + F = 40-45%, fine grained, randomly distributed. Other minerals are chlorite, muscovite, biotite, Fe-oxide, graphite, tourmaline and epidote."

Table B.17 Porosity and Density of Tournemire Shale (Niandou,1994)

Drying Temperature	Porosity	Density
65 °C	8.35%	2.72
80 °C	8.53%	2.73
150 °C	13.7%	2.76

Table B.18 Triaxial Tests on Tournemire Shale Specimens

Bedding Plane Orientation β (°)	Confining Pressure σ_3 (MPa)	Loading Sequence
0	0	2 Complete unloading
	1	1 Complete unloading, 3 Monotonic loading
	5	2 Partial unloading, 1 Complete unloading, 1 Monotonic loading
	10	1 Partial unloading, 1 Complete unloading, 1 Monotonic loading
	20	1 Complete unloading, 1 Monotonic loading
	25	2 Monotonic loading
	30	1 Partial unloading, 1 Complete unloading, 1 Monotonic loading
	40	1 Partial unloading, 1 Complete unloading, 1 Monotonic loading
	50	1 Partial unloading, 2 Monotonic loading
15	1	1 Monotonic loading
30	1	1 Monotonic loading
	5	1 Partial unloading
	40	1 Partial unloading
	50	1 Partial unloading
45	1	2 Monotonic loading, 2 Complete unloading
	5	1 Partial unloading
	20	1 Monotonic loading
	40	1 Partial unloading
	50	1 Monotonic loading, 1 Partial unloading
60	1	1 Monotonic loading
	5	1 Partial unloading
	20	1 Monotonic loading
	40	1 Partial unloading
	50	1 Partial unloading
70	1	1 Monotonic loading
75	1	1 Monotonic loading
90	1	3 Monotonic loading, 1 Complete unloading
	5	1 Complete unloading, 2 Partial unloading
	10	1 Monotonic loading, 1 Complete unloading
	20	1 Complete unloading
	30	1 Partial unloading
	40	1 Partial unloading
	50	1 Partial unloading

Table B.19 Axial Stress at Failure of Tournemire Shale Specimens (Niandou, 1994) (Unit: MPa)

β (°)	1	5	20	40	50
0	35.5957	60.1353	105.1894	144.002	159.84
20	29.9973				
30	20.1708	35.6297	83.9269	113.0089	129.7113
45	23.2693	41.1078	77.9447	109.8361	129.9991
60	25.5043	44.855		108.6105	
75	31.6297				
90	47.056	58.6232	102.8111	136.4335	154.866

Table B.20 Post-Peak Axial Stress of Tournemire Shale Specimens (Niandou, 1994) (Unit: MPa)

β (°)	1	20	50
0	17.37	68	
0	20.736		
15	8.43		
20	13.05	62.56	
30	10.19	57.8	123.74
45	9.585		
45	9		
60	12.92		
75	3.14		
90		67.23	170.62
90	13.1	64.5	164.44

Table B.21 Conventional Triaxial Strength of Himalayan Quartzitic Schist (Behrestaghi, 1996) (Unit: MPa)

β (°)	5	15	35	50	100
0	222.979	301.141	349.405	398.838	508.027
15	199.237	258.971	301.531	342.921	440.577
30	141	188.114	246.741	278.938	412.217
45	176.992	212.616	257.474	293.076	371.28
60	191.151	254.416	304.999	334.856	411.869
90	289.67	357.469	417.245	431.035	512.665

Note:

"This is a fine grained rock with very well developed schistosity. Quartz bands vary in thickness from 0.5 to 4 mm. The ground mass appearing in the form of schistose bands, and predominantly made up of crypto-crystalline to fine grained flaky micaceous (biotite) minerals, preferably oriented with fine grained recrystallized quartz which are in abundance. Subordinate and accessary minerals which are embedded in the schistose ground mass are the quartz porphyroblast, potash and plagioclase feldspars. The other accessaries present are some iron minerals and zircon. Based on the semi-quantitative estimation from X-ray diffractograms, the quartz constitutes about 43%, mica 15% and feldspar 12.6% of the rock, with clay minerals forming the rest. The predominant clay is kaolinite, and illite and chlorite are also present."

"The scanning electron micrographs ... obtained in perpendicular to the foliations show strong preferred orientation of the minerals, i.e., granular, irregular, fine quartz grains aligned in alternate arrangement with tabular flakes of micaceous minerals. This textural variation render the rock behaves anisotropically."

Table B.22 Conventional Triaxial Strength of Himalayan Chlorite Schist (Behrestaghi, 1996) (Unit: MPa)

β (°)	5	15	35	50	100
0	122.791	180	316.744	348.837	474.419
15	65.5814	143.721	266.512	304.186	397.674
30	62.7907	118.605	221.86	253.953	371.163
45	79.5349	129.767	181.395	245.581	332.093
60	90.6977	149.302	214.884	258.14	339.07
75	129.767	200.93	263.721		443.721
80				330.698	
90	173.023	233.023	316.744		482.791

Note:
"This is a very fine grained, highly chloritized basaltic rock. The rock is aphaneric, with well developed schistosity, having the quartz bands varying in thickness from 0.5 to 1 cm, highly altered chlorite in ground mass, with occasional porphyroblasts of augite. Thin sections show that the augites are pleochroic, weathered and chloritized along margins. Plagioclase varies in composition from labradorite to andesine. Flakes of muscovite and other ferromagnesium minerals have also been seen. The rock appears to be slightly over saturated with silica. It appears that the quartz bands are formed due to filling of the foliation planes. The rock contains 29% quartz, 25% chlorite, 11% mica, with clay minerals forming the rest of the constituents."

"The X-ray diffractogram indicates the presence of chlorite along with other minerals identified in thin section. The scanning electron micrographs taken perpendicular to the foliation plane reveal the textural contrast among the grains."

Table B.23 Conventional Triaxial Strength of Himalayan Quartz Mica Schist (Behrestaghi, 1996) (Unit: MPa)

β (°)	5	15	35	50	100
0	112.353	171.803	233.601	300.772	418.139
15	92.6897	138.232	216.222	297.291	397.682
30	74.5388	124.682	204.989	237.437	350.975
45	79.5294	99.6035	192.243	226.997	358.271
60	89.956	118.512	221.992	255.984	370.252
75	102.678	128.167	228.569	298.056	418.532
90	145.563	184.939	255.209	316.203	421.216

Note:
"This rock contains quartzitic bands of varying thickness from 1 to 1.5 cm, whereas micaceous bands are 1-2 mm in thickness and at times show ptygmatic folding. It is a coarse grained rock with well defined schistose texture. Recrystallized and elongated quartz grains with sutured boundaries show strong preferred orientation of the rock. Micaceous (biotite and muscovite) plates occurring in alternate order with respect to quartzitic bands also show strong preferred orientation. The presence of chlorite along with the aforementioned mineral assemblage suggests that the rock belongs to low grade regional metamorphic facies. Analysis of X-ray diffractogram of the rock reveals that quartz (31%), chlorite (26%) and mica (22%) are the most abundant minerals, followed by clay minerals such as kaolinite, sepiolite and illite forming the rest of its constituents."

"The scanning electron micrographs ... shows the coarse nature of grains in this rock along with strong preferred orientation of mica."

Table B.24 Conventional Triaxial Strength of Himalayan Biotite Schist (Behrestaghi, 1996) (Unit: MPa)

β (°)	5	15	35	50	100
0	80.0382	116.623	169.985	235.505	310.979
30	51.565	107.994	156.774	200.209	283.314
45	41.92	88.4315	163.878	205.807	295.754
60	74.2041	119.953	183.967	232.003	299.075
75	91.2446	144.579	219.31	239.117	302.396
90	102.95	149.415	222.612	269.115	322.458

Note:

"Megascopic study of this rock shows that it is characterized by thicker foliation planes than quartz mica schist. The quartz feldspathic bands varying in thickness from 2 to 7 mm and stretched to a length of 1-5 cm. Micaceous (biotite) flakes range in thickness from 2 to 5 mm. Thin section study of the rock showed that Biotite schist is a coarse grained rock with a well developed perfect schistose texture. Quartz grains are deformed and elongated, occurring alternatively with biotite mica flakes. Garnet occurs as an accessary and also shows preferred orientation."

"On the basis of analysis of X-ray diffractograms of the biotite schist, ..., it is found that biotite is the major constituent of the rock (56%), followed by quartz (10%), whereas clay minerals, especially sepiolite (20%), kaolinite (6%) and illite (5%), form the other constituents of this rock. Coarse nature and preferred orientation of the grains is evident from the scanning electron micrograph ...."

Table B.25 Axial Stress at Failure for Angers Schist (Duveau, 1998) (Unit: MPa)

β (°)	0	5	10	20	30	40
0	148.283	243.4263	240.1006	274.3325	340.4128	354.615
15	70.1885	95.56496	146.8347	158.0655	140.4212	187.4813
30	36.3574	37.74839	40.36171	42.5574	87.3441	97.249
45	10.59002	22.89935	26.33371	55.98475	60.4251	82.084
60	12.11816	23.84717	33.60024	54.6274	73.1269	88.0225
75	25.6078	56.00856	66.4578	95.79285	121.0013	139.5523
90	97.22125	189.5266	185.0632	240.0531	270.7164	336.9012

Note:
"The studied material is a middle Ordovician schist from Angers (France). It is a rock of the family of schists with weak metamorphism, and characterized by well marked schistosity planes which coincide with the stratification planes. The main mineral constituents of this rock are chlorite, muscovite and quartz. Small quantities of pyrite, calcite and chloritoide are also found. The size of grains varies from 10 to 20 mm."

Appendix C Amadei's Solution

Amadei (1983) and Lekhnitskii (1963) presented the solutions for an anisotropic homogeneous body bounded internally by a cylindrical surface of arbitrary cross-section. As stated in Chapter 5, their solutions are very general and a simplified version is implemented in this research. It would not be practical to describe the entire scope of their solutions and the detailed mathematical treatment. Therefore, only the derivations for the stress distribution around a circular hole, subject to a uniform internal pressure, embedded in a transversely isotropic medium will be described here. The purpose for this appendix is to help the reader to understand the MATLAB implementation (presented in Appendix D), instead of showing all the detailed derivations. For more details, the reader is referred to Amadei (1983) and Lekhnitskii (1963).

C.1 Problem Statement and Assumptions

A circular hole of radius a is embedded in a transversely isotropic medium, whose stress-strain relationship can be described by transversely isotropic linear elasticity. As shown in Figure C.1, a local coordinate system **xyz** is set up for the borehole, where **z** is the axis of the borehole while **x** and **y** form its normal cross-section. A cylindrical system (r, θ) is set up on the plane **xy** (shown in Figure C.2), so that any point in the **xyz** system can also be represented by a cylindrical system (r, θ, z). The problem is presented and solved in the **xyz** system.

Generalized plain strain conditions are assumed along the axis of the hole (i.e. the **z** axis), so that "all components of stress, strain, displacement, body and surface forces are to be identical in all planes perpendicular to the hole axis" (Amadei, 1983), i.e. the derivative of these quantities with regard to z are all zero.

In the **xyz** system, the far-field stress is expressed by:

$$[\sigma_0]_{xyz} = \begin{bmatrix} \sigma_{x,0} \\ \sigma_{y,0} \\ \sigma_{z,0} \\ \tau_{yz,0} \\ \tau_{zx,0} \\ \tau_{xy,0} \end{bmatrix} \tag{1}$$

The constitutive law of the material can be expressed by:

$$\begin{bmatrix} \varepsilon_x \\ \varepsilon_y \\ \varepsilon_z \\ \gamma_{yz} \\ \gamma_{zx} \\ \gamma_{xy} \end{bmatrix} = \begin{bmatrix} a_{11} & a_{12} & a_{13} & a_{14} & a_{15} & a_{16} \\ a_{21} & a_{22} & a_{23} & a_{24} & a_{25} & a_{26} \\ a_{31} & a_{32} & a_{33} & a_{34} & a_{35} & a_{36} \\ a_{41} & a_{42} & a_{43} & a_{44} & a_{45} & a_{46} \\ a_{51} & a_{52} & a_{53} & a_{54} & a_{55} & a_{56} \\ a_{61} & a_{62} & a_{63} & a_{64} & a_{65} & a_{66} \end{bmatrix} \begin{bmatrix} \sigma_{x,0} \\ \sigma_{y,0} \\ \sigma_{z,0} \\ \tau_{yz,0} \\ \tau_{zx,0} \\ \tau_{xy,0} \end{bmatrix} \tag{2}$$

or in a matrix form:

$$[\varepsilon]_{xyz} = [A][\sigma_0]_{xyz} \tag{3}$$

where $[A]$ is the elastic matrix of the material in the **xyz** coordinate system.

A uniform pressure q is applied on the wall of the hole, as shown in Figure C.2. Body forces are assumed to be absent.

It has been stated in Chapter 5 that this problem is divided into three sub-problems:

1. The far-field stress is applied to an anisotropic linear elastic medium with no opening.
2. The hole is introduced into the medium. Existing stresses are relieved to zero around the surface of the hole.
3. The surface of the hole is uniformly pressurized with the internal pressure.

The governing equations and the general method used to approach the problem will be introduced first. Each of the sub-problems is then treated separately.

C.2 Governing Equations and the Introduction of Analytic Functions $\phi_i(z_i)$ (i = 1,2,3)

With the assumptions stated above, the equation of equilibrium can be written as:

$$\begin{aligned} \frac{\partial \sigma_x}{\partial x} + \frac{\partial \tau_{xy}}{\partial y} &= 0 \\ \frac{\partial \tau_{xy}}{\partial x} + \frac{\partial \sigma_y}{\partial y} &= 0 \\ \frac{\partial \tau_{xz}}{\partial x} + \frac{\partial \tau_{yz}}{\partial y} &= 0 \end{aligned} \tag{4}$$

The strain-displacement equations are:

$$\begin{aligned} &\varepsilon_x = \frac{\partial u}{\partial x}; \varepsilon_y = \frac{\partial v}{\partial y}; \varepsilon_z = 0; \\ &\gamma_{yz} = -\frac{\partial w}{\partial y}; \gamma_{zx} = -\frac{\partial w}{\partial x}; \gamma_{xy} = -\left(\frac{\partial u}{\partial y} + \frac{\partial v}{\partial x}\right); \end{aligned} \tag{5}$$

The strain compatibility equations are:

$$\frac{\partial^2 \varepsilon_x}{\partial y^2}+\frac{\partial^2 \varepsilon_y}{\partial x^2}=\frac{\partial^2 \gamma_{xy}}{\partial x \partial y}$$
$$\frac{\partial \gamma_{zx}}{\partial y}-\frac{\partial \gamma_{yz}}{\partial x}=0 \tag{6}$$

Combining the condition $\varepsilon_z = 0$ in Equation (5) and the constitutive equation, Equation (2), σ_z can be expressed by:

$$\sigma_z=-\frac{1}{a_{33}}\left(a_{31}\sigma_x+a_{32}\sigma_y+a_{34}\tau_{yz}+a_{35}\tau_{zx}+a_{36}\tau_{xy}\right) \tag{7}$$

Two stress functions F(x,y) and $\Psi(x,y)$ are introduced to solve these equations. The stress components (other than σ_z) can be expressed as functions of F(x,y) and $\Psi(x,y)$:

$$\sigma_x=\frac{\partial^2 F}{\partial y^2};\sigma_y=\frac{\partial^2 F}{\partial x^2};$$
$$\tau_{xy}=-\frac{\partial^2 \mathrm{F}}{\partial x \partial y};\tau_{xz}=\frac{\partial \Psi}{\partial y};\tau_{yz}=-\frac{\partial \Psi}{\partial x}; \tag{8}$$

These expressions, together with the expression for σ_z (Equation (7)), can be substituted into the constitutive equation (Equation(2)), so that the strains can be expressed with F(x,y) and $\Psi(x,y)$. These strains can then be substituted into the compatibility equations (Equation (6)) to give the *Beltrami Michell equations of compatibility*:

$$L_4\mathrm{F}+L_3\Psi=0$$
$$L_3\mathrm{F}+L_2\Psi=0 \tag{9}$$

L_2, L_3, and L_4 are differential operators of the second, third and fourth order, which are defined by:

$$L_2=\beta_{44}\frac{\partial^2}{\partial x^2}-2\beta_{45}\frac{\partial^2}{\partial x \partial y}+\beta_{55}\frac{\partial^2}{\partial y^2}$$
$$L_3=-\beta_{24}\frac{\partial^3}{\partial x^3}+(\beta_{25}+\beta_{46})\frac{\partial^3}{\partial x^2 \partial y}-(\beta_{14}+\beta_{56})\frac{\partial^3}{\partial x \partial y^2}+\beta_{15}\frac{\partial^3}{\partial y^3} \tag{10}$$
$$L_4=\beta_{22}\frac{\partial^4}{\partial x^4}-2\beta_{26}\frac{\partial^4}{\partial x^3 \partial y}+(2\beta_{12}+\beta_{66})\frac{\partial^4}{\partial x^2 \partial y^2}-2\beta_{16}\frac{\partial^4}{\partial x \partial y^3}+\beta_{11}\frac{\partial^4}{\partial y^4}$$

where $\beta_{ij}=a_{ij}-\frac{a_{i3}a_{j3}}{a_{33}}$ $(i,j=1,2,4,5,6)$, and a_{ij} are the components of the elastic matrix [A] (refer to Equation (2)).

Lekhnitskii (1963) gave the general solution for Equation (9):

$$\begin{aligned} \mathrm{F} &= 2\,\mathrm{Re}(F_1(z_1)+F_2(z_2)+F_3(z_3)) \\ \Psi &= 2\,\mathrm{Re}(\lambda_1 F_1'(z_1)+\lambda_2 F_2'(z_2)+\frac{1}{\lambda_3}F_3'(z_3)) \end{aligned} \tag{11}$$

in which Re stands for the real part of its parameter. $F_i(z_i)$ (i = 1,2,3) are analytic function of the complex variables $z_i = x + \mu_i y$, where (x,y) is the location of the point whose stress components are calculated. μ_i (i = 1,2,3) are three roots of the equation:

$$l_4(\mu)l_2(\mu)-l_3^2(\mu)=0 \tag{12}$$

where l_2, l_3 and l_4 are the characteristic equations of the three differential operators L_2, L_3, L_4, respectively:

$$\begin{aligned} l_2 &= \beta_{44}-2\beta_{45}\mu+\beta_{55}\mu^2 \\ l_3 &= -\beta_{24}+(\beta_{25}+\beta_{46})\mu-(\beta_{14}+\beta_{56})\mu^2+\beta_{15}\mu^3 \\ l_4 &= \beta_{22}-2\beta_{26}\mu+(2\beta_{12}+\beta_{66})\mu^2-2\beta_{16}\mu^3+\beta_{11}\mu^4 \end{aligned} \tag{13}$$

Lekhnitskii (1963) proved that Equation (12) has only complex or purely imaginary roots. Three of these roots are the conjugate of the other three. μ_i (i = 1,2,3), therefore, are the three roots of Equation (12). λ_i (i = 1,2,3) are defined as:

$$\lambda_1=-\frac{l_3(\mu_1)}{l_2(\mu_1)};\lambda_2=-\frac{l_3(\mu_2)}{l_2(\mu_2)};\lambda_3=-\frac{l_3(\mu_3)}{l_4(\mu_3)}; \tag{14}$$

Lekhnitskii (1963) then introduced three analytic functions $\phi_i(z_i)$ (i = 1,2,3) which are defined by:

$$\phi_1(z_1)=F_1'(z_1);\phi_2(z_2)=F_2'(z_2);\phi_3(z_3)=\frac{1}{\lambda_3}F_3'(z_3); \tag{15}$$

Combining Equation (11) and (15), it is obtained that:

$$\begin{aligned} \frac{\partial \mathrm{F}}{\partial x} &= 2\,\mathrm{Re}(\phi_1(z_1)+\phi_2(z_2)+\lambda_3\phi_3(z_3)) \\ \frac{\partial \mathrm{F}}{\partial y} &= 2\,\mathrm{Re}(\mu_1\phi_1(z_1)+\mu_2\phi_2(z_2)+\lambda_3\mu_3\phi_3(z_3)) \\ \Psi &= 2\,\mathrm{Re}(\lambda_1\phi_1(z_1)+\lambda_2\phi_2(z_2)+\phi_3(z_3)) \end{aligned} \tag{16}$$

The stress components, which are expressed as functions of F(x,y) and $\Psi(x,y)$, are now expressed with $\phi_i(z_i)$ (i = 1,2,3):

$$\begin{aligned} \sigma_x &= 2\,\mathrm{Re}(\mu_1^2\phi_1'(z_1)+\mu_1^2\phi_2'(z_2)+\lambda_3\mu_1^2\phi_3'(z_3)) \\ \sigma_y &= 2\,\mathrm{Re}(\phi_1'(z_1)+\phi_2'(z_2)+\lambda_3\phi_3'(z_3)) \\ \tau_{yz} &= -2\,\mathrm{Re}(\lambda_1\phi_1'(z_1)+\lambda_2\phi_2'(z_2)+\phi_3'(z_3)) \\ \tau_{zx} &= 2\,\mathrm{Re}(\lambda_1\mu_1\phi_1'(z_1)+\lambda_2\mu_2\phi_2'(z_2)+\mu_3\phi_3'(z_3)) \\ \tau_{xy} &= -2\,\mathrm{Re}(\mu_1\phi_1'(z_1)+\mu_2\phi_2'(z_2)+\lambda_3\mu_3\phi_3'(z_3)) \end{aligned} \tag{17}$$

The problem of finding the stress distribution around the hole is now transformed to the problem of determining the three analytical functions $\phi_i(z_i)$ (i = 1,2,3). These analytical functions have to be determined from the boundary conditions introduced in each of the sub-problems.

C.3 Application of the Far-Field Stress

In the first sub-problem, the far-field stress is applied to the transversely isotropic medium with no opening. It is obvious that after this step, the stress in the medium is the assumed far-field stress $[\sigma_0]_{xyz}$.

C.4 Drilling a Hole with Zero Internal Pressure

A circular hold is then drilled in the transversely isotropic medium, with zero internal pressure. Along the wall of the hole, the applied stresses must be reduced to zero. For any point ($r = a$, θ) along the wall of the hole, the boundary conditions can be written as:

$$\begin{aligned}
\sigma_x \cos\theta + \tau_{xy} \sin\theta &= -(\sigma_{x,0} \cos\theta + \tau_{xy,0} \sin\theta) \\
\tau_{xy} \cos\theta + \sigma_y \sin\theta &= -(\tau_{xy,0} \cos\theta + \sigma_{y,0} \sin\theta) \\
\tau_{zx} \cos\theta + \tau_{yz} \sin\theta &= -(\tau_{zx,0} \cos\theta + \tau_{yz,0} \sin\theta)
\end{aligned} \tag{18}$$

Using Equation (17), these boundary conditions can be expressed as three equations of the analytical functions $\phi_i(z_i)$ (i = 1,2,3). These analytical functions are solved to be:

$$\begin{aligned}
\phi_1(z_1) &= \frac{1}{\Delta \xi_1}\left[(\mu_1 - \mu_3\lambda_2\lambda_3)\bar{a}_1 + (\lambda_2\lambda_3 - 1)\bar{b}_1 + \lambda_3(\mu_3 - \mu_2)\bar{c}_1\right] \\
\phi_2(z_2) &= \frac{1}{\Delta \xi_2}\left[(\lambda_1\lambda_3\mu_3 - \mu_1)\bar{a}_1 + (1 - \lambda_1\lambda_3)\bar{b}_1 + \lambda_3(\mu_1 - \mu_3)\bar{c}_1\right] \\
\phi_3(z_3) &= \frac{1}{\Delta \xi_3}\left[(\mu_1\lambda_2 - \mu_2\lambda_1)\bar{a}_1 + (\lambda_1 - \lambda_2)\bar{b}_1 + (\mu_2 - \mu_1)\bar{c}_1\right]
\end{aligned} \tag{19}$$

in which:

$$\Delta = (\mu_2 - \mu_1) + \lambda_2\lambda_3(\mu_1 - \mu_3) + \lambda_1\lambda_3(\mu_3 - \mu_2) \tag{20}$$

$$\xi_i = \frac{\frac{z_i}{a} + \sqrt{\left(\frac{z_i}{a}\right)^2 - 1 - \mu_i^2}}{1 - i\mu_i} \tag{21}$$

$$\bar{a}_1 = -\frac{a}{2}(\sigma_{y,0} - i\tau_{xy,0}); \bar{b}_1 = \frac{a}{2}(\tau_{xy,0} - i\sigma_{x,0}); \bar{c}_1 = \frac{a}{2}(\tau_{yz,0} - i\tau_{xz,0}); \tag{22}$$

The expressions of the analytical functions $\phi_i(z_i)$ (i = 1,2,3) in Equation (19) can be substituted into Equation (17) to give the stresses induced by drilling a hole with zero internal pressure. The

stresses induced in this step are denoted $[\sigma_h]_{xyz}$. After certain mathematical manipulations, it can be shown that the components of the induced stress can be written as:

$$\begin{aligned}
\sigma_{x,h} &= b_1\sigma_{x,0} + c_1\sigma_{y,0} + d_1\tau_{xy,0} + e_1\tau_{yz,0} + f_1\tau_{xz,0} \\
\sigma_{y,h} &= b_2\sigma_{x,0} + c_2\sigma_{y,0} + d_2\tau_{xy,0} + e_2\tau_{yz,0} + f_2\tau_{xz,0} \\
\tau_{xy,h} &= b_3\sigma_{x,0} + c_3\sigma_{y,0} + d_3\tau_{xy,0} + e_3\tau_{yz,0} + f_3\tau_{xz,0} \\
\tau_{zx,h} &= b_4\sigma_{x,0} + c_4\sigma_{y,0} + d_4\tau_{xy,0} + e_4\tau_{yz,0} + f_4\tau_{xz,0} \\
\tau_{yz,h} &= b_5\sigma_{x,0} + c_5\sigma_{y,0} + d_5\tau_{xy,0} + e_5\tau_{yz,0} + f_5\tau_{xz,0}
\end{aligned} \tag{23}$$

The stress component $\sigma_{z,h}$ is expressed by all other stress components based on Equation (7):

$$\sigma_{z,h} = -\frac{1}{a_{33}}\left(a_{31}\sigma_{x,h} + a_{32}\sigma_{y,h} + a_{34}\tau_{yz,h} + a_{35}\tau_{zx,h} + a_{36}\tau_{xy,h}\right) \tag{24}$$

The coefficients b_i, c_i, … f_i (i = 1,2,…,5) in Equation (23) are expressed by:

$$\begin{aligned}
b_1 &= -\mathrm{Re}[i\gamma_1\mu_1^2(\lambda_2\lambda_3 - 1) + i\gamma_2\mu_2^2(1-\lambda_1\lambda_3) + i\gamma_3\mu_3^2\lambda_3(\lambda_1 - \lambda_2)] \\
c_1 &= -\mathrm{Re}[\gamma_1\mu_1^2(\mu_2 - \mu_3\lambda_2\lambda_3) + \gamma_2\mu_2^2(\lambda_1\lambda_3\mu_3 - \mu_1) + \gamma_3\mu_3^2\lambda_3(\mu_1\lambda_2 - \mu_2\lambda_1)] \\
d_1 &= \mathrm{Re}[\gamma_1\mu_1^2(\lambda_2\lambda_3 - 1 + i\mu_2 - i\mu_3\lambda_2\lambda_3) + \gamma_2\mu_2^2(1-\lambda_1\lambda_3 + i\mu_3\lambda_1\lambda_3 - i\mu_1) \\
&\quad + \gamma_3\mu_3^2\lambda_3(\lambda_1 - \lambda_2 + i\mu_1\lambda_2 - i\mu_2\lambda_1)] \\
e_1 &= \mathrm{Re}[\mu_1^2\gamma_1\lambda_3(\mu_3 - \mu_2) + \mu_2^2\gamma_2\lambda_3(\mu_1 - \mu_3) + \mu_3^2\gamma_3\lambda_3(\mu_2 - \mu_1)] \\
f_1 &= -\mathrm{Re}[i\gamma_1\mu_1^2\lambda_3(\mu_3 - \mu_2) + i\gamma_2\mu_2^2\lambda_3(\mu_1 - \mu_3) + i\gamma_3\mu_3^2\lambda_3(\mu_2 - \mu_1)]
\end{aligned} \tag{25}$$

$$\begin{aligned}
b_2 &= -\mathrm{Re}[i\gamma_1(\lambda_2\lambda_3 - 1) + i\gamma_2(1-\lambda_1\lambda_3) + i\gamma_3\lambda_3(\lambda_1 - \lambda_2)] \\
c_2 &= -\mathrm{Re}[\gamma_1(\mu_2 - \mu_3\lambda_2\lambda_3) + \gamma_2(\lambda_1\lambda_3\mu_3 - \mu_1) + \gamma_3\lambda_3(\mu_1\lambda_2 - \mu_2\lambda_1)] \\
d_2 &= \mathrm{Re}[\gamma_1(\lambda_2\lambda_3 - 1 + i\mu_2 - i\mu_3\lambda_2\lambda_3) + \gamma_2(1-\lambda_1\lambda_3 + i\mu_3\lambda_1\lambda_3 - i\mu_1) \\
&\quad + \gamma_3\lambda_3(\lambda_1 - \lambda_2 + i\mu_1\lambda_2 - i\mu_2\lambda_1)] \\
e_2 &= \mathrm{Re}[\gamma_1\lambda_3(\mu_3 - \mu_2) + \gamma_2\lambda_3(\mu_1 - \mu_3) + \gamma_3\lambda_3(\mu_2 - \mu_1)] \\
f_2 &= -\mathrm{Re}[i\gamma_1\lambda_3(\mu_3 - \mu_2) + i\gamma_2\lambda_3(\mu_1 - \mu_3) + i\gamma_3\lambda_3(\mu_2 - \mu_1)]
\end{aligned} \tag{26}$$

$$\begin{aligned}
b_3 &= \mathrm{Re}[i\gamma_1\mu_1(\lambda_2\lambda_3 - 1) + i\gamma_2\mu_2(1-\lambda_1\lambda_3) + i\gamma_3\mu_3\lambda_3(\lambda_1 - \lambda_2)] \\
c_3 &= \mathrm{Re}[\gamma_1\mu_1(\mu_2 - \mu_3\lambda_2\lambda_3) + \gamma_2\mu_2(\lambda_1\lambda_3\mu_3 - \mu_1) + \gamma_3\mu_3\lambda_3(\mu_1\lambda_2 - \mu_2\lambda_1)] \\
d_3 &= -\mathrm{Re}[\gamma_1\mu_1(\lambda_2\lambda_3 - 1 + i\mu_2 - i\mu_3\lambda_2\lambda_3) + \gamma_2\mu_2(1-\lambda_1\lambda_3 + i\mu_3\lambda_1\lambda_3 - i\mu_1) \\
&\quad + \gamma_3\mu_3\lambda_3(\lambda_1 - \lambda_2 + i\mu_1\lambda_2 - i\mu_2\lambda_1)] \\
e_3 &= -\mathrm{Re}[\gamma_1\mu_1\lambda_3(\mu_3 - \mu_2) + \gamma_2\mu_2\lambda_3(\mu_1 - \mu_3) + \gamma_3\mu_3\lambda_3(\mu_2 - \mu_1)] \\
f_3 &= \mathrm{Re}[i\gamma_1\mu_1\lambda_3(\mu_3 - \mu_2) + i\gamma_2\mu_2\lambda_3(\mu_1 - \mu_3) + i\gamma_3\mu_3\lambda_3(\mu_2 - \mu_1)]
\end{aligned} \tag{27}$$

$$
\begin{aligned}
b_4 &= -\mathrm{Re}[i\gamma_1\mu_1\lambda_1(\lambda_2\lambda_3-1)+i\gamma_2\mu_2\lambda_2(1-\lambda_1\lambda_3)+i\gamma_3\mu_3(\lambda_1-\lambda_2)] \\
c_4 &= -\mathrm{Re}[\gamma_1\mu_1\lambda_1(\mu_2-\mu_3\lambda_2\lambda_3)+\gamma_2\mu_2\lambda_2(\lambda_1\lambda_3\mu_3-\mu_1)+\gamma_3\mu_3(\mu_1\lambda_2-\mu_2\lambda_1)] \\
d_4 &= \mathrm{Re}[\gamma_1\mu_1\lambda_1(\lambda_2\lambda_3-1+i\mu_2-i\mu_3\lambda_2\lambda_3)+\gamma_2\mu_2\lambda_2(1-\lambda_1\lambda_3+i\mu_3\lambda_1\lambda_3-i\mu_1) \\
&\quad +\gamma_3\mu_3(\lambda_1-\lambda_2+i\mu_1\lambda_2-i\mu_2\lambda_1)] \\
e_4 &= \mathrm{Re}[\gamma_1\mu_1\lambda_1\lambda_3(\mu_3-\mu_2)+\gamma_2\mu_2\lambda_2\lambda_3(\mu_1-\mu_3)+\gamma_3\mu_3(\mu_2-\mu_1)] \\
f_4 &= -\mathrm{Re}[i\gamma_1\mu_1\lambda_1\lambda_3(\mu_3-\mu_2)+i\gamma_2\mu_2\lambda_2\lambda_3(\mu_1-\mu_3)+i\gamma_3\mu_3(\mu_2-\mu_1)]
\end{aligned}
\tag{28}
$$

$$
\begin{aligned}
b_5 &= \mathrm{Re}[i\gamma_1\lambda_1(\lambda_2\lambda_3-1)+i\gamma_2\lambda_2(1-\lambda_1\lambda_3)+i\gamma_3(\lambda_1-\lambda_2)] \\
c_5 &= \mathrm{Re}[\gamma_1\lambda_1(\mu_2-\mu_3\lambda_2\lambda_3)+\gamma_2\lambda_2(\lambda_1\lambda_3\mu_3-\mu_1)+\gamma_3(\mu_1\lambda_2-\mu_2\lambda_1)] \\
d_5 &= -\mathrm{Re}[\gamma_1\lambda_1(\lambda_2\lambda_3-1+i\mu_2-i\mu_3\lambda_2\lambda_3)+\gamma_2\lambda_2(1-\lambda_1\lambda_3+i\mu_3\lambda_1\lambda_3-i\mu_1) \\
&\quad +\gamma_3(\lambda_1-\lambda_2+i\mu_1\lambda_2-i\mu_2\lambda_1)] \\
e_5 &= -\mathrm{Re}[\gamma_1\lambda_1\lambda_3(\mu_3-\mu_2)+\gamma_2\lambda_2\lambda_3(\mu_1-\mu_3)+\gamma_3(\mu_2-\mu_1)] \\
f_5 &= \mathrm{Re}[i\gamma_1\lambda_1\lambda_3(\mu_3-\mu_2)+i\gamma_2\lambda_2\lambda_3(\mu_1-\mu_3)+i\gamma_3(\mu_2-\mu_1)]
\end{aligned}
\tag{29}
$$

In these expressions, γ_i (i = 1,2,3) are defined by:

$$
\gamma_i = -\frac{a}{a\Delta\xi_i\sqrt{\left(\frac{z_i}{a}\right)^2-1-\mu_i^2}} \tag{30}
$$

With these coefficients, the stress induced in this sub-problem, $[\sigma_h]_{xyz}$, can be calculated through Equations (23) and (24).

C.5 Apply Uniform Internal Pressure q

An internal pressure q is finally applied along the wall of the hole. For any point ($r = a$, θ) along the wall of the hole, the boundary conditions are written as:

$$
\begin{aligned}
\sigma_x\cos\theta+\tau_{xy}\sin\theta &= q\cos\theta \\
\tau_{xy}\cos\theta+\sigma_y\sin\theta &= q\sin\theta \\
\tau_{zx}\cos\theta+\tau_{yz}\sin\theta &= 0
\end{aligned}
\tag{31}
$$

Using Equation (17), three equations of the analytical functions $\phi_i(z_i)$ (i = 1,2,3) can again be obtained. For this sub-problem, these analytical functions are solved to be:

$$
\begin{aligned}
\phi_1(z_1) &= q\Delta_1 a[(\mu_2-\mu_3\lambda_2\lambda_3)+i(\lambda_2\lambda_3-1)]/2 \\
\phi_2(z_2) &= q\Delta_2 a[(\lambda_1\lambda_3\mu_3-\mu_1)+i(1-\lambda_1\lambda_3)]/2 \\
\phi_3(z_3) &= q\Delta_3 a[(\mu_1\lambda_2-\mu_2\lambda_1)+i(\lambda_1-\lambda_2)]/2
\end{aligned}
\tag{32}
$$

in which:

$$\Delta_i = \frac{1}{\Delta\xi_i} \tag{33}$$

Substituting Equation (32) into Equation (17), the induced stress due to the application of a uniform internal pressure, $[\sigma_q]_{xyz}$, can be expressed by:

$$\sigma_{x,q} = l_1 q; \sigma_{y,q} = l_2 q; \tau_{xy,q} = l_3 q; \tau_{zx,q} = l_4 q; \tau_{yz,q} = l_5 q; \tag{34}$$

The stress component $\sigma_{z,q}$ is expressed by all other stress components based on Equation (7):

$$\sigma_{z,q} = -\frac{1}{a_{33}}\left(a_{31}\sigma_{x,q} + a_{32}\sigma_{y,q} + a_{34}\tau_{yz,q} + a_{35}\tau_{zx,q} + a_{36}\tau_{xy,q}\right) \tag{35}$$

The coefficients l_i (i = 1,2,…,5) in Equation (34) are expressed by:

$$\begin{aligned}
l_1 &= \mathrm{Re}[\gamma_1\mu_1^2\left((\mu_2 - \mu_3\lambda_2\lambda_3) + i(\lambda_2\lambda_3 - 1)\right) + \gamma_2\mu_2^2\left((\lambda_1\lambda_3\mu_3 - \mu_1) + i(1 - \lambda_1\lambda_3)\right) + \\
&\quad \lambda_3\gamma_3\mu_3^2\left((\mu_1\lambda_2 - \mu_2\lambda_1) + i(\lambda_1 - \lambda_2)\right)] \\
l_2 &= \mathrm{Re}[\gamma_1\left((\mu_2 - \mu_3\lambda_2\lambda_3) + i(\lambda_2\lambda_3 - 1)\right) + \gamma_2\left((\lambda_1\lambda_3\mu_3 - \mu_1) + i(1 - \lambda_1\lambda_3)\right) + \\
&\quad \lambda_3\gamma_3\left((\mu_1\lambda_2 - \mu_2\lambda_1) + i(\lambda_1 - \lambda_2)\right)] \\
l_3 &= -\mathrm{Re}[\gamma_1\mu_1\left((\mu_2 - \mu_3\lambda_2\lambda_3) + i(\lambda_2\lambda_3 - 1)\right) + \gamma_2\mu_2\left((\lambda_1\lambda_3\mu_3 - \mu_1) + i(1 - \lambda_1\lambda_3)\right) + \\
&\quad \lambda_3\gamma_3\mu_3\left((\mu_1\lambda_2 - \mu_2\lambda_1) + i(\lambda_1 - \lambda_2)\right)] \\
l_4 &= \mathrm{Re}[\lambda_1\gamma_1\mu_1\left((\mu_2 - \mu_3\lambda_2\lambda_3) + i(\lambda_2\lambda_3 - 1)\right) + \lambda_2\gamma_2\mu_2\left((\lambda_1\lambda_3\mu_3 - \mu_1) + i(1 - \lambda_1\lambda_3)\right) + \\
&\quad \gamma_3\mu_3\left((\mu_1\lambda_2 - \mu_2\lambda_1) + i(\lambda_1 - \lambda_2)\right)] \\
l_5 &= -\mathrm{Re}[\lambda_1\gamma_1\left((\mu_2 - \mu_3\lambda_2\lambda_3) + i(\lambda_2\lambda_3 - 1)\right) + \lambda_2\gamma_2\left((\lambda_1\lambda_3\mu_3 - \mu_1) + i(1 - \lambda_1\lambda_3)\right) + \\
&\quad \gamma_3\left((\mu_1\lambda_2 - \mu_2\lambda_1) + i(\lambda_1 - \lambda_2)\right)]
\end{aligned} \tag{36}$$

With these coefficients, the stress induced in this sub-problem, $[\sigma_q]_{xyz}$, can be calculated.

Finally, the stress distribution around a circular hole, subject to a uniform internal pressure, embedded in a transversely isotropic medium can be expressed by the superposition of the induced stresses from all three sub-problems:

$$[\sigma]_{xyz} = [\sigma_0]_{xyz} + [\sigma_h]_{xyz} + [\sigma_q]_{xyz} \tag{37}$$

The subscript "*xyz*" clearly shows that the calculated stress components are in the **xyz** system, which is the local frame for the borehole. With this stress obtained, it is straightforward to use tensor manipulation to obtain stress components in other coordinate systems.

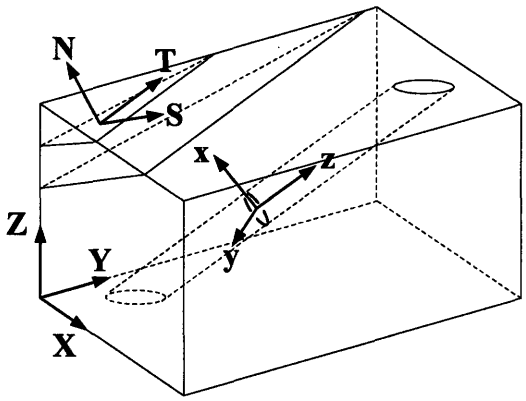

Figure C.1 Three Coordinate Systems in the Borehole Stability Problem

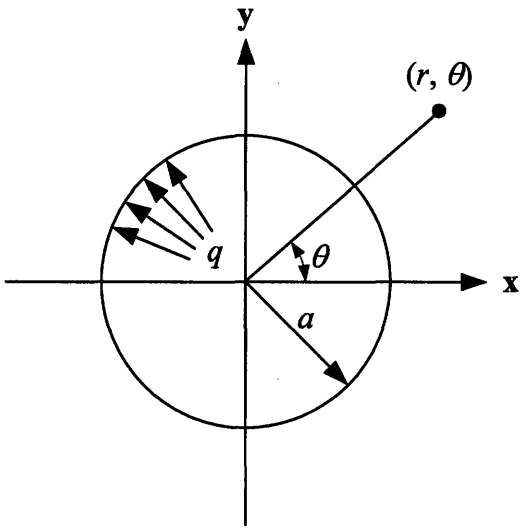

Figure C.2 Cross-Section of the Borehole and the Local Cylindrical System

Appendix D MATLAB Code

The MATLAB code that implements the solutions described in Appendix C is listed in this appendix. In order to make the program more readable, the variable names in the program correspond to their representations in the solutions. For example, `delta` stands for Δ, `gama` stands for γ, `kesi` stands for ξ, etc. While writing this program, the Fortran code named "Berni 2" by Amadei (Amadei, 1983) was consulted.

```
%%%%%%%%%%%%%%%%%%%%%%%%%%%%%%%%%%%%%%%%%%%%%%%%%%%%%%%%%%%%%%%%%%%%%%%%%%%%
% The MATLAB program that calculates the stress distribution of a circular %
% hole embedded in a transversely isotropic media                           %
% Author: Jianyong Pei                                                      %
% Dept. of Civil and Environmental Engineering, MIT, May 2008               %
%%%%%%%%%%%%%%%%%%%%%%%%%%%%%%%%%%%%%%%%%%%%%%%%%%%%%%%%%%%%%%%%%%%%%%%%%%%%

function [sgm_xyz, sgm_stn, sgm_rqz, sgm_eig] = Calculate_Stress_Around_Borehole_In_Anisotropic_Media ...
    (radius,theta,beta_n,alpha_n,beta_z,alpha_z,depth,p,q)

    %%% Parameters In %%%%
    % radius: radius of the point where the stress is calculated (m)
    % theta: theta value of the point where the stress is calculated (radian)
    % beta_n, alpha_n: Inclination and azimuth of the N direction (radian)
    % beta_z, alpha_z: Inclination and azimuth of the borehole axis (radian)
    % depth: the depth of the borehole (m)
    % p: the formation pore pressure (MPa)
    % q: the effective mud pressure in the borehole (MPa)
    %%% Parameters Out %%%
    % sgm_xyz: stress components in the xyz system (borehole local frame)
    % sgm_stn: stress components in the STN system (material system)
    % sgm_rqz: stress in the (r,theta,z) system (cylindrical borehole local frame)
    % sgm_eig: principal stresses
    %%% Stress Unit: MPa, Modulus Unit: MPa %%%

    %%% The anisotropic material properties %%%%%%%%%
    Es = 38882; En = 29329; vst = 0.25; vns = 0.2;
    Gns = Es*En/(Es+En+2*vns*Es); Gst = Es/2/(1+vst);
    %%%%%%%%%%%%%%%%%%%%%%%%%%%%%%%%%%%%%%%%%%%%%%%%
```

```
%%% Total vertical stress in MPa, assuming total density of rock is 2.5 t/m3
temp = 2.5*1000*10*depth/1.0e6;

%%% The in-situ effective stresses in MPa %%%
SGMV = temp-p; SGMh = 0.7*temp-p; SGMH = 0.85*temp-p;
SGM  = [SGMh     0.0      0.0;
        0.0      SGMH     0.0;
        0.0      0.0      SGMV];

%%% The borehole radius (m) %%%
a = 1.0;

%%% The elastic matrix of the transversely isotropic rock
E = [1/Es     -vst/Es    -vns/En  0       0       0;
    -vst/Es   1/Es       -vns/En  0       0       0;
    -vns/En   -vns/En    1/En     0       0       0;
    0         0          0        1/Gns   0       0;
    0         0          0        0       1/Gns   0;
    0         0          0        0       0       1/Gst];

%%% Calculation begins here %%%
while (theta < 0)
   theta = theta + 2*pi;
end
while (theta > pi + pi)
   theta = theta - 2*pi;
end

degree = theta*180/pi;
if (degree <=135 && degree >= 46)||(degree <= 315 && degree >=226)
```

```
    [T_STN, T_xyz, T_sgm_STN, T_eps_xyz] = ...
       Obtain_Transformation_Matrix_2(beta_z, alpha_z, beta_n, alpha_n);
    degree = degree - 90; theta = theta - pi/2;
else
    [T_STN, T_xyz, T_sgm_STN, T_eps_xyz] = ...
       Obtain_Transformation_Matrix_1(beta_z, alpha_z, beta_n, alpha_n);
end

A = T_eps_xyz*T_sgm_STN'*E*T_sgm_STN*T_eps_xyz';

sgm0 = T_xyz*SGM*T_xyz';

B = zeros(6,6);
for row = 1:6
    for col = 1:6
       B(row,col) = A(row,col) - A(row,3)*A(col,3)/A(3,3);
    end
end

temp6 = -B(1,5)^2+B(1,1)*B(5,5);
temp5 = 2*(B(1,4)*B(1,5)-B(1,1)*B(4,5)-B(1,6)*B(5,5)+B(1,5)*B(5,6));
temp4 = -B(1,4)^2-2*B(1,5)*B(2,5)+B(1,1)*B(4,4)+4*B(1,6)*B(4,5)-2*B(1,5)*B(4,6)+ ...
        2*B(1,2)*B(5,5)-2*B(1,4)*B(5,6)-B(5,6)^2+B(5,5)*B(6,6);
temp3 = 2*(B(1,5)*B(2,4)+B(1,4)*B(2,5)-B(1,6)*B(4,4)-2*B(1,2)*B(4,5)+B(1,4)*B(4,6)-B(2,6)*B(5,5)+ ...
        B(2,5)*B(5,6)+B(4,6)*B(5,6)-B(4,5)*B(6,6));
temp2 = -2*B(1,4)*B(2,4)-B(2,5)^2+2*B(1,2)*B(4,4)+4*B(2,6)*B(4,5)-2*B(2,5)*B(4,6)- ...
        B(4,6)^2+B(2,2)*B(5,5)-2*B(2,4)*B(5,6)+B(4,4)*B(6,6);
temp1 = 2*(B(2,4)*B(2,5)-B(2,6)*B(4,4)-B(2,2)*B(4,5)+B(2,4)*B(4,6));
temp0 = -B(2,4)^2+B(2,2)*B(4,4);
temp = [temp6, temp5, temp4, temp3, temp2, temp1, temp0];
```

```
r = roots(temp);

miu = [r(1), r(3), r(5)]; miu_bar = [r(2), r(4), r(6)];

l31 = B(1,5)*miu(1)^3-(B(1,4)+B(5,6))*miu(1)^2+(B(2,5)+B(4,6))*miu(1)-B(2,4);
l21 = B(5,5)*miu(1)^2-2*B(4,5)*miu(1)+B(4,4);
l32 = B(1,5)*miu(2)^3-(B(1,4)+B(5,6))*miu(2)^2+(B(2,5)+B(4,6))*miu(2)-B(2,4);
l22 = B(5,5)*miu(2)^2-2*B(4,5)*miu(2)+B(4,4);
l33 = B(1,5)*miu(3)^3-(B(1,4)+B(5,6))*miu(3)^2+(B(2,5)+B(4,6))*miu(3)-B(2,4);
l43 = B(1,1)*miu(3)^4-2*B(1,6)*miu(3)^3+(2*B(1,2)+B(6,6))*miu(3)^2-2*B(2,6)*miu(3)+B(2,2);

if (norm(l31)<1e-12)
   l31 = 0;
end
if (norm(l32)<1e-12)
   l32 = 0;
end
if (norm(l33)<1e-12)
   l33 = 0;
end

lambda = [-l31/l21, -l32/l22, -l33/l43];

delta = miu(2)-miu(1)+lambda(2)*lambda(3)*(miu(1)-miu(3))+lambda(1)*lambda(3)*(miu(3)-miu(2));

x = radius*cos(theta); y = radius*sin(theta);

z = [x+miu(1)*y, x+miu(2)*y, x+miu(3)*y];
sq1 = sqrt((z(1)/a)^2-1-miu(1)^2);
```

```
sq2 = sqrt((z(2)/a)^2-1-miu(2)^2);
sq3 = sqrt((z(3)/a)^2-1-miu(3)^2);
sq = [sq1, sq2, sq3];
if (degree > 90 && degree < 270)
   sq = -sq;
end

kesi1 = (z(1)/a + sq(1))/(1-i*miu(1));
kesi2 = (z(2)/a + sq(2))/(1-i*miu(2));
kesi3 = (z(3)/a + sq(3))/(1-i*miu(3));

kesi = [kesi1, kesi2, kesi3];

gama1 = -1.0/delta/kesi(1)/sq(1);
gama2 = -1.0/delta/kesi(2)/sq(2);
gama3 = -1.0/delta/kesi(3)/sq(3);

gama = [gama1, gama2, gama3];

b1 = -1*real(i*gama(1)*miu(1)^2*(lambda(2)*lambda(3)-1)...
          +i*gama(2)*miu(2)^2*(1-lambda(1)*lambda(3))...
          +i*gama(3)*miu(3)^2*lambda(3)*(lambda(1)-lambda(2)));

c1 = -1*real(gama(1)*miu(1)^2*(miu(2)-miu(3)*lambda(2)*lambda(3))...
          +gama(2)*miu(2)^2*(lambda(1)*lambda(3)*miu(3)-miu(1))...
          +gama(3)*miu(3)^2*lambda(3)*(miu(1)*lambda(2)-miu(2)*lambda(1)));

d1 = real(gama(1)*miu(1)^2*(lambda(2)*lambda(3)-1+i*miu(2)-i*miu(3)*lambda(2)*lambda(3))...
       +gama(2)*miu(2)^2*(1-lambda(1)*lambda(3)+i*miu(3)*lambda(1)*lambda(3)-i*miu(1))...
       +gama(3)*miu(3)^2*lambda(3)*(lambda(1)-lambda(2)+i*miu(1)*lambda(2)-i*miu(2)*lambda(1)));
```

```
e1 = real(miu(1)^2*gama(1)*lambda(3)*(miu(3)-miu(2))...
        +miu(2)^2*gama(2)*lambda(3)*(miu(1)-miu(3))...
        +miu(3)^2*gama(3)*lambda(3)*(miu(2)-miu(1)));

f1 = -1*real(i*gama(1)*miu(1)^2*lambda(3)*(miu(3)-miu(2))...
           +i*gama(2)*miu(2)^2*lambda(3)*(miu(1)-miu(3))...
           +i*gama(3)*miu(3)^2*lambda(3)*(miu(2)-miu(1)));

b2 = -1*real(i*gama(1)*(lambda(2)*lambda(3)-1)...
           +i*gama(2)*(1-lambda(1)*lambda(3))...
           +i*gama(3)*lambda(3)*(lambda(1)-lambda(2)));

c2 = -1*real(gama(1)*(miu(2)-miu(3)*lambda(2)*lambda(3))...
           +gama(2)*(lambda(1)*lambda(3)*miu(3)-miu(1))...
           +gama(3)*lambda(3)*(miu(1)*lambda(2)-miu(2)*lambda(1)));

d2 = real(gama(1)*(lambda(2)*lambda(3)-1+i*miu(2)-i*miu(3)*lambda(2)*lambda(3))...
        +gama(2)*(1-lambda(1)*lambda(3)+i*lambda(1)*lambda(3)*miu(3)-i*miu(1))...
        +gama(3)*lambda(3)*(lambda(1)-lambda(2)+i*miu(1)*lambda(2)-i*miu(2)*lambda(1)));

e2 = real(gama(1)*lambda(3)*(miu(3)-miu(2))...
        +gama(2)*lambda(3)*(miu(1)-miu(3))...
        +gama(3)*lambda(3)*(miu(2)-miu(1)));

f2 = -1*real(i*gama(1)*lambda(3)*(miu(3)-miu(2))...
           +i*gama(2)*lambda(3)*(miu(1)-miu(3))...
           +i*gama(3)*lambda(3)*(miu(2)-miu(1)));

b3 = real(i*gama(1)*miu(1)*(lambda(2)*lambda(3)-1)...
```

```
        +i*gama(2)*miu(2)*(1-lambda(1)*lambda(3))...
        +i*gama(3)*miu(3)*lambda(3)*(lambda(1)-lambda(2)));

c3 = real(gama(1)*miu(1)*(miu(2)-miu(3)*lambda(2)*lambda(3))...
        +gama(2)*miu(2)*(lambda(1)*lambda(3)*miu(3)-miu(1))...
        +gama(3)*miu(3)*lambda(3)*(miu(1)*lambda(2)-miu(2)*lambda(1)));

d3 = -1*real(gama(1)*miu(1)*(lambda(2)*lambda(3)-1+i*miu(2)-i*miu(3)*lambda(2)*lambda(3))...
           +gama(2)*miu(2)*(1-lambda(1)*lambda(3)+i*lambda(1)*lambda(3)*miu(3)-i*miu(1))...
           +gama(3)*miu(3)*lambda(3)*(lambda(1)-lambda(2)+i*miu(1)*lambda(2)-i*miu(2)*lambda(1)));

e3 = -1*real(miu(1)*gama(1)*lambda(3)*(miu(3)-miu(2))...
           +miu(2)*gama(2)*lambda(3)*(miu(1)-miu(3))...
           +miu(3)*gama(3)*lambda(3)*(miu(2)-miu(1)));

f3 = real(i*gama(1)*miu(1)*lambda(3)*(miu(3)-miu(2))...
        +i*gama(2)*miu(2)*lambda(3)*(miu(1)-miu(3))...
        +i*gama(3)*miu(3)*lambda(3)*(miu(2)-miu(1)));

b4 = -1*real(i*gama(1)*lambda(1)*miu(1)*(lambda(2)*lambda(3)-1)...
           +i*gama(2)*lambda(2)*miu(2)*(1-lambda(1)*lambda(3))...
           +i*gama(3)*miu(3)*(lambda(1)-lambda(2)));

c4 = -1*real(gama(1)*lambda(1)*miu(1)*(miu(2)-miu(3)*lambda(2)*lambda(3))...
           +gama(2)*lambda(2)*miu(2)*(lambda(1)*lambda(3)*miu(3)-miu(1))...
           +gama(3)*miu(3)*(miu(1)*lambda(2)-miu(2)*lambda(1)));

d4 = real(gama(1)*miu(1)*lambda(1)*(lambda(2)*lambda(3)-1+i*miu(2)-i*miu(3)*lambda(2)*lambda(3))...
        +gama(2)*miu(2)*lambda(2)*(1-lambda(1)*lambda(3)+i*lambda(1)*lambda(3)*miu(3)-i*miu(1))...
        +gama(3)*miu(3)*(lambda(1)-lambda(2)+i*miu(1)*lambda(2)-i*miu(2)*lambda(1)));
```

```
e4 = real(gama(1)*miu(1)*lambda(1)*lambda(3)*(miu(3)-miu(2))...
     +gama(2)*miu(2)*lambda(2)*lambda(3)*(miu(1)-miu(3))...
     +miu(3)*gama(3)*(miu(2)-miu(1)));

f4 = -1*real(i*gama(1)*miu(1)*lambda(1)*lambda(3)*(miu(3)-miu(2))...
       +i*gama(2)*miu(2)*lambda(2)*lambda(3)*(miu(1)-miu(3))...
       +i*gama(3)*miu(3)*(miu(2)-miu(1)));

b5 = real(i*gama(1)*lambda(1)*(lambda(2)*lambda(3)-1)...
     +i*gama(2)*lambda(2)*(1-lambda(1)*lambda(3))...
     +i*gama(3)*(lambda(1)-lambda(2)));

c5 = real(gama(1)*lambda(1)*(miu(2)-miu(3)*lambda(2)*lambda(3))...
     +gama(2)*lambda(2)*(lambda(1)*lambda(3)*miu(3)-miu(1))...
     +gama(3)*(miu(1)*lambda(2)-miu(2)*lambda(1)));

d5 = -1*real(gama(1)*lambda(1)*(lambda(2)*lambda(3)-1+i*miu(2)-i*miu(3)*lambda(2)*lambda(3))...
       +gama(2)*lambda(2)*(1-lambda(1)*lambda(3)+i*lambda(1)*lambda(3)*miu(3)-i*miu(1))...
       +gama(3)*(lambda(1)-lambda(2)+i*miu(1)*lambda(2)-i*miu(2)*lambda(1)));

e5 = -1*real(gama(1)*lambda(1)*lambda(3)*(miu(3)-miu(2))...
       +gama(2)*lambda(2)*lambda(3)*(miu(1)-miu(3))...
       +gama(3)*(miu(2)-miu(1)));

f5 = real(i*gama(1)*lambda(1)*lambda(3)*(miu(3)-miu(2))...
     +i*gama(2)*lambda(2)*lambda(3)*(miu(1)-miu(3))...
     +i*gama(3)*(miu(2)-miu(1)));

l1 = real(gama(1)*miu(1)*miu(1)*((miu(2)-miu(3)*lambda(2)*lambda(3))+i*(lambda(2)*lambda(3)-1))...
```

```
        +gama(2)*miu(2)*miu(2)*((lambda(1)*lambda(3)*miu(3)-miu(1))+i*(1-lambda(1)*lambda(3)))...
        +gama(3)*lambda(3)*miu(3)*miu(3)*((miu(1)*lambda(2)-miu(2)*lambda(1))+i*(lambda(1)-lambda(2))));

l2 = real(gama(1)*((miu(2)-miu(3)*lambda(2)*lambda(3))+i*(lambda(2)*lambda(3)-1))...
        +gama(2)*((lambda(1)*lambda(3)*miu(3)-miu(1))+i*(1-lambda(1)*lambda(3)))...
        +gama(3)*lambda(3)*((miu(1)*lambda(2)-miu(2)*lambda(1))+i*(lambda(1)-lambda(2))));

l3 = -1*real(gama(1)*miu(1)*((miu(2)-miu(3)*lambda(2)*lambda(3))+i*(lambda(2)*lambda(3)-1))...
           +gama(2)*miu(2)*((lambda(1)*lambda(3)*miu(3)-miu(1))+i*(1-lambda(1)*lambda(3)))...
           +gama(3)*lambda(3)*miu(3)*((miu(1)*lambda(2)-miu(2)*lambda(1))+i*(lambda(1)-lambda(2))));

l4 = real(gama(1)*lambda(1)*miu(1)*((miu(2)-miu(3)*lambda(2)*lambda(3))+i*(lambda(2)*lambda(3)-1))...
        +gama(2)*lambda(2)*miu(2)*((lambda(1)*lambda(3)*miu(3)-miu(1))+i*(1-lambda(1)*lambda(3)))...
        +gama(3)*miu(3)*((miu(1)*lambda(2)-miu(2)*lambda(1))+i*(lambda(1)-lambda(2))));

l5 = -1*real(gama(1)*lambda(1)*((miu(2)-miu(3)*lambda(2)*lambda(3))+i*(lambda(2)*lambda(3)-1))...
           +gama(2)*lambda(2)*((lambda(1)*lambda(3)*miu(3)-miu(1))+i*(1-lambda(1)*lambda(3)))...
           +gama(3)*((miu(1)*lambda(2)-miu(2)*lambda(1))+i*(lambda(1)-lambda(2))));

bb = -(A(3,1)*b1+A(3,2)*b2+A(3,4)*b5+A(3,5)*b4+A(3,6)*b3)/A(3,3);
cc = -(A(3,1)*c1+A(3,2)*c2+A(3,4)*c5+A(3,5)*c4+A(3,6)*c3)/A(3,3);
dd = -(A(3,1)*d1+A(3,2)*d2+A(3,4)*d5+A(3,5)*d4+A(3,6)*d3)/A(3,3);
ee = -(A(3,1)*e1+A(3,2)*e2+A(3,4)*e5+A(3,5)*e4+A(3,6)*e3)/A(3,3);
ff = -(A(3,1)*f1+A(3,2)*f2+A(3,4)*f5+A(3,5)*f4+A(3,6)*f3)/A(3,3);

ll = -(A(3,1)*l1+A(3,2)*l2+A(3,4)*l5+A(3,5)*l4+A(3,6)*l3)/A(3,3);

sgmxh = b1*sgm0(1,1)+c1*sgm0(2,2)+d1*sgm0(1,2)+e1*sgm0(2,3)+f1*sgm0(1,3);
sgmyh = b2*sgm0(1,1)+c2*sgm0(2,2)+d2*sgm0(1,2)+e2*sgm0(2,3)+f2*sgm0(1,3);
sgmzh = bb*sgm0(1,1)+cc*sgm0(2,2)+dd*sgm0(1,2)+ee*sgm0(2,3)+ff*sgm0(1,3);
```

```
sgmxyh = b3*sgm0(1,1)+c3*sgm0(2,2)+d3*sgm0(1,2)+e3*sgm0(2,3)+f3*sgm0(1,3);
sgmxzh = b4*sgm0(1,1)+c4*sgm0(2,2)+d4*sgm0(1,2)+e4*sgm0(2,3)+f4*sgm0(1,3);
sgmyzh = b5*sgm0(1,1)+c5*sgm0(2,2)+d5*sgm0(1,2)+e5*sgm0(2,3)+f5*sgm0(1,3);

sgmxq = l1*q;
sgmyq = l2*q;
sgmzq = l1*q;
sgmxyq = l3*q;
sgmxzq = l4*q;
sgmyzq = l5*q;

sgmh = [sgmxh   sgmxyh  sgmxzh;
        sgmxyh  sgmyh   sgmyzh;
        sgmxzh  sgmyzh  sgmzh];

sgmq = [sgmxq   sgmxyq  sgmxzq;
        sgmxyq  sgmyq   sgmyzq;
        sgmxzq  sgmyzq  sgmzq];

sgm_xyz = sgm0 + sgmh + sgmq;
[temp, sgm_eig] = eig(sgm_xyz);

sgm_stn = T_STN*T_xyz'*sgm_xyz*T_xyz*T_STN';

T = [cos(theta)^2    sin(theta)^2     0          0            0            sin(2*theta);
     sin(theta)^2    cos(theta)^2     0          0            0            -sin(2*theta);
     0               0                1          0            0            0;
     0               0                0          cos(theta)   -sin(theta)  0;
     0               0                0          sin(theta)   cos(theta)   0;
     -sin(2*theta)/2 sin(2*theta)/2   0          0            0            cos(2*theta)];
```

```
    temp = T*[sgm_xyz(1,1) sgm_xyz(2,2) sgm_xyz(3,3) sgm_xyz(2,3) sgm_xyz(3,1) sgm_xyz(1,2)]';
    sgm_rqz = [temp(1) temp(6) temp(5);
               temp(6) temp(2) temp(4);
               temp(5) temp(4) temp(3)];
end

function [T_STN, T_xyz, T_sgm_STN, T_eps_xyz] = ...
    Obtain_Transformation_Matrix_1(beta_z, alpha_z, beta_n, alpha_n)

    ls = cos(beta_n)*cos(alpha_n); ms = cos(beta_n)*sin(alpha_n); ns = -sin(beta_n);
    lt = -sin(alpha_n);            mt = cos(alpha_n);             nt = 0;
    ln = sin(beta_n)*cos(alpha_n); mn = sin(beta_n)*sin(alpha_n); nn = cos(beta_n);

    T_STN = [ls ms ns; lt mt nt; ln mn nn];

    lx = cos(beta_z)*cos(alpha_z); mx = cos(beta_z)*sin(alpha_z); nx = -sin(beta_z);
    ly = -sin(alpha_z);            my = cos(alpha_z);             ny = 0;
    lz = sin(beta_z)*cos(alpha_z); mz = sin(beta_z)*sin(alpha_z); nz = cos(beta_z);

    T_xyz = [lx mx nx; ly my ny; lz mz nz];

    T_sgm_STN = ...
        [ls*ls     ms*ms     ns*ns     2*ms*ns     2*ns*ls     2*ls*ms;
         lt*lt     mt*mt     nt*nt     2*mt*nt     2*nt*lt     2*lt*mt;
         ln*ln     mn*mn     nn*nn     2*mn*nn     2*nn*ln     2*ln*mn;
         lt*ln     mt*mn     nt*nn     mt*nn+mn*nt nt*ln+nn*lt lt*mn+ln*mt;
         ln*ls     mn*ms     nn*ns     ms*nn+mn*ns ns*ln+nn*ls ls*mn+ln*ms;
         ls*lt     ms*mt     ns*nt     ms*nt+mt*ns ns*lt+nt*ls ls*mt+lt*ms];
```

```
    T_eps_xyz = ...
        [lx*lx     mx*mx      nx*nx      mx*nx      nx*lx      lx*mx;
         ly*ly     my*my      ny*ny      my*ny      ny*ly      ly*my;
         lz*lz     mz*mz      nz*nz      mz*nz      nz*lz      lz*mz;
         2*ly*lz   2*my*mz    2*ny*nz    my*nz+mz*ny ny*lz+nz*ly ly*mz+lz*my;
         2*lz*lx   2*mz*mx    2*nz*nx    mx*nz+mz*nx nx*lz+nz*lx lx*mz+lz*mx;
         2*lx*ly   2*mx*my    2*nx*ny    mx*ny+my*nx nx*ly+ny*lx lx*my+ly*mx];

end

function [T_STN, T_xyz, T_sgm_STN, T_eps_xyz] = ...
    Obtain_Transformation_Matrix_2(beta_z, alpha_z, beta_n, alpha_n)

    ls = cos(beta_n)*cos(alpha_n); ms = cos(beta_n)*sin(alpha_n); ns = -sin(beta_n);
    lt = -sin(alpha_n);            mt = cos(alpha_n);             nt = 0;
    ln = sin(beta_n)*cos(alpha_n); mn = sin(beta_n)*sin(alpha_n); nn = cos(beta_n);

    T_STN = [ls ms ns; lt mt nt; ln mn nn];

    lx = -sin(alpha_z);            mx = cos(alpha_z);             nx = 0;
    ly = -cos(beta_z)*cos(alpha_z); my = -cos(beta_z)*sin(alpha_z); ny = sin(beta_z);
    lz = sin(beta_z)*cos(alpha_z);  mz = sin(beta_z)*sin(alpha_z);  nz = cos(beta_z);

    T_xyz = [lx mx nx; ly my ny; lz mz nz];

    T_sgm_STN = ...
        [ls*ls     ms*ms      ns*ns      2*ms*ns    2*ns*ls    2*ls*ms;
         lt*lt     mt*mt      nt*nt      2*mt*nt    2*nt*lt    2*lt*mt;
         ln*ln     mn*mn      nn*nn      2*mn*nn    2*nn*ln    2*ln*mn;
         lt*ln     mt*mn      nt*nn      mt*nn+mn*nt nt*ln+nn*lt lt*mn+ln*mt;
```

```
        ln*ls     mn*ms     nn*ns     ms*nn+mn*ns ns*ln+nn*ls ls*mn+ln*ms;
        ls*lt     ms*mt     ns*nt     ms*nt+mt*ns ns*lt+nt*ls ls*mt+lt*ms];

    T_eps_xyz = ...
        [lx*lx     mx*mx     nx*nx     mx*nx     nx*lx     lx*mx;
         ly*ly     my*my     ny*ny     my*ny     ny*ly     ly*my;
         lz*lz     mz*mz     nz*nz     mz*nz     nz*lz     lz*mz;
         2*ly*lz   2*my*mz   2*ny*nz   my*nz+mz*ny ny*lz+nz*ly ly*mz+lz*my;
         2*lz*lx   2*mz*mx   2*nz*nx   mx*nz+mz*nx nx*lz+nz*lx lx*mz+lz*mx;
         2*lx*ly   2*mx*my   2*nx*ny   mx*ny+my*nx nx*ly+ny*lx lx*my+ly*mx];

end
```